Insights on the upper-mantle structure of the Central-Western Mediterranean from seismic tomography: three study cases

Dissertation

for the doctoral degree
in Natural Sciences at the Department of
Geosciences

at the University of Hamburg

submitted by

Stephen Monna

born in London (United Kingdom)

Hamburg

2013

Als Dissertation angenommen vom Department Geowissenschaften

der Universität Hamburg aufgrund der Gutachten von

Prof. Dr. Torsten Dahm,

Dr. Harley Benz und Dr. Andrea Argnani

Hamburg, den 31. Mai 2013

Prof. Dr. Christian Betzler
Leiter des Departments Geowissenschaften

Preface

This is a cumulative thesis with a first part introducing the main technical aspects (Chapter 2), the study area, and the results coming out of the work I have completed together with my co-authors, which resulted in three papers (Chapter 3 and Appendix 1, 2 and 3). There are two common threads connecting the three study cases presented in this dissertation: 1) They all involve an application of seismic tomography, at various scales. 2) The three areas subject of the studies are part of the Central Western Mediterranean (CWM) region. In Chapter 3 the CWM is introduced, particularly the specific areas which are the object of the papers. Also, there is a discussion part which examines strengths and limits of the applied tomography techniques and delicate aspects in the interpretation of the models, with reference to our cases. Then, there is a separate discussion and conclusions chapter highlighting the main results of the work.
In the second part there are the Appendices that include the three papers, with the titles:

- Rock properties of the upper-crust in Central Apennines (Italy) derived from high-resolution 3-D tomography.

- Three-dimensional P wave attenuation and velocity upper mantle tomography of the Southern Apennines-Calabrian Arc subduction zone.

- New insights from seismic tomography on the complex geodynamic evolution of two adjacent domains: Gulf of Cadiz and Alboran Sea.

The first paper has been accepted an published by Geophysical Research Letters. The second accepted and published by Journal of Geophysical Research- Solid Earth. The third has been accepted by Journal of Geophysical Research- Solid Earth and is now in press.
The plan for this cumulative thesis was decided at the beginning of my work together with my supervisor Prof. Dr. Torsten Dahm. As the papers presented in this thesis have multiple authors, a final Section in the Appendix clarifies the contribution given by me and my co-authors in each paper.

Abstract

In this dissertation seismic tomography is used to find information on two key areas of the Central Western Mediterranean (CWM): the Apennines-Tyrrhenian Sea and the Gulf of Cadiz-Alboran Sea. Tomography is applied to earthquake seismic waveforms at different scales, and 3D models are produced for three study cases. The first study is a local earthquake tomography (LET), of the Colfiorito basin (Umbria-Marche, northern Apennines, Italy), based on crustal earthquakes arrival times from recordings of the 1997 seismic sequence. The second case is a study of the upper-most mantle of Southern Apennines-Tyrrhenian area where both traveltime and attenuation data from local intermediate-depth events have been inverted. The third study proposes a 3D model of the upper-mantle of the Alboran Sea-Gulf of Cadiz area based on seismic arrivals from teleseismic events.

The thesis is structured in the following way: the first part describes the methodology for traveltime and attenuation seismic tomography. Seismic anelastic attenuation is explained through a standard linear solid physical model, and the effect of seismic attenuation on waves propagating in the Earth is considered. Then, I introduce the problem of measuring anelastic attenuation for a seismic wave, concentrating on body waves. I developed an algorithm to calculate t^* which gives a measure of seismic wave attenuation along the wavepath. In particular, I applied the spectral ratio technique to calculate relative t^* (δt^*) on body waves. Then, the LET algorithm FDTOMO was modified so it is possible to invert the δt^* vector to obtain the Q_p (quality factor) 3D distribution. Finally, critical aspects in the interpretation of seismic tomography models are considered.

The second part of the thesis describes the three study cases. The CWM is introduced, the study cases are placed within this general area and presented. In the first case, the Colfiorito crustal structure is examined by inverting for V_p and V_s and by considering their ratio and product. The constant velocity blocks in the 3D inversion (which gives us the scale of this study) have a volume 2 x 2 (horizontal dimension) x 1 km^3. Taking into account the carbonatic sequence known to exist in the area, the interpretation of the 3D model is performed on the basis of changes in porosity, degree of fracturing and fluid pore pressure. We find that there are three volumes with distinct average

lithological properties. Volume A (depth range 1-5 km) is a volume of stiffer rock with higher crack density, saturated with fluid under low effective stress so cracks remain open. This volume could be mainly formed by stiffer, more permeable, high velocity carbonates. Volume B (depth range 2-6 km) contains a softer rock with smaller crack density and greater porosity. B could be a volume where softer, more porous and lower velocity components of the carbonate sequence are mostly present. Volume C is less fractured, as it is a low porosity stiffer rock, state possibly due to greater presence of high velocity anhydrite. This volume is scarcely affected by seismic activity, implying a more plastic behavior. The evolution in time and space of the 1997 seismic sequence (relocated in the 3D model) mostly within the fractured and fluid rich volume A agrees with a poro-elastic explanation where N-S fluid migration through A, possibly guided by the less permeable volume C, is closely related to N-S migration of seismicity.

In the second case, the spectral ratio technique is applied, followed by t (traveltimes) and δt^* inversion, to measure attenuation. Waveform data come from Calabrian arc slab intermediate-depth events ($depth > 70$ km). The V_p and Q_p models resolve the upper-most mantle (down to ~ 200 km depth). The good agreement between the strong Q_p and V_p anomalies confirms that lateral Q_p and V_p variations as mainly being caused by temperature changes and the presence of fluids or melt. This is confirmed by the fact that low Q_p and V_p anomalies are found in areas with very high heat flow. The main features of the model are: a steeply dipping high Q_p/V_p body (the slab), visible down to the bottom of the model, and a main low Q_p/V_p volume adjacent to the slab, found between 100 and 200 km depth, that we interpret as the mantle wedge proper. Branches of low Q_p/V_p which start from the mantle wedge and reach crustal depths, also below Vesuvius, could possibly represent pathways for melt and water. This anomaly could help explain why there are strong geochemical affinities between the subduction-related components of magmas from Vesuvius and Stromboli. Finally, transition zones across which we have strong variations of Q_p (between 50 and 100 %) and V_p (up to 10 %), correspond to important tectonic lines which have been proposed as the southwestern and northeastern limits of the oceanic Ionian lithosphere.

In the third case we obtained a 3D model of the upper-mantle of the Cadiz Gulf-Alboran Sea area starting from teleseismic waveforms. This area has proven to be quite complex, as reflected by its numerous and sometimes conflicting interpretations proposed in literature. Data coverage was extended with respect to previous studies thanks to the use of Ocean Bottom Seismometers (OBS) deployed during the NEAREST EU-project. Several relevant features are evident in the model, which goes down to 600 km depth. A clear high velocity anomaly is imaged for the first time under the NEAREST array, in the Atlantic domain. A second high velocity anomaly is imaged under the Alboran Sea down

to the transition zone. Interestingly, the two anomalies are separated by a low velocity zone, thus excluding the existence of a single slab coming from the Atlantic domain and subducting in the eastern direction below the Alboran Sea. Furthermore, the velocity distribution defines what we interpret as the passage from the Atlantic oceanic to the Iberian continental lithosphere.

Finally, a discussion part highlights the problems that affect the generation of a tomography model and its interpretation. For each case I describe the way these problems affect the specific tomography application and the interpretation of the models, and how they were treated.

Zusammenfassung

In der vorliegenden Dissertation werden, mittels seismischer Tomografie, die Krustenstrukturen zweier Gebiete im westlichen Teil des zentralen Mittelmeeres (CWM) untersucht: (i) der Bereich des Apennin und des Tyrrhenisches Meeres und (ii) der des Golfes von Cadiz und des Alboranbeckens. Tomografie wird auf seismische Wellenformen verschiedener Skalen angewendet, und 3D-Modelle werden für drei Fallstudien berechnet.

Als erste Untersuchung wurde eine Lokale Erdbebentomografie (LET) im Bereich des Colfiorito-Beckens (Umbrien-Marken, Nördlicher Apennin) durchgeführt, die auf Ankunftszeiten von Krustenbeben der seismischen Ereignisse von 1997 basiert. Die zweite Anwendung ist eine Studie des Oberen Mantels im Bereich des Südlichen Apennins und des Tyrrhenischen Meeres, wofür sowohl Laufzeiten, als auch Dämpfungsparameter von mitteltiefen Ereignissen invertiert werden. In der dritten Untersuchung wird, an Hand seismischer Ankunftszeiten von teleseismischen Ereignissen, ein 3D-Modell des Erdmantels, im Bereich zwischen dem Alboranbecken und dem Golf von Cadiz, erstellt.

Im ersten Teil der Arbeit werden die Methoden zur Laufzeit- und Dämpfungstomographie beschrieben. Seismische anelastische Dämpfung wird an Hand eines linearen physikalischen Standardmodells erklärt und der Effekt der seismischen Dämpfung, auf die sich im Erdkörper ausbreitenden seismischen Wellen, beschrieben. Als nächstes wird das Problem der Messung anelastischer Dämpfung von seismischen Wellen erläutert.

Im Rahmen der vorliegenden Arbeit wurde ein Algorithmus zur Berechnung des Parameters t^* entwickelt, der ein Maß für die Dämpfung von seismischen Wellen entlang des Strahlweges ist. Dazu wurde eine *Spectral-Ratio* Technik angewendet, die es gestattet, das relative t^* (δt^*) zu berechnen. Der LET Algorithmus FDTOMO wurde modifiziert, wodurch es nun möglich ist, den δt^* Vektor zu invertieren und die 3D-Verteilung des Q_p (Qualitätsfaktor) zu erhalten. Abschliessend werden kritische Aspekte bezüglich der Interpretation seismischer Tomografiemodelle diskutiert.

Im zweiten Teil der Arbeit werden drei Fallstudien beschrieben. Nach einer Einführung über das zentrale Mittelmeer, werden die einzelnen Untersuchungsgebiete vorgestellt. Im ersten Fall wird die Krustenstruktur unter dem Colfiorito-Becken untersucht, indem V_p und V_s invertiert, und sowohl ihr Verhältnis, als auch ihr Produkt, berücksichtigt werden. Die in der 3D-Inversion verwendeten Blöcke konstanter Geschwindigkeiten (deren

Dimension von der Grösse des Untersuchungsgebiet abhängen), haben ein Volumen von 2 x 2 (horizontal) x 1 km^3. Unter Berücksichtigung der für das Untersuchungsgebiet typischen karbonatischen Abfolge, wird die Interpretation des 3D-Modells auf der Basis von Porösitätsänderungen, dem Grad der Rissbildung und des Gesteinsporenfluiddrucks durchgeführt. Es wurden drei Volumen mit ausgeprägten mittleren lithologischen Eigenschaften gefunden. Volumen A (Tiefenbereich 1-5 km) besteht aus Fluid gesättigtem, sprödem Gestein mit einer hohen Rissdichte, das unter niedriger Spannung steht, so dass die Risse offen bleiben. Dieser Bereich könnte in erster Linie aus spröderen Karbonaten hoher Permeabilität und Geschwindigkeit bestehen. Das Volumen B (Tiefenbereich 2-6 km) setzt sich aus weicherem Gestein der Karbonatserie zusammen, das durch geringere Rissdichte, grössere Porösität und niedrigere Geschwindigkeiten charkterisiert ist. Das Volumen C ist weniger zerrüttet und besteht aus hartem, weitgehend rissfreiem Gestein, das sich wahrscheinlich durch das Vorkommen von Anhydrit (hohe seismische Geschwindigkeit) erklären lässt. Aufgrund seines plastischen Verhaltens, ist dieses Volumen durch schwache seismische Aktivität charakterisiert. Die räumliche und zeitliche Entwicklung der seismischen Sequenz von 1997, die im 3D-Modell grösstenteils in dem stark von Rissen durchsetzten und fluidreichen Volumen A relokalisiert wurde, steht im Einklang mit einer poroelastischen Deutung, bei der die Fluidmigration in Richtung A (N-S), möglicherweise beeinflusst durch das weniger permeable Volumen C, in direkter Beziehung zur N-S-Migration der Seismizität steht.

Im zweiten Fall wird die *Spectral-Ratio*-Technik angewendet, gefolgt von der Inversion der Parameter t (Laufzeit) und δt^*. Wellenformdaten stammen von seismischen Ereignissen aus dem intermediären Tiefenbereich des Kalabrischen *Slabs* ($Tiefe > 70$ km). Die V_p und Q_p Modelle lösen den Bereich des Oberen Mantels bis in eine Tiefe von $\sim$ 200 km auf. Die gute Übereinstimmung zwischen den hohen Q_p und V_p Anomalien bestätigt, dass laterale Q_p und V_p Variationen, vorallem durch Temperaturänderungen und durch die Präsenz von Fluiden oder Schmelze verursacht werden. Dies wird dadurch bestätigt, dass niedrige Q_p und V_p Anomalien in Bereichen mit hohem Wärmefluss gefunden wurden. Die Hauptmerkmale der Modelle sind: Eine steil einfallende Struktur mit hohen Q_p/V_p Werten (*slab*), die bis zum unteren Rand des Modell fortsetzt, und ein benachbarter Bereich zwischen 100 und 200 km Tiefe, mit vorrangig niedrigen Q_p/V_p Werten, die als Mantel-*Wedge* interpretiert werden können.

Zonen niedriger Q_p/V_p-Werte, die vom Mantel-*Wedge* bis in krustale Tiefen reicht, wie beispielsweise auch unter dem Vesuv, können als Aufstiegswege von Schmelze und Wasser interpretiert werden. Diese Anomalie könnte erklären, warum geochemische Affinitäten zwischen den der Subduktion zugeschriebenen Komponenten des Magmas von Vesuv und Stromboli bestehen. Transitionszonen in denen starke Q_p-Variationen (zwischen 50

und 100 %) beobachtet werden, stimmen mit wichtigen tektonischen Linien überein, die als südwestlicher und nordwestlicher Rand der ozeanischen Ionischen Lithosphäre vorgeschlagen wurden.

Im dritten Fall wurde für den Bereich des Golfes von Cadiz und des Alboranbeckens, unter Verwendung teleseismischer Wellenformen, ein 3D-Modell des Oberen Mantels erstellt. Zahlreiche, in der Literatur oft kontroverse Interpretationen, zeugen von der Komplexität der geodynamischen Entwicklung dieses Gebietes. Im Vergleich zu vorherigen Untersuchungen war die Datenüberdeckung, aufgrund zur Verfügung stehender Daten von Ozeanboden-Seismometern (OBS), die im Rahmen des NEAREST EU-Projekt installiert wurden, besser. Verschiedene signifikative Merkmale sind in dem bis in 600 km Tiefe reichenden Modell zu erkennen: Im Atlantischen Bereich, unterhalb des NEAREST-*Arrays*, wurde erstmals eine Hochgeschwindigkeitsanomalie gefunden. Eine zweite Zone hoher Geschwindigkeiten zeigt sich unterhalb des Alboranbeckens, hinunter bis zur Transitionszone. Interessanterweise sind diese beiden Anomalien durch eine Niedergeschwindigkeitsanomalie getrennt, womit die Existenz eines einzigen *Slabs* der vom Atlantik in östlicher Richtung bis unter das Alboranbecken subduziert, ausgeschlossen werden kann. Die Geschwindigkeitsverteilung definiert, was als Übergang vom Atlantischen Ozean zur Iberischen kontinentalen Lithosphäre interpretiert werden kann.

Im abschliessenden Diskussionsabschnitt werden die Problematiken diskutiert, die bei der Erstellung eines tomografischen Modells und seiner Interpretation auftreten können. Für jeden spezifischen Fall wird beschrieben, welchen Einfluss die einzelnen Probleme auf die spezifische tomografische Anwendung und die Modellinterpretation haben, und wie diese berücksichtigt werden.

1 Introduction

Seismic tomography in the last decades has given a fundamental contribution to our knowledge of the Earth. The global models, for example PREM (Dziewonski and Anderson 1981) or AK135 (Kennett et al. 1995), represent average properties of the earth, which depend, in this first approximation, only on depth. The radial symmetry of the global models brakes down as soon as we consider key elements of plate tectonics. The existence of subducting lithosphere, for example, implies strong lateral heterogeneity. Tomography gives us 3D models that take into account the lateral changes of seismic quantities that give us information on the physical state and chemical composition of the rock. In spite of its usefulness seismic tomography cannot guarantee a unique solution. Other independent information is needed to constrain the solution and obtain a more reliable interpretation of the tomography models. Although most tomography studies present only models of seismic velocity, anelastic attenuation measurements can give very useful complementary information. This is particularly true in cases where temperature plays a key role, as for example in subduction systems. In fact, seismic attenuation or its reciprocal quantity, the quality factor Q, is more sensitive to temperature variations than seismic velocity V, so while variations in Q can be used to image hot mantle material surrounding the slab, variations in V are more useful in imaging the colder fast slab (Romanowicz 1995; Roth et al. 2000). I was able to calculate 3D attenuation models after modifying the FDTOMO code by Benz et al. (1996), which, in its standard form, inverts for traveltime data.

In this dissertation seismic tomography is applied at different scales (crust, uppermost-mantle, upper mantle) to three areas within the Central-Western Mediterranean (CWM): the Central-Northern Apennines, the Calabrian Arc-Southern Apennines subduction system (Italy), and the SW Iberian margin-Gulf of Cadiz (Iberian peninsula). The crust and the upper-mantle of these key areas of the CWM will be investigated using body wave earthquake data. The development of these three areas is linked to the complex evolution in geological time of the CWM, an evolution which is still open to debate. A unifying model has been proposed (e.g. Malinverno and Ryan 1986; Lonergan and White 1997; Faccenna et al. 2004) where the Arcs of Gibraltar and Calabria are sym-

metrical end-members of the opening of the CWM which started about 35 Ma ago. In this view, subduction with sinking and roll-back was the main driving force, and slab-break off played an important role (Wortel and Spakman 2000). This model is not unanimously accepted: while there is common agreement that subduction and roll-back mechanism was a key factor and that it is possibly still active in the formation of the Liguro-Provençal and Tyrrhenian basins, the evolution of the SW Iberian margin is very controversial. Thanks to the inclusion in the tomographic inversion of long-term data series recorded at the seafloor, it was possible to investigate the little known upper mantle west of the Gibraltar Strait. In this new perspective we could put new constraints on the proposed geodynamic models for the area. An open question we tried to answer regards the present relation of the Atlantic and Alboran domains.

The theory of seismic tomography is introduced in Chapter 2, first for traveltime and subsequently for attenuation data. The physical meaning of seismic attenuation is briefly treated. A main part of this dissertation is concentrated on the development of an algorithm to measure seismic attenuation based on the spectral ratio method and on the calculation of 3D seismic attenuation models using the modified FDTOMO code. The spectral ratio method is described, implemented within an algorithm, and tested to prove its validity.
Chapter 3 starts with a general geodynamics overview of the CWM region. The three areas of interest in the CWM are briefly introduced. Then the main results of the tomography studies are described (the published and in press papers are in the Appendices). Seismic tomography applied at different scales brings out properties that reflect the geodynamic evolution of the CWM in the following cases:

- The crust (down to $\sim$ 12 km) at the border between the Central and Northern Apennines (local earthquake tomography based on crustal seismicity). The evolution of seismicity in space-time is connected in this study to the rock types found in the area and their structural pattern. These rock types reflect the marine paleoenvironmental setting found within the CWM mainly from the Mesozoic. The structural pattern was determined by the tectonic processes shaping the thrust and fold Apennines chain from the late Cenozoic to present.

- The uppermost-mantle (down to $\sim$ 200 km) of the Calabrian-Southern Apennines system (local earthquake tomography based on intermediate depth seismicity). This is very likely the only area in the CWM where there is active subduction. In this area there is also very recent extension, very high heat flow values and strong topography variations of the Moho and lithosphere. The 3-D models of

seismic attenuation and velocity can improve our knowledge of the slab/mantle wedge structure and be a starting point in determining the physical state of the asthenosphere (i.e., its temperature, the presence of melt and/or fluids) and its relation to volcanism found in this part of the CWM.

- The upper-mantle and mantle transition zone (down to 600 km depth) of the SW Iberian margin (teleseismic tomography based on events with epicentral distance $> 30°$). The use of OBS data allows us to better resolve the high velocity anomaly below the Alboran Sea, to have a first image at higher resolution then previously proposed of the upper-mantle of the Gibraltar Strait sector, and to establish how the two domains, west and east of the Gibraltar Strait, are related. There results can help us put some constraints on the geodynamic models that have been proposed so far for this part of the CWM.

Discussion Section 3.4 focuses first on critical aspects affecting the quality of tomography inversions with reference to our particular application of the methods. Strong and weak points are analyzed in each application. In particular, different factors which affect the resolution of the calculated seismic models are considered. The second part of the discussion is centered on the problems found in the interpretation of the tomography models. As there are various factors that determine the reliability of a model, recipes are necessary to reduce the ambiguity inherent in a tomography inversion solution. A description is given of the steps taken in the three works presented in this dissertation to reduce ambiguity and to arrive at a more solid interpretation.
In Chapter 4 the general conclusions of the dissertation are summarized.

2 Seismic tomography from traveltime and attenuation data

In this chapter there will be a brief presentation of discrete inverse theory underlying the seismic tomography methods used in this dissertation (for a more complete presentation please refer to Menke 1984). The basic equations of traveltime seismic tomography will be introduced. A brief presentation of the Local Earthquake Tomography (LET) and teleseismic tomography techniques used in this dissertation will be presented. Seismic attenuation is introduced. Then, in parallel with the traveltime case, the theory for seismic attenuation data inversion is introduced. The spectral ratio method used to obtain seismic attenuation data is explained. Following, there is the application of the theory, a description of the algorithm implemented to calculate the attenuation model, and the synthetic tests used to validate it. Finally, there is a discussion on the quality and interpretation of seismic tomography models, with specific reference to our study cases.

2.1 Seismic Tomography: basic theory

The application of seismic tomography includes the solution of an inverse problem, i.e. through an inverse procedure we find properties of the Earth's interior starting from (seismic) measurements collected at its surface. An inverse problem can be described by the general equation

$$\mathbf{d} = G(\mathbf{m}) \tag{2.1}$$

where $\mathbf{d}$ is the (known) data which depends on the (unknown) model $\mathbf{m}$ through G, in a possibly non-linear way, depending on the theory chosen to describe the problem. Often the problem is linearized and equation (2.1) can be expressed in the following way, similarly to what is done with the Taylor expansion of functions

$$\delta\mathbf{d} \simeq G\delta\mathbf{m} \tag{2.2}$$

and G, often called the *kernel* or the Jacoby matrix, becomes an NxM matrix of partial derivatives of the components of the N-dimensional vector $\mathbf{d}$ with respect to the components of the M-dimensional vector $\mathbf{m}$. The objective of the inversion procedure is to find a set of parameters $\mathbf{m}$ which best fits the data (in a way to be defined). At first sight it seems that the inversion problem can be solved simply by calculating the inverse of a matrix, but this is not obvious as G is generally not a square matrix, and the theory of the inverse of a rectangular matrix (*generalized inverse*) needs to be introduced. So, even for the simplified linear problem, a solution is not guaranteed and if it exists it is usually not unique for seismic tomography. This is often the case for inverse problems, and so they are considered mathematically ill-posed problems and need to be regularized by introducing *ad hoc* parameters which make the problem more treatable. Furthermore, in the case of seismic tomography, G has many elements therefore appropriate mathematical algorithms for large matrices are needed. We will see in equation 2.10, an example of regularization procedure for the least squares case. In the presented study cases, $\mathbf{d}$ will consist of quantities that are measured on seismic waveforms (arrival times and spectral ratios) and the unknown model parameters will be seismic velocity and attenuation distributions in a 3D volume which is appropriately defined in each case.

Now we will develop (2.2) for the case of velocity inversion and later we will show that a similar equation applies for attenuation inversion. Let us consider the line integral expressing the traveltime

$$t_\gamma = \int_\gamma \frac{ds}{V} \tag{2.3}$$

for the γ_{th} wavepath, where V, the velocity along the wavepath, is the unknown. As the wavepath depends on velocity distribution the relation between t and V is non-linear. The linearization procedure is performed by starting from a known velocity distribution V_0 and perturbating it. Often this calculation is carried out in a discrete manner as the Earth volume under study is divided into N_{cells} cells. Then (2.3) becomes

$$t_{ij} = \sum_{l=0}^{N_{cells}} (r_\gamma)_l / V_l = \sum_{l=0}^{N_{cells}} (t_\gamma)_l \tag{2.4}$$

V_l is the velocity in cell l, $(r_\gamma)_l$ is the wave-path length in cell l, with $(r_\gamma)_l = 0$ when the wave does not go through cell l, and $(t_\gamma)_l$ is the traveltime in cell l. This equation is re-written for convenience as $t_\gamma = \sum_{l=1}^{N_{cells}} (r_\gamma)_l S_l$ where $S_l = 1/V_l$ is the slowness vector. Then the linearized version of this equation is obtained by perturbating the slowness field starting from a known reference slowness distribution S_0, $\delta t_\gamma = \sum_{l=0}^{N_{cells}} \frac{\partial (t_\gamma)_l}{\partial S} |_{S_0} \delta S_l$ this for all the paths γ which correspond to all recorded N traveltimes. Then considering a matrix form we arrive at equation 2.2 used to invert for the slowness (velocity) field

$$\delta \mathbf{t} \simeq G\delta \mathbf{S} \tag{2.5}$$

and G is a NxM matrix ($M = N_{cells}$) whose elements are the partial derivatives which can be calculated, and represent the wave-path length changes in each cell for each station-event pair due to the slowness perturbation in that cell. The slowness perturbations with respect to a reference model are contained in the vector $\delta\mathbf{S}$.

The inversion is performed with an iterative procedure and matrix G is calculated at each step. The objective is to minimize the misfit between the observations and the traveltimes calculated through (2.5) at every step. In this algorithm, as is often the case, the misfit is the least squares measure.

To show its similarity to the velocity inversion, we now introduce the main equation for attenuation inversion

$$t^* = \int_i \frac{ds}{Q(f,r)V(r)} \tag{2.6}$$

where, with reference to equation 2.3, t^*, the data, plays the role of t, and Q the unknown quality factor plays the role of V and gives a measure of the attenuation of seismic waves. V is as before the velocity field, which now is considered known. In analogy to equation 2.4 the discrete version for t^* is

$$t^*_\gamma = \sum_{l=0}^{N_{cells}} (r_\gamma)_l / Q_l V_l = \sum_{l=0}^{N_{cells}} (t_\gamma)_l / Q_l \tag{2.7}$$

The physical meaning of Q and t^* will be clarified in Section 2.2.

2.1.1 Local Earthquake Tomography (LET)

Local Earthquake Tomography (LET) is local in the sense that traveltimes, from P and/or S waves, come from local earthquakes included in the study volume, and short period waveforms (e.g. $\sim 1 - 10$ Hz) are considered. A very important aspect in LET is the choice of the reference slowness distribution used to solve the linearized inverse problem (see previous paragraph). In the two LET studies here presented (Central Apennines and Calabrian Arc) the initial 3D model is constructed as a plane layer model based on the optimal 1D model. This optimal 1D model is calculated using the VELEST algorithm by Kissling et al. (1994, 1995) by minimizing the L_2 norm of traveltime residuals, starting from 1D models available in literature. This input model is the one that should best represent the average properties of the particular Earth volume that is under study. Furthermore, the seismic events are re-located in this model. The LET algorithm applied in this dissertation was proposed by Benz et al. (1996). In this

method the traveltime calculation is performed following the finite difference technique of Podvin and Lecompte (1991) which solves the Eikonal equation and reconstructs the propagation times of the wavefront on a grid. We are interested, in particular, in the first P and S phases arrivals. As the hypocenters are considered unknown, equation 2.5 needs another term and so it becomes (see for example Benz et al. 1996)

$$\delta \mathbf{t} = A\delta \mathbf{H} + G\delta \mathbf{S} \tag{2.8}$$

where $\mathbf{H}$ is the matrix of hypocenter partial derivatives.

Inversion of the hypocenter and slowness parameters can be performed separately thanks to the mathematical properties of the matrices (Pavlis and Booker 1980; Spencer and Gubbins 1980) and an equation of the same form of 2.5 is derived for slowness

$$\delta \mathbf{t}' = G'\delta \mathbf{S} \tag{2.9}$$

To regularize the inversion procedure a smoothing constraint is applied that controls the degree of model roughness (through the Laplacian of the velocity field). In other words, smoothing imposes some degree of continuity in the slowness distribution across blocks that are spatially close. Then the regularized version of equation 2.9 is

$$\begin{bmatrix} G' \\ kL \end{bmatrix} * \delta \mathbf{S} = \begin{bmatrix} \delta \mathbf{t}' \\ 0 \end{bmatrix} \tag{2.10}$$

L includes the smoothness constrains and k is a weighting parameter, to be chosen empirically for each problem, that controls the trade-off between the smoothness of the model and how well the data is fit. The solution of 2.10, i.e. the inversion for the slowness (velocity) structure, is performed with the least squares QR decomposition (LSQR) (Paige and Saunders 1982). As previously mentioned, the solution of the equations implies a discretization procedure (or parametrization) of the Earth volume under study, in particular in this method, cells. An optimal inversion cell size is controlled by the source-receiver geometry (i.e. distance between adjacent stations and the distribution of seismicity) and determined by trial inversions carried out with different block sizes and tests on synthetic data.

2.1.2 Teleseismic Tomography

Teleseismic tomography, unlike LET, is based on the inversion of traveltime data coming from distant earthquakes outside the study volume (in our case epicentral distance is between 25° and 95°). It is possible with teleseismic tomography to image greater depths

than with LET. In the presented Cadiz Gulf-Alboran Sea case, the bottom of the model is at 600 km depth (Appendix 3). The technique we employed is based on the procedure developed by Rawlinson et al. (2006) which maps relative arrival time residuals as three-dimensional P-wave velocity anomalies. The advantage of using relative residuals is that they are not significantly affected by (1) source mislocations (errors in origin time and hypocentral location), (2) differences between the actual and the reference source-receiver ray path below the investigated Earth volume, (3) large-scale variations in mantle structure (Aki et al. 1977; Evans and Achauer 1993). On the other hand, relative traveltimes do not produce absolute velocity values, but only relative perturbations calculated starting from an initial velocity model. In fact, this is a shortcoming of all relative residual inversions, independently of the type of observed parameter (see for example mathematical explanation in Appendix 2). In spite of this critical point for this type of inversion, a previous paper has shown that if the target volume is large enough, we may assume that the horizontally averaged velocities are close to the layer velocity of the initial model (Leveque and Masson 1999), which should be representative of the correct regional structure. To approximate the horizontal average velocities for the Earth volume under study, we corrected the arrival times for the station topography/bathymetry (negative values for the seafloor instruments). Also, the predicted traveltimes, based on the AK135 global velocity model (Kennett et al. 1995), were corrected for sedimentary and crustal structure.

Four velocity models were applied for the crustal correction (Table 1 in paper 3). These models were extracted from recent studies, and from the European Moho depth map by Grad et al. (2009). We consider these models as representative of the different average structure of the continental and oceanic domains within the study area (see inset in Figure 3.12). For more information about the applied teleseismic tomography method please refer to Appendix 3.

2.2 Seismic Anelastic attenuation: basic theory

In its path from the source to the receiver, the decrease of a seismic wave amplitude is caused by several processes. In some processes, elastic energy is conserved and redistributed within the wavefield: geometric spreading, scattering, and multipathing. On the other hand, elastic energy is not conserved and is converted into heat by a viscoelastic process, called intrinsic attenuation (or anelasticity, for an introduction to seismic wave anelasticity see, for example, Stein and Wysession 2003). If we consider a wave, the fraction of energy converted to heat during a cycle of loading (e.g., wavelength) can be expressed by the quality factor Q, defined as $Q^{-1} = -\Delta E/E$ ($\Delta E > 0$). The

decay of energy in a loading cycle can be measured in time at a fixed position (as for a standing wave, e.g, free oscillations) or in space, which is the form considered in this dissertation. In the case of linear stress-strain relationship amplitude $A \sim E^{1/2}$ and for small variations of energy in a cycle we have (this part of the treatment follows Aki and Richards 2002):

$$Q^{-1} = -2\Delta A/A \tag{2.11}$$

Also, for small variations we can consider

$$\frac{dA}{dx} = \frac{\Delta A}{\lambda} \tag{2.12}$$

with wavelength $\lambda = c/f$ (c is the phase velocity). Then, using 2.11, after integrating, 2.12 becomes:

$$A(x) = A_0 exp[-\frac{fx}{cQ}] \tag{2.13}$$

which is the spatial decay of the amplitude of a plane wave in a homogeneous medium. In a more realistic case (as is the heterogeneous Earth) we need to consider energy dissipation due to the other factors mentioned above, as for example geometric spreading. Furthermore, this relation assumes a constant Q along the wave-path; we will introduce a more general definition, in which Q can vary along the wave-path, and connect it to the definition of the quantity t^* (equation 2.6), that we use to measure the anelastic attenuation of seismic waves. To establish this connection we consider seismic wave amplitudes in the frequency domain. The amplitude spectrum of seismic waves measured at a receiver i from source j can be written as

$$A_{ij} = A_{0j}(f; \theta_i, \phi_i) S_i(f) A_{INSi}(f) B_{ij}(f) \tag{2.14}$$

where f is frequency, θ_i, ϕ_i the propagation direction from source j to receiver i, $A_{0j}(f; \theta_i, \phi_i)$ the source spectrum, $S_i(f)$ the receiver site effect, A_{INSi} the instrumental transfer function, $B_{ij}(f)$ the transfer function describing the amplitude decrease as the signal propagates along a ray inside crust + mantle. In particular $B_{ij}(f) = g_{ij} exp(-f\pi t^*)$ and

$$t^* = \int_i \frac{ds}{Q(f,r)V(r)} \tag{2.6}$$

As previously introduced, Q is the quality factor, V the velocity (P-wave or S-wave), the integration is on the ray path from source j to receiver i. t^* has the dimensions of time (e.g., of a few seconds length) and for the homogeneous case $t^* = traveltime/Q$. $g_{ij}(r)$ is a frequency independent factor describing the geometrical spreading of the wavefront. The term $B_{ij}(f)$ is a generalization of equation 2.13, which is valid for

the spatial decay of a plane wave in a homogeneous medium. In this more general case Q varies along the wavepath so an integral (t^*) appears in the exponential. The goal of most studies of seismic attenuation is to determine $Q(r)$ from measurements of $A(f)$. Here Q is an effective Q, which means it includes both the effects of intrinsic attenuation (elastic energy to heat conversion) and apparent (scattering) attenuation (see also 2.3.4). The problem has several unknowns, apart from $Q = Q(f, r)$, there is $A_0(f; \theta, \phi)$, $G(r)$, and the ray path itself. The basic approach is to either assume values or functional forms for the unknowns based on theory or observations or to remove the unknowns from the problem by spectral division. In particular, I applied the spectral ratio method (introduced in Section 2.3.1) to waveforms from intermediate-depth events in the Calabrian arc subduction zone.

Now a brief physical explanation of anelasticity (or visco-elasticity) will follow. Ludwig Boltzmann (Boltzmann 1874) was the first to introduce general mathematical relations describing the stress-strain relation for a visco-elastic solid. When visco-elasticity is involved in a deformation, in addition to an instantaneous elastic response, there is a delayed strain response. This means that the relation between stress and strain in the material of interest changes with time. The time variation of stress depends on strain and a stress relaxation function, while the time variation of strain depends on stress and a creep response function. Stress relaxation and creep response functions depend on the particular physical model used to describe the visco-elastic material. If strain amplitudes and stresses are small, then the superposition principle is valid and there is a linear relation between strain and applied stress. For a small stress $d\sigma$ applied at time t', the strain of the material is given in general by $d\epsilon(t) = J(t - t')d\sigma(t')$ where $J(t)$ is the creep response function (see for example Karato 2008). The response depends on the time delay $t - t'$.

In the case of a purely elastic solid $\sigma = E_1\epsilon$, and when a step strain function is applied: $\sigma = E_1 H(t)$ ($H(t)$ is the Heaviside function). On the other hand, in the anelastic case there is an other term $\psi(t)$, which is the relaxation function (from this point we follow the work of Kanamori and Anderson 1977).

$$\sigma(t) = E_1 H(t) + \psi(t) \tag{2.15}$$

A simple physical model used to understand the anelastic behavior of a material with a single relaxation mechanism, which can be applied to the short-term rehology of the Earth, is the standard linear solid (also called Zener model; e.g, Karato 2008). This model is composed by a spring in parallel to a dashpot plus another spring (Figure 2.1a). In this case 2.15 becomes

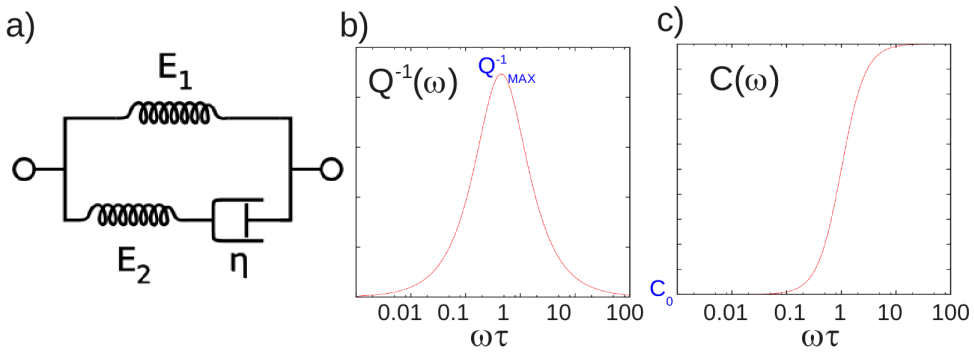

Figure 2.1: Standard linear solid. a) The physical model. b) Attenuation. c) Phase velocity dispersion. a) From http://www.enotes.com/

$$\sigma(t) = E_1 H(t) + E_2 e^{-t/\tau} \tag{2.16}$$

Spring E_1 represents the instantaneous purely elastic response, while dashpot η and spring E_2 represent the time-delayed visco-elastic response (relaxation function). In the case of harmonic strain, $\epsilon \simeq e^{i\omega t}$, and when the anelastic effect can be considered small (compared to the elastic term), it can be shown (see Kanamori and Anderson 1977) that for a plane wave traversing this visco-elastic medium:

$$Q^{-1}(\omega) = \frac{E_2}{E_1} \frac{\omega\tau}{1 + (\omega\tau)^2} \tag{2.17}$$

and

$$C(\omega) = C_0[1 + \frac{E_2}{2E_1} \frac{(\omega\tau)^2}{1 + (\omega\tau)^2}] \tag{2.18}$$

where $C_0 = (E_1/\rho)^{1/2}$. This models predicts an absorption peak, which depends on frequency and relaxation time constant $\tau = \eta/E_2$ (Figure 2.1b; Kanamori and Anderson 1977), and a dispersion curve which predicts (correctly for seismic waves) that higher frequencies arrive earlier (Figure 2.1c). For periods that are very short compared to τ the system behaves mostly in an elastic way, while for long periods the system behaves in a viscous way. The maximum absorption is obtained for waves at frequency $\omega = 1/\tau$. Observations on the attenuation of seismic waves travelling in the Earth have shown that Q is independent or weakly dependent on frequency, i.e $Q \sim \omega^\gamma$, for most seismological cases $\gamma = 0.2 - 0.4$ (e.g., Sipkin and Jordan 1979). This anelastic behavior of the Earth can be explained with a model based on the superposition of standard linear solids with different relaxation times, leading to a more realistic band-limited constant Q (Liu et al. 1976). Theoretical works started from a weak power-law frequency dependence of Q

to explain the viscoelastic behavior of the earth and model the propagation of seismic waves in an viscoelastic medium (e.g., Müller 1983).
Several physical mechanisms have been proposed to cause the dissipative process of intrinsic attenuation in rocks: frictional losses in solid rocks (friction at grain boundaries or cracks), viscous losses in fluids, and fluid flow in (partially) saturated porous rocks. Such mechanisms imply that attenuation is mainly controlled by quantities describing the physical state (e.g. confining pressure, temperature, saturation with fluids) rather than the chemical composition of the material under investigation (e.g. Haberland and Rietbrock 2001, and references therein). Temperature has an important effect on the attenuation of seismic waves travesring the Earth at all depths. Theoretical calculations (Karato 1993) and experimental work (e.g., see the review by Karato and Spetzler 1990, and references therein) have shown that the temperature derivative of velocity significantly increases if anelasticity is included. Large variations of seismic wave velocities can be explained by small variations in temperature just by incorporating the effect of anelasticity due to viscous flow (Karato 1993, Karato and Karki 2001). The above considerations can be expressed in mathematical terms as (Karato 1993)

$$\partial lnV/\partial T = \partial lnV_0/\partial T - (Q^{-1}/\pi)(H^*/RT^2) \tag{2.19}$$

where H^* is the activation enthalpy, R is the gas constant, Q the quality factor (frequency independent), T temperature, V_0 a reference seismic velocity. The first term on the right side expresses the elastic temperature dependence on T due to thermal expansion (also called anharmonic efect), while the second expresses the anelastic dependence of V versus T through Q. In more direct terms, we expect that if there are strong temperature variations in an area of interest, then there will be lateral variations of V that follow variations in Q. Most laboratory measurements on temperature dependence of V are done at frequencies that are very high ($\simeq 1MHz$) compared to seismic frequencies and are actually only measuring the first (elastic) term (Karato 1993). Such results carry the important implication that any calculation, or even a qualitative analysis, of temperature distribution starting from seismic velocity tomography models needs to take into account anelastic effects, thus measures of Q. Figure 2.2 illustrates the behavior of equation 2.19 for olivine (upper mantle). Equation 2.19 can be re-written as:

$$\partial V/V = \partial V_0/V_0 - [(Q^{-1}/\pi)(H^*/RT^2)] * \partial T \tag{2.20}$$

from which we can calculate the temperature variation which corresponds to a given velocity variation (for Vp or Vs). For example, a Vs variation of -6 % (with $Q \simeq$

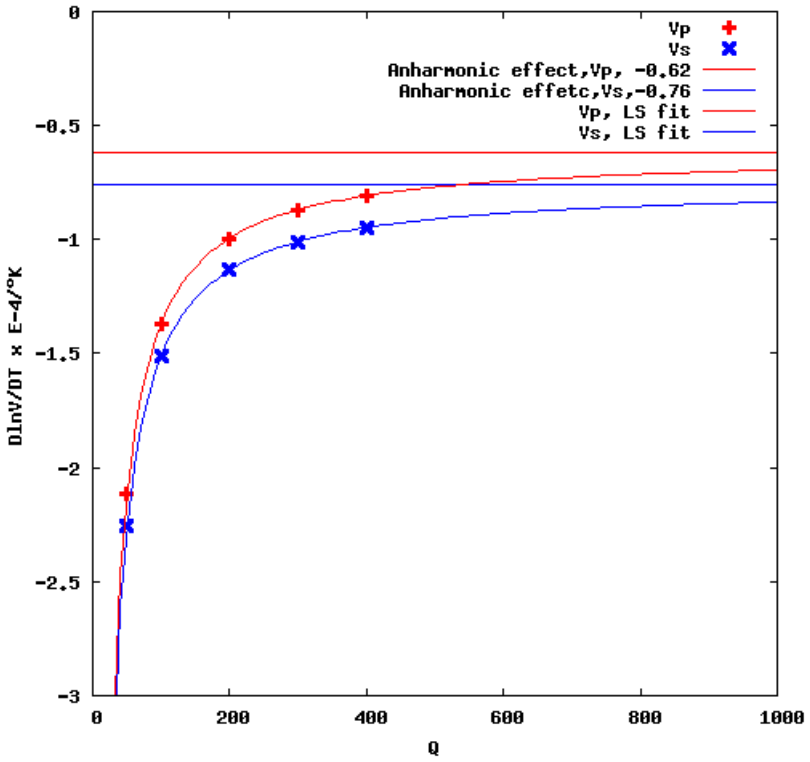

Figure 2.2: Temperature derivatives of seismic wave velocities. Values are calculated from equation 2.19, with $H^* = 500KJ/mol$, $T = 1600°K$, as in Karato and Spetzler 1990.

Rock State Change	Seismic Parameter Change			
	Qs	Qp	Qp/Qs	Vp/Vs
Increase temperature	smaller	smaller	larger	larger
Form partial melt	much smaller	smaller	much larger	much larger
Increase fracture abundance	smaller	smaller	larger	larger
Add gas or supercritical	larger	much smaller	much smaller	smaller

Table 2.1: Summary of changes in seismic parameters due to changes in rock state. From Sanders et al. 1995.

100), corresponds to a temperature variation of $\Delta T \simeq 790°K$, when only the thermal effect is considered, while $\Delta T \simeq 438°K$ if the anelastic contribution is included. The anharmonic term corresponds to the case $Q = \infty$ and the values for $\partial lnV_0/V_0$ (horizontal asymptotes in Figure 2.2) are from the experimental work of Isaak (1992). Apart from temperature, there are other important factors which can affect seismic velocities. Fluids, in particular water or hydrogen, can decrease mantle rock viscosity and thus decrease Q and V. Finally, chemical composition heterogeneity can also determine lateral changes in V and Q distribution. This could happen where, for example, there is a lateral passage from oceanic to continental lithosphere. Establishing in a quantitative way the relative contribution of temperature, water content and chemical composition variations to variations of V and Q is not an easy task. Table 2.1 shows in a qualitative way how seismic parameters vary within the continental crust due to the key factors of temperature, melt, rock fractures, and fluids, with respect to a normal crust or upper-mantle. A main objective in the presented study cases is to identify these key factors from the changes of seismic parameters imaged in the 3D tomography models.

2.3 Seismic attenuation tomography

2.3.1 Spectral ratio technique

As we have seen in paragraph 2.1, a measure of the anelastic attenuation of seismic waves is given by t^* (equation 2.6). As mentioned earlier, to measure t^* we apply the spectral ratio technique. The description of the spectral ratio technique and local attenuation tomography is mostly adapted from Teng (1968) and Sanders (1993). We have seen that for a plane wave traversing a heterogeneous medium the amplitude spectrum of seismic waves measured at a receiver i from source j can be written as:

$$A_{ij} = A_{0j}(f;\theta_i,\phi_i)S_i(f)A_{INSi}(f)B_{ij}(f) \tag{2.14}$$

with $B_{ij}(f) = g_{ij}exp(-f\pi t^*)$ and

$$t^* = \int_i ds \frac{ds}{Q(f,r)V(r)} \tag{2.6}$$

the unknowns, apart from $Q = Q(f,r)$, are $A_0(f,\theta,\phi)$, $G(r)$, and the ray path itself. The strategy here followed is to remove the unknowns from the problem by spectral division and to assume the following simplifying hypotheses:

Hypothesis 1. Although generally Q depends on f, it can be considered as frequency independent, at least in a limited frequency band of interest (for example, 1-5 Hz). In

this case $Q(f,r) = Q(r)$.

Hypothesis 2. Separation of source function in a time part and a spatial part $A_{0j}(f;\theta,\phi) = A_{0j}(\theta,\phi)A_{0j}(f)$

Using the previous approximations equation (2.14) becomes

$$A_{ij} = A_{0j}(\theta,\phi)A_{0j}(f)S_i(f)A_{INSi}(f)g_{ij}exp(-f\pi t^*) \tag{2.21}$$

There are several spectral ratio techniques one can use, but in general one spectrum is divided by another spectrum coming from the same source. If we consider two stations i and k recording an event from source j, we have that the ratio of their amplitude spectra is, from (2.21)

$$\frac{A_{ij}}{A_{kj}} = \frac{A_{0j}(\theta_i,\phi_i)A_{0j}(f)S_i(f)A_{INSi}(f)g_{ij}exp(-f\pi t^*_{ij})}{A_{0j}(\theta_k,\phi_k)A_{0j}(f)S_k(f)A_{INSk}(f)g_{kj}exp(-f\pi t^*_{kj})}$$

re-arranging the terms of the previous equation and erasing the common source function time part

$$\frac{S_k(f)A_{INSk}(f)A_{ij}(f)}{S_i(f)A_{INSi}(f)A_{kj}(f)} = \frac{A_{0j}(\theta_i,\phi_i)g_{ij}exp(-f\pi t^*_{ij})}{A_{0j}(f)g_{kj}exp(-f\pi t^*_{kj})}$$

Taking the natural logarithm from both sides we have

$$R(f) = lnc_1 + \pi(t^*_k - t^*_i)f \tag{2.22}$$

where $R(f) \equiv \ln\frac{S_k(f)A_{INSk}(f)A_{ij}(f)}{S_i(f)A_{INSi}(f)A_{kj}(f)}$ is a known numerical function (apart from the site effect), and $c_1 \equiv \frac{g_{ij}A_{0j}(\theta_i,\phi_i)}{g_{kj}A_{0j}(\theta_k,\phi_k)}$ is independent of frequency. Furthermore, from the definition (2.6) of t^* we have $t^*_k - t^*_i = (\int_k \frac{ds}{QV} - \int_i \frac{ds}{QV})$. Equation (2.22) is a linear relation in frequency. The slope

$$\delta t^*_{ki} = {t_k}^* - {t_i}^* \tag{2.23}$$

is called *differential attenuation* and it contains all the information concerning the difference of wave attenuation along paths i and k. The slope can be measured (see the algorithm described below) and inverted. In practice I have chosen to calculate a differential t^* with respect to the average t^* calculated for a given seismic event. Then equation 2.7 becomes

$$\delta t^*_{ij} = \overline{t^*_j} - \sum_{l=0}^{N_{cells}} (t_{ij})_l/Q_l \tag{2.24}$$

In the following subsections I will introduce the work I have done to calculate δt^*. To

show some of the technical problems encountered and the strategy that was followed to arrive at a stable and reliable estimate of δt^*, I will go into some detail. More information can be found in the Appendices and in particular in Appendix 2.

2.3.2 Spectral ratio algorithm

To calculate δt^* I have developed an algorithm following the theory described in published papers (e.g. Teng 1968 and Sanders 1993). A scheme of the algorithm is presented in Appendix 5. In addition to uncertainties stemming from the theoretical assumptions considered in 2.3.1, Evans and Zucca (1993) have pointed out the difficulties encountered in the application of the spectral ratio method, where several choices need to be made within the data processing. In particular care needs to be taken in the choice of the spectral estimator, the window length and the frequency band where the signal is considered.

In our application of the spectral ratio method we have kept in mind such considerations to minimize processing errors. We estimated the spectra using the multitaper method (MTM, Park et al. 1987; Mann and Lees 1996). In MTM several tapers are used and combined to optimize the trade-off between spectral leakage and resolution. The analysis was on 3 s of signal including the first Pn arrival, and 3 s of noise preceding the first arrival (Figure 2.3). In this way we have enough data points for a robust spectral estimate (150 points) while minimizing the possibility of having secondary phases in the selected record. Although the S waves are more sensitive to anelastic attenuation anomalies, we chose to work with the P waves because the S_n phase was not visible or barely visible (low S/N) for some stations, or not distinguishable from other phases (for example S to P converted phases). This choice was reinforced by the fact that the majority of the sensors were single (vertical) component. Figure 2.4 shows the spectral ratio calculated for an intermediate depth event from the Calabrian Arc slab recorded by station LCI (Lecce) in Puglia. The best fit gives us the slope and δt^* can be calculated with equation 2.22. Finally, the vector of δt^* values can be inverted using equation 2.24. In practice, I had to modify the FDTOMO code so that it could invert for Q starting from the δt^* vector. Tests were performed to make sure that these changes were applied correctly. More information on how the algorithm and the inversion procedure have been applied is given in Appendix 2.

2.3.3 Synthetic tests

To test the spectral ratio algorithm, I applied it to synthetic data in the case of Earth models for which analytical relations for differential attenuation are easily calculated.

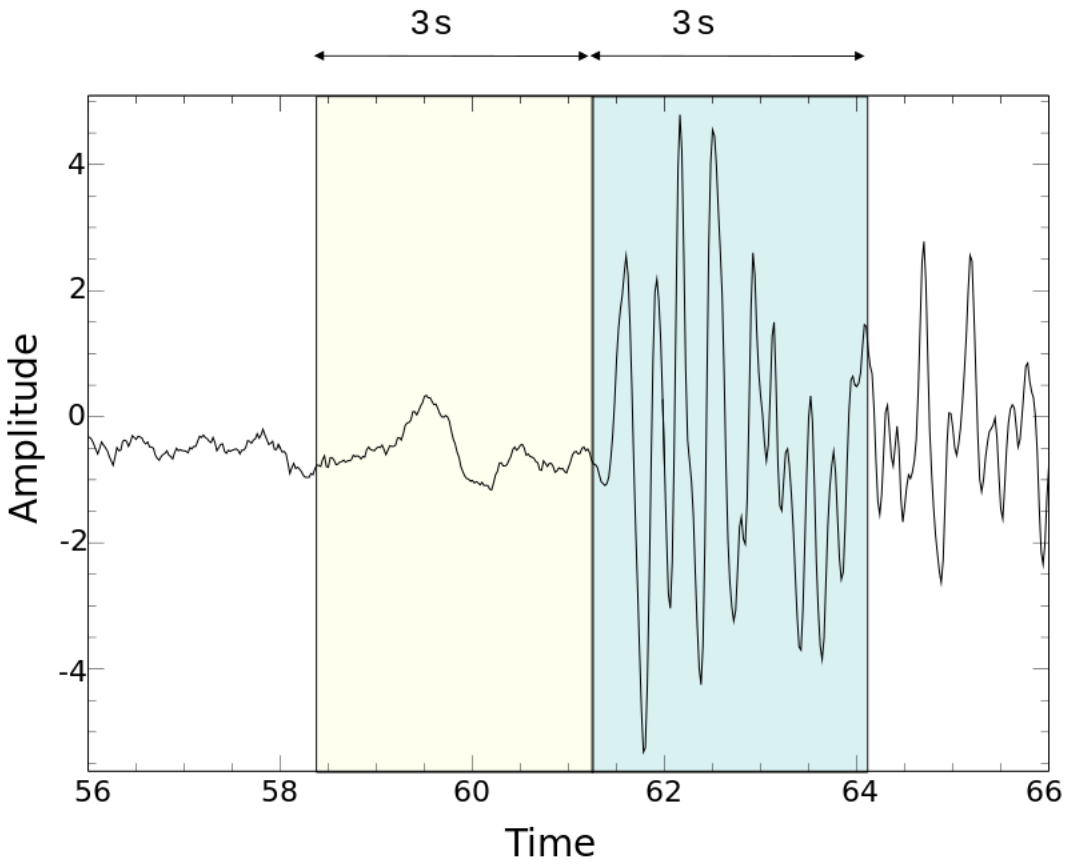

Figure 2.3: Example of selection of 3 s of noise (yellow area) and 3 s of data for spectral analysis (blue area).

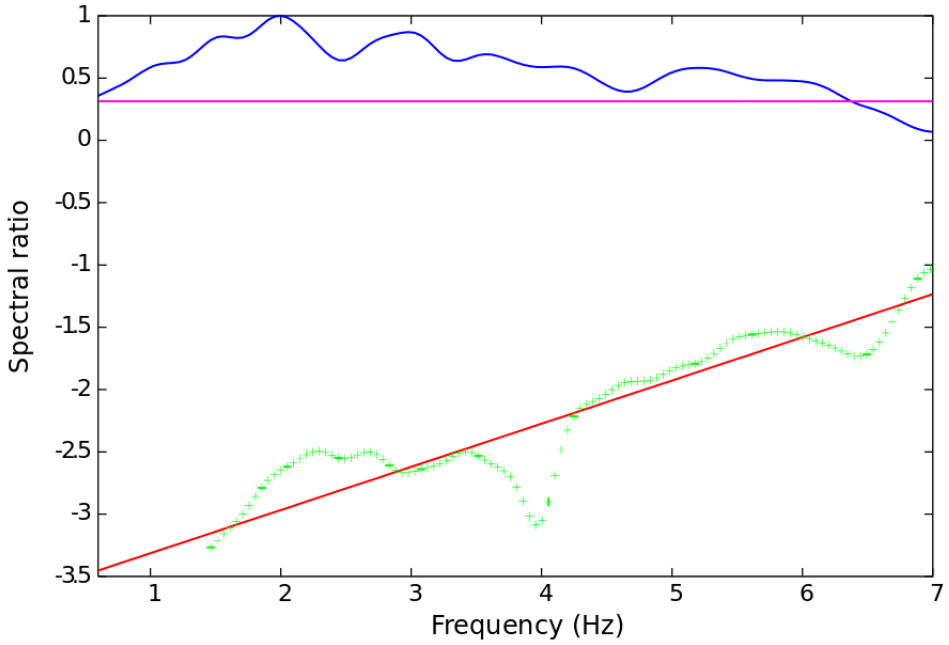

Figure 2.4: Example of accepted spectral ratio curve (green line with crosses) with best fitting line (in red). Blue line: S/N. Purple line S/N threshold. Spectral ratio is accepted only if S/N $>$ threshold in bandwidth $>$ 2Hz.

$Depth(km)$	$V(km/s)$	$Vs(km/s)$	$density(g/cm^3)$	Qp	Qs
0	7.8	4.5	3.3	600.	200
5	7.8	4.5	3.3	600.	200
7.5	7.8	4.5	3.3	600.	200
340	7.8	4.5	3.3	600.	200
360	7.8	4.5	3.3	600.	200
360	7.8	4.5	3.3	600.	200

Table 2.2: Main part of input file to the program pswell used to generate synthetic waveforms. Source depth is 355 km.

The algorithm's stability was then checked with respect to both the variations of controlling parameters and of added noise. The synthetic data are waveforms which are produced using the reflectivity method (Müller 1985; Dahm 1999). First, noiseless data is generated starting from a homogeneous half-space and then from a model comprising two contiguous homogeneous sectors; the synthetic source is comparable to recorded earthquakes of interests in terms of magnitude and depth. As a second step pseudo-random Gaussian noise is added to the synthetic data and error sources and error distribution are examined. Also, there is an evaluation on the effects of the variation of significant parameters on the stability of the algorithm. The first model, described in Table 2.2, is used as input to program pswell (Müller 1985; Dahm 1999). Figure 2.5 shows a record section were there is a sequence of recordings at 25 stations with constant spacing having epicentral distance from 150 to 350 km. The signal is recorded within the frequency band 0-4.95 Hz (sampling rate is 10 Hz), the source duration is 0.4 s; the source duration's inverse gives the cut-off frequency of the source spectrum, 2.5 Hz. Attenuation is described by the quality factors $Q_p = 600$ and $Q_s = 300$.

The slightly more complicated model comprised of two contiguous homogeneous sectors is shown in Figure 2.6. The rays travel within one or the other sector. Let's consider a reference station r and an other station i on the profile. We have previously seen how the spectral ratio between the amplitude of the signal from the same event recorded at two stations is calculated (equation 2.22). We rewrite it (for P or S wave) with the term a_{ir} including the part that is frequency independent, remembering that in this relation, linear in frequency, the slope is directly related to differential attenuation. The theoretical t^* can be easily calculated for this model, starting from the definition of t^* (equation 2.6). Supposing that there are two rays reaching receivers i and j, which travel within a sub-volume of constant Q and V then we have for i ${t_i}^* = \frac{\Gamma_i}{VQ_i}$, where Γ_i is the length of the ray path to station i. A similar equation holds for receiver r. As the ray paths are straight lines $t_i^* = \frac{\sqrt{h^2+{x_i}^2}}{VQ_i}$, where h is the hypocenter depth and x_i the

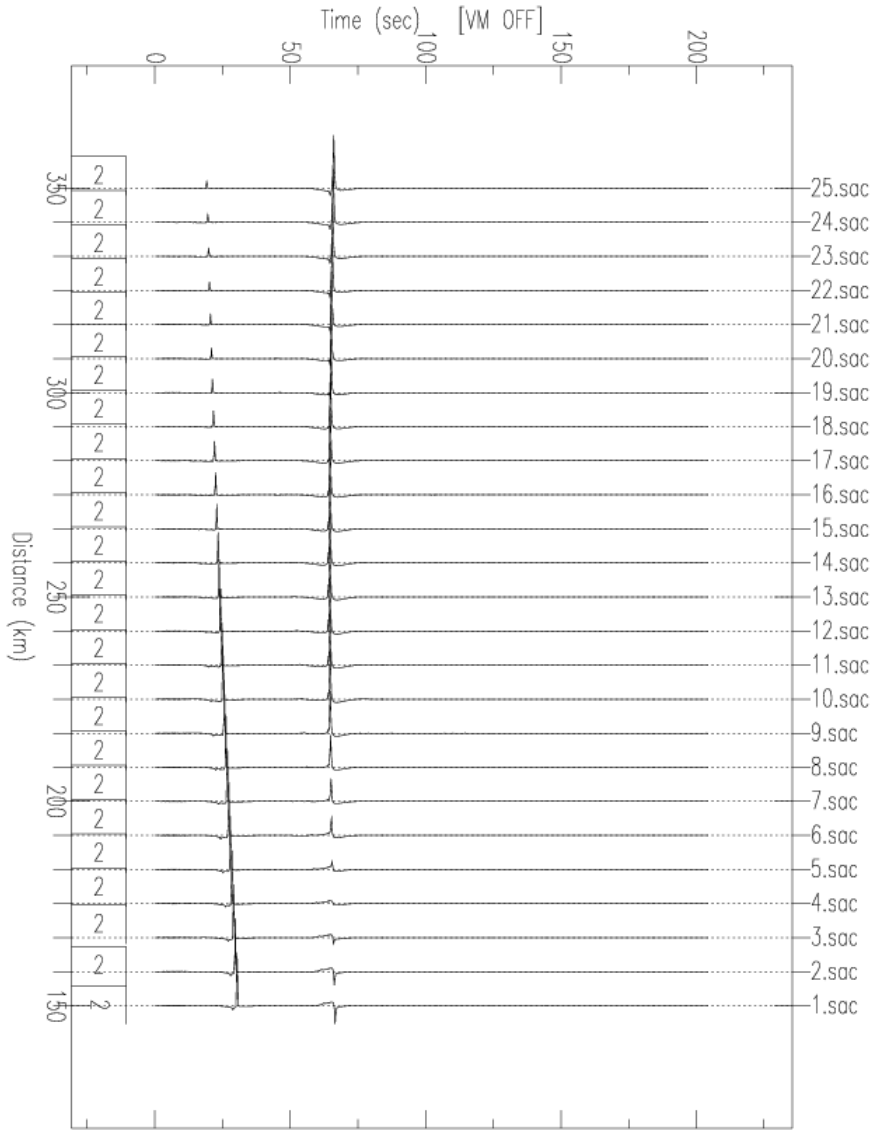

Figure 2.5: Record section of 25 stations recording a waveform described by model in Table 2.2.

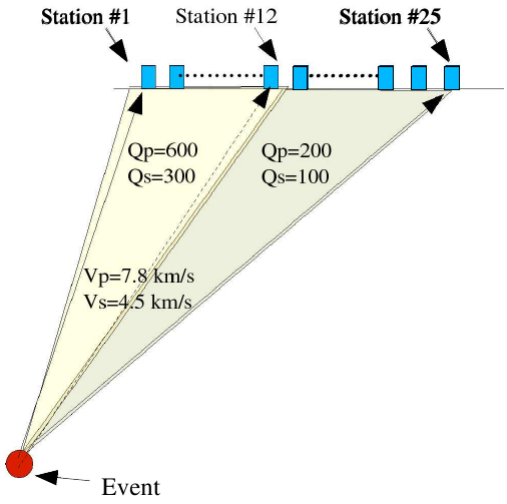

Figure 2.6: Model composed by two adjacent constant Q and V sub-spaces. Rays are completely contained in one of the sub-spaces

epicentral distance for station i. Then for the simple model described in Figure 2.6 (the homogeneous model is a special case), for both P or S, the relative t^* residual between the two stations is: $\delta t_{ri}^{*theor} = \frac{\sqrt{h^2+{x_r}^2}}{VQ_r} - \frac{\sqrt{h^2+{x_i}^2}}{VQ_i}$ and this value can be compared to the synthetic data δt_{ri}^{*synt}.

Now we show the comparison between δt_{ri}^{*synt} and δt_{ri}^{*theor} for the P and S waves in the simple model previously described by Figure 2.6, where the spectral ratio is taken with respect to one of the 25 stations. Stations 1-12 always receive waves traveling completely in the high-Q sector, and stations 13-25 always receive waves traveling completely in the low-Q sector. Reference station r is station 12 (high-Q sector) at epicentral distance 241.667 km, unless otherwise stated.

Figures 2.7 and 2.8 show a comparison between theoretical and synthetic δt^* when no noise is added and a homogeneous model (Table 2.2) is considered, so $Q_r = Q_i$, for P and S respectively.

A quick comparison of the maximum δt^* variation to the average error $\overline{E(\delta t^*)}$ committed in their calculation, shows for the P-wave $\frac{\overline{E(\delta t^*{}_p)}}{\Delta \delta t^*{}_p} = 0.001s/0.025s \simeq 4\%$ and for the S wave $\frac{\overline{E(\delta t^*{}_s)}}{\Delta \delta t^*{}_s} = 0.02s/0.08s \simeq 25\%$ the relative error is very large. This is due to the generation of an inhomogeneous wave at the critical angle as explained at the end of Appendix 4. This last aspect shows how important it is to be consistent in the use of a single (in this case P or S) phase. The error analysis for the two cases, constant Q and variable Q model, suggests something about the resolving power in our determination

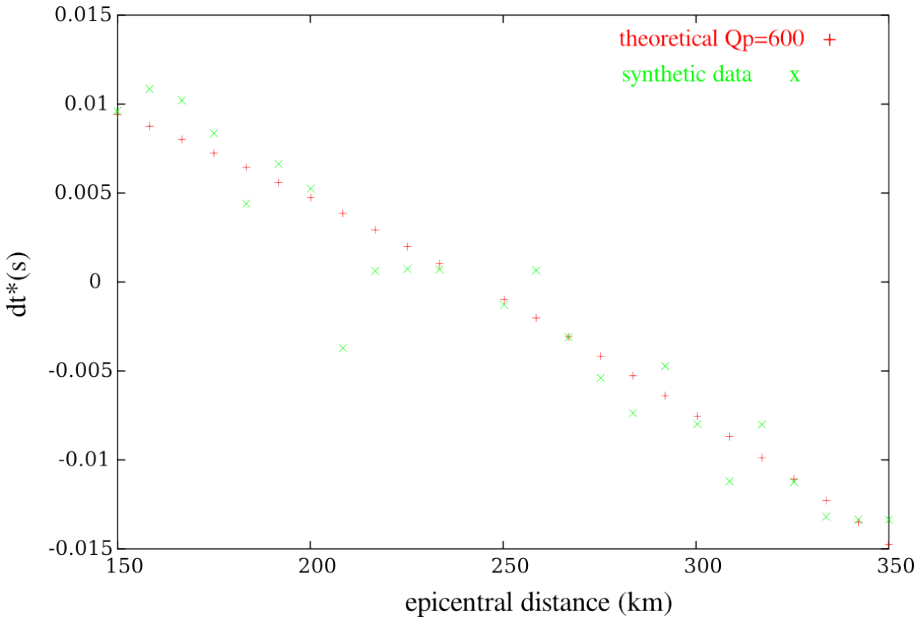

Figure 2.7: Comparison of synthetic and theoretical δt^* for the P-wave, $Q_p = 600$, $V_p = 7.8km/s$, no noise added.

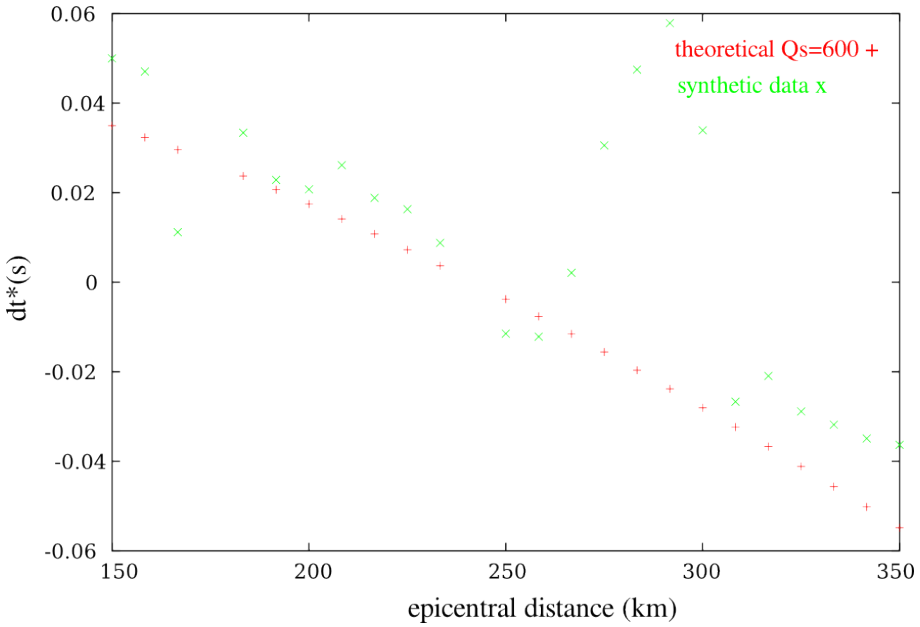

Figure 2.8: Comparison of synthetic and theoretical δt^* for the S-wave, $Q_s = 300$, $V_s = 4.5km/s$, no noise added.

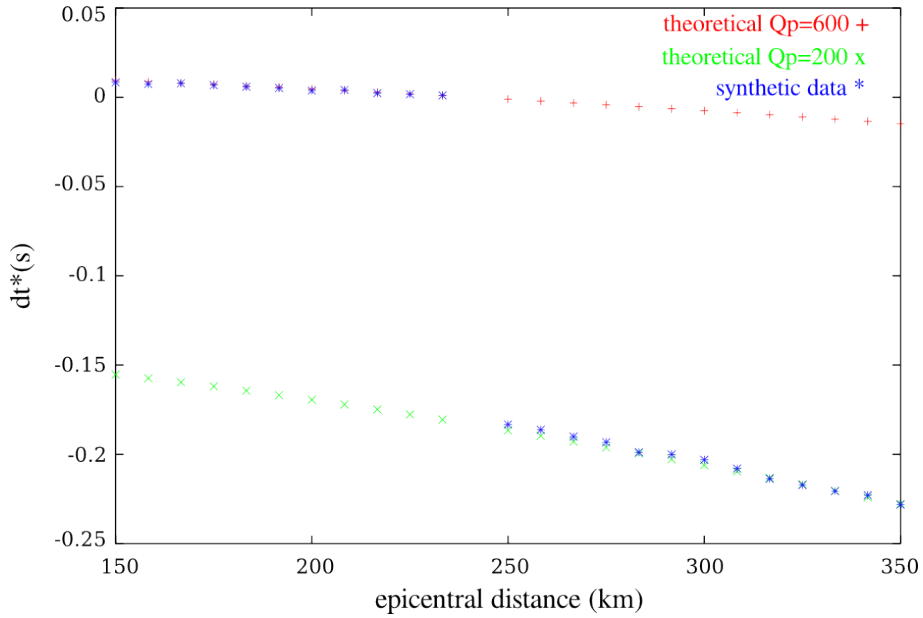

Figure 2.9: Comparison of synthetic and theoretical δt^*. P-wave, $Q_1 = 600$, $Q_2 = 200$, $V_p = 7.8km/s$, model as shown in Figure 2.6, no noise added

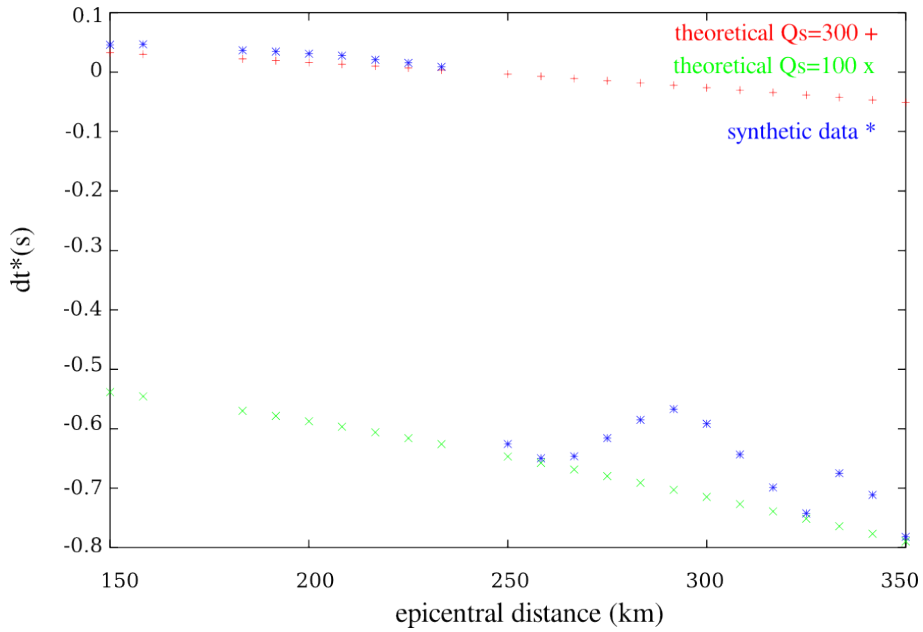

Figure 2.10: Comparison of synthetic and theoretical δt^*. S-wave, $Q_1 = 300$, $Q_2 = 100$, $V_s = 4.5km/s$, model as shown in Figure 2.6, no noise added.

of δt^*. In the case of two adjacent homogeneous sectors with strongly differing Q, as depicted in Figure 2.6) the average error $\overline{E(\delta t^*)}$ is small in comparison to $\Delta\delta t^*$, for both P (Figure 2.9) and S (Figure 2.10). On the other hand, when the spectral ratios are between stations that receive rays travelling in the same constant-Q Earth volume (or where there are small variations of Q), δt^* depends only on path length and relative errors are much larger. More results of the synthetic tests can be found in Appendix 4.

2.3.4 The contribution of the scattering process

Although in the application of the spectral ratio technique we have neglected or eliminated several unknown terms, it is still necessary to evaluate the contribution to effective attenuation coming from scattering loss caused by heterogeneities (Fehler et al. 1992; Sato et al. 2000). Since scattering results in shifting higher-frequency energy from the first arrival pulse to the coda of the seismic phase, one way to understand if scattering plays a major role is to check for a later high frequency arrival wavelet (Richards and Menke 1983; Evans and Zucca 1993, and references therein). To check the presence of this effect we calculated spectra and spectral ratios on data records of increasing length (2, 3, 4, 5, and 6 s) from several events. We found that as the window length is increased there is not a noticeable increase of high-frequency energy in the spectra and, although there are some differences in the δt^* values, the main anomalies shown in t^* residual maps are stable with respect to increase of the window length. These results confirm that we can neglect the contribution of scattering to attenuation in this case.

2.4 Reliability and interpretation of tomography models

The final objective of a tomography study is to produce a 3D model which gives a reliable representation of the distribution of seismic parameters in the study volume. Images of the model will show seismic anomalies which are usually associated with colored volumes, for example blue for high velocity and red for low velocity. Then the reliable seismic anomalies are identified and interpreted. This final result is not easily accomplished and care needs to be taken in each step of the process. I will now focus on general factors affecting the inversion procedure itself and the interpretation of the model. In Section 3.4.1 there will be a discussion on the important aspect of station-event geometry and on how the different problems were addressed in each study case.

2.4.1 Reliability of the inversion procedure

We have seen already in Section 2.1 that (tomography) inverse problems are often mathematically ill-posed, in fact usually there is a part of the model space that we are trying to resolve which is overdetermined and another part which is underdetermined, and only through a regularization procedure we can find a solution (or a family of solutions). This solution is a mathematical solution which does not necessarily represent the real Earth. In the methods that are usually applied in seismic tomography, the model space is explored in the vicinity of a point represented by a first initial model, which hopefully is a realistic representation of the average properties of the study volume. A sound choice of this initial model is necessary to arrive at a realistic 3D model solution of the inversion. Already in this first phase independent data is fundamental for the choice of a valid initial model on the basis of a priori conditions. Another important aspect of seismic tomography is that it is a non-linear procedure and we do not have an exact formula to calculate the model matrix from the data matrix, and there is no error propagation formula. There are several ways to measure how the data can give information on the model space through the inversion process. In the methods here applied the evaluation of the reliability and resolution of the 3D model was accomplished through tests based on synthetic data and examination of the ray coverage (see synthetic tests in Appendices 1, 2, and 3).

2.4.2 Interpretation of the model: general considerations

Once we identify the reliable features of the model, we proceed with their interpretation. Also this step is not straightforward, as the seismic anomalies can be explained in more than one way. A critical approach is necessary, since some associations that seem natural in the interpretation of tomography models, for example the positive correlation between high V_s, high density, and low temperatures in the mantle, are not always true (Anderson 2007 and references therein). Another important source of ambiguity in the interpretation of tomography models comes from our theory of Earth materials itself. This is especially true if one wants to have a quantitative estimate of physical parameters, for example derive temperature variations from lateral changes of seismic velocity values. In Section 2.2 we showed, through an example, how temperature variations calculated from a 3D velocity distribution could be overestimated if one only considers the elastic contribution in the derivative of temperature with respect to velocity, and that more realistic (smaller) values are obtained by considering also the effect of anelastic attenuation. Karato and Karki (2001) underlines how laboratory data needs to be carefully extrapolated for the Earth and for seismic frequencies, which is another delicate

aspect to keep in mind in the interpretation of tomography models. Finally, there are aspects of Earth theory that are controversial. For example, recent papers show that there is not a common agreement on the origin and state of seismic discontinuities as they were commonly accepted in the past, as the lithosphere-asthenosphere boundary (LAB) and the role of partial melting in determining the seismic properties of the asthenosphere (low velocities, high attenuation, and anisotropy). A very recent paper by Karato (2012), titled *On the origin of the asthenosphere*, reviews the different models of the asthenosphere on the basis of mineral physics and proposes a model where water content and its effect on viscosity plays a key role in the sharp reduction of seismic velocities across the LAB.

To minimize or at least reduce the ambiguity inherent in the interpretation of tomography models, it is very important to find cross evidence coming from independent data, when available, and to try to identify the main factors that affect the observed seismic parameters in the study area so we can make some predictions that can be verified. Constraints, even if they are qualitative, as for example the ones found in Table 2.1 can be very useful. In the three study cases considered in this dissertation and described in Chapter 3 we have tried to follow this procedure.

3 Seismic tomography of the Central-Western Mediterranean: three study cases

The CWM, and the Mediterranean region in general, is the product of a geodynamic evolution in which many aspects are still controversial. The complexity of the area is reflected in the spatial distribution of seismic properties. The 3D approach of seismic tomography is quite useful given the presence of strong lateral heterogeneity. The three cases are interesting for two reasons: 1) the study areas are distinct representative end members of the CWM evolution; 2) the studies are at crustal, upper-most mantle and upper mantle scale, thus they offer an opportunity to discuss the strengths (and limits) of seismic tomography in various conditions.
A general overview of the CWM will be given, underlining its complexity, although there is a widely accepted general model for its kinematic evolution, that will be presented. Following, the areas of interest will be introduced within the general context of the CWM area. Then, the individual studies are presented. The first case is a local earthquake tomography study (LET) of the crustal structure of the Colfiorito area (Northern Apennines, Figure 3.1 No. 1) based on crustal events traveltime data. The second case is a LET study of the upper-most mantle of the Calabrian Arc-southern Apennines system (Figure 3.1 No. 2), based on data from intermediate depth seismic events. In the third case the upper mantle seismic velocity structure of the Cadiz Gulf-Alboran Sea system is explored with teleseismic tomography (Figure 3.1 No. 3). Finally, there is a discussion on how the three seismic tomography models were interpreted, keeping in mind the key factors that determine seismic parameters as introduced in Chapter 2. The second part of the discussion focuses on the strengths and limits of the three tomography applications, with reference to our specific experimental conditions.

3.1 The Central-Western Mediterranean

The Mediterranean is part of a diffuse convergent margin hundreds of kilometers wide, between the African and Eurasian plates. One of the outstanding and controversial fea-

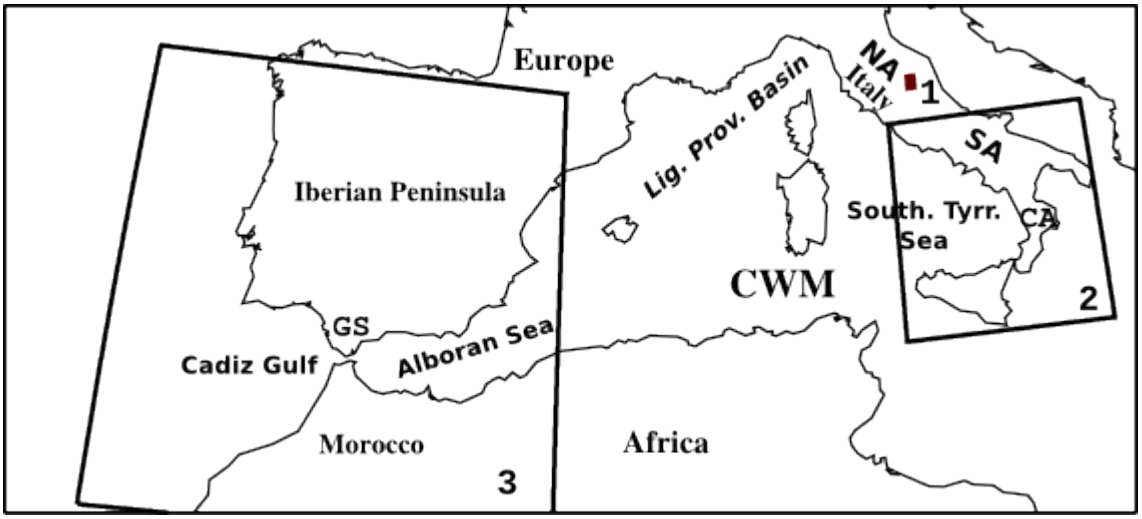

Figure 3.1: Map of the Central Western Mediterranean area (CWM). Boxes indicate study areas. 1: Colfiorito. 2: Calabrian Arc-Southern Apennines. 3: Cadiz Gulf-Alboran Sea. GS=Gibraltar Strait. NA=Northern Apennines. SA=Southern Apennines. CA=Calabrian Arc.

tures of this region is the presence of large-scale extension within a convergent domain. The complexity of this region (the Mediterranean and the CWM in particular) is reflected on the number of key factors which affected (and are possibly still affecting) its geodynamic evolution. In particular:

- The Africa-Eurasia compression ($\sim$ 1 cm/year), active during the formation of the Mediterranean, at present about a few mm/year in the NW direction.
- The gravitational sinking (negative buoyancy) of oceanic lithosphere leading to subduction.
- The differential velocity between Africa-Eurasia convergence rate and trench retreat leading to oceanic slab rollback.
- The existence of micro-plates and basins within the subduction zone. These blocks reacted differently to subduction, possibly by inhibiting it (e.g., Adria, Apulian blocks), and by initiating slab tears.
- The role of asthenospheric flow, possibly small-scale convection, and its interplay with the subducting slab(s).

Given all these factors it is not surprising that there is not a unique mechanism that can explain the evolution of this region, and that many open questions remain. In spite of this complex scenario, some unifying models for the evolution of the CWM have been proposed. Kinematic reconstructions show that the western Mediterranean extensional

basins developed between the convergence (active since 84-118 Ma; Dewey et al. 1989) of the European and African plates. A number of lithospheric blocks existed at 38 Ma, before the opening of the WM, at the European margin (Balearic, Corsica-Sardinia, Calabrian-Peloritan) and at the African margin (Apulia, Panormide, Iblei), together with basins (Dewey et al. 1989). The motion of these smaller blocks was a primary factor in determining the geology that is observed today often overriding Africa-Europe convergence (Dewey et al. 1989). In particular, the formation of the Apennines was caused by counter-clockwise rotation (with respect to Europe) and collision of the Corsica-Sardinia block with the western margin of the Adria block (Patacca and Scandone 1989). Figure 3.2 from Faccenna et al. (2004) shows a widely accepted kinematic evolution of the western Mediterranean in the past 35 Ma. While for the kinemematic evolution of the area there is general consensus, identifying the causes of this evolution is much more controversial. Several authors have proposed subduction-rollback as the main driving mechanism for the extension process in the western Mediterranean (e.g., Malinverno and Ryan 1986; Royden 1993; Lonergan and White 1997; Wortel and Spakman 2000). An important factor proposed to explain the evolution of subduction in the western Mediterranean comes from the interaction between lithospheric slabs and asthenosphere which could possibly result into slab tear or detachment. Lateral migration of slab detachment has been proposed as a key element of lithosphere dynamics in the Mediterranean region in the last 20-30 Ma, being especially important in the final stage of subduction (Wortel and Spakman 2000). More recently Faccenna et al. (2004), on the basis of mantle tomography images, surface geology data and plate kinematics, introduce the concept of a Western Mediterranean Subduction Zone (WMSZ) and explain the formation the two narrow Arcs of Gibraltar and Calabria as the final result of lateral segmentation of a single wide WMSZ in the subduction-rollback opening of the Western Mediterranean. In this last model mantle flow plays a key role in the fragmentation and deformation of the Gibraltar and Calabrian slabs (Figure 3.2). A number of observations point to the presence of subduction below the northern Apennines and of active subduction in the Calabrian Arc, where there is a well defined Wadati-Benioff zone contained in a high seismic velocity body (as imaged by tomography studies), and subduction-related magmatism. The three study areas considered in this dissertation reflect the complex geodynamic evolution of the CWM, each representing a distinct end member of this evolution. In the Northern Apennines (NA) subduction of oceanic lithosphere of the Adria microplate has possibly ceased due to the arrival of continental lithosphere. The position of the NA with respect to the convergence direction is anomalous, in fact the tectonic stresses are NE-SW, at $\sim 90^{\circ}$ with to the general Africa-Eurasia convergence direction. So, the NA are an example of the effect of the micro-plates in the CWM. The

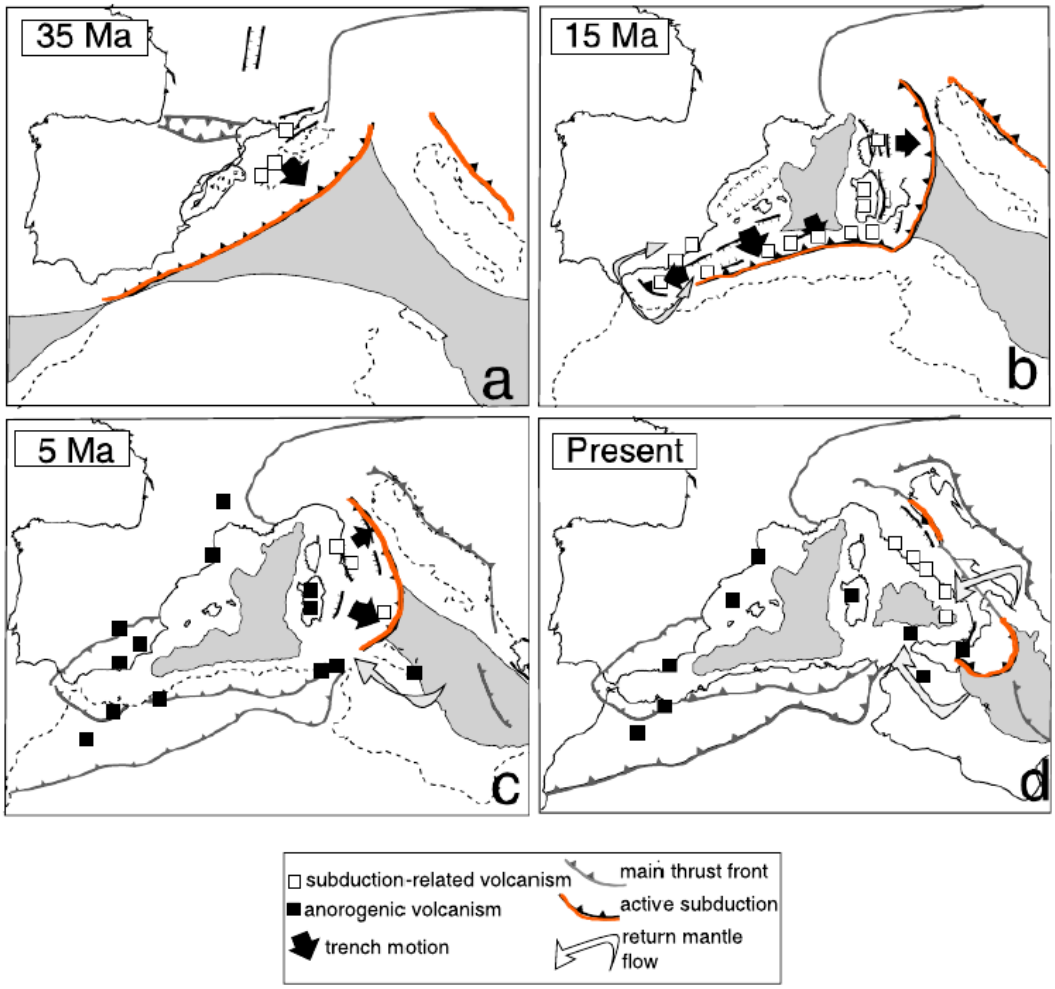

Figure 3.2: Reconstruction of the evolution of the Mediterranean region in relative (Eurasia fixed) reference frame in four stages from 35 Ma to present-day. Deep basin centers are marked in grey. The locations of the magmatic centers and their bearing with subduction process are marked with solid (anorogenic) and open (subduction-related) squares. From Faccenna et al. (2004)

present stress state in the Northern Apennines is an open question.
The Calabrian arc, together with the Aegean, is the only site that presents active subduction zone in the Mediterranean, where a Wadati-Benioff plane and an active volcanic arc exists. A small segment of oceanic slab is here visible down to 660 km, likely representing the final stage of subduction. Here we find the typical volcanic Island arc (the Aeolian Islands) with magmatic products that are subduction related .
In spite of the attractiveness of the unifying picture given by the WMSZ model, the present state and origin of the Alboran Sea-Gibraltar system is quite controversial. Several authors suggest that subduction of oceanic lithosphere (active or extinct) caused extension within the Alboran Basin in the Miocene by slab rollback (Royden 1993; Lonergan and White 1997; **?**; Gutscher et al. 2002) or by slab detachment (Zeck 1996). On the other hand, another group of authors present an evolution for the Alboran basin initiating with lithospheric thickening during the Paleogene caused by the collision of Europe and Africa. The thickened continental lithosphere was later ($\sim 20Ma$) detached by convective removal (Platt and Vissers 1989) or by delamination (Calvert et al. 2000). The collapse of this lithosphere caused extension of the Alboran basin and uplift around the margin.
Figure 3.3 is a cartoon of the CWM summarizing the stress regime and the main processes that have likely determined the geodynamic evolution of the study areas. From this map we see that for each of the three cases we find a different state of the CWM evolution.

3.2 The Tyrrhenian-Apennines system

According to a widely accepted model the Tyrrhenian-Apennines system is the result of a complex convergence of about 1 cm/a (Faccenna et al. 2001), at present a few millimeters per year (D'Agostino et al. 2008), between the African plate, the Eurasian plate and several microplates (Faccenna et al. 1996; Rosenbaum and Lister 2004). Starting $\sim 26Ma$ ago the Liguro-Provençal basin formed, followed by the Tyrrhenian basin starting in the late Miocene ($\sim 13 - 10Ma$), from the sinking and rollback of the dense Mesozoic oceanic Ionian lithosphere in the east-southeast direction (Argnani 2000, and references therein). A kinematic reconstruction for the Tyrrhenian-Apennines system based on the subduction-rollback hypothesis, is shown in Figure 3.4 (Rosenbaum and Lister 2004). According to this reconstruction due to a differential rollback speed (starting $\sim 6 - 5Ma$ ago) between the northern part of the Tyrrhenian Sea (slower) and the southern part (faster), the main slab at one point divided in two segments which are now visible in tomographic models below the northern Apennines and below the Calabrian

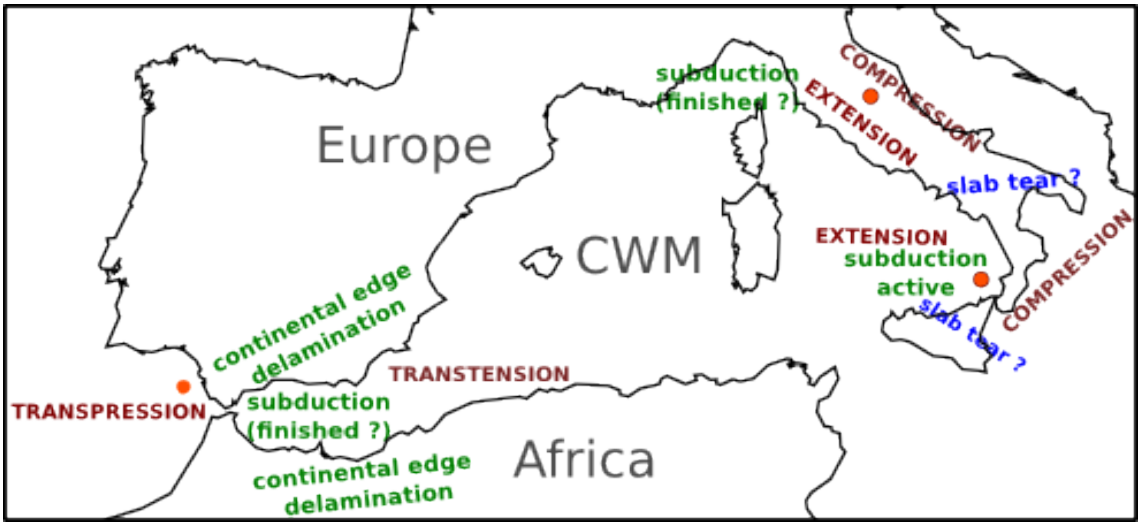

Figure 3.3: Cartoon of the CWM describing the present stress field and the geodynamic processes in the study areas. Orange circles give a general location of the study areas. Brown labels indicate the present stress regime. Green labels indicate geodynamic processes, active or extinct. Blue labels indicate possible sites of slab tears.

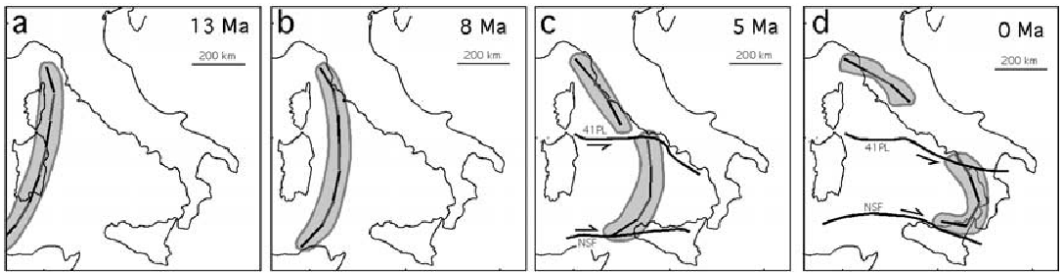

Figure 3.4: From Rosenbaum and Lister (2004) (verbatim): Maps showing the evolution of the subducting lithospheric slab beneath Italy since the late Miocene (relative to present-day coastlines). Shaded areas are surface projections of the slab at depths of 30-100 km based on the tomographic model of Lucente et al. (1999) and the results of our reconstruction. Note that the reconstruction predicts tearing of the slab at the latest Messinian ($\sim 65Ma$) and a subsequent period of rapid rollback in the southern Tyrrhenian Sea. Abbreviations are 41PL, 41 parallel strike-slip fault zone; NSF, North Sicily Fault.

Arc respectively (Rosenbaum and Lister 2004, and references therein). The sites for the slab tear are identified with two transcurrent structures, one in the north starting at parallel 41° N and the other in the south continuing in mainland Sicily (Figure 3.4). During this fast extensional episode in the southern Tyrrhenian (estimated in 60-100 $kmMa^{-1}$ by Rosenbaum and Lister 2004) new oceanic crust was formed in the Vavilov and Marsili basins (Figure 3.7).
Apennines building is a still active process of shortening and extension linked to the opening of the Tyrrhenian Sea. Currently the Apennines are characterized by extension in the internal part and compression in the external part. This thrust and fold belt is the result of ongoing destruction, going from west to east, of the internal parts of the orogen by extensional processes (Rosenbaum and Lister 2004 and references therein). Tomographic studies suggest the existence of subduction below the Alps and the northern Apennines, where we find subcrustal seismicity (e.g., Chiarabba et al. 2005). The cold-fast material imaged in tomographic studies of the northern Apennines has been interpreted as subducting Adriatic lithosphere, although it is debated if subduction is active or not (see for example Benoit et al. 2011). Interestingly, no subcrustal seismicity has been recorded from the central and southern Apennines (e.g., Di Stefano et al. 1999). This finding, together with the presence in several tomography models of a low-velocity anomaly underlying the central-southern Apennines, has been interpreted by several authors as a discontinuity of the slab (see 3.2.2 and references therein).
The Umbria-Marche sector of the thrust and fold belt lies within a zone which marks the passage, going from north to south, from the area containing deep seismicity to the area where it is absent. The location of the southern edge of the northern Apennines slab is under debate, as it is commonly placed at 42° (e.g. Rosenbaum and Lister 2004 based on the tomography model of Lucente et al. (1999) but recently it has been proposed to be more north, at 43° (Benoit et al. 2011).

The first case presented is a LET (Local Earthquake Tomography) study of the crust of the Colfiorito area in the Umbria region (Colfiorito town latitude 43° 1′), which is at the southern border of the northern Apennines slab. The second case is a LET of the uppermost mantle of the Southern Apennines-Calabrian Arc subduction zone.

3.2.1 Crustal LET of the Colfiorito area (Umbria-Marche, Northern Apennines)

The Umbria region, is characterized by Pliocene ($\sim 1.7-5Ma$) active extensional Apennine tectonics (Collettini et al. 2000). These tectonics generated continental basins with a general NNW-SSE trend, bordered either by WSW-dipping or ENE-dipping normal

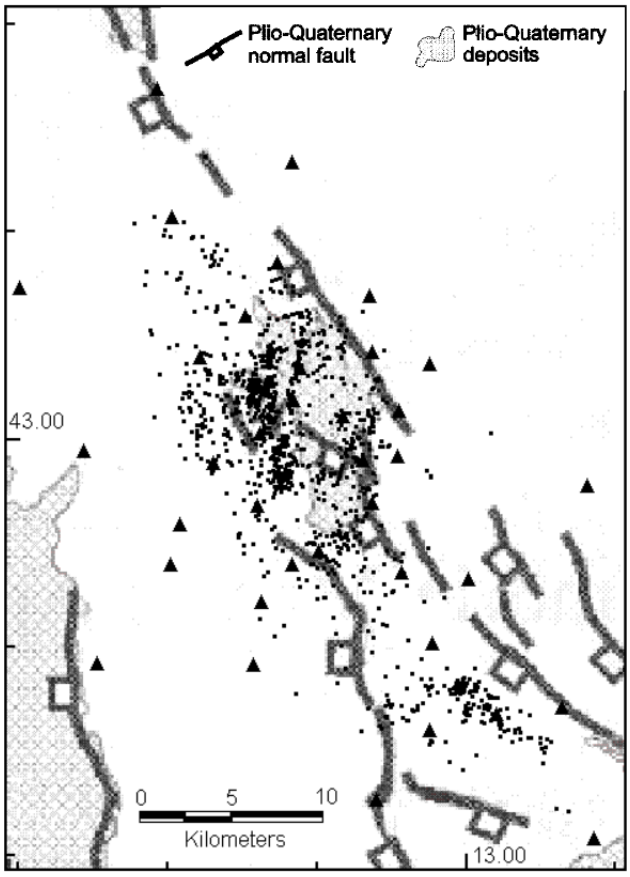

Figure 3.5: Map of the Colfiorito area: Dots represent epicenters of events re-located in the 3D model and triangles the used stations. Adapted from Boncio and LaVecchia (2000).

faults striking in the same direction (Bally et al. 1986; Barchi et al. 1998a). These faults are interpreted as being dissected by minor trans-extensional oblique elements (Cello et al. 1997). The largest structural feature in the region is the 100 km-long Val Tiberina basin which is controlled by a ENE-dipping master fault (Alto Tiberina fault; Barchi et al. 1998a). East of the Val Tiberina basin, the Colfiorito basin is another minor extensional basin (Figure 3.5), possibly on the hangingwall of the Alto Tiberina fault, directly affected by the 1997 Umbria-Marche seismic sequence (maximum magnitude Mw 6.0, Deschamps et al. 2000; Michelini et al. 2000). Tomographic interpretations have been used, both with active and passive seismic techniques, to infer differences in physical properties of rocks (e.g., Robertson 1987; Koch 1992; Sanders et al. 1995; Lees and Wu 2000). This interpretative approach is based on theoretical models, laboratory observations and in situ measurements (Tatham 1982). Velocity of seismic waves in sedimentary

Volume	$\delta V_p/V_p$ (%)	$\delta\Psi/\Psi$ (%)	$\delta r/r$ (%)	Depth range (km)
A	+ (6.0)	+ (11)	+ (2.8)	1–5
B	− (3.5)	− (3.5)	0	2–6
C	+ (2.0)	+ (3.5)	0	3–6

Table 3.1: Anomaly volumes with sign and peak value.

rocks depends mainly on mineral composition; consolidation and cementation of the rock matrix; porosity (total pore and crack volume), pore and crack geometry and their fluid content; effective rock stress (defined as confining pressure minus pore pressure) and temperature (Schön 1996). Pore and crack geometry is described by the aspect-ratio parameter α, that is, the ratio of the minimum dimension to the maximum dimension of the crack or pore ($\alpha = 1$ for a spherical pore; $\alpha << 1$ for a flat crack). Presence of very low α cracks (flat cracks, in the range $10^{-3} - 10^{-2}$), even in a predominantly porous ($\alpha \simeq 1$) sedimentary rock, can have a strong effect on the rocks bulk elastic properties (Tatham 1982; Koch 1992). In our local tomography study we calculated high-resolution 3D P and S-wave velocity models of the crust of the Colfiorito basin by inverting first arrival times from the 1997 aftershock sequence using the method described in 2.1.1. From the original data set of 2,538 located events,we selected 1,125 well-located earthquakes recorded on 39 stations. This resulted in 16,417 P- and 15,598 S-phase first arrival times. The distribution of stations and events allow the investigation of a volume extending about 24x40x6 km^3. Ambiguities that usually arise analyzing only Vp and Vs, can be resolved by the use of their ratio and product (Lees and Wu 2000). For sedimentary rocks Vp/Vs is sensitive to the presence of pore fluids and to concentration of cracks for a given total porosity. Laboratory and borehole measurements have found Vp/Vs to increase with the concentration of fluid saturated cracks (both micro- and macrocracks) in a condition of low effective stress (Moos and Zoback 1983). In particular, this was also verified for fluid saturated carbonates by Robertson (1987), comparing the model of Toksöz et al. (1976) with *in situ* measurements. The other quantity, $Vp*Vs$, is sensitive to variations of porosity in sedimentary rocks (Iverson et al. 1989; Lees and Wu 2000). A lower $Vp*Vs$ value implies an increase of porosity. We interpret Vp, $r = Vp/Vs$ and $\Psi = Vp*Vs$ anomalies as produced by different rock types having different pore-pressure and fracturing state. Figure 3.6 shows significant horizontal slices of the calculated 3D models, where, within the well-resolved part of the model, we identify three anomaly volumes: A) SE of Colfiorito, the most noticeable, where we have positive Vp, r and Ψ anomalies; B) NW of Colfiorito, where we have negative Vp and Ψ anomalies and average values of r; C) W of Colfiorito, NW-SE direction, where we find positive Vp and

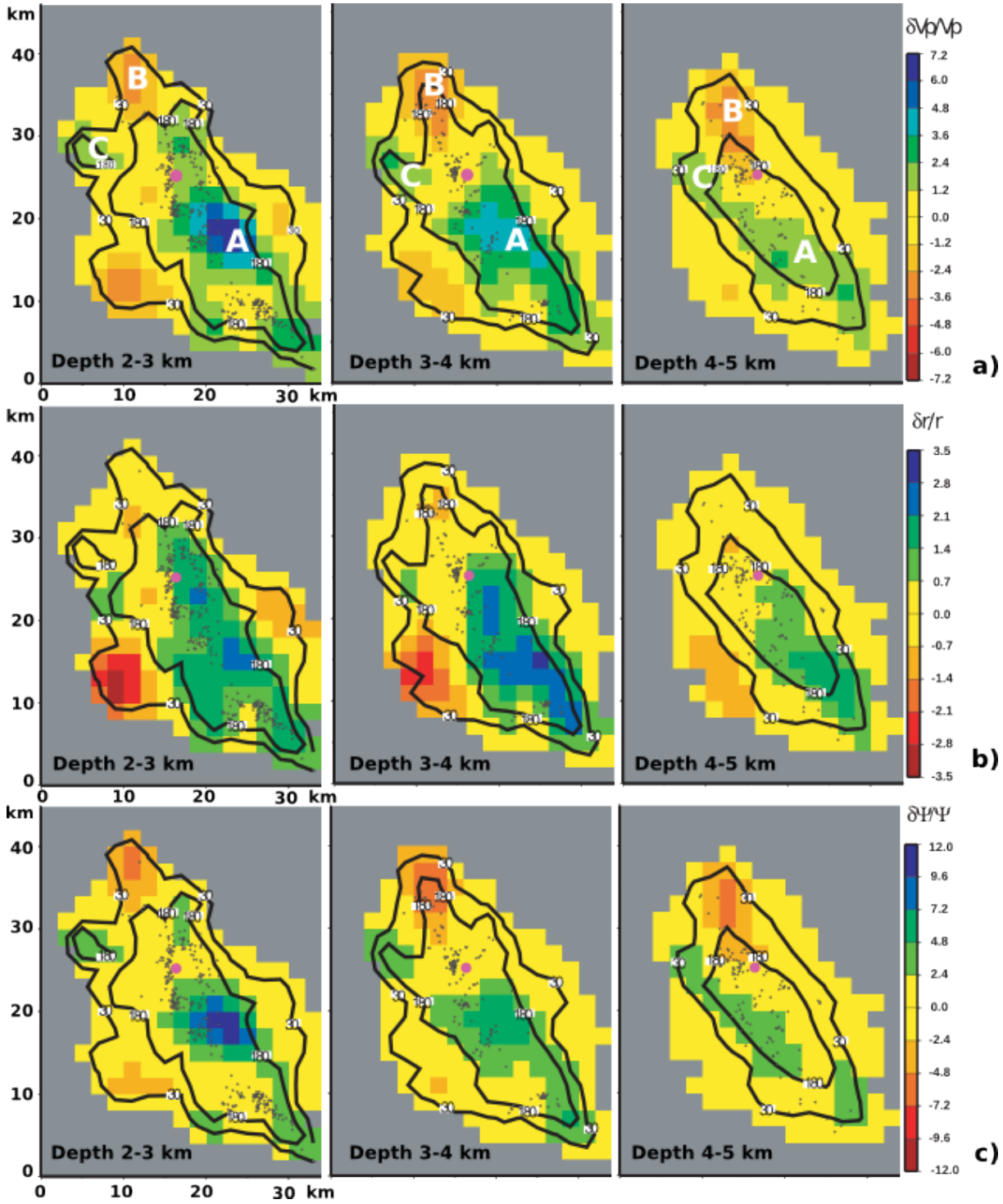

Figure 3.6: Maps at various depths for $\delta Vp/Vp$ (a), $\delta r/r$ (b) and $\delta\Psi/\Psi$ (c). The color yellow is associated to the initial 1-D model value for each layer. Only seismicity in each layer is depicted. Only blocks covered by at least 1 ray are plotted. The purple dot shows the location of Colfiorito town. Contour lines show coverage for the P-wave (a) and S-wave (b and c).

Rock	Vp (km/s)	Depth range (km)	Thickness (km)
MA (CS)	5.2[a]	0 ÷ 3[c]	2[c]
CM (CS)	6.0[b]	0 ÷ 3[c]	2[c]
EV	6.1[a]	3 ÷ 6[c]	

CS = Carbonatic Sequence, MA = *Maiolica* type, CM = *Calcare Massiccio*, EV = Evaporites (Anhydrite). Adapted values from:
[a]*Barchi et al.* [1998b].
[b]*Bally et al.* [1986].
[c]*Boncio and Lavecchia* [2000].

Table 3.2: Rock types in the study volume and average properties.

Ψ anomalies and average r values (Table 3.1) for a schematic description). Based on the knowledge of the areas rock types (Table 3.2) we propose the following interpretation: A: A volume of stiffer rock with higher crack density, saturated with fluid under low effective stress so cracks remain open, explaining high r values and high Ψ values. Low effective stress is possibly due to higher pore pressure. Volume A could be mainly formed by stiffer, more permeable, high velocity carbonates (e.g., Calcare Massiccio). A similar interpretation is given by Nicholson and Simpson (1985) for a layer with analogous characteristics in the New Madrid area (Central U.S.A.), confirmed by a drilling test.

B: Lower Vp, average r, and lower Ψ values imply a softer rock with smaller crack density and greater porosity. B could be a volume where softer, more porous and lower velocity components of the carbonate sequence are mostly present (e.g., Maiolica).

C: Less fractured, low porosity stiffer rock (high Vp, high Ψ, average r). This could be due to greater presence of high velocity anhydrite (as Triassic evaporite). Interestingly this volume is scarcely affected by seismic activity, implying a more plastic behavior.

Given that the Umbria-Marche aftershock sequence developed for several months, an explanation based on elastic properties only seems unsatisfactory and a poroelastic approach is preferable. Other authors have considered the role of fluid diffusion in the 1997 Umbria-Marche sequence (Cocco et al. 2000; Ripepe et al. 2000; Miller et al. 2004; Chiarabba et al. 2009). The great majority of aftershock seismic activity evolved in volume A, or at the interface with the other two volumes, where we hypothesize the presence of a stiffer rock, more permeable, fluid saturated, and under high pore pressure. Under such condition we can explain the slow SE migration of the sequence with mobility of fluids in A, gradually increasing pore pressure thus decreasing shear resistance of rock. Presence of evaporite, with low permeability, in the strip-like volume C, could be responsible of a fluid-channeling effect in the NW-SE direction. More information on this study is available in Appendix 1.

3.2.2 Uppermost mantle LET of the Southern Apennines-Calabrian Arc subduction zone

At present, in a region extending only a few 100 km we find oceanic (Ionian plate and Tyrrhenian Basin) and continental (African and Apulian/Adriatic) lithospheres interacting together with the asthenosphere within a subduction system where the Ionian slab is one of the narrowest subduction zones worldwide. In such a small area the topography of the asthenosphere varies greatly, between about 150 km and $10-30$ km and different magmatic provinces, ranging from Island Arc Basalt (IAB)-type to Ocean Island Basalt (OIB)-type, occur in close proximity (Figure 3.7). In spite of a large number of geological and geophysical studies, the position and interaction between oceanic and continental lithosphere, asthenosphere and subducting plate, the relationship between magma genesis and the evolution of the Tyrrhenian Basin, is still open to debate (e.g., Malinverno and Ryan 1986; Faccenna et al. 2001; Rosenbaum and Lister 2004; Peccerillo 2005). At present there is evidence for active subduction process of the Ionian oceanic lithosphere of Mesozoic age (Catalano et al. 2001) beneath the Calabrian Arc, where there is mostly seismicity between 160 and 370 km depth (Frepoli et al. 1996). The spatial distribution of the deep events shows a Wadati-Benioff zone dipping $\simeq 70NW$ beneath the southern Tyrrhenian, down to 500 km depth (Cimini 1999, and references therein). The slab has been associated with a high-velocity anomaly seen in several traveltime tomographic models, at different scales (e.g., Selvaggi and Chiarabba 1995, Lucente et al. 1999, Cimini and Gori 2001, Piromallo and Morelli 2003, Spakman and Wortel 2004, Montuori et al. 2007, and Neri et al. 2009). Tomographic cross-sections show a narrow slab which becomes horizontal in the transition zone on the 660 km discontinuity between upper and lower mantle (Piromallo and Morelli 2003; Spakman and Wortel 2004). Further evidence for subduction is the presence of magmatism associated with subduction of the Ionian lithosphere (Serri 1990; Serri et al. 2001). Interestingly, no subcrustal seismicity has been recorded from the southern and central Apennines (e.g., Di Stefano et al. 1999). This finding, together with the presence in several tomography models of a low-velocity anomaly below the southern Apennines, has led to explanations that differ mainly in considering the subducting slab either as continuous or as torn/detached. Within the southern Tyrrhenian Basin high heat flow values have been measured, exceeding 200 mW/m^2 (Della Vedova et al. 1991a, Della Vedova et al. 1991b; Zito et al. 2003), which correspond to areas of thinned crust (down to 10 km), and very shallow asthenosphere (up to 10-30 km) (Pontevivo and Panza 2006, and references therein). These areas correspond to two subbasins, the Vavilov and the Marsili and their respective volcanoes (Figure 3.7). The negative magnetic pattern in the southwestern part of Italy and the

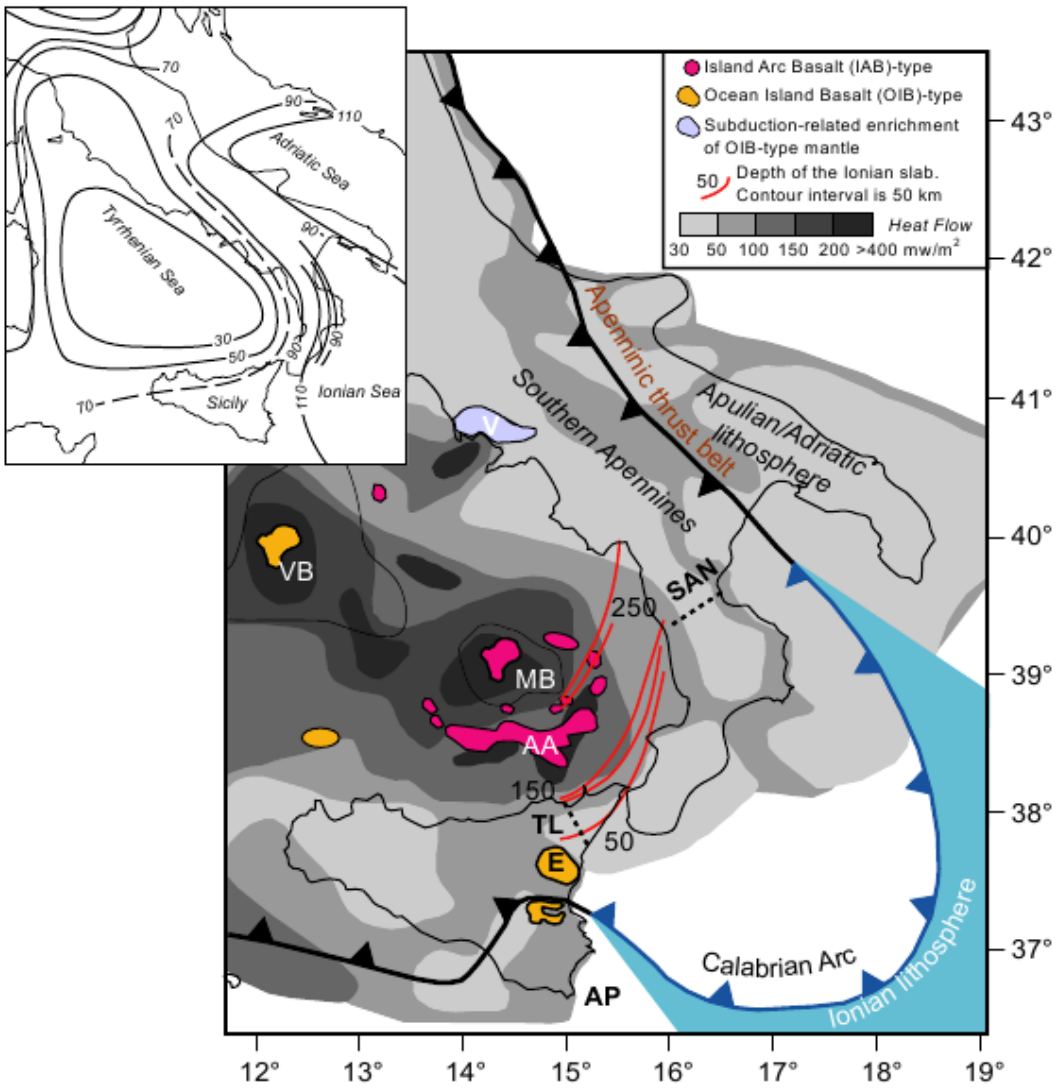

Figure 3.7: Study area, adapted from Cimini (2004) with permission. Heat flow values from Della Vedova et al. (1991b). Dominant volcanic magma sources from Trua et al. (2004). Wadati-Benioff zone (red curves) inferred from seismicity relocated in this studys 3D velocity model. Inset shows lithosphere thickness, simplified from Calcagnile and Panza (1981). Abbreviations are as follows: VB, Vavilov Basin; AA, Aeolian Arc; MB, Marsili Basin; TL, Tindari-Letojanni tectonic line; E, Mount Etna; AP, African plate; SAN, Sangineto tectonic line; V, Vesuvius.

Tyrrhenian coast agrees with the presence of high heat flow, pointing to a very shallow 600°C isotherm (Speranza and Chiappini 2002).

The LET method described in Section 2.1.1 was applied to P-wave traveltime data from intermediate depth ($\sim 70-300$ km depth range) earthquakes of the Calabrian arc. To have complementary information we also calculated t^* data for the same waveforms and inverted them to calculate a 3D Qp model, following the technique described in Section 2.1 and in 2.3.1. The study area includes a part of the eastern sector of the Marsili Basin, and in general, areas with high heat flow where we expect large lateral temperature variations, thus large variations in seismic Qp and Vp. The complete work is presented in Appendix 2, here I will describe the main results. We find the following interesting features from the interpretation of the main anomalies in the calculated 3D Qp and Vp models (refer to Figures 3.8, 3.9, and 3.10):

1. The mantle wedge and pathways for fluid/melts: The part of the main low-Qp /low-Vp anomaly found in proximity of the Wadati-Benioff zone where there is intense seismic activity (150–200 km depth). This main low-Qp /low-Vp anomaly located, between 100 and 200 km depth, below the eastern part of the Marsili Basin where there are very high heat flow values, and branches out to reach Moho depths in the direction of the Vesuvius and the southern Apennines, toward northern Sicily and toward the southwestern tip of Calabria and the Ionian Sea. It appears that part of the low-Qp /low-Vp anomaly below Calabria/Ionian Sea could be separated by a volume of high-Qp /high-Vp from the rest of the low-Qp /low-Vp anomaly, but a study with higher resolution is necessary to confirm this.

The position of this low-Qp /low-Vp anomaly and its elongated form can be explained by dehydration of the slab (and its embrittlement) where fluids lower the melting temperature of the overlying asthenosphere. Then, the low-Qp anomaly is caused by presence of fluids and melt, and the branches could represent pathways for fluid and melt migration through the mantle wedge up to crustal depths. This pattern can help in imaging the flow of hot mobile material in this area and to better understand its relation to volcanism. In particular, it can help our understanding of the strong geochemical affinities between magmas found at Stromboli and Vesuvius. A link between a strong low-Qp anomaly in the mantle wedge, seismicity at 100–200 km depth, slab dehydration, and mantle melting has been observed by Schurr et al. (2003) for the Andean subduction zone.

2. The subducting Ionian lithosphere: represented by a high-Vp (to a lesser extent Qp) anomaly (HVA) containing the intermediate depth seismicity. This steeply descending volume is seen down toward the bottom of the model (about 200 km), is limited by volumes of LVA/LQA and by transition zones corresponding to important tectonic struc-

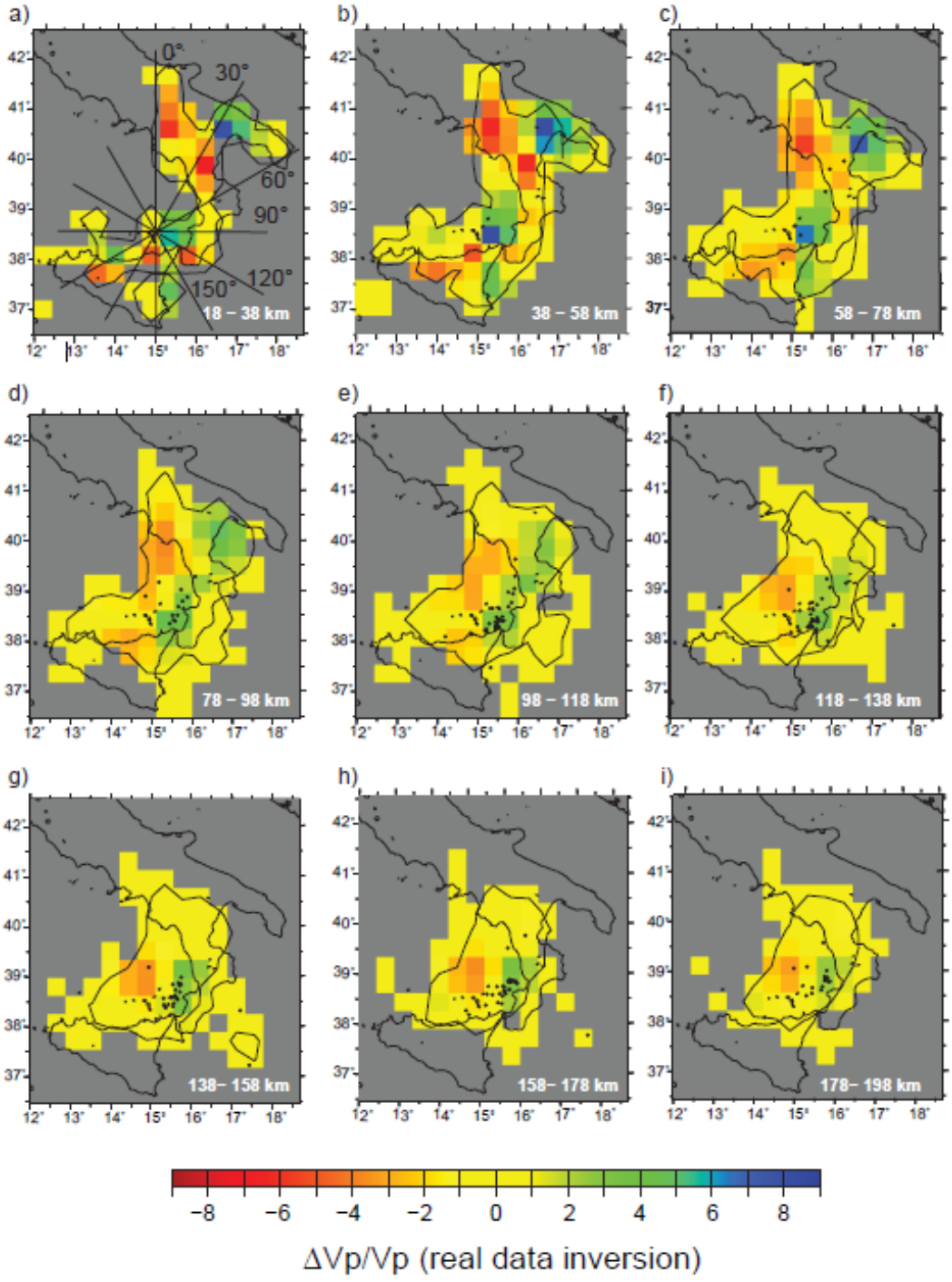

Figure 3.8: Maps of the 3D Vp model obtained by real data inversion (percent variation). In a) lines represent profiles for cross-sections. Black circles represent hypocenters relocated in the 3D Vp model.

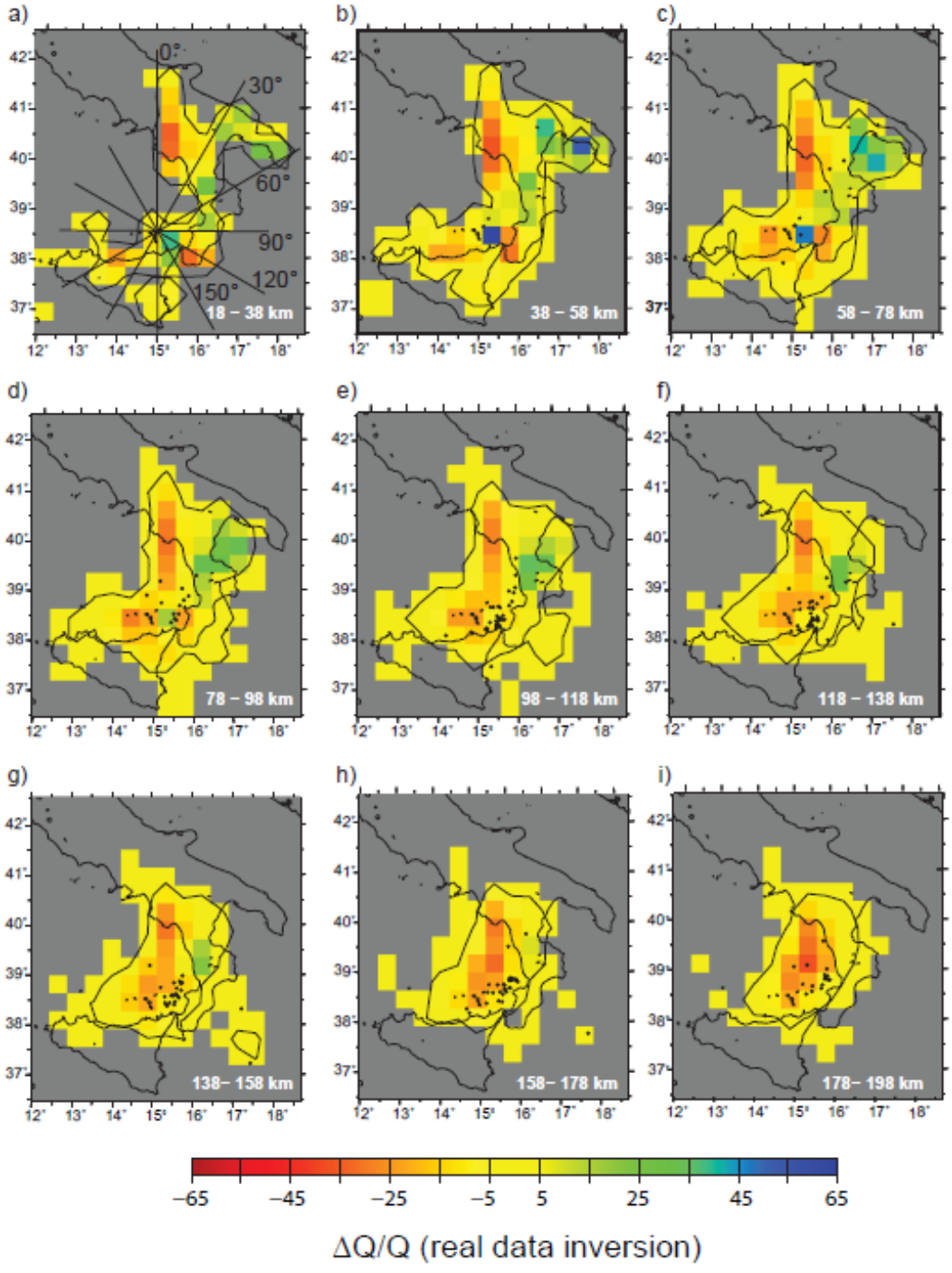

Figure 3.9: Maps of the 3D QP model obtained by real data inversion (percent variation). Profiles in a) are the same as in figure 3.8.

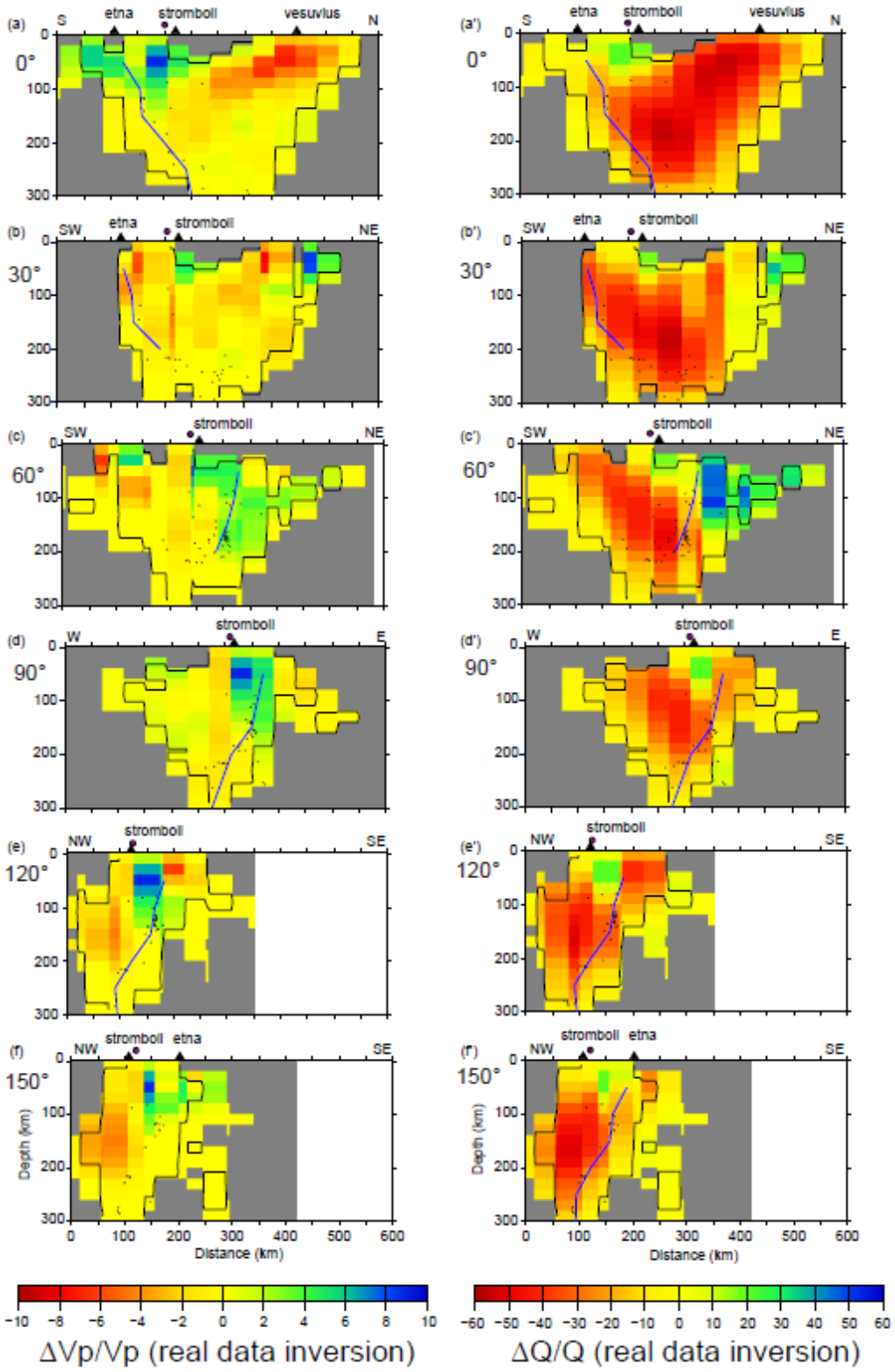

Figure 3.10: Cross sections of 3D Vp and Qp models (real data). Sections are along profiles shown in Figures 3.8 and 3.9. Sections are every 30°, where the angle is measured in the clockwise direction starting from north, and they all go through the point shown as a purple dot.

tures (see point 4 below).

3. The thick Adriatic continental lithosphere and the continuity of the slab: imaged by a high-Qp /high-Vp anomaly,this volume of rock together with the subducting Ionian lithosphere appear in the models as a continuous body forming a waveguide in which the high-frequency part of the wavefield from deep events can propagate. The very efficient transmission of P and S waves from deep slab events to Apulia leads us to think that, in agreement with Mele (1998), at the scale of the considered wavelengths (about 110 km) the waves are sampling a rock volume (the subducting slab + Adriatic lithosphere) having continuous rheological and physical properties. This observation excludes a large scale complete slab detachment.

4. Transition zones which correspond to the limits of the slab: we have strong variations of Qp (between 50 and 100 %) and Vp (up to 10 %), corresponding to important tectonic lines (SAN and TL in Figure 3.7) which have been proposed as the southwestern and northeastern limits of the oceanic Ionian lithosphere (Marani and Trua 2002, and references therein). Interestingly, the position of the low-Qp /low-Vp anomalies correspond to sites for slab windows or slab detachment hypothesized by other authors and by the Gvirtzman and Nur (1999) model to explain Mount Etna's relation to the subduction zone and the rapid vertical growth of the Marsili volcano Marani and Trua (2002). More information on this study is found in Appendix 2.

3.3 Upper mantle teleseismic tomography of the Cadiz Gulf-Alboran Sea area

The third case presented is a teleseismic tomography study of the SW Iberian margin and Alboran Sea based on teleseismic arrival times. The 3D model was computed down to 600 km depth. The geodynamic evolution of the southwestern Iberian margin and the Alboran Sea is the result of the complex interaction between the African and Eurasian plates (Figure 3.11). At present, there is convergence between the two plates at a rate of $\sim 5mm/year$ (Stich et al. 2006). The plate boundary is clearly defined from the Gloria fault to the Gorringe Bank (Zitellini et al. 2009). From the Gorringe Bank proceeding to the east, across the Strait of Gibraltar, the boundary is diffuse (Sartori et al. 1994) with different locations having been proposed for it. A narrow band of deformation (SWIM Fault Zone, SFZ in Figure 3.11), is considered as a precursor to the formation of a new transcurrent plate boundary between Iberia and Africa (Zitellini et al. 2009). Two main geodynamic evolution models have been proposed so far in literature for the Alboran Basin System:

1) Collision of Europe and Africa led to lithospheric thickening during the Paleogene.

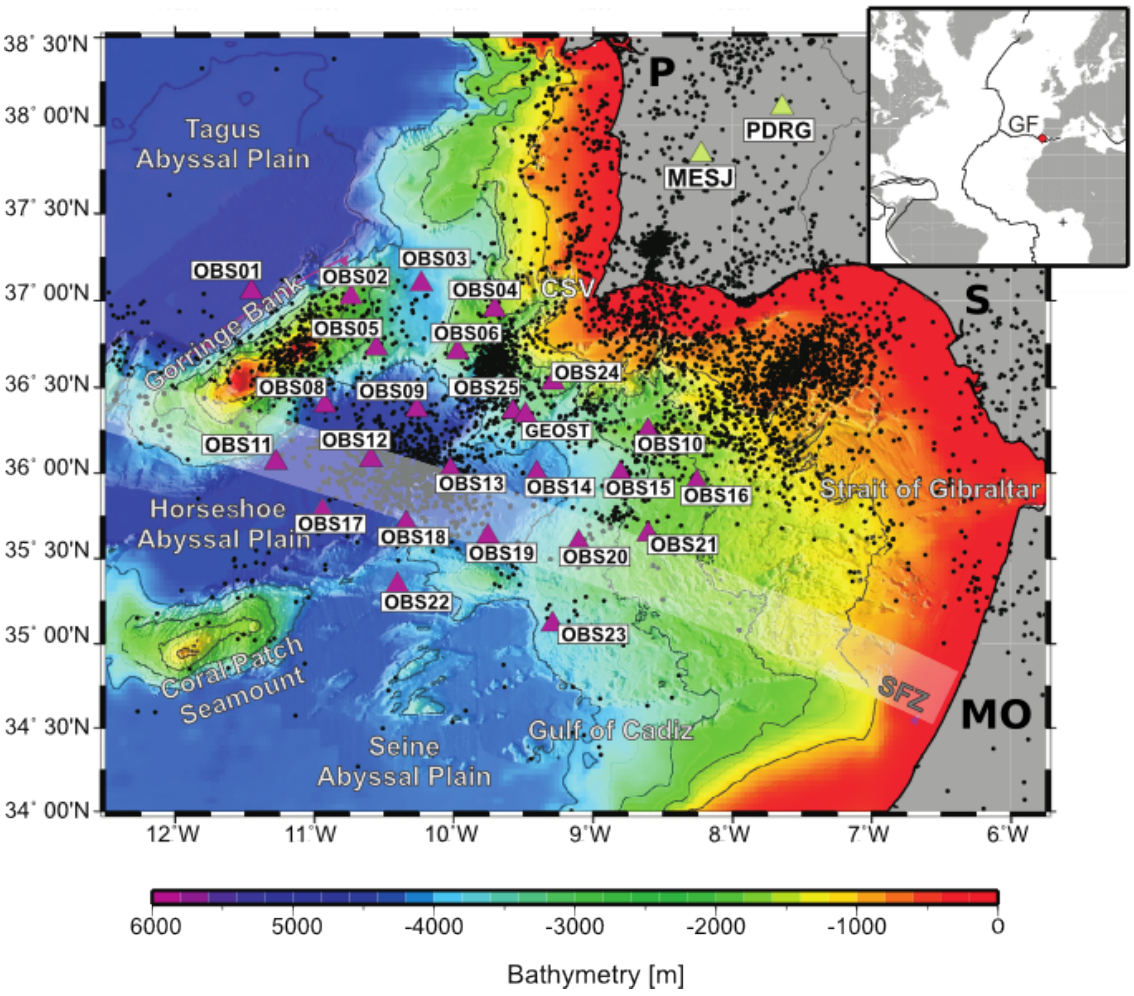

Figure 3.11: Map of the Gulf of Cadiz and surrounding regions showing seismicity related to the main tectonic features and the NEAREST land stations and marine network (triangles). The marine network includes 24 OBS plus GEOSTAR seafloor observatory. Purple and green triangles represent marine and land stations used in the present study. Epicentral locations are from the bulletin of the Institute of Meteorology Lisbon (http://www.meteo.pt/en/publicacoes/tecnico-cientif/noIM/boletins/). CSV=Cap St. Vincent; E=Spain; P=Portugal; MO=Morocco. In inset, GF=Gloria Fault. Adapted from Geissler et al. (2010).

The thickened continental lithosphere was later ($\sim$ $20Ma$) detached by convective removal (Platt and Vissers 1989) or by delamination (Seber et al. 1996; Calvert et al. 2000). The collapse of this lithosphere caused extension of the Alboran basin and uplift around the margin.

2) Subduction of oceanic lithosphere caused extension within the Alboran Basin in the Miocene by slab rollback (Royden 1993; Lonergan and White 1997; **?**; Gutscher et al. 2002) or by slab detachment (Zeck 1996). Starting from their geometric and structure similarity, a common origin has been proposed for the Calabrian (Central Mediterranean), and Gibraltar Arcs. In this reconstruction the Arcs formed from the fragmentation of a single subduction zone during the tectonic evolution of the Central-Western Mediterranean region (Faccenna et al. 2004, and references therein).

Different geophysical observations have been interpreted within the proposed geodynamic models. Magma evolution in time and space shows a volcanism which could be explained by a subduction scenario (Duggen et al. 2004), but it has also been invoked in support of delamination (Zeck 1996) and of the convective removal models (Platt and Vissers 1989; Platt 1998; Turner et al. 1999). Tomographic studies show a high velocity body under the Alboran Sea, which has been interpreted as a continuous subducting slab (Gutscher et al. 2002; Piromallo and Morelli 2003), as slab break-off (Blanco and Spakman 1993), and as lithosphere which has undergone delamination (Calvert et al. 2000). The pattern obtained from seismic anisotropy studies supports models involving a westward retreating slab (Buontempo et al. 2008; Bokelmann et al. 2011; Diaz et al. 2010). Measures on dispersion of P waves are compatible with subducted oceanic lithosphere (Bokelmann et al. 2011).

The two domains, Alboran Sea and Atlantic domain (Gulf of Cadiz), east and west of the Gibraltar Strait, show differences in their geophysical and seismological characters. In the Alboran domain Bouguer anomalies modeling shows that the base of the lithosphere ranges from 140 km depth in the Gibraltar Strait to less than 45 km depth in the easternmost Alboran Sea (Tornè et al. 2000; Zeyen et al. 2005). The average heat flow in the western Alboran basin is $69 \pm 6 mW/m^2$ with a generally increasing trend towards the center and to the east. In contrast, the heat flow pattern in the eastern Alboran Basin shows an average value of $124 \pm 8 mW/m^2$ which remains rather constant over the whole area (Polyak et al. 1996). Moderate superficial seismicity and a seismic gap between 20-60 km depth has been observed in the Alboran Sea (Figure 3.12). There is intermediate seismicity, located near the Strait of Gibraltar within 120 km depth and distributed in a very narrow N-S oriented vertical band (Seber et al. 1996). Deep earthquakes are rare and occur at the bottom of the transition zone ($\sim$ 630 km depth) under southern Spain in the Granada area (Buforn et al. 2004), and no Benioff zone is

visible. Under the Alboran Sea and southern Spain mostly extensional and strike-slip focal mechanisms are reported and combination of seismic and GPS data points to a transestensional regime (Stich et al. 2003; Stich et al. 2006).

In the Atlantic domain, heat flow is high above the Horseshoe Abyssal Plain (about $52 - 59\ mW/m^2$) and it decreases eastward across the Gulf of Cadiz prism, attaining minimum values ($\simeq 40\ mW/m^2$) towards the Gibraltar Strait (Grevemeyer et al. 2009). The low values and trend of heat flow are typical of active thrusting, and could be explained by an east-dipping subduction model, which may or may not be active (Grevemeyer et al. 2009, and references therein). There is evidence in the Gulf of Cadiz for sub-crustal earthquakes down to 60 km depth. A recent study based on the NEAREST marine array data (Geissler et al. 2010) shows that the observed seismicity is contained in a seismogenic layer of 140 Ma old oceanic lithosphere, and aligned along NNE-SSW and WNW-ESE striking structures. In the Gulf of Cadiz repeated GPS measurements and focal mechanisms, which are mainly reverse and strike slip, point to a transpressive plate boundary (Stich et al. 2005; Geissler et al. 2010). These studies show that there is a change of stress regime going across the Gibraltar Strait from transestensional in the Alboran domain to transpressive in the Atlantic domain.

Tomographic models proposed so far do not give much information on the upper-mantle structure west of Gibraltar Strait, due to the lack of long-term data series at the sea bottom. In particular, a clear image of the transition between the African and Eurasian continental domain, and the Atlantic oceanic domain is still lacking. Knowledge of the Atlantic domain and of the passage to the Alboran domain can also put some constraints on the models describing the geodynamic evolution of the Alboran domain. An open question is the present relation of the Atlantic and Alboran domains. This study presents a 3D P-wave upper-mantle tomography model of the SW Iberian margin and Alboran Sea based on teleseismic arrival times recorded by Iberian and Moroccan land stations and by a seafloor network deployed for in the Gulf of Cadiz area during the EC-NEAREST project (http://www.ismar.cnr.it/projects/international-projects/progetti-conclusi/nearest-project). The 3D model was computed for the upper-mantle down to 600 km depth. The inversion technique is introduced in Section 2.1.2. In the following the tomography study is presented along with the main results. A more detailed description can be found in Appendix 3.

The investigated area, which includes the Alboran Sea and the Gulf of Cadiz, has proven to be quite complex, as reflected by the numerous and sometimes conflicting interpretations found in literature. Despite several geophysical measurements, a more comprehensive understanding of the area has been hindered by the lack of long-term instrumental coverage at sea. The NEAREST experiment, thanks to seafloor seismo-

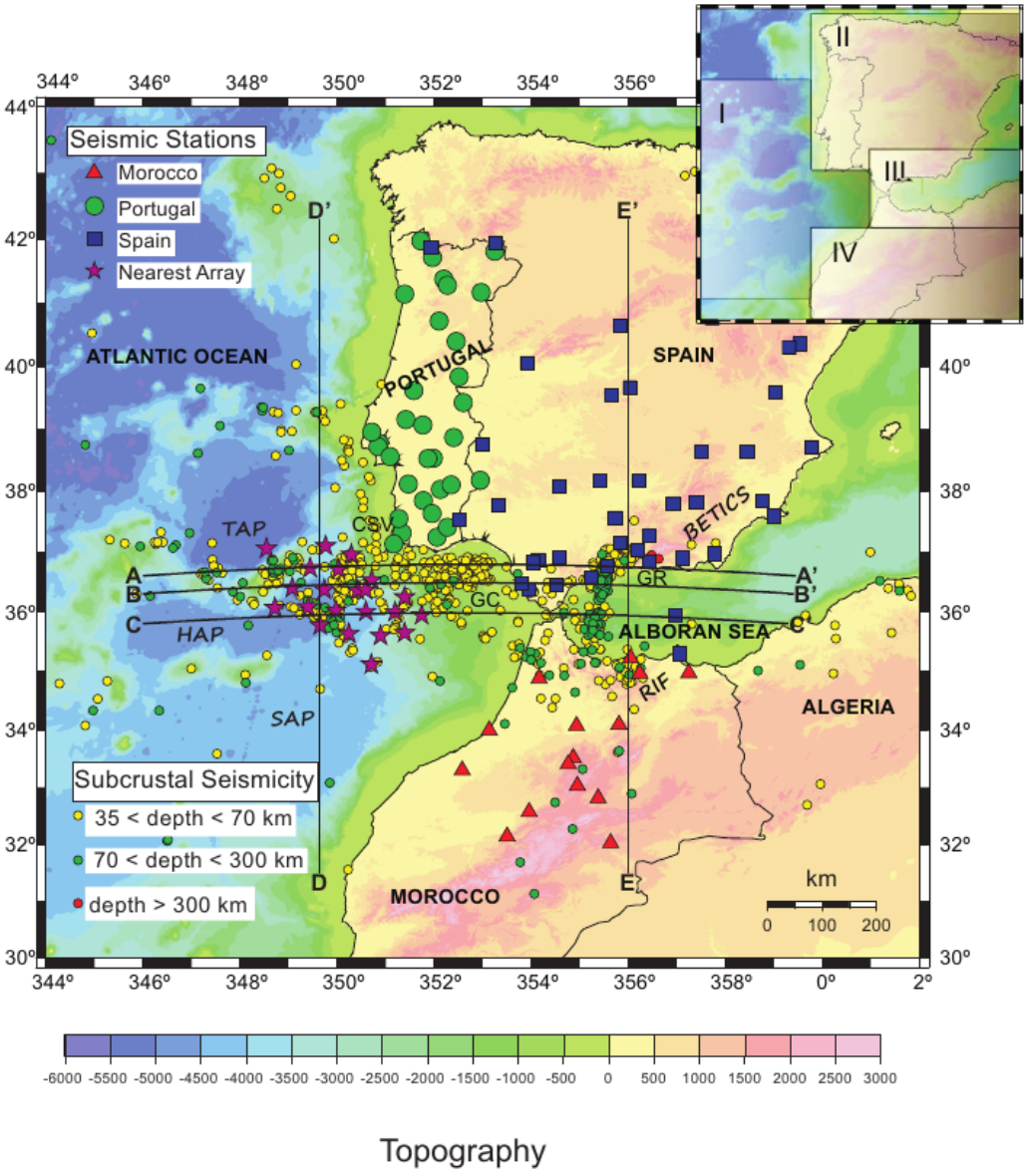

Figure 3.12: Map of seismic stations used for the tomographic inversion. Stars represent marine stations from the NEAREST array (2007-2008 experiment; 24 OBS/H, GEOSTAR), and 2 broadband land stations (MESJ, PDRG; Southern Portugal). The integrated array consists of 111 receivers. Colored dots represent sub-crustal seismicity at different depth intervals. Land stations are part of the permanent networks of Spain (blue squares), Portugal (green circles), and Morocco (red triangles). Hypocentral locations are from http://www.02.ign.es/ign/layoutIn/sismoFormularioCatalogo.do (Instituto Geogrfico Nacional Spain, IGN). GR=Granada area; CSV=Cap St. Vincent; GC=Gulf of Cadiz; SAP=Seine Abyssal Plain; HAP=Horseshoe Abyssal Plain; TAP=Tagus Abyssal Plain. AA', BB', CC', DD', and EE' show the traces of the profiles shown in Figures 3.14 and 3.15. The inset shows the four regions used for the crustal corrections of traveltime residuals.

logical recordings, allows us to better resolve the upper-mantle structure of this area. The NEAREST seafloor seismic network was deployed for 1 year (August 2007-August 2008) in the Gulf of Cadiz and off-shore Cap St. Vincent, with average spacing of ~ 50 km (Figure 3.11). This network comprised 24 stations (OBS/H) from the German DEPAS pool, each equipped with a 3-component Guralp CMG-40T broadband seismometer with 60 s-50 Hz response (OBS) and a High Tech HTI-04-PCA/ULF hydrophone (OBH). The same type of seismometer was installed on board the GEOSTAR deep-sea multiparameter observatory deployed in the same period. Furthermore, two broadband land stations were installed in southern Portugal at the beginning of the experiment. Figure 3.12 shows the seismic stations used in the inversion for the velocity structure. The dataset was selected from over 200 $Mw5.5$ events, which occurred during the experiment, with epicentral distance between 30° and 95°. To pick the first P-arrival on the waveform data we employed the semi-automated multi-channel cross-correlation technique (MCCC; VanDecar and Crosson 1990) on the vertical channel of the unfiltered data (more information can be found in Appendices 3 and 6). To obtain better ray coverage we also added 89 teleseisms recorded by the Moroccan, Portuguese, and Spanish seismic networks in the period January 2007-June 2009. The corresponding arrival times were extracted from the ISC bulletin (http://www.isc.ac.uk), which also includes readings of later arrivals as pP, sP, PcP, and core phases as PKPdf. Our teleseismic dataset consists of 152 events (130 P, 16 pP, 3 sP, 3 PcP) with at least 10 P-wave recordings, for a total of 6238 P-wave arrival times for the tomography. Epicentral locations were provided by the NEIC earthquake catalogs (http://earthquake.usgs.gov/research). The azimuthal equidistance map is shown in Appendix 3.

The following discussion will focus on the Atlantic (SW Iberian margin and Cadiz Gulf) and Alboran Sea domains. We discuss our results with reference to the two main geodynamic models mentioned previously, i.e. subduction and delamination below the Alboran Sea.

Implications for subduction with roll-back. Consistently with previous tomography studies (Calvert et al. 2000; Piromallo and Morelli 2003; Spakman and Wortel 2004), our model shows a high velocity body below the Alboran Sea area (HVA3, Figures 3.13, 3.14 and 3.15), suggesting the presence of cold, fast lithosphere visible down to the bottom of our model at 600 km. Thanks to our improved dataset, with respect to previous studies, we are able to have a more reliable and defined image of this high velocity body. HVA3 extends continuously from the southern Iberian Margin, below the Granada area where the scarce deep seismicity occurs, to under the Alboran Sea where there is intermediate depth seismicity. Its geometry is L-shaped at shallower depths, while below 300 km it shows an elongated shape extending towards the Strait of

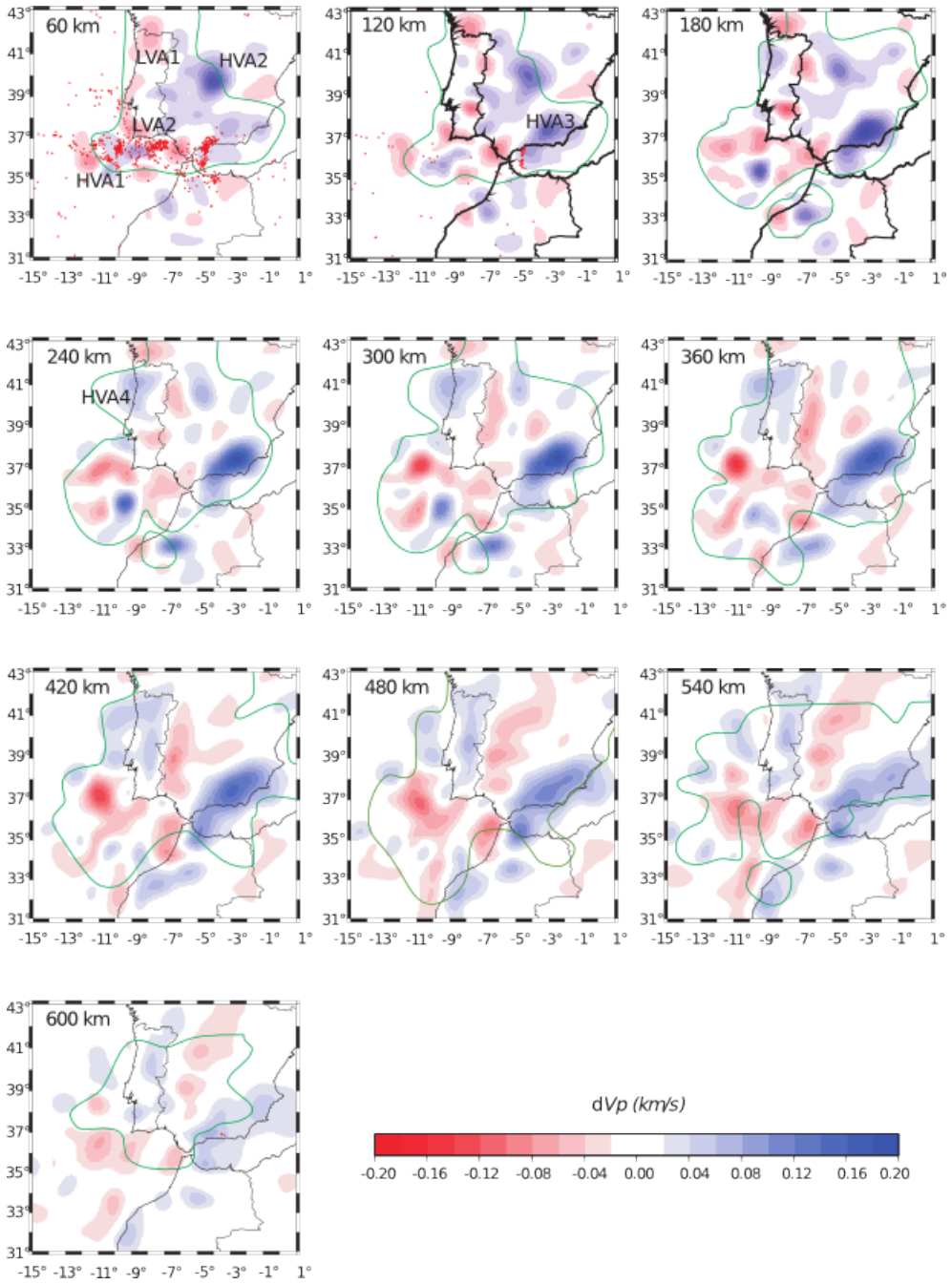

Figure 3.13: Horizontal slices through the 3D solution model showing the lateral heterogeneities in the upper mantle structure investigated. Labels show the depth at which the slices are taken. The P-wave velocity model is represented as perturbations from the composite starting model. Dots represent the local seismicity at the slice depth within +/- 30 km. The green line includes the resolved part of the model, this line was drawn on the basis of the checkerboard test. Hypocenter locations of local seismicity comes from the IGN catalog 1980- 2010 (812 events with $M > 3$, and $depth > 35$ km).

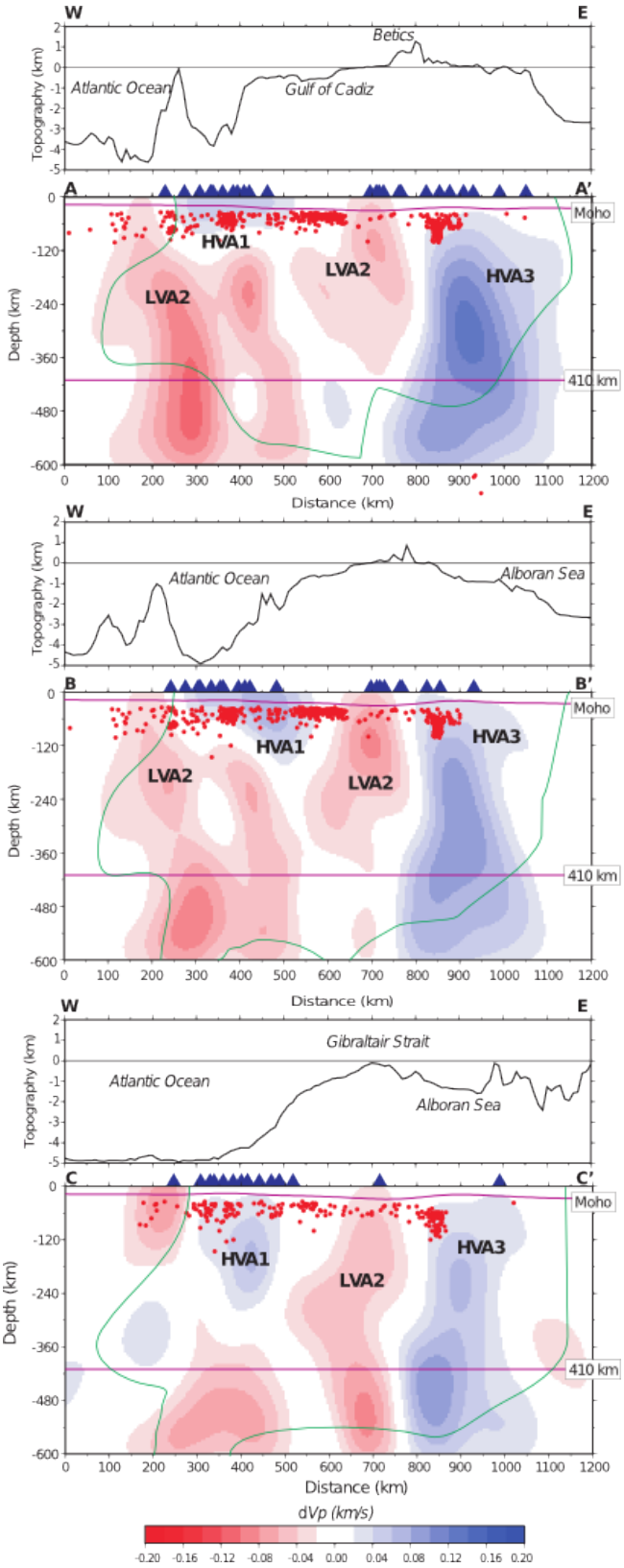

Figure 3.14: Cross-sections through the 3-D solution model (Continues on next page)

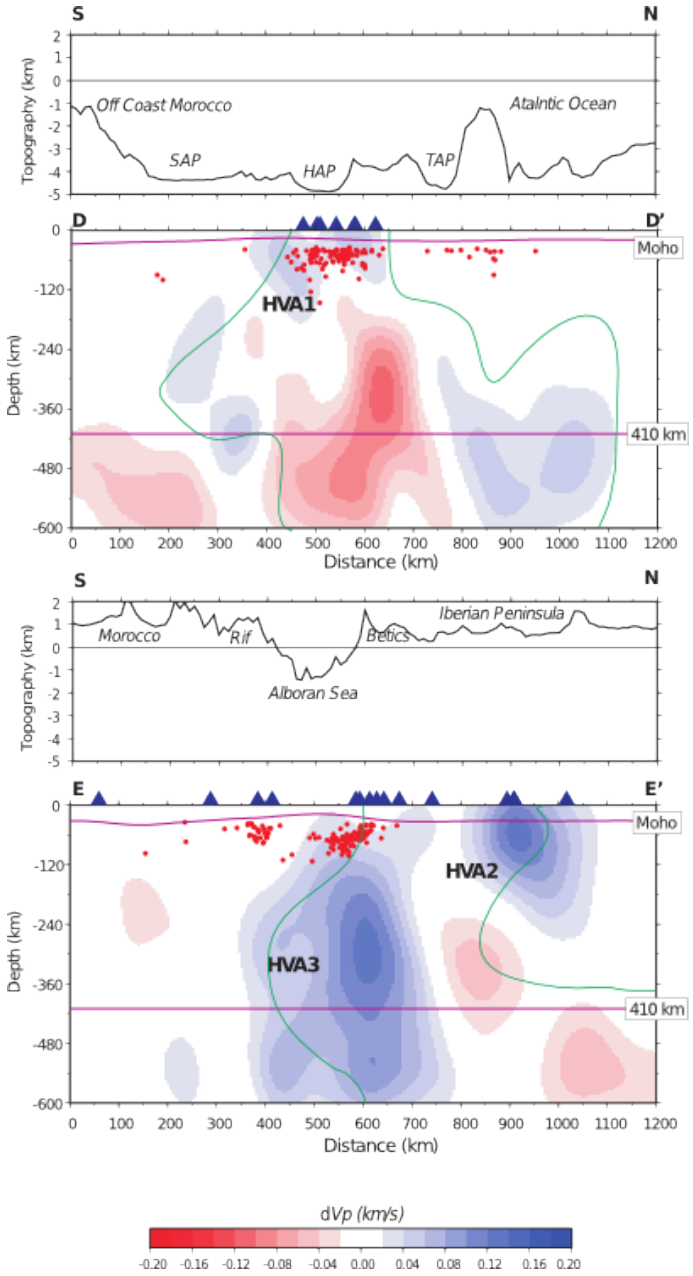

Figure 3.15: computed along the great circle paths shown in 3.12 a) Cross-sections AA, BB , and CC' display the seismic structure from West to East. b) Cross-sections DD and EE' cut the modeled volume from South to North. In DD', SAP is the Seine Abyssal Plain, HAP the Horseshoe Abyssal Plain, TAP the Tagus Abyssal Plain. Blue triangles and red dots indicate the seismic stations and the sub-crustal seismicity located within a 100 km-wide zone centered on the profile. Topography/bathymetric profiles are from the GlobalIntegratedTopo/Bathymetry Grid (GINA) (Lindquist et al. 2004). Moho topography is from the European Moho depth map (Grad et al. 2009). The green line includes the resolved part of the model. Hypocenters deeper than 600 km show the deep events below the Granada region (AA').

Gibraltar, and northern Morocco. Recent geophysical observations point to the effects of subduction (active or extinct) with westward roll-back of oceanic lithosphere below the Alboran Sea. Anisotropy patterns are more consistent with a slab roll-back model than with delamination or convective removal of lithosphere models (Buontempo et al. 2008; Diaz et al. 2010). Seismic wave dispersion measurements point to the oceanic nature of the sinking lithosphere (Bokelmann and Maufroy 2007). All these observations suggest the existence of subduction with roll-back, either active or extinct, below the Alboran Sea. Some authors have proposed the existence of a continuous lithospheric slab going from the Atlantic domain, across the Gibraltar Strait, to below the Alboran Sea (Gutscher et al. 2002, and references therein). But subduction, if it exists, must be either very slow or finished, as implied by GPS data which show small to none differential motion across the Gibraltar Strait (Stich et al. 2006; Serpelloni et al. 2007). An important element imaged in our model is a strong discontinuity between the seismic structure of the lithospheres in the Alboran and Atlantic domains (cross sections AA', BB, and CC' in Figure 3.14), which is not resolved by previous tomographic studies. Although the part just south of the Gibraltar Strait is poorly resolved, especially in the shallower layers (Figure 3.13), the synthetic test shows that if there were a continuous slab coming from the Atlantic domain subducting below the Alboran Sea, we should be able to detect it.

Implications for delamination. Not all data can be explained by a subduction roll-back mechanism. In fact, although deep seismicity is usually associated with a subduction process, the intermediate depth seismicity below the Alboran Sea has a distribution which is not typical of subduction zones. In contrast to the nearby Calabrian Arc (Central Mediterranean, see for example Montuori et al. 2007) which also has a small curvature radius, there is no well defined Benioff plane. Intermediate depth seismicity is found only within the top of the high velocity body represented by HVA3 (Figures 3.14 and 3.15). There seems to be a gap of seismicity between 30-50 km (Buforn et al. 2004), while a great majority of hypocenters are found above 150 km depth. Similarly, in the Vrancea area there is a gap between 40-70 km depth, while intermediate depth seismicity is contained above 170 km depth. The seismic gap for Vrancea has been explained as being possibly due to a decoupled seismogenic zone from the overriding plate (Sperner et al. 2001). Furthermore, studies of igneous rocks also imply a complex geodynamic time-space evolution of the Western Mediterranean region. Thermal models for metamorphic units from the floor of the Alboran Basin are consistent with post-collisional rapid exhumation and associated heating. Geochemical and geochronological data show a transition from post-collisional subduction-related to intraplate-type magmatism which occurred between 6.3 and 4.8 Ma (Duggen et al. 2005). These processes

imply a role for lithospheric delamination (Platt 1998).

Now we will try to determine a geodynamic evolution that is compatible with the above constraints and our tomography. The high velocity body under the Alboran Sea area appears as isolated, adjacent to a pronounced low velocity anomaly, and possibly separated from the overlying lithosphere. The recovered geometry suggests its evolution in time: the older section of the slab, corresponding to a planar deeper part (Figure 3.13), was subjected to roll-back and not (or minimally) deformed by Africa-Eurasia compression, while the younger, shallower part, found above $\sim$ 300 km depth, was subjected both to roll-back and compression, and still is subjected to the African-Eurasia compression which caused its arcuate shape. The separation of the high velocity oceanic lithospheric structure in the Atlantic and Alboran domains in our model is consistent with a subduction with westward roll-back process that has come to a stop east of the Gibraltar Strait, in agreement with the reconstruction proposed by Lonergan and White (1997). This evolution of the slab geometry also agrees with the sequence of tectonic events reconstructed by Iribarren et al. (2007) who favor a westward slab retreat process active from Middle to Late Miocene time. Successively, oceanic subduction with roll-back triggered continental-edge delamination under northwestern Africa and southern Iberia, as proposed by Duggen et al. (2005) on the basis of petrological studies.

Now we will comment other interesting parts of the model. A clear high velocity anomaly, HVA1, is imaged for the first time under the NEAREST array, in an area roughly underlying the Horseshoe Abyssal Plain. This area is part of a diffuse convergent margin where old oceanic lithosphere is hypothesized (Zitellini et al. 2009; Geissler et al. 2010). The thickness of HVA1 ($\sim 80 - 150$ km in cross-sections AA'-BB', in Figure 3.14) agrees with values proposed in literature for old ($\sim 140Ma$) oceanic lithosphere (McKenzie et al. 2005; Conrad and Lithgow-Bertelloni 2006). Low velocity anomalies are also visible, LVA1 and LVA2. LVA2 together with HVA1, define what we interpret as the passage from the Atlantic oceanic to the Iberian continental lithosphere (Figures 3.13 and 3.14). The passage from HVA1 to LVA2, in the SW-NE direction, is in good agreement with the position of the south Portuguese stress regime anomaly observed by (Stich et al. 2003 and marks the transition from oceanic to continental crust. HVA1 is visible, form the crust down to sub-lithospheric depths The E-W shape of HVA1 suggests incipient subduction (3.14). In fact, the Gorringe bank is considered an example of young incipient margin that could develop into a subduction zone (Gurnis et al. 2004).

At sub-lithospheric depths, below the Atlantic domain, we image wide areas of lower than standard P-wave seismic velocities (LVA2), down to the bottom of our model. At these depths it is commonly agreed that temperature plays a first order role in determining lateral seismic velocity heterogeneity (e.g. Ranalli 1996), so we interpret

such low values (down to $\simeq -0.16$ km/s, about -2 % of the reference value) as being due to the presence of a hot upper mantle. Isotopic and geochemical studies show that the magmatism of western Portugal and of the adjacent Atlantic domain that occurred during the Mesozoic can be explained by the presence of a common sub-lithospheric regional mantle melting anomaly (Merle et al. 2006; Miranda et al. 2009, and references therein). Recent data show that this thermal anomaly is likely the source of tertiary and quaternary alkaline magmatism in the eastern North Atlantic region (Merle et al. 2006; Grange et al. 2010). The space-time evolution of magmatism in this region has been explained by assuming that the Iberian plate has rotated (about 30° anti-clockwise) above a fixed deep-rooted thermal anomaly (mantle plume; Sibuet et al. 2004; Grange et al. 2010).
Although it is outside the main area of interest, we briefly comment on the persistent feature HVA4, imaged beneath Portugal from 180 km depth down to the bottom of the model. Generally, high velocity bodies found at these depths are associated to colder and denser sinking lithosphere commonly considered of oceanic origin.

3.4 Discussion

The generation and interpretation of a tomography model is not a strightforward process. In Section 2.4 some general factors which determine the non-uniqueness inherent in tomography inversion and in model interpretation were introduced. This Section will focus on how these factors affected our particular applications of tomography and the steps that were taken to minimize the sources of ambiguity. I will first consider aspects related to the inversion procedure, then, in the next subsection will concentrate on the interpretation process.

3.4.1 Some critical aspects of seismic tomography with reference to our cases

Seismic tomography was applied at different scales to three study cases within the CWM area: local earthquake tomography (LET) at crustal and uppermost-mantle depths, and teleseismic tomography at upper mantle depths. Studying the interior of the Earth using tomography is like putting on glasses which only allow us to see objects (anomalies) of a given dimension, in a blurry way. Often, "ghosts" can appear in the tomographic images, and it is very important to distinguish the ghosts from the reliable features that are suitable for the interpretation. What I have learned is that there is not a best tomographic method, but there are tools that should be chosen accordingly to the prob-

lem at hand. It is important to establish the scale and reliability of the objects that we see. Ideally, we can design a tomography experiment where we have just the right station-earthquake distribution to detect the anomalies that we expect to find, but this is usually not possible and the experimental geometry puts heavy limitations on what we can resolve.
Station-event distribution (or experimental geometry) is the first factor to consider. It determines both the parametrization size and the amount of artefacts that will be produced by the inversion, and thus the quality of the tomographic image. To "get a feeling" for the resolving power and weak points of the experimental geometry in each application, it was necessary to perform many inversions (my colleague G.B. Cimini performed the teleseismic inversion for the Cadiz case). Synthetic tests were also very important in this part of the work. A good station-event geometry, of course, is heavily dependent on data availability. In the case of crustal LET we are strongly limited by the number of earthquakes within the crustal volume we want to study. To remedy this limitation active seismic experiments are performed. Similarly, if we want to apply LET to study the upper-mantle, we depend on the existence of sub-crustal earthquakes within the study volume, as for example those observed in active subduction zones. Teleseismic tomography presents an opposite situation, data availability is guaranteed (we just need to wait long enough) as there is basically a constant rate for global seismicity; for example, on the average, there are 139 earthquakes per year with magnitude between 6 and 6.9 (http://earthquake.usgs.gov/earthquakes/eqarchives/year/eqstats.php).

In the Colfiorito LET a high resolution tomography was possible (the scale of the resolved anomalies can be down to a few km) due to a very good station-event geometry. The other two cases were affected by problems. In the Calabrian Arc study earthquakes where clustered in space thus determining a fan-like ray geometry which led to smearing in the vertical direction. Furthermore, part of the study volume was below the sea where there was a lack of station coverage. In this case the scale of the resolved anomalies cannot be smaller than several 10 km. Due to this experimental setting strong regularization was necessary in the inversion procedure, and only a qualitative analysis was possible. The Cadiz-Alboran Sea case is also not ideal in terms of station-event distribution. Here the geometry is given by the epicentral distance-azimuth distribution of the events, which is determined by the location of the areas of the world that present strong seismicity. The geometry is limited by the lack of coverage at sea and in north Africa, but at the same time, a strong point of our study is the availability of precious data from the OBS deployed in the Gulf of Cadiz area. In this study the scale of the imaged anomalies is much greater (100 km). Furthermore, the Cadiz case is affected by the

typical problem of teleseismic tomography, i.e. the rays are quasi-parallel in the vertical direction. For this reason the images are affected by smearing in the vertical direction. In spite of these problems, thanks to improved coverage and resolution with respect to previous published 3D models, we could test implications coming from geodynamic models proposed in literature.

Another factor affecting the resolution capability of the data is the wavelength of the seismic waves. Although the traveltime tomography methods we applied are based on ray theory, actually, the waves have finite frequency, and they are sensitive to objects that have sizes of the order of their wavelength. More precisely, the Fresnel zone gives us the volume that is sampled by the waves. Ray theory is valid if the characteristic length of the heterogeneity of the medium traversed by the waves is much greater than the Fresnel zone. For local earthquakes we can have frequencies up to tens of Hz. In our LET cases bandwidth was limited by the use of short period sensors and by seismic attenuation. The measured wavelengths where a few hundred meters for the Colfiorito case and a few km for the Calabrian Arc case. For teleseismic tomography wavelengths are much greater, and they depend on the type of seismic phase. The dominating *P*-phase wavelength in the Cadiz Gulf case is in the order of a few tens of kilometers.

Finally, an important aspect which determines the quality of the inversion procedure comes from the errors affecting the detection of seismic phase arrivals on the seismograms. Of course, in any case, this detection capability increases with increasing signal/noise. Usually small errors affect high frequency arrivals for local earthquakes, where the errors of a good quality P-phase reading can be in the order of a few hundreds of a second. The S-phase is usually harder to detect to to the P-wave coda. For teleseismic waveform data the situation is more delicate, even for P-phases which are the first arrivals, it can be hard to hand pick the first arrival, especially when the wave does not have an impulsive onset. A method based on waveform similarity, as multi-channel correlation can help in reducing the error. Another source of variability in teleseismic inversions can be the use of ISC arrival times for which there is no associated picking error. The error for this heterogeneous dataset can only be quantified *a posteriori* by statistical means (Morelli and Dziewonski 1987; Gudmundsson et al. 1990).

3.4.2 Interpreting the models for the three cases

We have seen in Section 2.4 that a seismic anomaly found in a tomography model can be explained in multiple ways. For example, a decrease of V_s can be associated to the presence of fluids or to a temperature increase. The strategy we followed to reduce this

ambiguity was to determine the key factors that were acting in each particular case. This procedure was also based on cross evidence coming from independent data. The main factors affecting lateral velocity variations in the crust and upper mantle are: temperature, lithology and fluids (see in particular Table 2.1).

In the Colfiorito case we are dealing with continental crust in a tectonically active region where high lateral heterogeneity is expected. Thanks to heat flow measurements we know that temperature variation here is not a key factor, and so the interpretation was based on (average) lithology and fluids. It was important to identify and calculate seismic quantities from the P and S-wave traveltime inversion that strongly depend on chemical composition and lithology. In this way properties predicted from the 3D model can be compared to independent observations. A first constraint came from geological data on the average rock lithology expected at a given depth. The other important constrain came from laboratory measurements of seismic wave velocities for the main rock types found in this area both in dry and wet conditions. These measurements could then be compared to values of absolute seismic velocity obtained in the tomography model. V_p/V_s and $V_p * V_s$ distribution helped us determine the role of fluids and the porosity of the rocks.

In the second case, pertaining to the Calabrian arc, we are dealing with an active subduction zone, concentrating mainly on the uppermost mantle. We know that temperature does play an important role, in fact, in this area very high heat flow values have been measured and very strong temperature gradients are expected throughout. Fluids are also expected to play a role in supra-slab volumes at intermediate depths. Finally, strong lithological variations are also expected, for example when passing from oceanic to continental domains. Even though t^* measurements are affected by large errors, the use of Q tomography helped us in distinguishing the causes behind V and Q anomalies, in particular the role of temperature.

In the third case we focused on the reliable features of the model and on how this information could bring new constraints to the conflicting geodynamic interpretations for the area, keeping in mind that tomographic images are a snapshot of the current situation. To diminish the degree of non-uniqueness in our interpretation we considered bonds given by independent observations coming from other seismology studies, e.g, dispersion and anisotropy data, and other disciplines, e.g., petrology. As in the Calabrian arc case, we find that, in spite of the large errors affecting this model, the variation of seismic parameters are strong enough to produce anomalies that can be reliably inter-

preted, although in a qualitative way.

In all the study cases we carefully calculated a realistic starting model, which, as we have seen (Subsection 2.4.1), is a fundamental initial condition to obtain a reasonable 3D model. Also, all the anomalies that were interpreted were well-resolved and had a size that was equal or greater than the resolution capabilities of the data.
The final objective of a tomography work is to be able to measure absolute seismic quantities, to make some assumptions thanks to them, and perhaps to calculate other parameters from these quantities, as, for example temperature or density. At the same time we need to be aware of the limits of our results, as these estimated quantities strongly depend on our initial model choice and on the regularization procedure. Furthermore, a realistic estimate of the errors associated with these measurements is hard to produce. The Colfiorito LET inversion allowed some quantitative predictions, thanks to the very favorable station-event geometry, while in the other cases only qualitative results could be found. In spite of all these limits, the variations of seismic parameters in the Calabrian arc and Cadiz Gulf studies were strong enough to produce tomographic anomalies well above the noise level. Although a quantitative approach is preferable (given that it is not over-interpreted), qualitative results (or qualitative cromo-tomography, QCT; Anderson 2007) can also give useful information.

4 Discussion and conclusions

This dissertation had a twofold objective. The first objective was to study three different areas which are representative end members of the Cental Western Mediterranean (CWM) geodynamic evolution. The CWM, and the Mediterranean region in general, is the product of a complex geodynamic evolution so that many aspects are still controversial. The second objective was to apply seismic tomography techniques at different scales to address interesting problems that are related to the evolution of the CWM. Since seismic attenuation can give important information in subduction zones (but not only there), a main part of the thesis was devoted to develop a way to measure anelastic attenuation on seismic waveforms and to invert this data to calculate a 3D model.

In summary, the main results presented in this dissertation are:

- An algorithm to calculate t^* values starting from seismograms. A modified version of the Local Earthquake Tomography (LET) code FDTOMO (Benz et al. 1996) to calculate Q models by inverting relative t^* measurements. Synthetic tests were performed to check the correctness of the procedure.

- A 3D Vp and Vs (and derived quantities) crustal model of the Colfiorito basin in the northern Apennines (Italy) calculated with FDTOMO. Seismic anomalies were interpreted on the basis of changes in porosity, degree of fracturing, and fluid pore pressure. Data came from the Cofiorito aftershock sequence which lasted about three months, following the 26 September 1997 Mw 5.7 and Mw6.0 main shocks (22 aftershocks with $M > 4$).

From this tomography model it was possible to identify the distribution of the main rock types, i.e Maiolica and Calcare Massiccio (members of the carbonatic sequence), and Evaporites. The development in space and time of the 1997 seismic sequence could be better understood by considering the poro-elastic properties and fracturing state of the involved rock types and their structural pattern. These rock types reflect the marine paleo-environmental setting found within this part of the CWM, which formed mainly in the Mesozoic. The structural pattern was determined by the tectonic processes shaping

the thrust and fold Apennines chain from the late Cenozoic to present. Since it can give us information on the evolution in space-time of seismicity, this study can be useful for seismic hazard assessment. This approach has also been applied to other areas in the world where there is a strong poro-elastic effect (e.g. Lin and Shearer 2009).

- A 3D model of the uppermost mantle of the southern Tyrrhenian-Apennines area calculated with LET. This was an application of the seismic attenuation algorithm and t^* inversion. The comparison of Vp and Qp distributions confirms the role of temperature and shows the mantle wedge and its relation to intermediate-depth Calabrian slab events. Geochemical affinities of Stromboli and Vesuvius magmatic products could be associated to a low Qp/Vp channel, going from below Stromboli towards the Vesuvius. Strong discontinuities in the Qp/Vp distribution agree well with important tectonic structures. The slab is not completely detached, at least as seen by the short period waves considered in this study.

- A 3D model of the upper mantle of the Alboran Sea-Cadiz Gulf area obtained with teleseismic tomography (inversion performed by G. Cimini, co-author of the paper) with the integration in the dataset of waveforms from OBS deployed during the NEAREST experiment. Several interesting features are observed in the model. The first is the high velocity anomaly below the Alboran Sea, already observed in previous tomography studies (Calvert et al. 2000; Piromallo and Morelli 2003; Spakman and Wortel 2004), better constrained in its lateral extension and geometry by this study. This anomaly does not appear as a continuous slab coming from the Atlantic domain, west of the Gibraltar Strait. Another interesting aspect is a lateral seismic discontinuity which we interpret as the passage from Atlantic oceanic to Iberian continental lithosphere.

There are geometrical and structural similarities in the two subduction zones (Gibraltar and Calabrian). An evolution model explains these similarities by hypothesizing that the two arcs come from the fragmentation of a single subduction zone during the tectonic evolution of the CWM (Faccenna et al. 2004). At the same time there are important differences in the two cases that could be explained by the fact that the two arcs have been subjected to similar processes but at different times. An important difference, for example, is in the type of seismicity distribution in space: while there is a clear Benioff plane in the Calabrian zone (e.g. Frepoli et al. 1996, Cimini 1999), such a feature is not observed in the Gibraltar zone (e.g. Seber et al. 1996, Buforn et al. 2004). Also, in the Calabrian case several studies point to a continuous subduction which starts in the Ionian domain (e.g. Gallais et al. 2011, Polonia et al. 2011) and dips in the north-

west direction below the Tyrrhenian lithosphere (e.g. Piromallo and Morelli 2003). Slab continuity is confirmed by our analysis of short-period waveform attenuation. On the other hand, our results exclude that the high velocity body found below the Alboran Sea down to the bottom of the transition zone is part of a continuous slab that comes from the Atlantic domain and thus disprove geodynamic reconstructions that are based on a single slab coming from the Atlantic domain (e.g. Royden 1993, Gutscher et al. 2002). The east-west discontinuity of the Alboran slab, considerations on the geometry of the slab reconstructed in our model, together with constraints coming from other studies, lead us to a favored geodynamic view which has been proposed by other authors (Lonergan and White 1997, Iribarren et al. (2007), Duggen et al. 2005). In this view the present situation comes from a now extinct oceanic subduction with westward roll-back; the subduction stopped in front of the Gibraltar Strait and was possibly followed by other geodynamic processes, such as continental delamination.

In the three cases an effort was put forth to minimize various sources of ambiguity that affect tomographic work. Great care was applied in the calculation of a valid starting model for the 3D inversion on the basis of available and up-to-date independent data. Furthermore, in the LET studies an algorithm was applied to search for the "minimum" 1D model. A thorough knowledge of how the experimental setting (station-event geometry) affects results, was achieved by performing many inversions of real data using different values of the regularization parameters. Also, tests based on synthetic data were used extensively to determine the resolution and limits of the data. Non uniqueness in the interpretation of the models was reduced by using constraints coming from independent data from several disciplines. For each tomography application the scale of the interpreted anomalies were within the resolution limits of the data. For the two study cases at larger scale, Southern Apennines-Calabrian arc and Cadiz Gulf-Alboran Sea, the information extracted from the models was mainly qualitative. In the Colfiorito case a more quantitative approach was possible, and we could calculate quantities from the model that can be used as predictors to determine the rock properties.

In summary, it is important to define the limits of the data set, which depend on the station-event geometry and the wavelength of the seismic waves. These limits determine the scale of our problem through the choice of the appropriate grid or cell size to parametrize the Earth. The next step is to define the parts of the model that are well defined and the parts that are affected by inversion artefacts or that are not resolved by the data. The well resolved parts of the model are the ones that are used in the interpretation. Finally, independent data should be used to reduce ambiguities in the

interpretation.

The use of seafloor seismic stations has proven crucial to have more reliable and extended models of the Calabrian (Montuori et al. 2007) and the Gibraltar arcs (our study). This approach should be expanded in the future with more long-term broadband OBS campaigns. Although a lot is already known for the Calabrian arc subduction zone, a clear image going from south to north of the upper mantle of the area, including the subducting Ionian lithosphere, is still missing due to the lack of long-term broadband OBS data in the Ionian domain. Due to the small spatial extension of the NEAREST array our view was limited. Some interesting aspects of the SW Iberian margin that could be better addressed by extending the OBS observations are: to have a better definition of the transition between the African and the European lithospheres east of the Gloria fault; to confirm and have a better view of the possible incipient subduction in the Gorringe Bank area suggested by our images; to have a more complete evaluation of the extension and geometry of the diffuse low velocity zone we found in the Atlantic domain and to confront this observation with the plume hypothesis (e.g. Sibuet et al. 2004; Grange et al. 2010)). By extending the OBS array in the northern direction, west of Portugal, we can better study one of the persistent features we observe, i.e. the high velocity anomaly HVA4 imaged below Portugal from 180 km depth down to the bottom of the model at 600 km depth. All these pieces can be put together to create in a wider picture, a picture that puts constraints on the geodynamic models of this complex area.

Bibliography

K. Aki and P. G. Richards. *Quantitative seismology*. University Science Books, sausalito, California, 2002.

K. Aki, A. Christofferson, and E. Husebye. Determination of the three-dimensional seismic structure of the lithosphere. *J. Geophys. Res.*, 82:277 – 296, 1977.

B. Alessandrini, L. Filippi, and A. Borgia. Upper-crust tomographic structure of the Central Apennines, Italy, from local earthquakes. *Tectonophysics*, 339:479 – 494, 2001.

A. Amato, B. Alessandrini, and G. B. Cimini. Teleseismic wave tomography of Italy. In H. M. Iyer and K. Hirahaha, editors, *Seismic Tomography: Theory and Practice*, pages 361 – 397. Chapman and Hall, London, 1993.

D. L. Anderson. *The New Theory of the Earth*. Cambridge University Press, 2007.

A. Argnani. The southern Tyrrhenian subduction system: Recent evolution and neotectonic implications. *Ann. Geofis.*, 43:585 – 607, 2000.

P. Baccheschi, L. Margheriti, and M. S. Steckler. Seismic anisotropy reveals focused mantle flow around the Calabrian slab (Southern Italy). *Geophys. Res. Lett.*, 34 (L05302), 2007. doi: 10.1029/2006GL028899.

A. W. Bally, L. Burbi, C. Cooper, and R. Ghelardoni. Balanced sections and seismic reflection profiles across the Central Apennines. *Mem. Soc. Geol. It.*, 35:257 – 310, 1986.

S. Barba, R. Di Giovambattista, and G. Smeriglio. Italian seismic databank allows on-line access. *Eos Trans. AGU*, 76(9):89, 1995. doi: 10.1029/95EO00042.

M. R. Barchi, A. De Feyter, M. B. Magnani, G. Minelli, G. Pialli, and B. M. Sotera. The structural style of the Umbria-Marche fold and thrust belt. *Mem. Soc. Geol. It.*, 52:557 – 578, 1998a.

M. R. Barchi, G. Minelli, G. Pialli, and B. M. Sotera. The CROP03 profile: A synthesis of results on deep structures of the Northern Apennines. *Mem. Soc. Geol. It.*, 52:383 – 400, 1998b.

M. H. Benoit, M. Torpey, K. Liszewski, V. Levin, and J. Park. P and S wave upper mantle seismic velocity structure beneath the northern Apennines: New evidence for the end of subduction. *Geochem. Geophys. Geosyst.*, 12(Q06004), 2011. doi: 10.1029/2010GC003428.

H. M. Benz, B. A. Chouet, P. B. Dawson, J. C. Kahr, R. A. Page, and J. A. Hole. Three-dimensional P and S wave velocity structure of Redoubt Volcano, Alaska. *J. Geophys. Res.*, 101:8111 – 8128, 1996.

F. Bianco, E. Del Pezzo, M. Castellano, J. Ibanez, and F. Di Luccio. Separation of intrinsic and scattering attenuation in the Southern Apennine zone, Italy. *Geophys. J. Int.*, 150:10 – 22, 2002. doi: 10.1046/j.1365-246X.2002.01696.x.

H. Bijwaard and W. Spakman. Nonlinear global P-wave tomography by iterated linearised inversion. *Geophys J Int.*, 141:71 – 82, 2000.

M. J. Blanco and W. Spakman. The P-wave velocity structure of the mantle below the Iberian Peninsula: Evidence for a subducted lithosphere below southern Spain. *Tectonophy.*, 221:13 – 34, 1993.

G. Bokelmann and E. Maufroy. Mantle structure under Gibraltar constrained by dispersion of body waves. *Geophys. Res. Lett.*, 34(L22305), 2007. doi: 10.1029/2007GL030964.

G. Bokelmann, E. Maufroy, L. Buontempo, J. Morales, and G. Barruol. Testing oceanic subduction and convective removal models for the Gibraltar arc: Seismological constraints from dispersion and anisotropy. *Tectonophys.*, 2011. doi: 10.1016/j.tecto.2010.08.004.

L. Boltzmann. *Zur Theorie der elastischen Nachwirkung. Sitzungsberichte der Mathematisch-Naturwissenschaftlichen Classe der Kaiserlichen Akademie der Wissenschaften*, volume 70. Wiener Berichte, 1874.

P. Boncio and G. LaVecchia. A geological model for the Colfiorito earthquakes (September October 1997, central Italy). *J. Seismol*, 4:345 – 356, 2000.

P. Boncio, F. Ponziani, F. Brozzetti, M. Barchi, G. Lavecchia, and G. Pialli. Seismicity and extensional tectonics in the Northern Umbria-Marche Apennines. *Mem. Soc. Geol. It.*, 52:539 – 555, 1998.

E. Buforn, M. Bezzeghoud, A. Udias, and C. Pro. Pure Appl. Geophys. 161:623 – 646, 2004.

L. Buontempo, G. H. R. Bokelmann, G. Barruol, and J. Morales. Seismic anisotropy beneath southern Iberia from SKS splitting. *Earth. Planet. Sci. Lett.*, 273:237 – 250, 2008. doi: 10.1016/j.epsl.2008.06.024.

G. Calcagnile and G. F. Panza. The main characteristics of the lithosphere-asthenosphere System in Italy and surrounding regions. *Pure Appl. Geophys.*, 119:865 – 879, 1981. doi: 10.1007/BF01131263.

A. Calvert, E. Sandvol, D. Seber, M. Barazangi, F. Vidal, G. Alguacil, and N. Jabour. Propagation of regional seismic phases (Lg and Sn) and Pn velocity structure along the AfricaIberia plate boundary zone: Tectonic implications. *Geophys. J. Int.*, 142: 384 – 408, 2000. doi: 10.1046/j.1365-246x.2000.00160.x.

G. Carrara and NEAREST Team. NEAREST 2008 CRUISE PRELIMINARY REPORT R/V URANIA, 1st Aug 2008- 04th Sept 2008. Technical report.

R. Catalano, C. Doglioni, and S. Merlini. On the Mesozoic Ionian Basin. *Geophys. J. Int.*, 144:49 – 64, 2001. doi: 10.1046/j.0956-540X.2000.01287.x.

G. Cello, S. Mazzoli, E. Tondi, and E. Turco. Active tectonics in the Central Appenines and possibile implications for seismic hazard analysis in peninsular Italy. *Tectonophysics*, 272:43 – 68, 1997.

H.-X. Cheng and B. L. N. Kennett. Frequency dependence of seismic wave attenuation in the upper mantle beneath the Australian region. *Geophys. J. Int.*, 150:45 – 57, 2002. doi: 10.1046/j.1365-246X.2002.01677.x.

C. Chiarabba, L. Jovane, and R. Di Stefano. A new view to the Italian seismicity using 20 years of instrumental recordings. *Tectonophysics*, 395:251 – 268, 2005. doi: 10.1016/j.tecto.2004.09.013.

C. Chiarabba, P. De Gori, and F. Speranza. The southern Tyrrhanian subduction zone: Deep geometry, magmatism and Plio-Pleistocene evolution. *Earth. Planet. Sci. Lett.*, 268:408 – 423, 2008. doi: 10.1016/j.epsl.2008.01.036.

C. Chiarabba, P. De Gori, and E. Boschi. Pore-pressure migration along a normal-fault system resolved by time-repeated seismic tomography. *Geology*, 37:67 – 70, 2009.

G. B. Cimini. P wave deep velocity structure of the southern Tyrrhenian subduction zone from nonlinear teleseismic traveltime tomography. *Geophys. Res. Lett.*, 26:3709 – 3712, 1999. doi: 10.1029/1999GL010907.

G. B. Cimini. Tomographic studies of the deep structure of the Tyrrhenian-Apennine system. In M. P. Marani, F. Gamberi, and E. Bonatti, editors, *From Seafloor to Deep Mantle: Architecture of the Tyrrehanian Backarc Basin*, volume XLIV of *Mem. Descr. Carta Geol. dIt*, pages 15 – 28. Agenzia per la Prot. dellAmbiente e per i Serv. Tec. (APAT), Rome, 2004.

G. B. Cimini and P. De Gori. Nonlinear P wave tomography of subducted lithosphere beneath the central-southern Apennines (Italy). *Geophys. Res. Lett.*, 28:4387 – 4390, 2001. doi: 10.1029/2001GL013546.

S. Civello and L. Margheriti. Toroidal mantle flow around the Calabrian slab (Italy) from SKS splitting. *Geophys. Res. Lett.*, 2004. doi: 10.1029/2004GL019607.

M. Cocco, C. Nostro, and G. Ekstrom. Static stress changes and fault interaction during the 1997 Umbria-Marche earthquake sequence. *J. Seismol.*, 4:501 – 516, 2000.

C. Collettini, M. Barchi, C. Pauselli, C. Federico, and G. Pialli. Seismic expression of active extensional faults in northern Umbria (central Italy). *J. Geodyn.*, 29:309 – 321, 2000.

C. P. Conrad and C. Lithgow-Bertelloni. Influence of continental roots and asthenosphere on plate-mantle coupling. *Geophys. Res. Lett.*, 33, 2006. doi: 10.1029/2005GL025621.

H. P. Crotwell, T. J. Owens, and J. Ritsema. The TauP Toolkit : Flexible Seismic Travel-Time and Raypath Utilities. *Seismological Research Letters*, 70:154 – 160, 1999. doi: 10.1785/gssrl.70.2.154.

N. D'Agostino, A. Avallone, D. Cheloni, E. D'Agostino, S. Mantenuto, and G. Selvaggi. Active tectonics of the Adriatic region from GPS and earthquake slip vectors. *J. Geophys. Res.*, 113(B12413):817 – 825, 2008. doi: 10.1029/2008JB005860.

T. Dahm. *Rechnerpractikum: Methoden zur Berechnung synthetischer Seismogramme (Methods to calculate synthetic seismograms)*. Germany, 1999.

E. Del Pezzo, M. Simini, and J. M. Ibanez. Separation of intrinsic and scattering Q for volcanic areas: A comparison between Etna and Campi Flegrei. *J. Volcanol. Geotherm. Res.*, 70:213 – 219, 1996. doi: 10.1016/0377-0273(95)00056-9.

B. Della Vedova, F. Mongelli, G. Pellis, and G. Zito. Campo regionale del flusso di calore nel Tirreno. pages 817 – 825, Rome, 1991a. Esagrafico.

B. Della Vedova, F. Mongelli, G. Pellis, P. Squarci, L. Taffi, and G. Zito. *Heat flow map of Italy*. Cons. Naz. delle Ric., Pisa, Italy, 1991b.

A. Deschamps, F. Courboulex, S. Gaffet, A. Lomax, J. Virieux, A. Amato, A. Azzara, B. Castello, C. Chiarabba, G. B. Cimini, M. Cocco, M. Di Bona, L. Margheriti, F. Mele, G. Selvaggi, L. Chiaraluce, D. Piccinini, and M. Ripepe. Spatio-temporal distribution of seismic activity during the Umbria-Marche crisis, 1997. *Journal of Seismology*, 4:377 – 386, 2000. doi: 10.1023/A:1026568419411.

J. F. Dewey, M. L. Helman, E. Turco, D. H. W. Hutton, and S. D. Knott. Kinematics of the western Mediterranean. volume 1, pages 265 – 283, 1989.

R. Di Stefano, C. Chiarabba, F. Lucente, and A. Amato. Crustal and uppermost mantle structure in Italy from the inversion of P-wave arrival times: Geodynamic implications. *Geophys. J. Int.*, 139:483 – 498, 1999. doi: 10.1046/j.1365-246x.1999.00952.x.

J. Diaz, J. Gallart, A. Villaseñor, F. Mancilla, A. Pazos, D. Córdoba, J. A. Pulgar, P. Ibarra, and M. Harnafi. Mantle dynamics beneath the Gibraltar Arc (western Mediterranean) from shearwave splitting measurements on a dense seismic array. *Geophys. Res. Lett.*, 2010. doi: 10.1029/2010GL044201.

S. Duggen, K. Hoernle, P. van den Bogaard, and C. Harris. Magmatic evolution of the Alboran Region: The role of subduction in forming the western Mediterranean and causing the Messinian Salinity Crisis. *Earth and Planet. Sci. Lett.*, 218:91 – 108, 2004.

S. Duggen, K. Hoernle, P. Bogaard, and D. Garbe-Schönberg. Post-collisional transition from subduction- to intraplate-type magmatism in the westernmost Mediterranean: Evidence for continental-edge delamination of subcontinental lithosphere. *J. Petr.*, 46:1155 – 1201, 2005. doi: 10.1093/petrology/egi013.

A. M. Dziewonski and D. L. Anderson. Preliminary reference Earth model. *Phys. Earth Planet. Inter.*, 25:297 – 356, 1981.

A. M. Dziewonski and F. Gilbert. The effect of small, aspherical perturbations on travel times and a re-examination of the corrections for the ellipticity. *Geophys. J. R. Astron. Soc.*, 44:7 – 17, 1976.

John W. Eaton. *GNU Octave Manual*. Network Theory Limited, 2002. ISBN 0-9541617-2-6.

J. R. Evans and U. Achauer. Teleseismic velocity tomography using the ACH method: Theory and application to continental-scale studies. In H. M. Iyer and K. Hirahara, editors, *Seismic Tomography: Theory and practice*, pages 319 – 360. Chapman & Hall, London, 1993.

J. R. Evans and J. J. Zucca. Active high-resolution seismic tomography of compressional wave velocity and attenuation structure at Medicine Lake volcano, northern California Cascade Range. *J. Geophys. Res.*, 93:15,016 – 15,036, 1988.

J. R. Evans and J. J. Zucca. Active source, high-resolution (NeHT) tomography: Velocity and Q. In H. M. Iyer and K. Hirahaha, editors, *Seismic Tomography: Theory and Practice*, pages 695 –732. Chapman and Hall, London, 1993.

C. Faccenna, P. Davy, J.-P. Brun, R. Funiciello, D. Giardini, M. Mattei, and T. Nalpas. The dynamics of back-arc extension: An experimental approach to the opening of the Tyrrhenian Sea. *Geophys. J. Int.*, 126:781 – 795, 1996.

C. Faccenna, F. Funiciello, D. Giardini, and P. Lucente. Episodic back-arc extension during restricted mantle convection in the central Mediterranean. *Earth. Planet. Sci. Lett.*, 187:105 – 116, 2001. doi: 10.1016/S0012-821X(01)00280-1.

C. Faccenna, C. Piromallo, A. Crespo-Blanc, L. Jolivet, and F. Rossetti. Lateral slab deformation and the origin of the western Mediterranean arcs. *Tectonics*, 2004. doi: 10.1029/2002TC001488.

M. Fehler, M. Hoshiba, H. Sato, and K. Obara. Separation of scattering and intrinsic attenuation for the Kanto-Tokai region, Japan, using measurements of S-wave energy versus hypocentral distance. *Geophys. J. Int.*, 108:787 – 800, 1992. doi: 10.1111/j.1365-246X.1992.tb03470.x.

A. Frepoli, G. Selvaggi, C. Chiarabba, and A. Amato. State of stress in the Southern Tyrrhenian subduction zone from faultplane solutions. *Geophys. J. Int.*, 125:879 – 891, 1996. doi: 10.1111/j.1365-246X.1996.tb06031.x.

F. Gallais, M.-A. Gutscher, D. Graindorge, N. Chamot-Rooke, and D. Klaeschen. A Miocene tectonic inversion in the Ionian Sea (central Mediterranean): Evidence from multichannel seismic data. *J. Geophys. Res.*, 116(B12108), 2011. doi: 0.1029/2011JB008505.

W. H. Geissler, L. Matias, D. Stich, F. Carrilho, W. Jokat, S. Monna, A. IbenBrahim, F. Mancilla, M.-A. Gutscher, V. Sallares, and N. Zitellini. Focal mechanisms for

subcrustal earthquakes in the Gulf of Cadiz from a dense OBS deployment. *Geophys. Res. Lett.*, L18309(37), 2010. doi: 10.1029/2010GL044289.

E. Giampiccolo, S. Gresta, and F. Rasconá. Intrinsic and scattering attenuation from observed seismic codas in southeastern Sicily. 145:55 – 66, 2004. doi: 10.1016/j.pepi.2004.02.004.

R. Di Giovambattista and S. Barba. An estimate of hypocentre location accuracy in a large network: Possible implications for tectonic studies in Italy. *Geophys. J. Int.*, 129:124 – 132, 1997. doi: 10.1111/j.1365-246X.1997.tb00941.x.

S. Goes, R. Govers, and P. Vacher. Shallow mantle temperatures under Europe from P and S wave tomography. *J. Geophys. Res.*, 105(11):153 – 11 – 170, 2000. doi: 10.1029/1999JB900300.

A. González, M. Torné, D. Córdoba, N. Vidal, L. M. Matias, and J. Díaz. Crustal thinning in the Southwestern Iberia margin. *Geophys. Res. Lett.*, 23(18):2477 – 2480, 1996.

M. Grad, T. Tiira, and ESC Working Group. The Moho depth map of the European Plate. *Geophys. J. Int.*, 176:279 – 292, 2009. doi: 10.1111/j.1365-246X.2008.03919.x.

M. Grange, U. Schärer, R. Merle, J. Girardeau, and G. Cornen. Plume-Lithosphere Interaction during Migration of Cretaceous Alkaline Magmatism in SW Portugal: Evidence from U-Pb Ages and Pb-Sr-Hf Isotopes. *J. Petr.*, 51(5):1143 – 1170, 2010.

I. Grevemeyer, N. Kaul, and A. Kop. Heat flow anomalies in the Gulf of Cadiz and off Cape San Vincente, Portugal. *Mar. Petrol. Geol.*, 26:795 – 804, 2009.

O. Gudmundsson, J. H. Davies, and R. W. Clayton. Stochastic analysis of global travel-time data: mantle heterogeneity and random errors in the isc data. *Geophysical Journal International*, 102(1):25–43, 1990. ISSN 1365-246X. doi: 10.1111/j.1365-246X.1990.tb00528.x. URL `http://dx.doi.org/10.1111/j.1365-246X.1990.tb00528.x`.

M. Gurnis, C. Hall, and L. Lavier. Evolving force balance during incipient subduction. *Geochem. Geophys. Geosyst.*, 5, 2004. doi: 10.1029/2003GC000681.

M. A. Gutscher, J. Malod, J. P. Rehault, I. Contrucci, F. Klingelhoefer, L. M. Victor, and W. Spakman. Evidence for active subduction beneath Gibraltar. *Geology*, 30: 1071 – 1074, 2002. doi: 10.1130/0091-7613.

Z. Gvirtzman and A. Nur. The formation of Mount Etna as the consequence of slab rollback. *Nature*, 401:782 – 785, 1999. doi: 10.1038/44555.

C. Haberland and A. Rietbrock. Attenuation tomography in the western central Andes: A detailed insight into the structure of a magmatic arc. *J. Geophys. Res.*, 106 - B6 (11):151 – 111, 2001. doi: 10.1029/2000JB900472.

B. R. Hacker, S. M. Peacock, G. A. Abers, and S. D. Holloway. Subduction factory: 2. Are intermediate-depth earthquakes in subducting slabs linked to metamorphic dehydration reactions? *J. Geophys. Res.*, 108 - B1:2030, 2003. doi: 10.1029/2001JB001129.

M. Hoshiba, A. Rietbrock, F. Sherbaum, H. Nakahara, and C. Haberland. Scattering attenuation and intrinsic absorption using uniform and depth dependent modelApplication to full seismogram envelope recorded in northern Chile. *J. Seismol.*, 5:157 – 179, 2001. doi: 10.1023/A:1011478202750.

S. Husen, R. Quintero, E. Kissling, and B. Hacker. Subduction-zone structure and magmatic processes beneath Costa Rica constrained by local earthquake tomography and petrological modelling. *Geophys. J. Int.*, 155:11 – 32, 2003.

L. Iribarren, J. Vergés, F. Camurri, J. Fullea, and M. Fernandez. The structure of the Atlantic-Mediterranean transition zone from the Alboran Sea to the Horseshoe Abyssal Plain (Iberia-Africa plate boundary). *Mar. Geol.*, 243:97 – 119, 2007.

D. G. Isaak. High-Temperature Elasticity of Iron-Bearing Olivines. *J. Geophys. Res.*, 97(B2):18711885, 1992. ISSN 0148-0227. doi: http://dx.doi.org/10.1029/91JB02675.

F. Italiano, M. Martelli, G. Martinelli, and P. M. Nuccio. Geochemical evidence of melt intrusions along lithospheric faults of the southern Apennines, Italy: Geodynamic and seismogenic implications. *J. Geophys. Res.*, 105, 2000. doi: 10.1029/2000JB900047.

W. P. Iverson, B. A. Fahmy, and S. B. Smithson. Vp*Vs from mode-converted P-SV reflections. *Geophysics*, 54:843 – 852, 1989.

H. Kanamori and D. L. Anderson. Importance of physical dispersion in surface wave and free oscillation problems: Review. *Rev. Geophys.*, 15(1):105 – 112, 1977. doi: 10.1029/RG015i001p00105.

S. Karato. Importance of anelasticity in the interpretation of seismic tomography. *Geophys. Res. Lett.*, 20:1623 – 1626, 1993. doi: doi:10.1029/93GL01767.

S. Karato. Deformation of Earth Materials: an introduction to the Rehology of Solid Earth. pages 1–463. Cambridge University Press, Cambridge, 2008.

S. Karato. On the origin of the asthenosphere. *Earth Planet. Sci. Lett.*, 321322(0):95 – 103, 2012. doi: 10.1016/j.epsl.2012.01.0010.

S. Karato and B. Karki. Origin of lateral variation of seismic wave velocities and density in the deep mantle. *J. Geophys. Res.*, 106, 2001. doi: 10.1029/2001JB000214.

S. Karato and H. A. Spetzler. Defect microdynamics in minerals and solid state mechanisms of seismic wave attenuation and velocity dispersion in the mantle. *Rev. Geophys.*, 28:399 – 421, 1990. doi: doi:10.1029/RG028i004p00399.

B. L. N. Kennett, M. S. Sambridge, and P. R. Williamson. Subspace methods for large scale inverse problems involving multiple parameter classes. *Geophys. J. Int.*, 94:237 – 247, 1988.

B. L. N. Kennett, E. R. Engdahl, and R. Buland. Constraints on seismic velocities in the Earth from traveltimes. *Geophys. J. Int.*, 122:108 – 124, 1995. doi: 10.1111/j.1365-246X.1995.tb03540.x.

E. Kissling, W. L. Ellsworth, D. Eberhart-Phillips, and U. Kradolfer. Initial reference models in local earthquake tomography. *J. Geophys. Res.*, 19:646, 1994.

E. Kissling, U. Kradolfer, and H. Maurer. VELEST users guide-short introduction. Technical report, Inst. of Geophys. and Swiss Seismol. Serv., Zurich, 1995.

M. Koch. A numerical study on the determination of the 3-D structure of the lithosphere by linear and non-linear inversion of teleseismic travel times. *Geophys. J. R. Astron. Soc.*, 80:73 – 93, 1985.

M. Koch. Bootstrap inversion for vertical and lateral variations of the S wave structure and the Vp/Vs-ratio from shallow earthquakes in the Rhinegraben seismic zone, Germany. *Tectonophysics*, 210:91 – 115, 1992.

J. M. Lees and H. Wu. Poissons ratio and porosity at Coso geothermal area, California. *J. Volcanol. Geotherm. Res.*, 95:157 – 173, 2000.

J.-J. Leveque and F. Masson. From ACH tomographic models to absolute velocity models. *Geophys. J. Int.*, 137:621 – 629, 1999.

J. J. Leveque, L. Rivern, and G. Wittlinger. On the use of the checker-board test to assess the resolution of tomographic inversions. *Geophys. J. Int.*, 115:313 – 318, 1993.

G. Lin and P. M. Shearer. Evidence for water-filled cracks in earthquake source regions. *Geophys. Res. Lett.*, 36(L17315), 2009. doi: 10.1029/2009GL039098.

K. G. Lindquist, K. Engle, D. Stahlke, and E. Price. Global Topography and Bathymetry Grid Improves Research Efforts. *Eos Trans. AGU*, 85(19):186, 2004.

H.-P. Liu, D. L. Anderson, and H. Kanamori. Velocity dispersion due to anelasticity; implications for seismology and mantle composition. *Geophys. J. Royal Astronom. Soc.*, 47:41 – 58, 1976. doi: 10.1111/j.1365-246X.1976.tb01261.x.

L. Lonergan and N. White. Origin of the Betic-Rif mountain belt. *Tectonics*, 16:504 – 522, 1997.

F. P. Lucente, C. Chiarabba, G. B. Cimini, and D. Giardini. Tomographic constraints on the geodynamic evolution of the Italian region. *J. Geophys. Res.*, 104:307 – 320, 1999. doi: 10.1029/1999JB900147.

A. Malinverno and W. B. F. Ryan. Extension in the Tyrrhenian sea and shortening in the Apennines as a result of arc migration driven by the sinking of the lithosphere. *Tectonics*, 5:227 – 245, 1986. doi: doi:10.1029/TC005i002p00227.

M. E. Mann and J. M. Lees. Robust estimation of background noise and signal detection in climatic time series. *Clim. Change*, 33:409 – 445, 1996. doi: 10.1007/BF00142586.

M. P. Marani and T. Trua. Thermal constriction and slab tearing at the origin of a superinflated spreading ridge: Marsili volcano (Tyrrhenian Sea). *J. Geophys. Res.*, 2002. doi: 10.1029/2001JB000285.

D. McKenzie, J. Jackson, and K. Priestley. Thermal structure of oceanic and continental lithosphere. *Earth Plan. Sci. Lett.*, 233:337 – 349, 2005.

G. Mele. High-frequency wave propagation from mantle earthquakes in the Tyrrhenian Sea: New constraints for the geometry of the south Tyrrhenian subduction zone. *Geophys. Res. Lett.*, 25:2877 – 2880, 1998. doi: 10.1029/98GL02175.

G. Mele, A. Rovelli, D. Seber, and M. Barazangi. Shear wave attenuation in the lithosphere beneath Italy and surrounding regions: Tectonic implications. *J. Geophys. Res.*, 102, 1997. doi: 10.1029/97JB00262.

G. Mele, A. Rovelli, and D. Seber. Compressional velocity structure and anisotropy in the uppermost mantle beneath Italy and surrounding regions. *J. Geophys. Res.*, 103, 1998. doi: doi:10.1029/98JB00596.

W. Menke. Geophysical data analysis. Discrete inverse theory. 1984.

R. Merle, U. Schärer, J. Girardeau, and G. Cornen. Cretaceous seamounts along the continent-ocean transition of the Ibeian margin: U-Pb ages and Pb-Sr-Hf isotopes. *Geochem. Cosmochim. Acta*, 70:4950 – 4976, 2006.

A. Michelini, D. Spallarossa, M. Cattaneo, A. Govoni, and A. Montanari. The 1997 Umbria-Marche (Italy) earthquake sequence: Tomographic images obtained from data of the GNDT-SSN temporary network. *J. Seismol.*, 4:415 – 433, 2000.

S. Miller, C. Collettini, L. Chiaraluce, M. Cocco, M. R. Barchi, and T. Kohl. Aftershock driven by a high pressure CO2 source at depth. *Nature*, 427:724 – 727, 2004.

R. Miranda, V. Valadares, P. Terrinha, J. Mata, M. do Rosario Azevedo, M. Gaspar, J. C. Kulberg, and C. Ribeiro. Age constrains on the Late Cretaceous alkaline magmatism on the West Iberian Margin. *Cretaceous Res.*, 30:575 – 586, 2009.

F. Mongelli, G. Zito, B. Della Vedova, G. Pellis, P. Squarci, and L. Taffi. *Geothermal regime of Italy and surrounding seas, in Exploration of the Deep Continental Crust.* Springer-Verlag, New York, 1991.

F. Mongelli, P. Harabaglia, G. Martinelli, P. Squarci, and G. Zito. Nuove misure di flusso geotermico in Italia meridionale: Possibili implicazioni sismotettoniche. volume Atti - 14 - Convegno - del - Gruppo - Naz - di - Geofisica - della - Terra - Solida, pages 929 – 939, Rome, 1996.

C. Montuori, G. B. Cimini, and P. Favali. Teleseismic tomography of the southern Tyrrhenian subduction zone: New results from seafloor and land recordings. *J. Geophys. Res.*, 2007. doi: doi:10.1029/2005JB004114.

D. Moos and M. D. Zoback. In situ studies of velocity in fractured cristalline rocks. *J. Geophys. Res*, 88:2345 – 2358, 1983.

A. Morelli and M. Dziewonski. Topography of the core-mantle boundary and lateral homogeneity of the liquid core. *Nature*, 325:678 – 683, 1987.

G. Müller. Rheological properties and velocity dispersion of a medium with power-law dependence of Q on frequency. *J. Geophys.*, 54:20 – 29, 1983.

G. Müller. The reflectivity method: A tutorial. *J. Geophys.*, 58:153 – 174, 1985.

G. Neri, B. Orecchio, C. Totaro, G. Falcone, and D. Presti. Subduction beneath southern Italy close the ending: Results from seismic tomography. *Seismol. Res. Lett.*, 80(1): 63 – 70, 2009.

C. Nicholson and D. W. Simpson. Changes in Vp/Vs with depth: Implications for appropriate velocity models, improved earthquake locations, and material properties of the upper crust. *Bull Seismol. Soc. Am.*, 75:1105 – 1123, 1985.

A. Nur and J. R. Booker. Aftershocks caused by pore fluid flow? *Science*, 175:885 – 887, 1972.

P. G. Okubo, H. M. Benz, and B. A. Chouet. Imaging the crustal magma source beneath Mauna Loa and Kilauea Volcanoes, Hawaii. *Geology*, 25:867 – 870, 1997.

C. C. Paige and M. A. Saunders. LSQR: An algorithm for sparse linear equations and sparse least squares. *Trans. Math. Software*, 8:43 – 71, 1982.

G. F. Panza, R. B. Raykova, E. Carminati, and C. Doglioni. Upper mantle flow in the western Mediterranean. *Earth. Planet. Sci. Lett.*, 257:200 – 214, 2007. doi: 10.1016/j.epsl.2007.02.032.

J. Park, C. R. Lindberg, and F. L. Vernon III. Multitaper spectral analysis of high-frequency seismograms. *J. Geophys. Res.*, 92, 1987. doi: 10.1029/JB092iB12p12675.

E. Patacca and P. Scandone. Post-Tortonian mountain building in the Apennines: The role of the passive sinking of a relic lithosphere. In A. N. Lincei, editor, *The Lithosphere in Italy, Adv. Earth Sci. Res.*, volume 80, pages 157 – 176. Rome, 1989.

G. L. Pavlis and J. R. Booker. The mixed discrete continuous inverse problem: Application to the simultaneous determination of earthquake hypocenters and velocity structure. *J. Geophys. Res.*, 85:4801 – 4810, 1980.

A. Peccerillo. Geochemical similarities between the Vesuvius, Phlegraean Fields and Stromboli volcanoes: Petrogenic, geodynamic and volcanological implications. *Mineral. Petrol.*, 73:93 – 105, 2001. doi: doi:10.1007/s007100170012.

A. Peccerillo. *Plio-Quaternary Volcanism in Italy: Petrology, Geochemistry.* Berlin, 2005.

C. Piromallo and A. Morelli. Imaging the Mediterranean upper mantle by P wave travel time tomography: Preliminary results. *Annal. Geofis.*, 40:963 – 979, 1997.

C. Piromallo and A. Morelli. P wave tomography of the mantle under the Alpine-Mediterranean area. *J. Geophys. Res.*, 2003. doi: 10.1029/2002JB001757.

J. P. Platt. Thermal evolution, rate of exhumation, and tectonic significance of metamorphic rocks from the floor of the Alboran extensional basin, western Mediterranean. *Tectonics*, 17:671 – 689, 1998.

J. P. Platt and R. L. M. Vissers. Extensional collapse of thickened continental lithosphere: A working hypothesis for the Alboran Sea and the Gibraltar arc. *Geology*, 17: 540 – 543, 1989.

P. Podvin and I. Lecompte. Finite difference computation of travel times in very contrasted velocity models: A massively parallel approach and its associated tools. *Geophys. J. Int.*, 105:271 – 284, 1991.

A. Polonia, L. Torelli, P. Mussoni, L. Gasperini, A. Artoni, and D. Klaeschen. 30 (TC5018), 2011. doi: 10.1029/2010TC002821.

B. G. Polyak, M. Fernàndez, M. D. Khutorskoy, J. I. Soto, I. A. Basov, M. C. Comas, V. Y, Khain, B. Alonso, G. V. Agapova, I. S. Mazurova, A. Negredo, V. O. Tochitsky, J. Linde, N. A. Bogdanov, and E. Banda. Heat flow in the Alboran Sea, western Mediterranean. *Tectonophys*, 263:191 – 218, 1996.

G. Pontevivo and G. F. Panza. The lithosphere-asthenosphere system in the Calabrian Arc and surrounding seassouthern Italy. *Pure Appl. Geophys.*, 163, 2006. doi: 10.1007/s00024-006-0093-3.

G. Ranalli. Seismic tomography and mineral physics. In E. Boschi, G. Ekström, and A. Morelli, editors, *Seismic Modelling of the Earth Structure*, pages 443 – 459. Ist. Naz. di Geofis., Rome, 1996.

N. Rawlinson, A. M. Reading, and B. L. N. Kennett. Lithospheric structure of Tasmania from a novel form of teleseismic tomography. *J. Geophys. Res.*, 111(B02301), 2006. doi: 10.1029/2005JB003803.

P. G. Richards and W. Menke. The apparent attenuation of a scattering medium. *Bull. Seismol. Soc. Am.*, 73:1005 – 1021, 1983.

M. Ripepe, D. Piccinini, and L. Chiaraluce. Foreshock sequence of the September 26th, 1997 Umbria-Marche earthquakes. *J. Seismol*, 4:387 – 389, 2000.

J. D. Robertson. Carbonate porosity from S/P traveltime ratios. *Geophysics*, 52:1346 – 1354, 1987.

B. Romanowicz. A global tomographic model of shear attenuation in the upper mantle. *J. Geophys. Res.*, 100, 1995. doi: doi:10.1029/95JB00957.

G. Rosenbaum and G. S. Lister. Neogene and Quaternary rollback evolution of the Tyrrhenian Sea, the Apennines, and the Sicilian Maghrebides. *Tectonics*, 2004. doi: 10.1029/2003TC001518.

E. G. Roth, D. A. Wiens, and D. Zhao. An empirical relationship between seismic attenuation and velocity anomalies in the upper mantle. *Geophys. Res. Lett.*, 27:601 – 604, 2000. doi: 10.1029/1999GL005418.

L. H. Royden. Evolution of retreating subduction boundaries formed during continental collision. *Tectonics*, 12:629 – 638, 1993.

C. O. Sanders. Local earthquake tomography: Attenuation–theory and results. In Chapman and Hall, editors, *Seismic Tomography: Theory and Practice*, pages 676 – 694. London, 1993.

C. O. Sanders, L. D. Nixon, and E. A. Schwartz. Seismological evidence for magmatic and hydrothermal structure in Long Valley caldera from local earthquake attenuation and velocity tomography. *J. Geophys. Res.*, 100:8311 – 8326, 1995.

R. Sartori, L. Torelli, N. Zitellini, D. Peis, and E. Lodolo. Eastern segment of the AzoresGibraltar line (centraleastern Atlantic): An oceanic plate boundary with diffuse compressional deformation. *Geology*, 22:555 – 558, 1994.

H. Sato, M. Fehler, and R.-S. Wu. Scattering and attenuation of seismic waves in the lithosphere. In Elsevier, editor, *Handbook of Earthquake and Engineering Seismology*, volume 13, chapter 13, pages 195 – 208. New York, 2000.

J. H. Schön. Physical properties of rocks. In K. Helbig and S. Treitel, editors, *Handbook of Geophysical Exploration Seismic Exploration*, volume 18. Pergamon, New York, 1996.

B. Schurr, G. Asch, A. Rietbrock, R. Trumbull, and C. Haberland. Complex patterns of fluid and melt transport in the central Andean subduction zone revealed by attenuation tomography. *Earth. Planet. Sci. Lett.*, 215:105 – 119, 2003. doi: 10.1016/S0012-821X(03)00441-2.

D. Seber, M. Barazangi, A. Ibenbrahim, and A. Demnati. Geophysical evidence for lithospheric delamination beneath the Alboran Sea and Rif-Betic mountains. *Nature*, 379:785 – 790, 1996.

G. Selvaggi and C. Chiarabba. Seismicity and P-wave velocity image of the southern Tyrrhenian subduction zone. *Geophys. J. Int.*, 121:818 – 826, 1995. doi: 10.1111/j.1365-246X.1995.tb06441.x.

E. Serpelloni, G. Vannucci, S. Pondrelli, A. Argnani, G. Casula, M. Anzidei, P. Baldi, and P. Gasperini. Kinematics of the Western Africa-Eurasia plate boundary from

fochal mechanisms and GPS data. *Geophys. J. Int.*, 169:1180 – 1200, 2007. doi: 10.1111/j.1365-246X.2007.03367.x.

G. Serri. Neogene-Quaternary magmatism of the Tyrrhenian region: Characterization of the magma sources and geodynamic implications. *Mem. Soc. Geol. Ital.*, 41:90 – 94, 1990.

G. Serri, F. Innocenti, and P. Manetti. Magmatism from Mesozoic to present: Petrogenesis, time-space distribution and geodynamic implications. In G. B. Vai and P. I. Martini, editors, *Anatomy of a Mountain: The Apennines and the Adjacent Mediterranean Basins*, pages 77 – 104. Springer, New York, 2001.

J. A. Sethian and A. M. Popovici. 3-D traveltime computation using the fast marching method. *Geophysics*, 64:516 – 523, 1999.

T. Sgroi, T. Braun, T. Dahm, and F. Frugoni. An improved seismicity picture of the southern Tyrrhenian area by the use of OBS and landbased networks: The TYDE experiment. *Ann. Geophys.*, 49:801 – 817, 2006.

Z. H. Shomali, F. Keshvari, J. Hassanzadeh, and N. Mirzaei. Lithospheric structure beneath the Zagros collision zone resolved by non-linear teleseismic tomography. *Geophys. J. Int.*, 187:394 – 406, 2011. doi: 10.1111/j.1365-246X.2011.05150.x.

J.-C. Sibuet, S. P. Srivastava, and W. Spakman. Pyrenean orogeny and plate kinematics. *J. Geophys. Res.*, 109(B08104), 2004. doi: 10.1029/2003JB002514.

S. A. Sipkin and T. H. Jordan. Frequency dependence of Qscs. *Bull. Seismol. Soc. Am.*, 69(4):1055 – 1079, 1979.

W. Spakman. Delay time tomography of the upper mantle below Europe, the Mediterranean, and Asia Minor. *Geophys. J. Int.*, 107:309 – 332, 1991. doi: 10.1111/j.1365-246X.1991.tb00828.x.

W. Spakman and R. Wortel. A tomographic view on western Mediterranean geodynamics. In *The Transmed Atlas: The Mediterranean Region from Crust to Mantle*, pages 31 – 52. Springer, New York, 2004.

C. Spencer and D. Gubbins. Travel-time inversion for simultaneous earthquake location and velocity structure determination in laterally varying media. *Geophys. J.R. Astron. Soc.*, 63:95 – 116, 1980.

F. Speranza and M. Chiappini. Thick-skinned tectonics in the external Apennines, Italy: New evidence from magnetic anomaly analysis. *J. Geophys. Res.*, 2002. doi: 10.1029/2000JB000027.

B. Sperner, F. Lorenz, K. Bonjer, S. Hettel, B. Müller, and F. Wenzel. Slab break-off or abrupt cut or gradual detachment? New insights from Vrancea Region (SE Carpathians, Romania). *Terra Nova*, 13(3):172 – 179, 2001.

F. D. Stacey, M. T. Gladwin, B. McKavanagh, A. T. Linde, and L. M. Hastie. Anelastic damping of acoustic and seismic pulses. *Geophysical Surveys*, 2:133 – 151, 1975.

S. Stein and M. Wysession. *An Introduction to Seismology, Earthquakes and. Earth Structure*. Blackwell Publishing, Oxford, 2003.

D. Stich, C. J. Ammon, and J. Morales. Moment tensor solutions for small and moderate earthquakes in the Ibero-Maghreb region. *J. Geophys. Res.*, 108(B3):2148, 2003. doi: 10.1029/2002JB002057.

D. Stich, F. Mancilla, and J. Morales. Crust-mantle coupling in the Gulf of Cadiz (SW-Iberia). *Geophys. Res. Lett.*, 32(L13306), 2005. doi: 10.1029/2005GL023098.

D. Stich, E. Serpelloni, F. Mancilla, and J. Morales. Kinematics of the Iberia-Maghreb plate contact from seismic moment tensors and GPS observations. *Tectonophysics*, 426:295 – 317, 2006.

R. H. Tatham. Vp/Vs and lithology. *Geophysics*, 47:336 – 344, 1982.

T. L. Teng. Attenuation of body waves and the Q structure of the mantle. *J. Geophys. Res.*, 73:2195 – 2208, 1968. doi: 10.1029/JB073i006p02195.

F. J. Tilmann, H. M. Benz, K. F. Priestley, and P. G. Okubo. P wave velocity structure of the uppermost mantle beneath Hawaii from travel time tomography. *Geophys. J. Int.*, 146:594 – 606, 2001.

M. N. Toksöz, C. H. Cheng, and T. Aytekin. Velocities of seismic waves in porous rock. *Geophysics*, 41:621 – 645, 1976.

M. Tornè, M. Fernàndez, M. C. Comas, and J. I. Soto. Lithospheric structure beneath the Alboran Basin: Results from 3D gravity modeling and tectonic relevance. *J. Geophys. Res.*, 105(B2):3209 – 3228, 2000.

T. Trua, G. Serri, and P. L. Rossi. Coexistence of IAB-type and OIB-type magmas in the southern Tyrrhenian back-arc basin: Evidence from recent seafloor sampling and the

geodynamic implications. In M. P. Marani, F. Gamberi, and E. Bonatti, editors, *From Seafloor to Deep Mantle: Architecture of the Tyrrehanian Backarc Basin*, volume 44 of *Mem. Descr. Carta Geol. dIt*, pages 83 – 96. Agenzia per la Prot. dellAmbiente e per i Serv. Tec. (APAT), Rome, 2004.

S. P. Turner, J. P. Platt, R. M. M. George, S. P. Kelley, D. G. Pearson, and G. M. Nowell. Magmatism associated with orogenic collapse of the BeticAlboran Domain, SE Spain. *J. Petrol.*, 40:1011 – 1036, 1999.

J. C. VanDecar and R. S. Crosson. Determination of teleseismic relative phase arrival times using multi-channel cross-correlation and least squares. *Bull. Seismol. Soc. Am.*, 80:150 – 169, 1990.

A. Villaseñor, H. M. Benz, L. Filippi, G. De Luca, R. Scarpa, G. Patané, and S. Vinciguerra. Three-dimensional P-wave velocity structure of Mt. Etna, Italy. *Geophys. Res. Lett.*, 25:1975 – 1978, 1998.

P. Wessel and W. H. F. Smith. Free software helps map and display data. *Eos Trans. AGU*, 72(41):441, 1991.

Thomas Williams, Colin Kelley, and many others. Gnuplot 4.4: an interactive plotting program. `http://gnuplot.sourceforge.net/`, March 2010.

M. J. R. Wortel and W. Spakman. Subduction and slab detachment in the Mediterranean-Carpathian region. *Science*, 290:1910 – 1917, 2000.

H. P. Zeck. Betic-Rif orogeny: Subduction of Mesozoic Tethys lithosphere under eastward drifting Iberia, slab detachment shortly before 22 Ma, and subsequent uplift and extensional tectonics. *Tectonophys.*, 254:1 – 16, 1996.

H. Zeyen, P. Ayarza, M. Fernàndez, and A. Rimi. Lithospheric structure under the western African-European plate boundary: A transect across the Atlas Mountains and the Gulf of Cadiz. *Tectonics*, 24(TC2001), 2005. doi: 10.1029/2004TC001639.

N. Zitellini, E. Gràcia, L. Matias, P. Terrinha, M. A. Abreu, G. DeAlteriis, J. P. Henriet, J. J. Dañobeitia, D. G. Masson, T. Mulder, R. Ramella, L. Somoza, and S. Diez. The quest for the AfricaEurasia plate boundary west of the Strait of Gibraltar. *Earth. Planet. Sci. Lett.*, 280:13 – 50, 2009. doi: 10.1016/j.epsl.2008.12.005.

G. Zito, F. Mongelli, S. De Lorenzo, and C. Doglioni. Terra Nova. 15:425 – 432, 2003. doi: 10.1046/j.1365-3121.2003.00507.x.

Appendices

1 Rock properties of the upper-crust in Central Apennines (Italy) derived from high-resolution 3-D tomography

GEOPHYSICAL RESEARCH LETTERS, VOL. 30, NO. 7, 1408, doi:10.1029/2002GL016780, 2003

Rock properties of the upper-crust in Central Apennines (Italy) derived from high-resolution 3-D tomography

Stephen Monna
Istituto Nazionale di Geofisica e Vulcanologia, Rome, Italy

Luisa Filippi
Dipartimento della Protezione Civile-Ufficio Servizio Sismico Nazionale, Rome, Italy

Laura Beranzoli and Paolo Favali[1]
Istituto Nazionale di Geofisica e Vulcanologia, Rome, Italy

Received 17 December 2002; revised 7 March 2003; accepted 13 March 2003; published 11 April 2003.

[1] High-resolution 3-D P and S-wave velocity models of a central sector of the Apennines (Central Italy) are computed by inverting first arrival times from an aftershock sequence (September–December, 1997) following the M_w 5.7 and M_w 6.0 Umbria-Marche earthquakes that occurred on September 26, 1997. The high quality of the data set, especially for the S-wave, allows us to compute 3-D variations in V_p, V_p/V_s and $V_p \cdot V_s$. The anomalies can be interpreted as lateral changes in rock type and fracturing, which control fluid diffusion and variation in pore pressure. This is in agreement with a poro-elastic view that can be inferred from the spatio-temporal evolution of the seismic sequence. *INDEX TERMS:* 5104 Physical Properties of Rocks: Fracture and flow; 5114 Physical Properties of Rocks: Permeability and porosity; 7230 Seismology: Seismicity and seismotectonics; 8180 Tectonophysics: Evolution of the Earth: Tomography. **Citation:** Monna, S., L. Filippi, L. Beranzoli, and P. Favali, Rock properties of the upper-crust in Central Apennines (Italy) derived from high-resolution 3-D tomography, *Geophys. Res. Lett.*, *30*(7), 1408, doi:10.1029/2002GL016780, 2003.

1. Introduction

[2] Tomographic interpretations have been used, both with active and passive seismic techniques, to infer differences in physical properties of rocks [e.g., *Robertson*, 1987; *Koch*, 1992; *Sanders et al.*, 1995; *Lees and Wu*, 2000]. This interpretative approach is based on theoretical models, laboratory observations and *in situ* measurements [*Tatham*, 1982].

[3] Velocity of seismic waves in sedimentary rocks depends mainly on mineral composition; consolidation and cementation of the rock matrix; porosity (total pore and crack volume), pore and crack geometry and their fluid content; effective rock stress (defined as confining pressure minus pore pressure) and temperature [*Schön*, 1996]. Pore and crack geometry is described by the aspect-ratio parameter α, that is, the ratio of the minimum dimension to the maximum dimension of the crack or pore ($\alpha = 1$ for a spherical pore; $\alpha \ll 1$ for a flat crack). Presence of very low α cracks (flat cracks, in the range $10^{-3} \div 10^{-2}$), even in a predominantly porous ($\alpha \sim 1$) sedimentary rock, can have a strong effect on the rock's bulk elastic properties [*Tatham*, 1982; *Koch*, 1992].

[4] Ambiguities that usually arise analyzing only V_p and V_s, can be resolved by the use of their ratio and product [*Lees and Wu*, 2000]. For sedimentary rocks V_p/V_s is sensitive to the presence of pore fluids and to concentration of cracks for a given total porosity. Laboratory and borehole measurements have found V_p/V_s to increase with the concentration of fluid saturated cracks (both micro- and macro-cracks) in a condition of low effective stress [*Moos and Zoback*, 1983]. In particular, this was also verified for fluid saturated carbonates by *Robertson* [1987], comparing the model of *Toksöz et al.* [1976] with *in situ* measurements. The other quantity, $V_p \cdot V_s$, is sensitive to variations of porosity in sedimentary rocks [*Iverson et al.*, 1989; *Lees and Wu*, 2000]. A lower $V_p \cdot V_s$ value implies an increase of porosity.

[5] In this paper we calculate high-resolution 3-D P and S-wave velocity models of a central sector of the Apennines (Central Italy, Umbria-Marche) by inverting first arrival times from an aftershock sequence occurred from September to December 1997. We interpret V_p, V_p/V_s and $V_p \cdot V_s$ anomalies as produced by different rock types having different pore-pressure and fracturing state.

2. Geology and Tectonics

[6] The Umbria region, is characterized by Pliocene active extensional tectonics [*Collettini et al.*, 2000]. These tectonics generated continental basins with a general NNW-SSE trend, bordered either by WSW-dipping or ENE-dipping normal faults striking in the same direction [*Bally et al.*, 1986; *Barchi et al.*, 1998a]. These faults are interpreted as being dissected by minor trans-extensional oblique elements [*Cello et al.*, 1997]. The largest structural feature in the region is the 100-km-long Val Tiberina basin which is controlled by a ENE-dipping master fault (Alto Tiberina fault) [*Barchi et al.*, 1998a]. East of the Val Tiberina basin, the Colfiorito basin is another minor extensional basin, possibly on the hangingwall of the Alto Tiberina fault, directly affected by the 1997 Umbria-Marche seismic sequence. The sequence started with

[1]Also at Universita' degli Studi "G. d'Annunzio," Campus Universitario, Chieti Scalo, Italy.

0094-8276/03/2002GL016780$05.00

Table 1. Rock Types in the Study Volume and Average Properties

Rock	Vp (km/s)	Depth range (km)	Thickness (km)
MA (CS)	5.2[a]	0 ÷ 3[c]	2[c]
CM (CS)	6.0[b]	0 ÷ 3[c]	
EV	6.1[a]	3 ÷ 6[c]	

CS = Carbonatic Sequence, MA = *Maiolica* type, CM = *Calcare Massiccio*, EV = Evaporites (Anhydrite). Adapted values from:
[a]*Barchi et al.* [1998b].
[b]*Bally et al.* [1986].
[c]*Boncio and Lavecchia* [2000].

M_w 5.7 and M_w 6.0 earthquakes that were followed by intense swarm (more than 2,500 events) migrating towards SE. The epicentral region occupies a 12 × 40 km^2 area extending parallel to the Apennines, and the hypocenters were confined within 8 km in depth [*Deschamps et al.*, 2000; *Michelini et al.*, 2000].

[7] The main geologic units in the area are, starting from the surface: Miocene Plio-Pleistocene turbidites, Jurassic-Paleogene carbonatic sequence, Triassic evaporates (anhydrites). Table 1 shows representative members of groups of rocks having similar material properties largely comprised in our study volume, and estimates of their average V_p, depth of maximum concentration and layer thickness in which they predominate.

3. Data and Method

[8] We used P and S-wave arrival times from the Italian National Seismic Network managed by INGV and from digital three-component temporary networks operated by different Italian and French institutions from September 26 to November 3 [*Deschamps et al.*, 2000, *Michelini et al.*, 2000]. From the original data set of 2,538 located events, we selected earthquakes with at least 10 phases (P and/or S) read, gaps smaller than 150 degrees and total RMS residuals smaller than 0.5 s. The final data set used for the inversion consists of 1,125 well-located earthquakes recorded on 39 stations. This resulted in 16,417 P- and 15,598 S-phase first arrival times. The distribution of stations and events allow the investigation of a volume extending about 24 × 40 × 6 km^3 (Figure 1a).

Table 2. Best-Fitting 1-D Starting Model[a]

Depth (km)	−2	2	4	6	8
V_p (km/s)	4.1	5.6	6.2	6.4	6.8

[a]Origin of depth scale is at sea level.

[9] Calculation of an accurate 3-D velocity model requires at least a good initial 1-D velocity model. The initial 1-D model used in this study was obtained by inversion of the P-wave data for a best-fit depth-varying 1-D model using the method of *Kissling et al.* [1994, 1995] and 1-D models available from literature [*Boncio et al.*, 1998; *Michelini et al.*, 2000; *Alessandrini et al.*, 2001]. The best-fitting model (Table 2) was then used to relocate the earthquake sequence.

[10] We used the inversion method of *Benz et al.* [1996], which has been applied to understanding seismicity patterns and geology and volcanic structures [*Okubo et al.*, 1997; *Villaseñor et al.*, 1998]. This method uses a finite difference technique [*Podvin and Lecompte*, 1991] to compute accurate travel times through a complex velocity structure and the efficient least squares QR (LSQR) algorithm [*Paige and Saunders*, 1982] for simultaneous inversion for the velocity structure and hypocenters. Smoothing constraints are applied to control the degree of model roughness allowed in the inversion. An optimal inversion block size is controlled by the source-receiver geometry (i.e. distance between adjacent stations and the distribution of seismicity) and determined by trial inversions carried out with different block sizes and checkerboard synthetic tests. Trial results determined that the most appropriate inversion cell size is 2 × 2 × 1 km (larger in the horizontal dimension). To ensure accurate calculations of the travel times through the model, we used 1 × 1 × 0.5 km constant velocity cells. The smoothing parameter value was gradually decreased during the iteration process, allowing for a compromise between model stability and minimization of the data misfit.

[11] The final P and S-wave velocity model resulted in a 26% and 20% reduction in the arrival-time RMS, respectively. The initial S-wave velocity model was derived from the initial P-wave model using V_p/V_s = 1.85, calculated from the least square fit between the P and S wave travel time pairs.

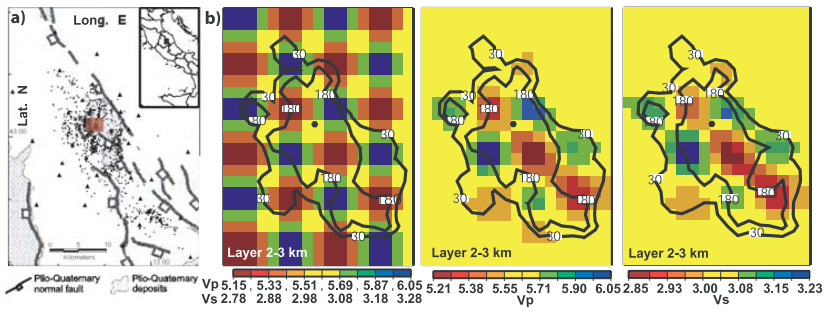

Figure 1. All figures represent the same area. The red square (a) and black dot (b) represent Cofiorito town area. (a) Map of the studied area: Dots represent re-located selected events and triangles the used stations. (Adapted from *Boncio and Lavecchia* [2000]). (b) Checkerboard test: Input model for the layer 2–3 km is on the left, P- and S-wave output on the right side. Contour lines, also reported on the input image for comparison, represent coverage values for 30 and 180 km cumulated ray path per block (about 10 and 60 rays per block, respectively).

Table 3. Anomaly Volumes With Sign and Peak Value

Volume	$\delta V_p/V_p$ (%)	$\delta\Psi/\Psi$ (%)	$\delta r/r$ (%)	Depth range (km)
A	+ (6.0)	+ (11)	+ (2.8)	1–5
B	– (3.5)	– (3.5)	0	2–6
C	+ (2.0)	+ (3.5)	0	3–6

[12] Checkerboard resolution tests for both the P-and S-wave dataset show that velocity anomalies larger than about 8 km on a side are well-determined to depth of approximately 6 km (Figure 1b). The test also showed that the significant anomalies discussed in the study are within well-resolved portions of the model. The average value of the reconstructed anomaly contrast is around ±5%, a value comparable to the ones found in other tomography studies of the same area [*Michelini et al.*, 2000, *Alessandrini et al.*, 2001]. Furthermore, significant anomalies are within areas that are well sampled (more than 10 rays per block), as evident from the analysis of P- and S-wave ray-path coverage.

4. Results and Interpretation

[13] Map views of percent variations of V_p and percent perturbations of $\Psi = V_p \cdot V_s$ and $r = V_p/V_s$ [*Lees and Wu*, 2000] of three significant 1-km thick layers are reported in Figure 2. We clearly identify three anomaly volumes within the well covered part of our study area: A) SE of Colfiorito, the most noticeable, where we have positive V_p, r and Ψ anomalies; B) NW of Colfiorito, where we have negative V_p and Ψ anomalies and average values of r; C) W of Colfiorito, NW-SE direction, where we find positive V_p and Ψ anomalies and average r values (see Table 3 for a schematic description).

[14] Our model interpretation is based on arguments given in the introduction and knowledge of the area's rock types (see Table 1). We propose the following:

[15] A: A volume of stiffer rock with higher crack density, saturated with fluid under low effective stress so cracks remain open, explaining high r values and high Ψ values. Low effective stress is possibly due to higher pore pressure. Volume A could be mainly formed by stiffer, more permeable, high velocity carbonates (e.g., *Calcare Massiccio*). A similar interpretation is given by *Nicholson and Simpson* [1985] for a layer with analogous characteristics in the New Madrid area (Central U.S.A.), confirmed by a drilling test.

[16] B: Lower V_p, average r, and lower Ψ values imply a softer rock with smaller crack density and greater porosity. B could be a volume where softer, more porous and lower

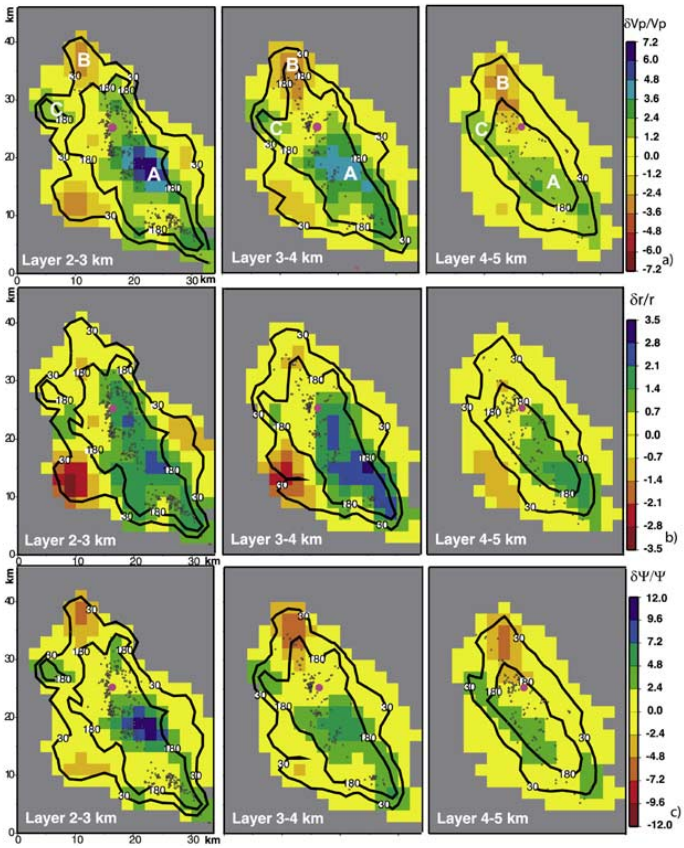

Figure 2. Maps at various depths for $\delta V_p/V_p$ (a), $\delta r/r$ (b) and $\delta\Psi/\Psi$ (c). The colour yellow is associated to the initial 1-D model value for each layer (see Table 2 for initial V_p values). Only seismicity in each layer is depicted. Only blocks covered by at least 1 ray are plotted. The purple dot shows the location of Colfiorito town. Contour lines show coverage for the P-wave (Figure 1a) and S-wave (Figures 1b and 1c).

velocity components of the carbonate sequence are mostly present (e.g., *Maiolica*).

[17] C: Less fractured, low porosity stiffer rock (high Ψ, average r). This could be due to greater presence of high velocity anhydrite (as Triassic evaporite). Interestingly this volume is scarcely affected by seismic activity, implying a more plastic behavior.

[18] Given that the Umbria-Marche aftershock sequence developed for several months, an explanation based on elastic properties only seems unsatisfactory and a poro-elastic approach is preferable. Previous authors have suggested a role of fluid diffusion in the 1997 Umbria-Marche sequence [*Cocco et al.*, 2000; *Ripepe et al.*, 2000] also in agreement with the dilatancy diffusion model of *Nur and Booker* [1972]. The great majority of aftershock seismic activity evolved in volume A, or at the interface with the other two volumes, where we hypothesize the presence of a stiffer rock, more permeable, fluid saturated, and under high pore pressure. Under such condition we can explain the slow SE migration of the sequence with mobility of fluids in A, gradually increasing pore pressure thus decreasing shear resistance of rock. Presence of evaporite, with low permeability, in the strip-like volume C, could be responsible of a fluid-channeling effect in the NW-SE direction.

[19] A link between the anomaly volumes and structural trends of this area of the Central Apennines will be investigated in a future study.

5. Conclusions

[20] The distribution of a large number of events from the 1997 Umbria-Marche earthquake sequence and a well-distributed local seismic network allowed for the computation of high resolution tomographic images of this part of the Central Appenines. The analysis and comparison of Vp, Vp/Vs and Vp · Vs contributes to our understanding of the geology and rheologic properties of the area. Results show three distinct anomalies, which are interpreted to be produced by changes in porosity, degree of fracturing, and fluid pore pressure. Considering that the study is restricted to depths less than 8 km and that the area is characterized by low heat-flow [*Mongelli et al.*, 1991], temperature is not considered as a controlling factor on velocity variation in the region. Our model agrees with a poro-elastic view of the spatio-temporal evolution of this long-lasting seismic sequence.

[21] **Acknowledgments.** We thank H. M. Benz for his support and advice. B. Alessandrini, C. Doglioni, and F. Frugoni for their helpful suggestions. Many thanks to the colleagues of the former RMS unit of ING, especially R. Azzara and G. Selvaggi, for making the data available. We are also grateful to the colleagues of the Servizio Sistemi di Monitoraggio of DPC-SSN. We thank Roberto Scarpa and an anonymous reviewer for their comments.

References

Alessandrini, B., L. Filippi, and A. Borgia, Upper-crust tomographic structure of the Central Apennines, Italy, from local earthquakes, *Tectonophysics*, *339*, 479–494, 2001.

Bally, A. W., L. Burbi, C. Cooper, and R. Ghelardoni, Balanced sections and seismic reflection profiles across the Central Apennines, *Mem. Soc. Geol. It.*, *35*, 257–310, 1986.

Barchi, M. R., A. De Feyter, M. B. Magnani, G. Minelli, G. Pialli, and B. M. Sotera, The structural style of the Umbria-Marche fold and thrust belt, *Mem. Soc. Geol. It.*, *52*, 557–578, 1998a.

Barchi, M. R., G. Minelli, G. Pialli, and B. M. Sotera, The CROP03 profile: A synthesis of results on deep structures of the Northern Apennines, *Mem. Soc. Geol. It.*, *52*, 383–400, 1998b.

Benz, H. M., B. A. Chouet, P. B. Dawson, J. C. Kahr, R. A. Page, and J. A. Hole, Three-dimensional P and S wave velocity structure of Redoubt Volcano, Alaska, *J. Geophys. Res.*, *101*, 8111–8128, 1996.

Boncio, P., and G. Lavecchia, A geological model for the Colfiorito earthquakes (September–October 1997, central Italy), *J. Seismol*, *4*, 345–356, 2000.

Boncio, P., F. Ponziani, F. Brozzetti, M. Barchi, G. Lavecchia, and G. Pialli, Seismicity and extensional tectonics in the Northern Umbria-Marche Apennines, *Mem. Soc. Geol. It.*, *52*, 539–555, 1998.

Cello, G., S. Mazzoli, E. Tondi, and E. Turco, Active tectonics in the Central Appenines and possibile implications for seismic hazard analysis in peninsular Italy, *Tectonophysics*, *272*, 43–68, 1997.

Cocco, M., C. Nostro, and G. Ekstrom, Static stress changes and fault interaction during the 1997 Umbria-Marche earthquake sequence, *J. Seismol.*, *4*, 501–516, 2000.

Collettini, C., M. Barchi, C. Pauselli, C. Federico, and G. Pialli, Seismic expression of active extensional faults in northern Umbria (central Italy), *J. Geodyn.*, *29*, 309–321, 2000.

Deschamps, A., et al., Spatio-temporal distribution of seismic activity during the Umbria-Marche crisis, 1997, *J. Seismol.*, *4*, 377–386, 2000.

Iverson, W. P., B. A. Fahmy, and S. B. Smithson, $V_p \cdot V_s$ from mode-converted P-SV reflections, *Geophysics*, *54*, 843–852, 1989.

Kissling, E., W. L. Ellsworth, D. Eberhart-Phillips, and U. Kradolfer, Initial reference models in local earthquake tomography, *J. Geophys. Res.*, *99*, 19,635–19,646, 1994.

Kissling, E., U. Kradolfer, and H. Maurer, VELEST user's guide-short introduction, technical report, Inst. of Geophys. and Swiss Seismol. Serv., Eidg. Tech. Hochsch., Zurich, 1995.

Koch, M., Bootstrap inversion for vertical and lateral variations of the S wave structure and the V_p/V_s-ratio from shallow earthquakes in the Rhinegraben seismic zone, Germany, *Tectonophysics*, *210*, 91–115, 1992.

Lees, J. M., and H. Wu, Poisson's ratio and porosity at Coso geothermal area, California, *J. Volcanol. Geotherm. Res.*, *95*, 157–173, 2000.

Michelini, A., D. Spallarossa, M. Cattaneo, A. Govoni, and A. Montanari, The 1997 Umbria-Marche (Italy) earthquake sequence: Tomographic images obtained from data of the GNDT-SSN temporary network, *J. Seismol.*, *4*, 415–433, 1997.

Mongelli, F., G. Zito, B. Della Vedova, G. Pellis, P. Squarci, and L. Taffi, Geothermal regime of Italy and surrounding seas, in *Exploration of the Deep Continental Crust*, edited by V. Ceramak and L. Rybach, pp. 381–394, Springer-Verlag, New York, 1991.

Moos, D., and M. D. Zoback, In situ studies of velocity in fractured cristalline rocks, *J. Geophys. Res.*, *88*, 2345–2358, 1983.

Nicholson, C., and D. W. Simpson, Changes in V_p/V_s with depth: Implications for appropriate velocity models, improved earthquake locations, and material properties of the upper crust, *Bull Seismol. Soc. Am.*, *75*, 1105–1123, 1985.

Nur, A., and J. R. Booker, Aftershocks caused by pore fluid flow?, *Science*, *175*, 885–887, 1972.

Okubo, P. G., H. M. Benz, and B. A. Chouet, Imaging the crustal magma source beneath Mauna Loa and Kilauea Volcanoes, Hawaii, *Geology*, *25*, 867–870, 1997.

Paige, C. C., and M. A. Saunders, LSQR: An algorithm for sparse linear equations and sparse least squares, *Trans. Math. Software*, *8*, 43–71, 1982.

Podvin, P., and I. Lecompte, Finite difference computation of travel times in very contrasted velocity models: A massively parallel approach and its associated tools, *Geophys. J. Int.*, *105*, 271–284, 1991.

Ripepe, M., D. Piccinini, and L. Chiaraluce, Foreshock sequence of the September 26th, 1997 Umbria-Marche earthquakes, *J. Seismol*, *4*, 387–389, 1997.

Robertson, J. D., Carbonate porosity from S/P traveltime ratios, *Geophysics*, *52*, 1346–1354, 1987.

Sanders, C. O., L. D. Nixon, and E. A. Schwartz, Seismological evidence for magmatic and hydrothermal structure in Long Valley caldera from local earthquake attenuation and velocity tomography, *J. Geophys. Res.*, *100*, 8311–8326, 1995.

Schön, J. H., Physical properties of rocks, in *Handbook of Geophysical Exploration Seismic Exploration*, vol. 18, edited by K. Helbig and S. Treitel, Pergamon, New York, 1996.

Tatham, R. H., V_p/V_s and lithology, *Geophysics*, *47*, 336–344, 1982.

Toksöz, M. N., C. H. Cheng, and T. Aytekin, Velocities of seismic waves in porous rock, *Geophysics*, *41*, 621–645, 1976.

Villaseñor, A., H. M. Benz, L. Filippi, G. De Luca, R. Scarpa, G. Patanè, and S. Vinciguerra, Three-dimensional P-wave velocity structure of Mt. Etna, Italy, *Geophys. Res. Lett.*, *25*, 1975–1978, 1998.

L. Beranzoli, P. Favali, and S. Monna, Istituto Nazionale di Geofisica e Vulcanologia, Via di Vigna Murata 605, 00143 Roma, Italy. (monna@ingv.it)

L. Filippi, Dipartimento della Protezione Civile-Ufficio Servizio Sismico Nazionale, Via Curtatone 3, 00185 Roma, Italy.

2 Three-dimensional P wave attenuation and velocity upper mantle tomography of the southern Apennines-Calabrian Arc subduction zone

JOURNAL OF GEOPHYSICAL RESEARCH, VOL. 114, B06304, doi:10.1029/2008JB005677, 2009

Three-dimensional *P* wave attenuation and velocity upper mantle tomography of the southern Apennines–Calabrian Arc subduction zone

Stephen Monna[1] and Torsten Dahm[2]

Received 7 March 2008; revised 10 January 2009; accepted 24 March 2009; published 10 June 2009.

[1] We propose a 3-D crust–upper mantle seismic attenuation (Q_P) model of the southern Apennines–Calabrian Arc subduction zone together with a 3-D velocity (V_P) model. The Q_P model is calculated from relative t^* using the spectral ratio method and the V_P from traveltime data. The final data set used for the inversion of the V_P model consists of 2400 traveltime arrivals recorded by 34 short-period stations that are part of the Italian National Seismic Network, and for the Q_P model, 2178 *Pn* phases recorded by a subset of 32 stations. Traveltimes and waveforms come from 272 intermediate-depth Calabrian slab events. This 3-D model of attenuation, together with the 3-D velocity model, improves our knowledge of the slab/mantle wedge structure and can be a starting point in determining the physical state of the asthenosphere (i.e., its temperature, the presence of melt and/or fluids) and its relation to volcanism found in the study area. Main features of the Q_P and V_P models show that the mantle wedge/slab, in particular, the area of highest attenuation, is located in a volume underlying the Marsili Basin. The existence and shape of this main low-Q_P (and low-V_P) anomaly points to slab dehydration and fluid/material flow, a process that may explain the strong geochemical affinities between the subduction-related magmas from Stromboli and Vesuvius. Other interesting features in the models are strong lateral variations in Q_P and V_P that are put in relation with known important tectonic structures and volcanic centers in the area.

Citation: Monna, S., and T. Dahm (2009), Three-dimensional *P* wave attenuation and velocity upper mantle tomography of the southern Apennines–Calabrian Arc subduction zone, *J. Geophys. Res.*, *114*, B06304, doi:10.1029/2008JB005677.

1. Introduction

[2] According to a widely accepted model the Tyrrhenian-Apennine system is the result of a complex convergence of about 1 cm/a [*Faccenna et al.*, 2001] (at present a few millimeters per year [*D'Agostino et al.*, 2008]) between the African plate, the Eurasian plate and several microplates [*Rosenbaum and Lister*, 2004; *Faccenna et al.*, 1996]. Starting $\sim$ 26 Ma ago the Liguro-Provencal and Tyrrhenian basins formed due to the sinking and rollback of the dense Mesozoic oceanic Ionian lithosphere in the east-southeast direction [*Argnani*, 2000, and references therein]. In its final stage this process led to the formation of two back arc subbasins within the Tyrrhenian Sea: the Vavilov (4.3–3.6 Ma) and the Marsili (<2 Ma) (Figure 1) [*Marani and Trua*, 2002, and references therein]. At present, in a region extending only a few 100 km we find oceanic (Ionian plate and Tyhrrenian Basin) and continental (African and Apulian/Adriatic) lithospheres interacting together with the asthenosphere within a subduction system where the Ionian slab is one of the narrowest subduction zones worldwide. In such a small area the topography of the asthenosphere varies greatly, between about 150 km and 10–30 km and different magmatic provinces, ranging from Island Arc Basalt (IAB) -type to Ocean Island Basalt (OIB) -type, occur in close proximity (Figure 1).

[3] In spite of a large number of geological and geophysical studies, the position and interaction between oceanic and continental lithosphere, asthenosphere and subducting plate, the relationship between magma genesis and the evolution of the Tyrrhenian Basin, is still open to debate [e.g., *Malinverno and Ryan*, 1986; *Faccenna et al.*, 2001; *Rosenbaum and Lister*, 2004; *Peccerillo*, 2005].

[4] At present there is evidence for active subduction process of the Ionian oceanic lithosphere of Mesozoic age [*Catalano et al.*, 2001] beneath the Calabrian Arc, where there is mostly seismicity between 160 and 370 km depth [*Frepoli et al.*, 1996]. The spatial distribution of the deep events shows a Wadati-Benioff zone dipping $\sim$ 70° NW beneath the southern Tyrrhenian, down to 500 km depth [*Cimini*, 1999, and references therein]. The slab has been associated with a high-velocity anomaly seen in several traveltime tomographic models, at different scales (e.g., *Selvaggi and Chiarabba* [1995], *Lucente et al.* [1999], *Cimini and De Gori* [2001], *Piromallo and Morelli* [2003], *Spakman and Wortel* [2004], *Montuori et al.* [2007], and very recently by *Neri et al.* [2009]). Tomographic cross sections show a narrow slab which becomes horizontal in the transition zone on the 660 km discontinuity between upper and lower mantle [*Piromallo and Morelli*,

[1]Istituto Nazionale di Geofisica e Vulcanologia, Rome, Italy.
[2]Institut für Geophysik, Universität Hamburg, Hamburg, Germany.

0148-0227/09/2008JB005677$09.00

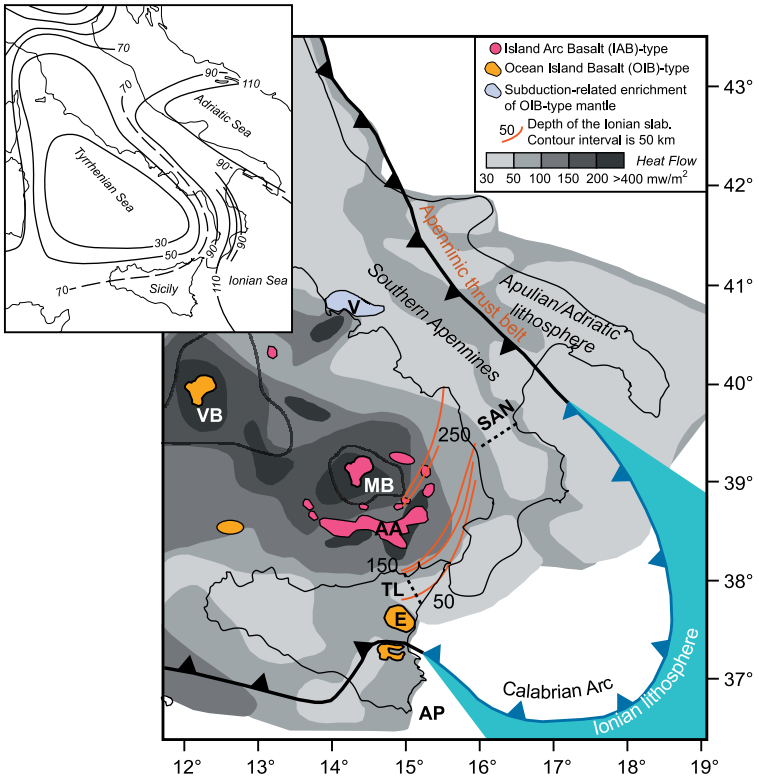

Figure 1. Study area, adapted from *Cimini* [2004] with permission. Heat flow values from *Della Vedova et al.* [1991b]. Dominant volcanic magma sources from *Trua et al.* [2004]. Wadati-Benioff zone (red curves) inferred from seismicity relocated in this study's 3-D velocity model. Inset shows lithosphere thickness, simplified from *Calcagnile and Panza* [1981]. Abbreviations are as follows: VB, Vavilov Basin; AA, Aeolian Arc; MB, Marsili Basin; TL, Tindari-Letojanni tectonic line; E, Mount Etna; AP, African plate; SAN, Sangineto tectonic line; V, Vesuvius.

2003; *Spakman and Wortel*, 2004]. Further evidence for subduction is the presence of magmatism associated with subduction of the Ionian lithosphere [*Serri*, 1990; *Serri et al.*, 2001]. Interestingly, no subcrustal seismicity has been recorded from the southern and central Apennines [e.g., *Di Stefano et al.*, 1999]. This finding, together with the presence in several tomography models of a low-velocity anomaly below the southern Apennines, has led to explanations that differ mainly in considering the subducting slab either as continuous or as torn/detached.

[5] Within the southern Tyrrhenian Basin high heat flow values have been measured, exceeding 200 mW/m^2 [*Della Vedova et al.*, 1991a, 1991b; *Zito et al.*, 2003], which correspond to areas of thinned crust (down to 10 km), and very shallow asthenosphere (up to 10–30 km) [*Pontevivo and Panza*, 2006, and references therein]. These areas correspond to two subbasins, the Vavilov and the Marsili and their respective volcanoes (Figure 1). The negative magnetic pattern in the southwestern part of Italy and the Tyrrhenian coast agrees with the presence of high heat flow, pointing to a very shallow 600°C isotherm [*Speranza and Chiappini*, 2002].

[6] Seismic anelastic attenuation is a very useful measurement in a subducting system where temperature plays a key role, as it gives information which is complementary to seismic velocity studies. In fact, seismic attenuation or its reciprocal quantity, the quality factor Q, is more sensitive to temperature variations than seismic velocity V, so while variations in V are more useful to image the colder fast slab, variations in Q can be used to image hot mantle material surrounding the slab [*Romanowicz*, 1995]. In this study we present a 3-D V_P model together with a 3-D Q_P model of the southern Apennines–Calabrian Arc subduction zone. Our study area includes a part of the eastern sector of the Marsili Basin, and in general, areas with high heat flow (Figure 1) where we expect large lateral temperature variations, thus large variations in seismic Q_P and V_P. We have calculated 3-D Q_P and V_P models by inverting, respectively, data calculated with the spectral ratio method and traveltime data, from P waves generated by local deep events in the Calabrian Arc subduction zone.

[7] The spectral ratio method involves a delicate procedure, for this reason the application of the method and the simplifying theoretical assumptions we make are explained

in detail (section 2 and the appendix). We then show how we generate *P* wave V_P and Q_P models starting from short-period recordings of mostly intermediate-depth slab events (between 70 and 300 km depth), and their reliability through synthetic tests and other arguments (section 3). Following their description, the V_P and Q_P models are compared with other data and discussed (section 4).

[8] This 3-D model of attenuation, together with the 3-D velocity model, can improve our knowledge on the slab/mantle wedge structure and be a starting point to determine the physical state of the asthenosphere (i.e., temperature, presence of melt and/or fluids) and possibly its relation to volcanism found in the study area.

2. Data and Method

2.1. Instruments and Earthquake Selection

[9] The seismic waveforms used in the present study were recorded by the Italian Telemetered Seismic Network (ITSN) of the Istituto Nazionale di Geofisica e Vulcanologia (INGV), from 1990 to 2002. In the ITSN signal is transmitted through phone lines from the seismic station to INGV where it is A-D converted (12 bit Reftec digitizers), with a sampling frequency of 50 Hz [*Barba et al.*, 1995]. Natural frequency is at 1 Hz and the signal amplitude can be considered flat between 1 and 5 Hz after telemetry. Most of the stations are only equipped with a vertical component sensor.

[10] The accuracy of earthquake location in our study area was limited because of the shape of the Italian peninsula, strong lateral velocity variations, and the uneven station distribution [see, e.g., *Di Giovambattista and Barba*, 1997]. The lack of station coverage in the northwest (Tyrrhenian Sea) and southeast (Ionian Sea) decreases the accuracy of hypocenter locations and limits resolution of tomography models. A great improvement is expected when data will be available from permanent or very long term OBS (Ocean Bottom Seismometer) networks deployed in the uncovered areas.

[11] Arrival times and localizations of the starting data set are based on the CSI1.1 catalog, which includes a relocalized selected set of events extracted from the INGV bulletin. *S* phases are used when reliably picked. Event locations have reasonably small azimuthal gaps when events occur on land (<180°) and are larger for events at sea (<240°). Most of the hypocenter locations have RMS < 1s, and for deep events horizontal epicentral errors are <6–10 km and vertical errors <10 km [*Chiarabba et al.*, 2005].

[12] The final data set selected in this study for the V_P and Q_P inversion is composed by a great majority of events having gap <200° (80%) and number of phases per event >8 (90%). The robustness of the inversion procedure with respect to the vertical error in hypocenter location will be considered in section 3.3. In total we used for the V_P inversion about 2400 *Pn* traveltimes from 272 well localized events recorded by 34 stations, and for the Q_P inversion about 2100 *Pn* waveforms recorded by a subset of 32 stations. Events have mostly intermediate depth (70–300 km depth range) and are associated with the subduction process. For most of such events the moment magnitude has not been calculated and for some neither the duration or M_l magnitudes. The strongest events in the data set have $M_w < 5$, and many of them had to be discarded due to clipping.

[13] Although the *S* waves are more sensitive to anelastic attenuation anomalies, we chose to work with the *P* waves for the fact that for some stations the *Sn* phase was not visible or barely visible (low S/N), or not distinguishable from other phases (for example *S* to *P* converted phases). This choice was reinforced by the fact that the majority of the sensors were single (vertical) component. The selected *Pn* waveforms were then processed using the spectral ratio method to obtain a 3-D Q_P model. Further explanation on the criteria for the selection of data used in the Q_P inversion is given in section 2.3.

2.2. Spectral Ratio Method (Theory)

[14] In this work seismic wave attenuation data comes from the Fourier amplitude spectra of recorded *Pn* seismic phases. We now introduce some mathematical aspects, following *Teng* [1968] and *Sanders* [1993].

[15] The amplitude spectrum of seismic waves measured at a receiver i from source j can be written as

$$A_{ij} = A_{0j}(f;\theta_i,\varphi_i)S_i(f)A_{\mathrm{INS}}(f)B_{ij}(f), \tag{1}$$

where f is frequency, θ_i, φ_i is the propagation direction from source j to station i, $A_{0j}(f;\ \theta_i,\ \varphi_i)$ is the source spectrum, $S_i(f)$ is the receiver site effect, $A_{\mathrm{INS}i}(f)$ is the instrument transfer function, and $B_{ij}(f)$ is the transfer function describing the amplitude decrease as the signal propagates along a ray inside crust and mantle.

[16] In particular, we have $B_{ij}(f) = G_{ij}\exp(-\pi f t^*)$, where $t^* = \int_i ds/[Q(f,\ r)V(r)]$ and Q is the quality factor, V is velocity (*P* wave or *S* wave), the integration is on the raypath from source j to receiver i (t^* has the dimensions of time), and $G_{ij} = G_{ij}(r)$ is a frequency-independent factor describing the geometrical spreading of the wavefront.

[17] After making some simplifying hypotheses and mathematical passages which are described in the appendix, we obtain the linear equation:

$$lnA_{ij} - \overline{lnA_j} = C_{ij} + f\pi\left(\overline{t_j^*} - t_{ij}^*\right) = C_{ij} + \pi f \Delta t_{ij}^*, \tag{2}$$

where $\overline{t_j^*} = (1/N_j)\sum_{i=1}^{N_j} t_{ij}^*$ is the average t^* for event j. Variable Δt_{ij}^* is often called relative t^*.

[18] As a result of the spectral ratio, the frequency-dependent source term, the site effect term and the instrumental response have been eliminated from equation (2) and all terms independent on frequency are included in C_{ij}. The source radiation pattern only affects the signal to noise amplitude ratio (S/N). If for a specific event a station lies near a nodal plane, that particular signal is rejected due to its low S/N. The spectral ratio method has the advantage of calculating Δt_{ij}^* by eliminating the source term and it is in general more robust compared to other techniques which rely on the accurate knowledge of the absolute value of the signal amplitude.

[19] As the linear dependence on f in (2) strongly depends on hypothesis I (see the appendix), any departure from the hypothesis will show up as nonlinearity in the spectral ratio. Therefore, as we will see later in section 2.3, linearity will be a factor for data selection.

[20] The Δt_{ij}^* are calculated through equation (2) starting from the spectral ratios of amplitudes of selected waveforms, and are later inverted to find a (relative) Q model, as the following shows. Using a formalism which is identical to the one generally used for traveltime data inversion we write the definition of t^* in discrete terms. After parameterization of the Earth volume under study with rectangular cells identified with the index l, we have for a generic raypath from event j to station i:

$$t_{ij}^* = \sum_{l=1}^{N_{\text{cells}}} (t_{ij})_l / Q_l, \tag{3}$$

where $(t_{ij})_l$ is the traveltime in cell l (in which V and Q are constant), $(t_{ij})_l = 0$ if the ray does not go through the lth cell, and N_{cells} is the total number of cells in the model. As our data are the Δt_{ij}^* (relative t^*) calculated from equation (2), we need to modify (3) into

$$\Delta t_{ij}^* = \overline{t_j^*} - \sum_{l=1}^{N_{\text{cells}}} (t_{ij})_l / Q_l = \frac{1}{N_j} \sum_{i=1}^{N_j} \sum_{l=1}^{N_{\text{cells}}} (t_{ij})_l / Q_l - \sum_{l=1}^{N_{\text{cells}}} (t_{ij})_l / Q_l,$$

which can be rewritten as

$$\Delta t_{ij}^* = \sum_{l=1}^{N_{\text{cells}}} 1/Q_l \left[\overline{(t_j)_l} - (t_{ij})_l \right], \tag{4}$$

where $\overline{(t_j)_l} = (1/N_j) \sum_{l=1}^{N_j} (t_j)_l$ is the average traveltime in the lth cell for event j.

[21] If the velocity structure and source locations are given, (4) becomes a linear equation in the unknown vector $1/Q = [1/Q_1, 1/Q_2, \ldots ....1/Q_{N\text{cells}}]$, which is formally identical to the one generally used for traveltime inversion (i.e., substitute t to Δt^*, raypath lengths to relative traveltimes, and velocity to quality factor) where the traveltime part in the square brackets can be calculated directly in the known velocity model. So the matrix to be inverted is composed of elements Δt_{ij}^*, where $i = 1, \ldots, N_{\text{stations}}$ and $j = 1, \ldots, N_{\text{events}}$.

2.3. Spectral Ratio Method (Application)

[22] In addition to uncertainties stemming from the theoretical assumptions considered in section 2.2, *Evans and Zucca* [1993] have pointed out the difficulties encountered in the application of the spectral ratio method, where several choices need to be made within the data processing, in particular the spectral estimator, the choice of the window length and the frequency band. In our application of the spectral ratio method we have kept in mind such considerations to minimize processing errors. We estimated the spectra using the multitaper method [*Park et al.*, 1987; *Mann and Lees*, 1996] using three 4-pi Slepian tapers. The analysis was on 3 s of signal including the first *Pn* arrival, and 3 s of noise preceding the first arrival (Figure 2a). In this way we have enough data points for a robust spectral estimate (150 points) while minimizing the possibility of having secondary phases in the selected record.

[23] To insure the quality of the data we took several steps. First, we selected seismic waveforms automatically according to their signal-to-noise ratio (S/N), where S/N >3 in a frequency band at least 3 Hz wide. Second, we decided if the spectral ratio was linear enough by a visual inspection and then by checking the RMS value in the least squares linear fit. In this way data which was accepted complied with the linearity hypothesis, i.e., that the frequency dependence of Q can be neglected as discussed in section 2.2 (Figures 2b–2d) and in the appendix. Third, an event is accepted if at least 5 associated waveforms are accepted. Furthermore, we checked for data consistency by plotting residual maps, similarly to what is done with traveltime data, and polar plots. Figure 3 shows polar plots of a significant subset of stations, where consistency of Δt^* data is clear and some important features found in the 3-D Q model are already evident.

[24] The nonlinearity present in some of the spectral ratios where S/N > threshold, as in Figures 2b and 2d, can be explained with a frequency-dependent Q as shown by *Cheng and Kennett* [2002] using the spectral ratio method on data recorded in Australia. A linear approximation of the spectral ratio (frequency-independent Q) is usually valid in a restricted frequency band, while a nonlinear dependence (frequency-dependent Q) must be considered for broader frequency bands when there is significant curvature of the spectral ratio. This is another advantage of the spectral ratio method as it gives us a measure (curvature) of the dependency of Q on frequency.

[25] Although in the application of the spectral ratio technique we have neglected or eliminated several unknown terms, it is still necessary but difficult to quantify the relative contribution to attenuation of anelastic effects and scattering loss caused by heterogeneities [*Fehler et al.*, 1992; *Sato et al.*, 2000]. Since scattering results in shifting higher-frequency energy from the first arrival pulse to the coda of the seismic phase, one way to understand if scattering plays a major role is to check for a later high-frequency arrival wavelet [*Richards and Menke*, 1983; *Evans and Zucca*, 1993, and references therein]. To check the presence of this effect we calculated spectra and spectral ratios on data records of increasing length (2, 3, 4, 5, and 6 s) from several events. We find that as the window length is increased there is not a noticeable increase of high-frequency energy in the spectra, also, although there are some differences in the Δt^* values, the main anomalies shown in residual maps are stable with respect to increase of the window length, confirming that we can neglect the contribution of scattering to attenuation in this case. Studies of *S* wave coda attenuation show a predominant role of intrinsic over scattering attenuation in the southern Apennines [*Bianco et al.*, 2002] and in southeastern Sicily [*Giampiccolo et al.*, 2004]. On the other hand, *S* wave coda studies in volcanic areas show a relevant role of scattering for Etna and for the Campi Flegrei [*Del Pezzo et al.*, 1996]. It is difficult to compare our work with the above mentioned studies, because they consider crustal events, and mostly because they use constant and/or two-layer velocity models. *Hoshiba et al.* [2001] show in the case of events in Southeastern Chile (having also subcrustal depths), how the choice of the velocity model influences the estimation of the scattering strength. In fact, the authors point out that the coda part of the seismograms can be even entirely produced, with no additional scattering, by introducing strong discontinuities in

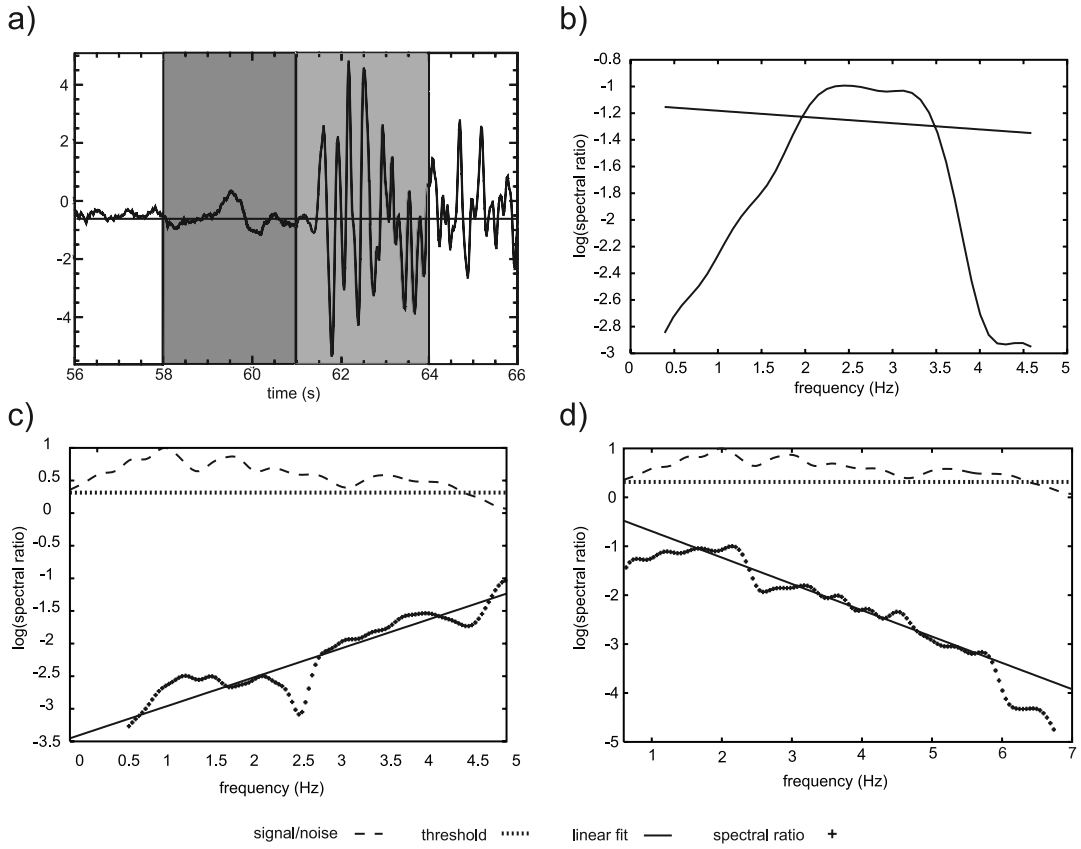

Figure 2. (a) Example of selection of 3 s of noise (dark shaded area) and 3 s of data for spectral analysis (light shaded area). (b) Case for rejected spectral ratio due to high nonlinearity. (c) Accepted spectral ratio (lower curve) and best linear fit for station LCI receiving a wave undergoing small attenuation (positive slope). The upper curve represents S/N and comparison with threshold value, used for selection. (d) Same as Figure 2c, but for station SGO receiving a wave going through an attenuating medium (negative slope). For location of stations LCI and SGO, see Figure 4. In Figures 2c and 2d, S/N spectra are normalized to unity and the threshold value corresponds to absolute value = 3. All scales are linear.

depth and lateral variations in V, such as the ones we expect and find in our study area.

3. Inversion and Models' Reliability

3.1. Inversion of Δt^* Data (Theory)

[26] As we have seen (section 2.2) the equations for t^* (Δt^*) are formally the same as the ones for traveltimes (relative traveltimes). In our inversion procedure we calculate theoretical t^* on raypaths in a given 3-D velocity model, where the sources are fixed. This procedure is based on theory and experimental data showing, in first approximation, that variations of t^* depend only on Q. In fact, we consider, similarly to *Evans and Zucca* [1988], small variations,

$$\delta t_i^* = \delta\left(\pi \int_i \frac{ds}{QV}\right) = \pi \int_i ds\delta\left(\frac{1}{QV}\right), \tag{5}$$

with $\delta(1/QV) = -\delta V/Q_{\mathrm{ref}}V_{\mathrm{ref}}^2 - \delta Q/V_{\mathrm{ref}}Q_{\mathrm{ref}}^2$, where Q_{ref} and V_{ref} are the starting reference values.

[27] Supposing that $\delta Q \gg \delta V$. Then $\delta(1/QV) \approx -\delta Q/(V_{\mathrm{ref}}Q_{\mathrm{ref}}^2 = \delta(Q^{-1})/V$, and (5) becomes

$$\delta t_i^* \approx \pi \int_i ds \frac{\delta(Q^{-1})}{V} = \pi \int_i dt\delta(Q^{-1}). \tag{6}$$

So the linearity in the relationship between variations in t^* and Q relies on the hypothesis that $\delta Q \gg \delta V$. Experimental data and rheological models of the mantle, show that the temperature dependence of V and Q is respectively linear and exponential [*Romanowicz*, 1995, and references therein]. The hypothesis is particularly valid in our study area where we expect large temperature variations.

3.2. V_P and Q_P Inversion

[28] The calculation of a 3-D P wave velocity model using the code FDTOMO of *Benz et al.* [1996], led to

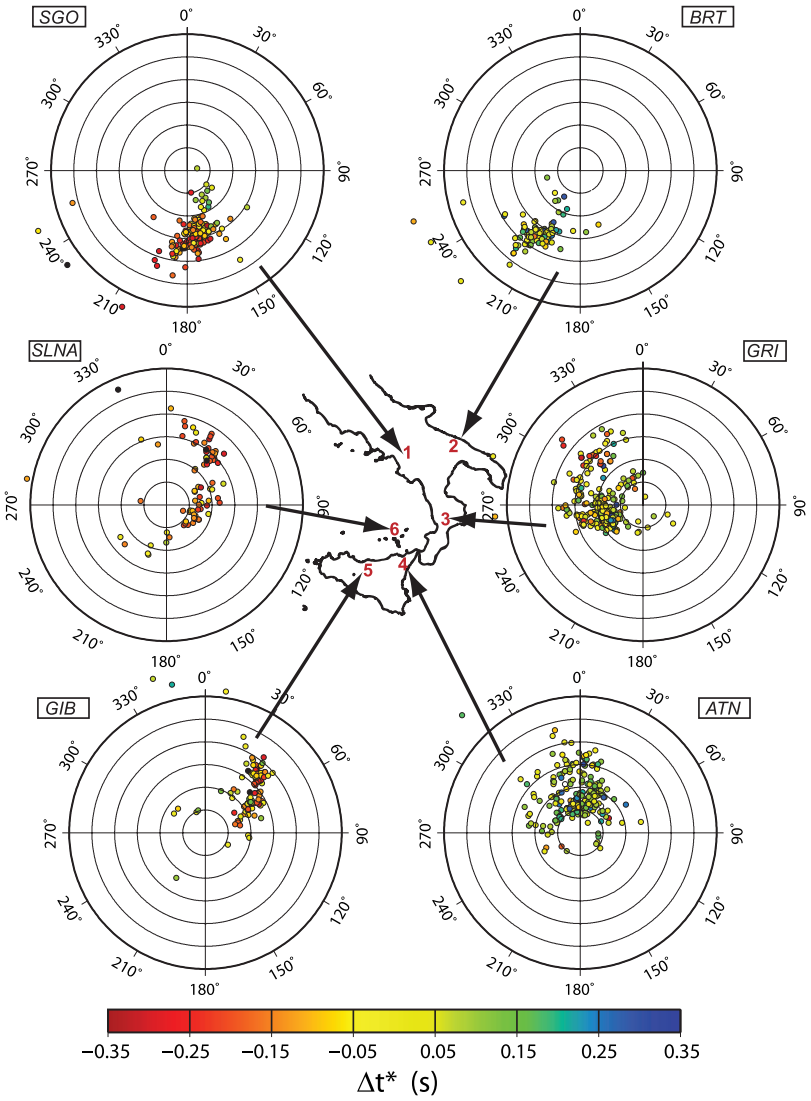

Figure 3. Single station polar plots: 1, SGO; 2, BRT; 3, GRI; 4, ATN; 5, GIB; 6, SLNA. Dots represent events recorded by the station; their color is proportional to Δt^*. Circles are every 100 km and represent station-event hypocentral distance. Angle represents back azimuth.

improved earthquake locations and to more realistic seismic paths used to calculate the 3-D Q_P model. In the inversion procedure used to calculate the 3-D V_P model it is necessary to start from a reliable 1-D model. To find a good initial 1-D velocity model, we inverted traveltime data from a selected subset of 150 events and stations using the method of *Kissling et al.* [1994, 1995]. We started from a seven-layer model compatible with local models found in literature for above Moho depths [*Sgroi et al.*, 2006, and references therein], and global model ak135 for below Moho depths [*Kennett et al.*, 1995]. The first and last layers of the model were fixed as they are poorly constrained by the data. Final travel time RMS calculated in the best fitting 1-D model (Table 1) was 0.4 s for this selected subset of 150 events. Then, we simultaneously inverted the travel time data both for hypocenter location and velocity in a 3-D model, starting from the calculated initial best fitting 1-D model. FDTOMO uses a finite difference technique for travel time calculation [*Podvin and Lecompte*, 1991] and the least squares QR decomposition (LSQR routine [*Paige and Saunders*, 1982]) for simultaneous inversion of velocity structure and hypocenters.

[29] After performing several real data inversions and synthetic tests (see section 3.3) using different parameterization sizes, we determined the best cell size for the inversion part to be 40 × 40 × 20 km^3 (larger in the

Table 1. Best Fitting 1-D Starting Model[a]

Depth (km)	V_P (km/s)
−2	4.0
5	5.9
20	7.1
30	8.3
40	8.3
100	8.7
300	9.0

[a]Origin of the model is at sea level.

horizontal dimension). For a more accurate travel time calculation through the model we used $10 \times 10 \times 10$ km^3 constant velocity cells. A smoothing constrain was gradually lowered during 5 iterations to allow a compromise between model stability and minimization of data misfit. The final total travel time RMS is about 0.6s, from an initial value of about 1s.

[30] To calculate the 3-D Q_P model we used the same set of 272 well localized events (section 2.1) and the inversion was performed using raypaths calculated within the final 3-D velocity model. The inversion of relative t^* data was performed on a modified version of the FDTOMO code starting with a uniform Q_P model. The investigated volume is about $450 \times 600 \times 300$ km^3 (Figure 4), although the resolved region is smaller (sections 3.3 and 4.3).

3.3. Models' Reliability

[31] One way to evaluate how a given station event distribution will determine the 3-D model of a given seismic quantity (e.g., V, Q), is to perform synthetic tests. As a first test we have inverted synthetic data, for V_P and Q_P, calculated in a checkerboard model (Figures 5a–5d). For V_P we see that there are large areas that are well resolved down to about 200 km depth, that the anomalies are recovered with varying amplitude, and that some smearing is found in the SW-NE direction. Test model reconstruction is best for the upper strata and extension of resolved area decreases with depth (Figures 5a and 5b). Similarly for the Q_P model (Figures 5c and 5d), but reconstructed areas have a smaller extension than for V_P and the amplitude of anomalies is quite underestimated due to the regularization (damping and smoothing) procedure. The possibility of smearing in the SW-NE direction is confirmed by the raypath distribution (Figure 4).

[32] By performing several inversions using different values of the regularization parameters (damping and number of iterations in LSQR, smoothing constrain on the model), we have noticed for Q_P, that some parts of the study volume tend to achieve anomaly values that are greater than the starting model if regularization is too lax. This information served as a guideline for the real t^* data inversion, where conservative regularization values were chosen.

[33] After the real data inversion we performed spike tests, where the test anomalies were placed in a position roughly mimicking the anomalies found in the models coming from real data inversion (section 4.3). Recovery of the input synthetic model is quite good for V_P (Figures 6 and 7), with small smearing of the low-V_P anomaly at superficial depths, mostly in the southwest direction and some smearing and shifting in the vertical direction of the high- V_P anomaly (Figures 6, 7c, and 7d).

[34] For Q_P, recovery of the main anomalies is less efficient than for V_P (Figures 8 and 9a–9d), and greater smearing and shifting is found for the low-Q_P anomaly mostly in the vertical-southwest direction (Figures 8, 9a, and 9b) and also for the high-Q_P anomalies smeared in the southwestern direction. Also, smearing and shifting of anomalies merges the two high-Q_P anomalies at higher depths into a single body (Figure 8). In general shifting and smearing can extend about 1–2 cell sizes. In Figure 9b it might appear that a high-Q_P anomaly was introduced by the inversion procedure. Its existence can be explained by noticing that the anomaly is present in the input model (Figure 9c) but, as it is close to the profiles' intersection point and was slightly shifted during the inversion, it is mapped into the neighboring section plane. Summarizing, in general the anomalies are well recovered in sign and position, even at the edge of the models although smearing and shifting of anomalies occurs, especially for Q_P. In the interpretation (section 4.4) we will take into account the possibility of shifting and smearing in real data inversion, and will interpret reliable anomalies at a scale and resolution which is much larger than the extension of the artifacts seen in the synthetic tests.

[35] In seismic tomography studies shifting and smearing is mainly due to event station distribution, as it happens, for example, when events are concentrated within a narrow slab

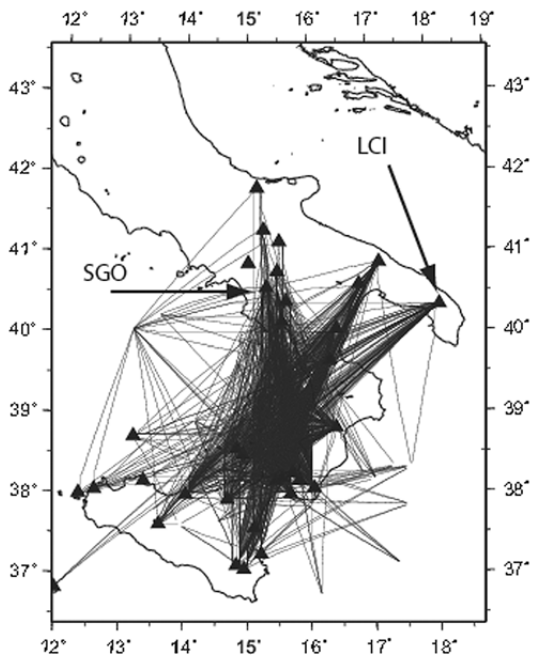

Figure 4. Study area and paths of all rays used in this study projected on the horizontal plane. Triangles represent the stations used in the study. Arrows point to stations SGO and LCI (see Figure 2).

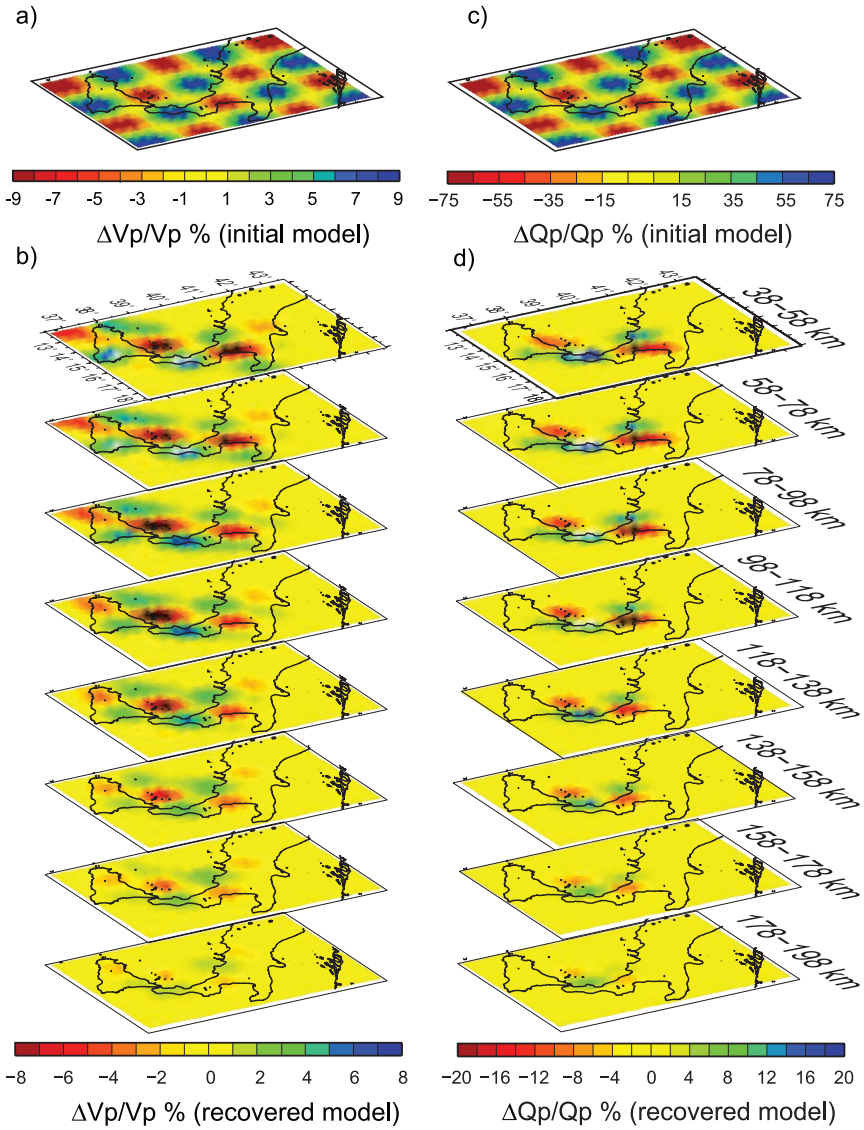

Figure 5. Checkerboard synthetic tests. (a) V_P input (initial) model. (b) V_P output (recovered) model. (c) Q_P input (initial) model. (d) Q_P output (recovered) model.

leading to a fanlike ray distribution. In our case, we can see from synthetic tests that this particular station event distribution may lead, as expected, to shifting and smearing of anomalies.

[36] Given that both Q_P and V_P inversions rely on the same station event geometry we need to invoke other causes to explain their different behavior with regards to artifacts. First, t^* data is noisier than t data thus needing stronger inversion regularization, which in turn causes more pronounced smearing for Q_P than for V_P. Second, another possible cause for artifacts in the Q_P model is that we are inverting *relative* t^* data. In fact, if we consider equation (4), we find that one can add an arbitrary constant to the relative t^* data in the square bracket. Substituting in the square bracket of the right side of (4) the new variable $(t_{ij})_l = (t_{ij})_l + C_j$, with C_j arbitrary constant, we have

$$(t_{ij})_l - \overline{(t_j)}_l = (t_{ij})_l + C_j - (1/N_j)\sum_{l=1}^{N_j}\left[(t_j)_l + C_j\right] = (t_{ij})_l - \overline{(t_j)}_l,$$

where the constant C_j is common to all the cells traversed by the rays from event j. In this way data are determined by direct calculation from a Q_P model minus an arbitrary

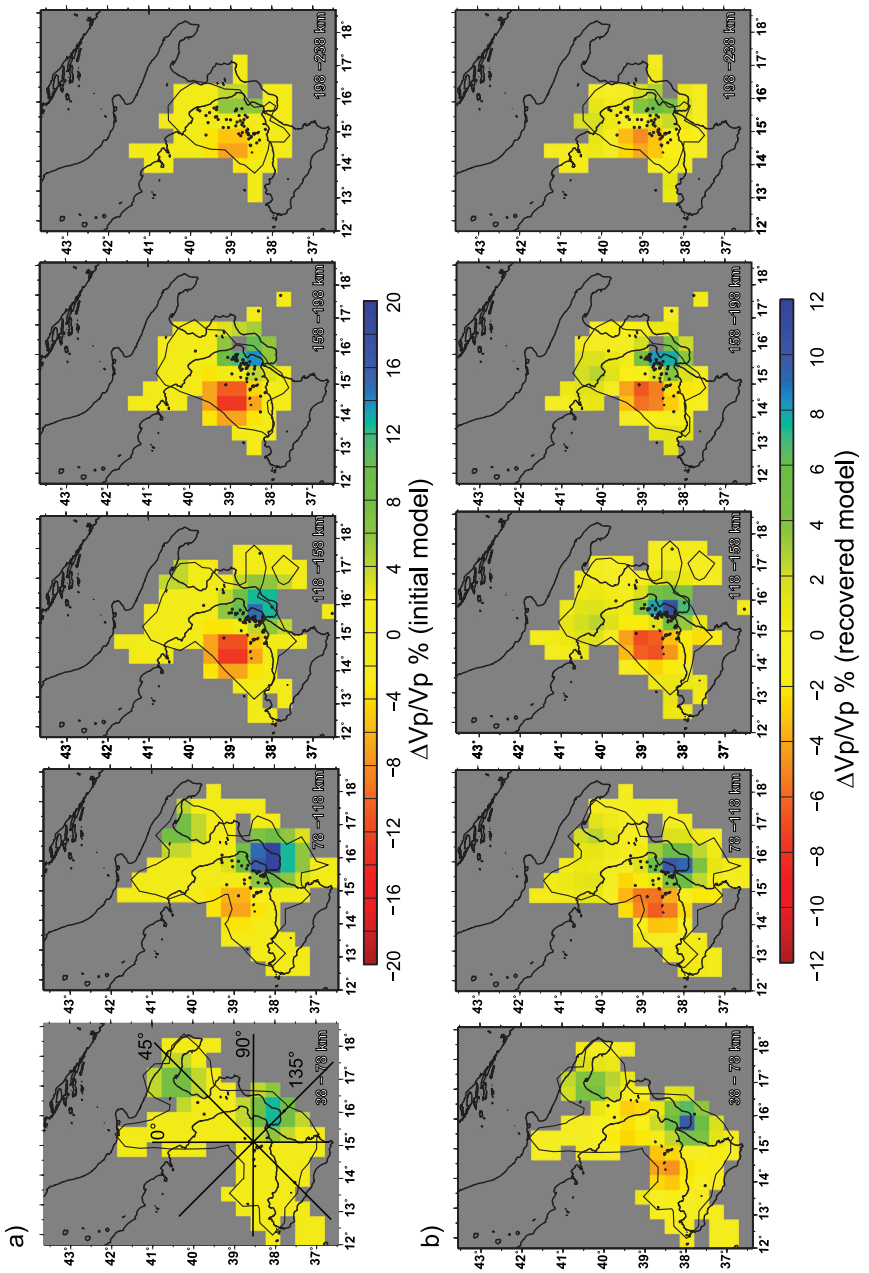

Figure 6. Spike synthetic test for V_P, maps. (a) Input model. (b) Output model. Lines in Figure 6a (at 38–78 km) represent profiles for sections in Figures 7 and 9. Here and elsewhere, circles represent hypocenters (found in each model map or section) localized in a 3-D velocity model calculated from real data. Here and elsewhere, the bold curve includes cells crossed by at least four rays.

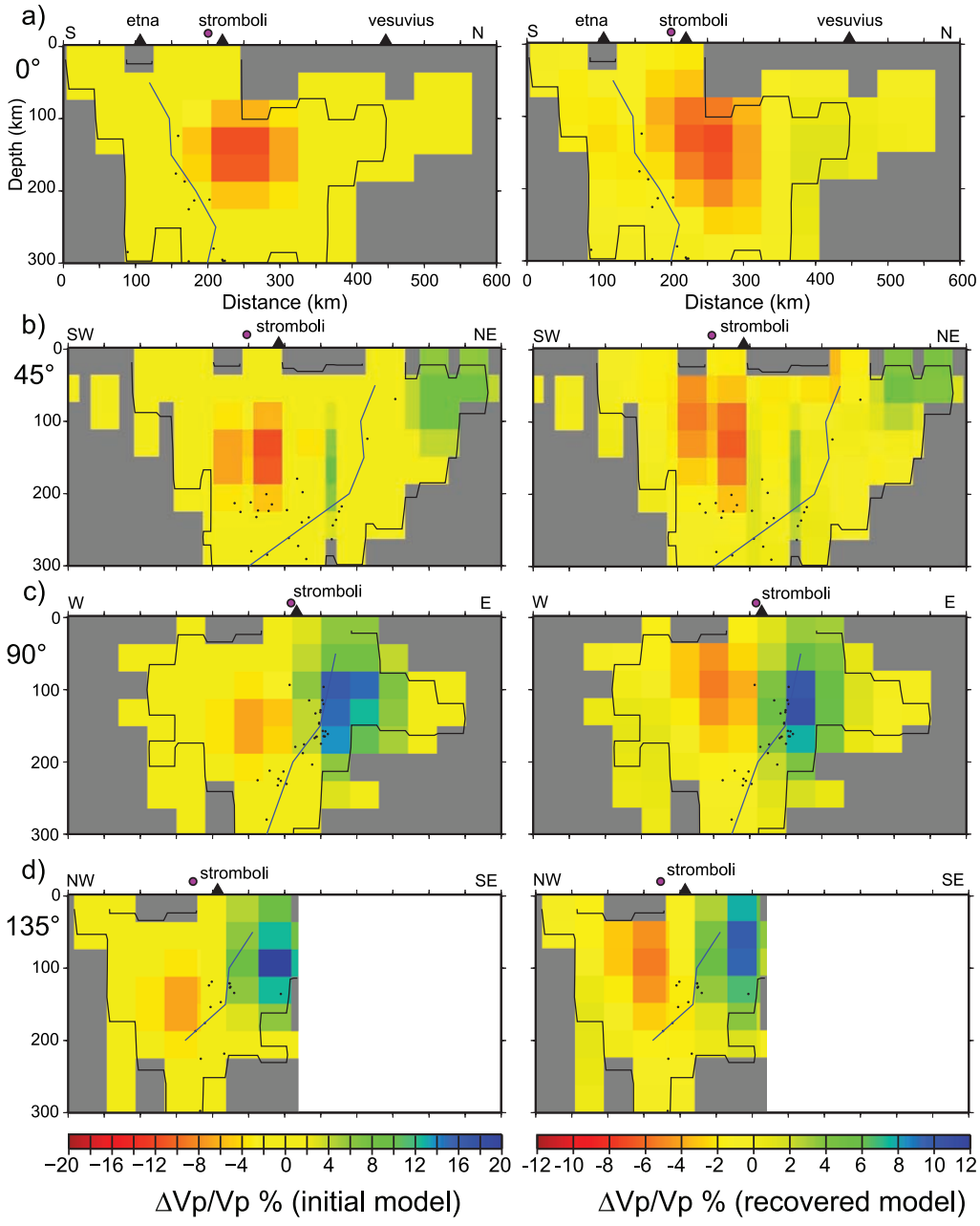

Figure 7. Spike synthetic test for V_P, cross sections. Sections are along profiles shown on Figure 6. On the left is the input (initial) model, and on the right is the output (recovered) model. Sections are every 45°, where the angle is measured in the clockwise direction starting from north, and they all go through the point shown as a purple circle. Here and elsewhere, blue curves are found by interpolation of the profiles with the red curves described in Figure 1 (inferred Wadati-Benioff zone). Block size in Figures 7, 9, and 12 varies for some diagonal sections (excluding 0° and 90°) as cells can be cut to different sizes depending on the position and angle of the bisecting plane.

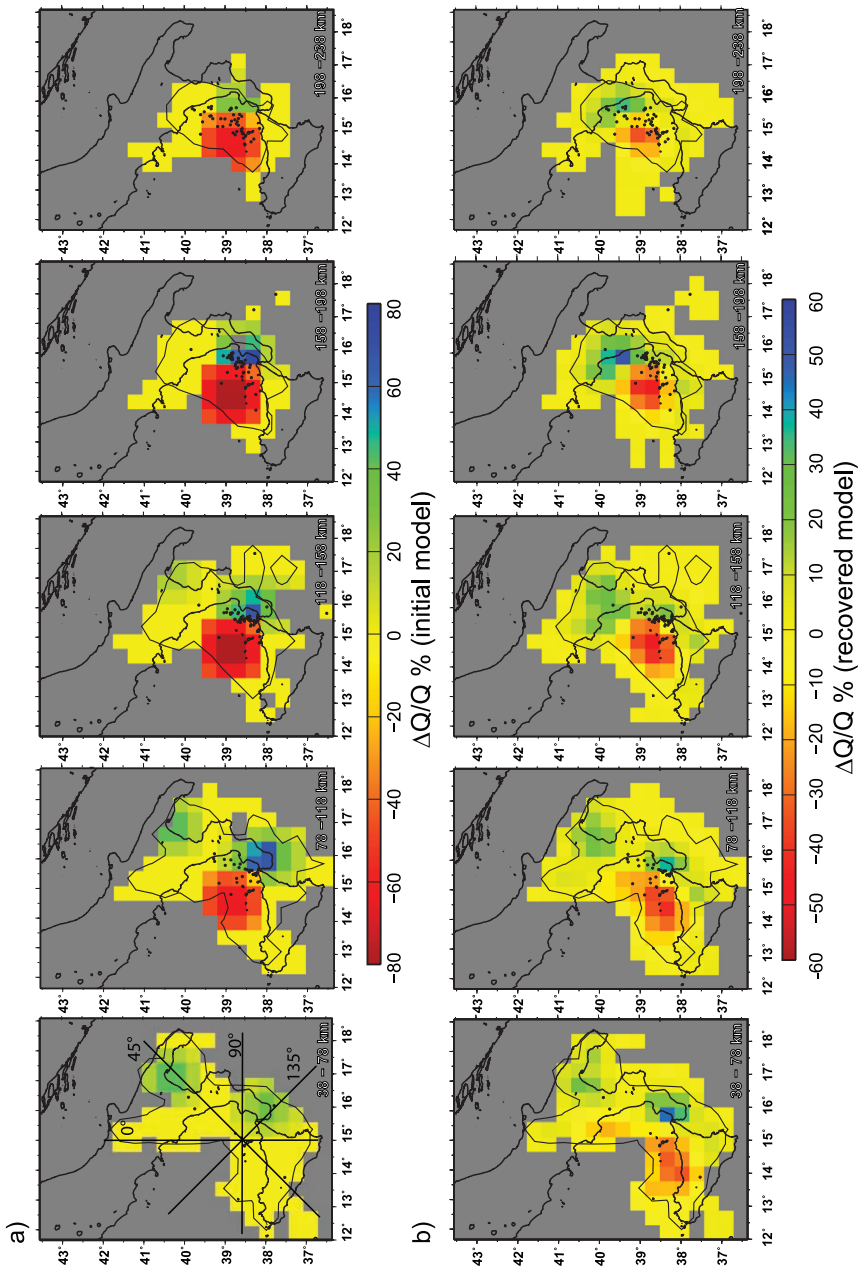

Figure 8. Spike synthetic test for Q_P, maps. (a) Input model. (b) Output model. Lines where profiles are taken are the same as in Figure 6.

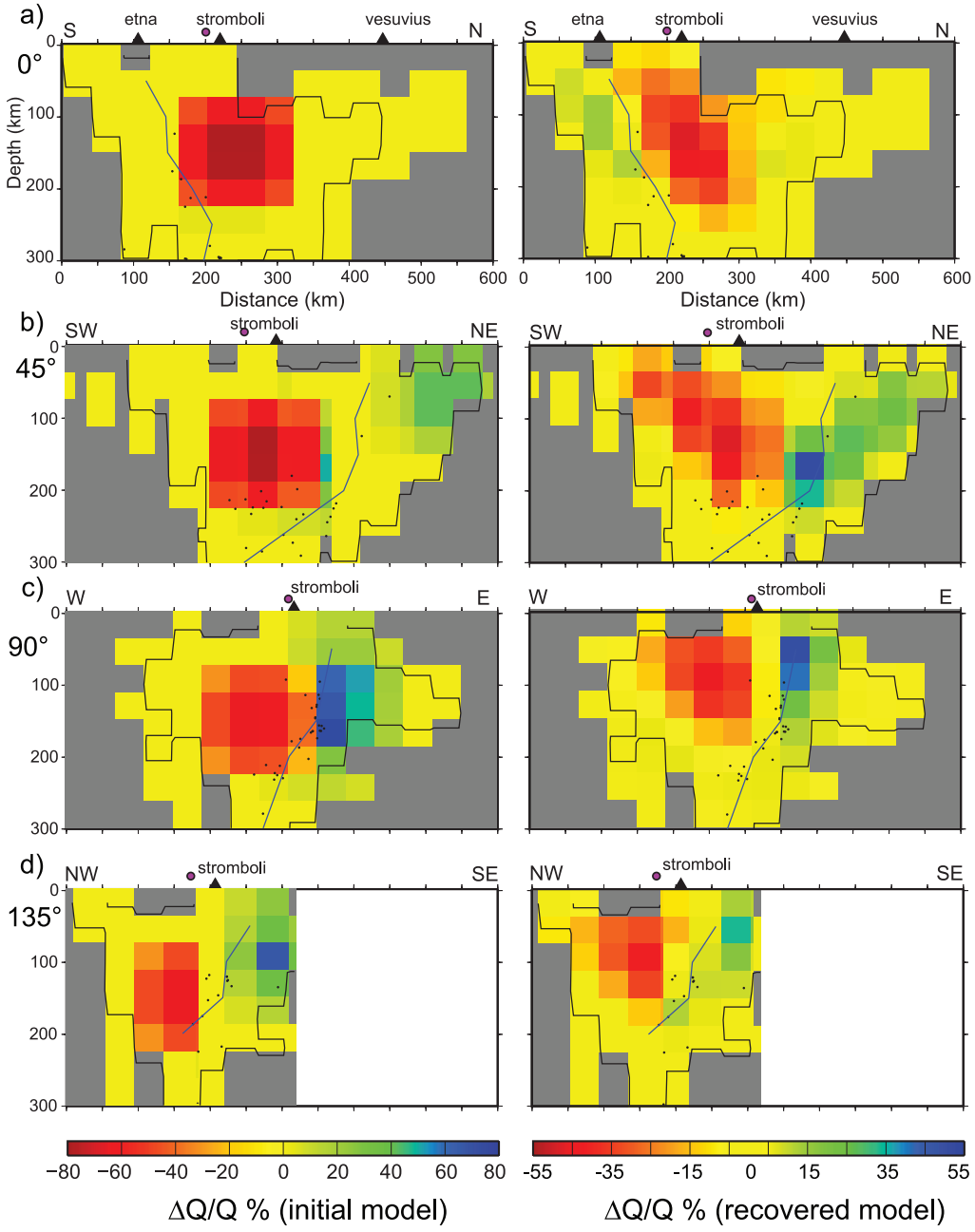

Figure 9. Spike synthetic test for Q_P, cross sections. Sections are along profiles shown in Figures 6a and 8a, as for V_P. On the left is the input (initial) model, and on the right is the output (recovered) model.

vector of constants $C = (C_1, C_2, \ldots\ldots, C_{Nevents})$. This type of problem is common to all inversions of relative residual data. To test the independence of the procedure on the initial Q_P model we have performed the inversion by starting from different Q_P values and found final models that strongly resemble each other, confirming the theoretical result.

[37] We now try to estimate how the error on t^* propagates on the error on Q_P within our approximation, i.e., neglecting errors coming from the calculation of the velocity model. Starting from (6) we have the linear relation for a generic raypath

$$\delta t^*_{\text{path}} \approx \pi \int_{\text{path}} dt\delta(Q^{-1}) \,. \tag{7}$$

If we consider an average error on attenuation $\overline{\delta(Q^{-1})}$, then $\delta t^*_{\text{path}} \approx \pi\overline{\delta(Q^{-1})}$ * $\text{time}_{\text{path}}$. From our linear fit, if we take $\delta t^*_{\text{path}} = 0.02$ s, which can be considered as an upper limit, and $\text{time}_{\text{path}} = 30$ s, which can be considered as average path traveltime, then

$$\frac{\overline{\delta Q}}{Q} = \frac{Q\overline{\delta t^*_{\text{path}}}}{\pi t^*_{\text{path}}} = \frac{600 * 0.01 \text{ s}}{\pi * 30 \text{ s}} \approx 0.06,$$

where $\overline{\delta t^*_{\text{path}}} = \delta t^*_{\text{path}}/\sqrt{4} = 0.01$ as there are at least four rays going through each cell that we accept for interpretation.

[38] As expected data obtained with spectral ratio procedures is quite prone to errors, but we can see with this first rough estimate that although the error is quite large, measured variations in Q_P for anomalies that are interpreted are about one order of magnitude larger. The magnitudes of the variations are even greater if we consider the differences between high-Q_P and low-Q_P anomalies, which are used for the model interpretation (section 4.4).

[39] To further check the robustness of the real data *Vp* inversion we performed a test by shifting down the initial hypocenter location by 10 km and verified that the final model closely resembled the unperturbed data inversion.

[40] A final observation, which will be extended in the next section, relevant for confirming the models' reliability, is that there is quite a good agreement between Q_P and V_P anomalies as would be expected if temperature is the main quantity controlling V_P and Q_P variations.

4. Discussion

4.1. Relationship Between *V* and *Q* Anomalies and Thermodynamic Quantities

[41] Several studies have found a direct correlation between velocity and attenuation (or Q) anomalies in some regions of the mantle where temperature is the controlling parameter [e.g., *Romanowicz*, 1995; *Roth et al.*, 2000]. As we have already mentioned, Q has larger sensitivity than V with respect to temperature. Theoretical calculations [*Karato*, 1993] and experimental work (e.g., see the review by *Karato and Spetzler* [1990, and references therein]) have shown that anelasticity significantly increases the temperature derivative of velocity. By incorporating the effect of anelasticity due to viscous flow, large variations of seismic wave velocities can be explained by small variations in temperature [*Karato*, 1993; *Karato and Karki*, 2001]. The above considerations can be expressed in mathematical terms as [*Karato*, 1993] $\partial \ln V/\partial T = \partial \ln V_0/\partial T - (Q^{-1}/\pi)(H^*/RT^2)$, where H^* is the activation enthalpy, R is the gas constant, Q the quality factor (frequency independent), T temperature, V_0 a reference seismic velocity. The first term on the right side expresses the elastic temperature dependence on T due to thermal expansion, while the second expresses the anelastic dependence of V versus T through Q. In more direct terms, we expect that if there are strong temperature variations in an area of interest, then there will be lateral variations of V that follow variations in Q. Most laboratory measurements on temperature dependence of V are done at frequencies that are very high ($\sim$ 1 Mhz) compared to seismic frequencies and are actually only measuring the first (elastic) term [*Karato*, 1993]. Such results carry the important implication that any calculation, or even a qualitative analysis, of temperature distribution starting from seismic velocity tomography models needs to take into account anelastic effects, thus measures of Q.

[42] Another important aspect to be considered in subduction zones is the possible presence of fluids within regions of low-Q and low-V as, for example, the mantle wedge. Fluids, in particular water or hydrogen, can decrease mantle rock viscosity thus decreasing Q and V. Finally, chemical composition heterogeneities can also determine lateral changes in V and Q distribution. This could happen where, for example, there is a heterogeneity of oceanic and continental lithosphere.

[43] Establishing in a quantitative way the relative contribution of temperature, water content and chemical composition variations to variations of V and Q is not an easy task and it is outside the scope of this paper.

4.2. Seismic Velocity and Other Geophysical Measurements in the Area

[44] Before describing the main features of the V_P and Q_P models from this study we briefly overview relevant results from previous studies. Starting from elastic and anelastic data, *Goes et al.* [2000] derived a model for temperature distribution in Europe's shallow mantle (50–200 km depth), and proposed that seismic velocity anomalies are mainly controlled by temperature. In their model, temperatures in the Tyrrhenian Basin are among the highest, approaching the dry solidus, and differences between temperatures derived from *Vp* and *Vs* are explained as possibly due to partial melting.

[45] Heat flow measurements have shown a pattern parallel to the Calabrian Arc increasing toward the Tyrrhenian sea up to values exceeding 200 mW/m^2 [*Della Vedova et al.*, 1991a, 1991b; *Zito et al.*, 2003] (Figure 1). Also, surface wave inversion studies find progressive thinning of the crust and of the lithosphere and a very shallow crust-mantle transition zone, down to less than 10 km deep, in the southern Tyrrhenian [e.g., *Calcagnile and Panza*, 1981] (inset in Figure 1). Tomographic models from inversion of surface wave dispersion curves constrained by other geophysical data, show a variable topography of the asthenosphere in the Calabrian Arc subduction zone [*Pontevivo and Panza*, 2006; *Panza et al.*, 2007].

[46] There are several published 2-D and 3-D body wave velocity models for the area, at all scales: teleseismic [e.g., *Lucente et al.*, 1999; *Cimini and De Gori*, 2001], regional

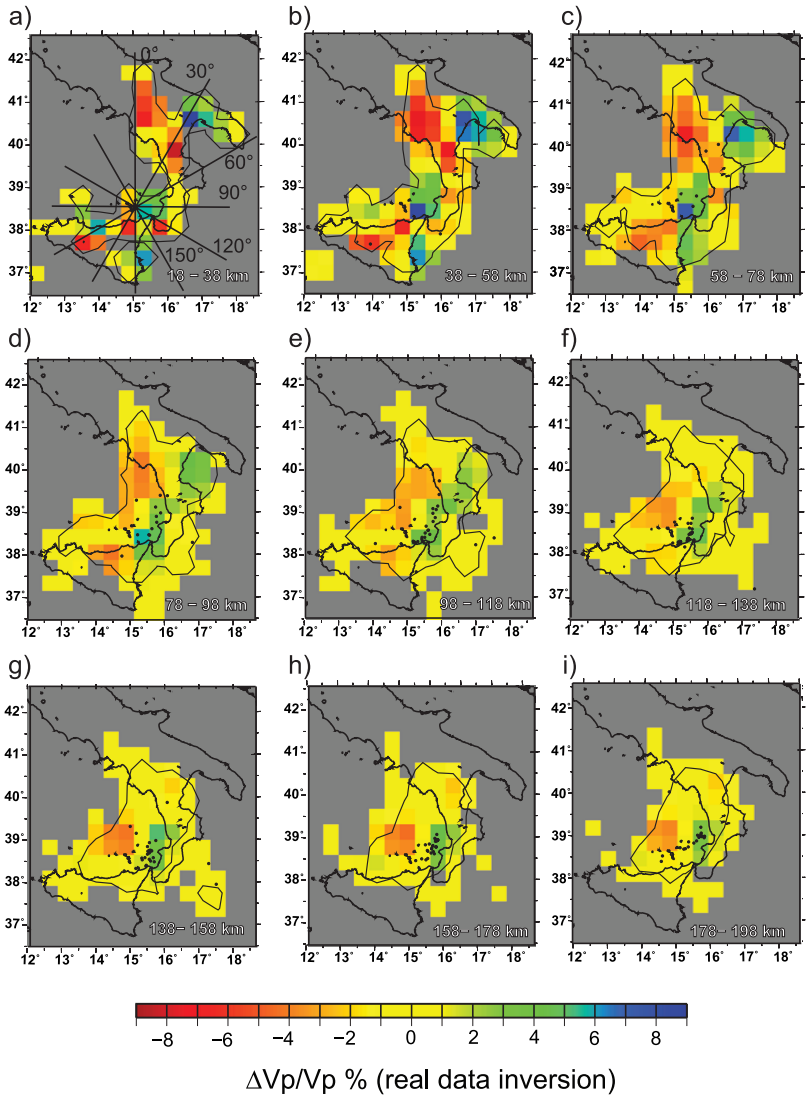

Figure 10. Maps of the 3-D V_P model obtained by real data inversion. In Figure 10a, lines represent profiles for cross sections. Black circles represent hypocenters relocated in the 3-D V_P model.

earthquake traveltime data [e.g., *Mele et al.*, 1998; *Piromallo and Morelli*, 2003; *Spakman and Wortel*, 2004], and local crustal earthquakes [*Di Stefano et al.*, 1999]. Recently, *Montuori et al.* [2007] performed a 3-D inversion of teleseismic waves including recordings from ocean bottom seismometers. The most recent 3-D velocity inversions of the area based on body wave recordings from local deep slab events were performed by *Chiarabba et al.* [2008] and *Neri et al.* [2009]. All authors find a high-velocity anomaly which is associated with the subducting slab.

[47] Several regional- and global-scale models show a low-velocity anomaly under the southern Apennines, found already above 200–250 km [e.g., *Spakman*, 1991; *Piromallo and Morelli*, 1997, 2003; *Cimini and De Gori*, 2001]. The interpretation of this last anomaly has been controversial, and explained mainly as subducting continental lithosphere, as lithosphere attenuated by a hot asthenospheric wedge, or as mobile asthenospheric mantle due to shallow slab window or detachment. Furthermore, *SKS* splitting analysis has shown a fast direction following the whole Calabrian Arc, below the southern Apennines, interpreted as mantle flow below the slab [*Baccheschi et al.*, 2007].

[48] Previous attenuation studies proposed that the high-velocity Ionian slab serves as a waveguide, transmitting efficiently high-frequency, high-amplitude body waves from mantle earthquakes toward the surface [*Mele*, 1998]. The same author and coworkers find that *S* waves traveling toward the north of the slab are very attenuated and

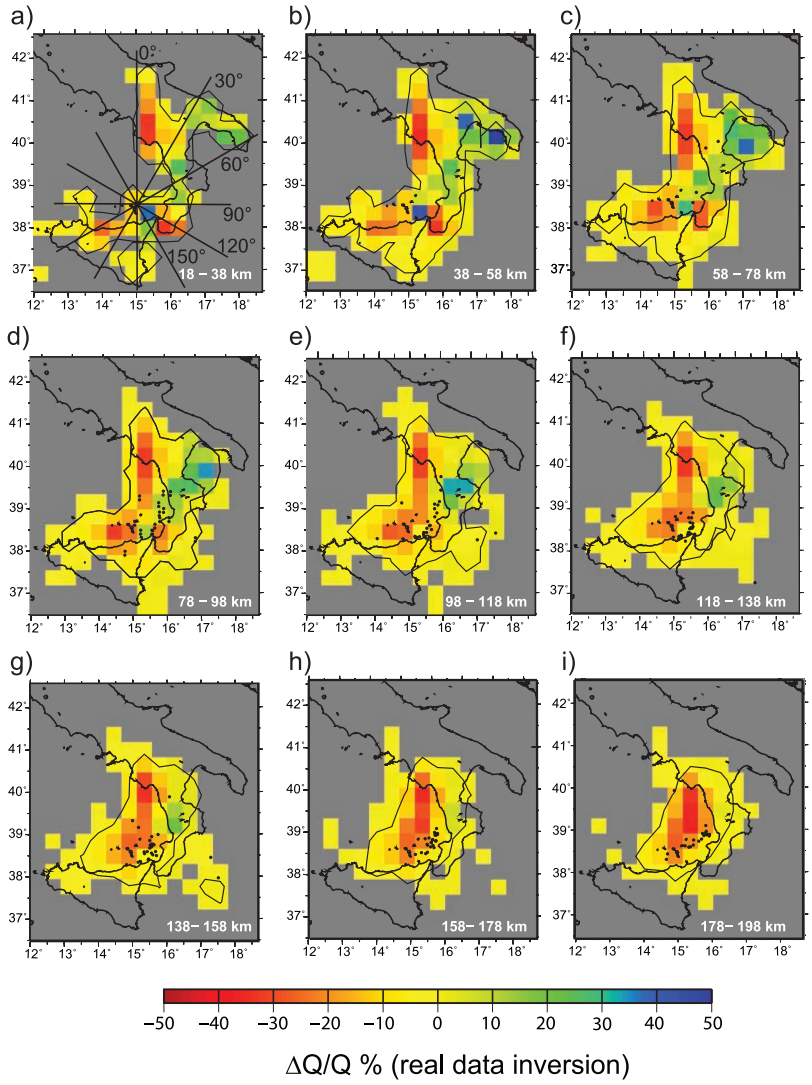

Figure 11. Maps of the 3-D Q_P model obtained by real data inversion. Profiles in Figure 11a are the same as in Figure 10.

hypothesize a zone of partially molten material beneath the Tyrrehnian Sea [*Mele et al.*, 1997]. Very recently a paper presenting V_P, V_P/V_S and Q_P models of the Southern Tyrrhenian subduction zone coming from inversion local events was published [*Chiarabba et al.*, 2008]. This paper is somewhat complementary to ours both in methodology and scope. A comparison will be presented in section 4.4.

[49] Another identified feature is a low-V_P area surrounding the slab. Recently this anomaly pattern has been identified by anisotropy studies from *SKS* splitting [*Civello and Margheriti*, 2004] and traveltime tomography [*Montuori et al.*, 2007] and interpreted respectively as mantle flow around the western edge of the slab or around the slab in ringlike fashion.

[50] Finally, it is important to mention studies of the complex Plio-Quaternary magmatism in the Tyrrhenian Sea and nearby regions, which show a broad compositional variation, pointing to a strongly heterogeneous upper mantle and a complex geodynamic evolution of the area [see, e.g., *Peccerillo*, 2005, and references therein]. An open issue in petrological studies of southern Tyrrhenian magmatism is the coexistence of IAB and OIB magmas and the way such magmas are generated.

4.3. Results: Description of V_P and Q_P Models

4.3.1. Maps

[51] Starting from the deepest layer (178–198 km section) we find a low-V_P anomaly (*LVA*) just north-northeast

of the Aeolian Arc and a low-Q_P anomaly (*LQA*), which encompasses the Arc and extends north (Figures 10i and 11i). Both the *LQA* and *LVA* are centered at a position underlying the eastern part of the Marsili Basin (Figure 1). The next recognizable feature in the V_P model is a high-V_P anomaly (*HVA*) adjacent to the *LVA* and east-southeast of it. This pattern is visible at shallower depths and starting from the map between 138 and 158 km also a high-Q_P anomaly (*HQA*) is present. The *LQA* and *LVA* extend toward north and south (e.g., Figures 10e and 11e), and the *HVA* and *HQA* extend in the northeast direction (Figures 10d and 11d). At 58–78 km depth two *HVA* are visible under Apulia and north of Calabria (Figure 10c), separated by a *LVA*, while the *HQA* still appears as a continuous body (Figure 11c), but this difference could also be due to the stronger regularization in the Q_P inversion compared to the V_P inversion, or a smearing effect as discussed in section 3.3. Also, at the same depth, the *LVA* and *LQA* start to appear as composed by two separate parts, one extending under the southern Apennines and one toward northern Sicily. Between 18 and 58 km depth a *LQA/LVA* appears under the southern tip of Calabria (Figures 10a, 10b, 11a, and 11b).

[52] For both V_P and Q_P models some transition zones, where there are strong lateral variations, are visible (Figures 10 and 11). In particular, beneath the Aeolian Arc, down to about 200 km depth, there is a clear passage from a *HVA* to a *LVA* going from E to W. Seismicity is included within the *HVA* or just next to it, and is not found under the western part of the Aeolian islands (west of about the 15° E meridian). The *HVA/LVA* (and average Q_P/*LQA*) transition zone continues to the south and encompasses a volume just east of mount Etna. Another interesting strong transition zone is the one going from a *HQA/HVA* (Apulian/Adriatic lithosphere) toward a *LQA/LVA* in the NW direction (southern Apennines). Finally, we observe a difference between Q_P and V_P models: in the most superficial layers (Figures 10a, 10b, 11a, and 11b) the *HQA* seems continuous, extending east (Apulian/Adriatic lithosphere), while the *HVA* is interrupted at more superficial depths by a the *LVA* below Calabria.

4.3.2. Cross Sections

[53] The north-south section in the V_P model (Figure 12a) shows a continuous *HVA* extending in the north direction down to 140 km. A *LVA* is also visible starting at about 120 km depth and rising in channel fashion toward the north. The same section for Q_P (Figure 12b) shows the *HQA* down to 100 km and a broad *LQA* starting from near the Benioff plane, below 200 km depth, and rising in the north direction, similarly to the *LVA*. The section at 30° shows for the V_P model (Figure 12c) a small *HVA* in the northeast, a small *HVA* between Stromboli and Calabria, and a *LVA* starting at about 220 km depth and rising vertically toward Stromboli and Etna. Similarly for Q_P (Figure 12d), but the *HQA* is more faint and the *LQA* more broad and defined in the southwest direction. The sections at 60° (Figures 12e and 12f) well show the *HQA* and *HVA* dipping southwest. The *LVA* is faint while the *LQA*, starting from near the Wadati-Benioff zone, where there is intense seismicity, extends in the southeast direction toward northern Sicily. The west-east sections (90°; Figures 12g and 12h) show a steeply dipping *HVA* and smaller *HQA* and two *LVA*s which appear as rising vertically from below the Aeolian Arc and below the southern tip of Calabria, respectively. In the 120° sections (Figures 12i and 12j) the separation between the two *LQA*s and the corresponding *LVA*s by a *HQA*/*HVA* volume is quite evident. Finally, the sections at 150° (Figures 12k and 12l) shows again for the V_P model the dipping HQA/*HVA* and its adjacent *LQA*/*LVA* below the Aeolian Arc.

[54] One factor to be kept in mind for the interpretation of anomalies found in the V_P and Q_P models is that due to a high value of the smoothing regularization parameter used in the inversion for Q_P, the anomalies will be more smeared in the Q_P model than for the V_P model. Smearing is possible, as shown by the synthetic tests, due to station event geometry and to the use of relative residuals (section 3.3). Furthermore, the choice of a high value of the damping parameter in the LSQR algorithm for the Q_P inversion leads to a underestimation of the intensity of the anomalies. Finally, values for both V_P and Q_P in cells in the deepest part of the models are greatly underestimated, due to earthquake distribution and smaller number of rays passing through these cells, as also shown by the synthetic tests (section 3.3).

4.4. Interpretation

[55] We now discuss the geophysical meaning of the anomalies found in the 3-D Q_P and V_P models and suggest some possible implications that can improve our understanding of the southern Tyrrhenian-Apennines system. As we have seen in section 2.3 scattering is not a main factor in the attenuation of seismic waves in this study, at least in the considered frequency range and at the scale of this work, so we interpret Q_P anomalies as dependent on the degree to which elastic energy is converted into heat (anelasticity).

[56] The good agreement between V_P and Q_P anomalies confirms the important role of anelasticity in this study and we will interpret lateral Q_P and V_P variations as mainly caused by lateral temperature variations and the presence of fluids or melt (section 4.1). Chemical heterogeneities could be invoked where there is a different distribution of V and Q anomalies, although, as mentioned earlier, establishing quantitatively how the different factors determine variations of Q and V is a difficult task and it is outside of the scope of the present work. In fact, there is a resolved part of the models, underlying part of Calabria in the top 80 km approximately at latitude 39.5° and longitude 16.5°, where Q_P and V_P have different behavior since we find there a *LVA* and an average Q/*HQA*. This different behavior could be explained by lateral variations in chemical composition, in particular this rock volume could represent a transition zone between, continental (Apulian/Adriatic) and, oceanic (Ionian) lithosphere. The *LVA* is in fact part of a continuous low-*Vp* body going from the Southern Apennines to Sicily which is also found in other *Vp* tomography models [*Di Stefano et al.*, 1999; *Chiarabba et al.*, 2008] and corresponds to a strong minimum of Bouguer values which implies the presence of low-density rock, and possibly that continental crust is involved in the subduction process [*Di Stefano et al.*, 1999].

[57] In general the distribution of persistent *LQA*/*LVA* anomalies agree with measurements of the area's heat flow, confirming the important role of temperature in determining lateral Q_P and V_P variations. In particular the root of the

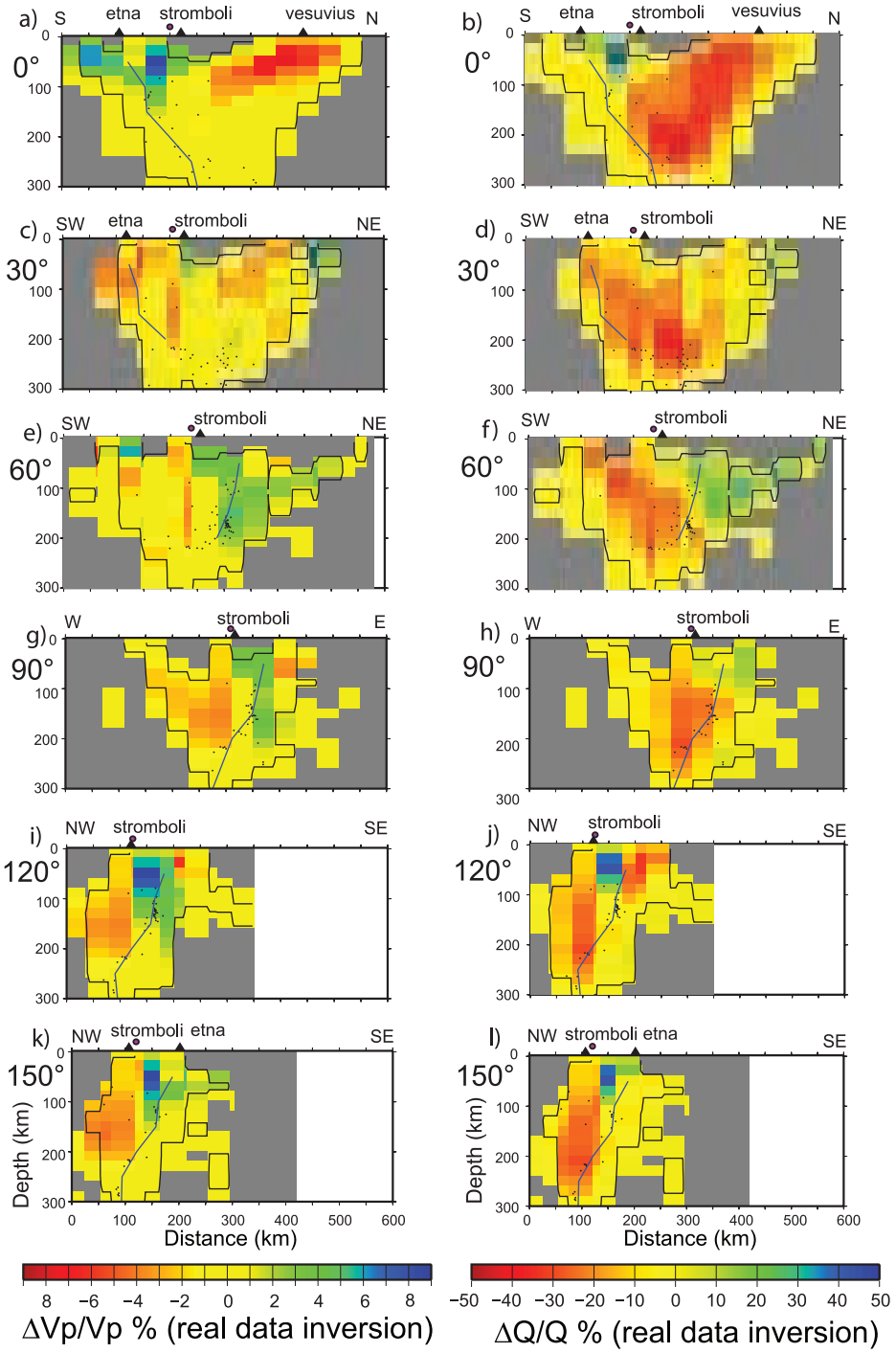

Figure 12. Cross sections of 3-D V_P and Q_P models (real data). Sections are along profiles shown in Figures 10a and 11a. Sections are every 30°, where the angle is measured in the clockwise direction starting from north, and they all go through the point shown as a purple dot.

low-Q_P/low-V_P volume found north of the Aeolian islands corresponds to an area where there is very high heat flow (over 200 mW/m^2; see Figure 1) [*Zito et al.*, 2003], very shallow asthenosphere (up to 10 km [*Pontevivo and Panza*, 2006]) and is located below the eastern part of the Marsili Basin. We are unable to establish the extension of this volume given our station event distribution, especially in the NW direction and at depth.

[58] The main *HVA* containing most of the deep seismicity starting from Southern Calabria and extending in the northeast direction and well visible down to about 220 km, better delineates the steep subducting Ionian lithosphere (Figures 10 and 12, left), and partially corresponds to a volume of high-Q_P (Figures 11 and 12, right). Although the synthetic tests show smearing along the SW-NE direction, the fact that transmission of *P* and *S* waves from deep slab events to Apulia is very efficient, leads us to think that, in agreement with *Mele* [1998], at the scale of the considered wavelengths (about 1–10 km) the waves are sampling a rock volume (the subducting slab) having continuous rheological and physical properties.

[59] The main *LQA*/*LVA* volume adjacent to the slab, found between 100 and 200 km depth, we interpret as the mantle wedge proper. From the mantle wedge there are branches of low Q_P/low V_P which reach crustal depths, and could possibly represent pathways for melt and water as will be discussed in greater depth later. Waves going through these volumes of low-Q_P/low-V_P rock are very attenuated: *P* waves going from the slab to stations in the northern part of the study area have a lower frequency content and *S* waves are not visible in many cases as also shown by *Mele* [1998] and confirmed by our inspection of the waveforms.

[60] To better understand the meaning of this 3-D attenuation and velocity structure we will now continue the interpretation of other features found in the model starting from the forearc region in the southern part and going north.

[61] 1. Going west from the SE edge of the model, where we find a high-V_P anomaly (average *Q*) there is a transition evident at all depths in the V_P model, which we interpret as the passage from the old, cold and fast (as referred to seismic wave velocities) Ionian oceanic lithosphere, to the African continental lithosphere. Interestingly, within the transition zone we find Mount Etna, so we infer that the hot material in the forearc region is related to the feeding system of Mount Etna. The superficial low-Q_P (low-V_P) anomaly under southwestern Calabria we interpret as asthenosphere overlying a volume of fast rock (Ionian lithosphere), in agreement with the interpretation of models coming from the inversion of surface wave dispersion data [*Pontevivo and Panza*, 2006]. This volume of attenuating slow rock seems separated from the rest of the mantle wedge (see section at 120°; Figures 12i and 12j), by a volume of faster less attenuating lithosphere. Furthermore, the position of the shallow *LQA*s nearby Mount Etna (southwestern Calabria, northern Sicily) agree with possible sites of slab windows, as proposed in the model by *Gvirtzman and Nur* [1999], which explains the volcano's relation to the subduction zone. This model suggests that the molten superficial material in the forearc region feeding Mount Etna is not originated in the mantle wedge, but by suction of mantle material from under the African plate, thus the OIB-type magmatism found at Mount Etna (Figure 1). A word of caution is needed regarding the *LQA*/*LVA* nearby northern Sicily since we have seen in the spike test that smearing can cause a similar (artificial) anomaly (section 3.3).

[62] 2. Continuing to the north, we still find the E-W transition zone, now also evident in the Q_P model down to 58–78 km and in the V_P model down to all depths, dividing the volume under the Aeolian Arc and separating the eastern Aeolian islands (Stromboli and Panarea) from the rest. This transition area corresponds to an important NNW-SSE tectonic line (Tindari-Letojanni (TL); see Figure 1) traversing Salina, Lipari and Vulcano, which has been interpreted as the southern edge of the Ionian slab [*Marani and Trua*, 2002, and references therein]. Furthermore, *Mele* [1998] shows that *S* waves traveling from the slab through the sector west of the TL are either absent or greatly attenuated. The TL divides the Aeolian Arc in sectors that show different characters, for example, active volcanism is restricted only below the central-eastern sector, deep slab seismicity is observed only below the eastern sector, and there are along-arc variations in magma composition [*Peccerillo*, 2005].

[63] 3. Continuing to the eastern tip of the model, the area of *HQA*/*HVA* under Apulia well corresponds to thick continental lithosphere (>90 km [*Pontevivo and Panza*, 2006]) and low heat flow values [*Zito et al.*, 2003]. From Apulia, going in the NW direction we have the next important transition zone, with a sharp change to low Q_P/low V_P under the southern Apennines. This *LQA*/*LVA* anomaly corresponds to a broader low-V_P region found in other larger-scale tomographic models [e.g., *Lucente et al.*, 1999], as mentioned in section 4.2, extending from the Northern Apennines to Calabria along the Tyrrhenian coast. Heat flow measurements in sites along the southern Apennines have shown values which are very high for a continental area [*Mongelli et al.*, 1996]. Furthermore, a study on helium isotope ratios measured in sites along the southern Apennine chain shows a release of a large amount of mantle helium [*Italiano et al.*, 2000]. The authors, through geophysical arguments, explain such anomalous gas fluxes as caused by uprise of mantle wedge asthenosphere which produces melt rising into the crust along lithospheric faults. On the basis of these results we interpret this shallow *LQA* found below the southern Apennines as caused by presence of shallow asthenosphere and, at more superficial depths, by partially molten rock.

[64] 4. Similarly from what we have found for the southwestern part of the model with the TL fault system, a strong Q_P variation happens across an area which includes superficially the onshore Sangineto structure in Calabria (SAN in Figure 1) that, together with other structures at sea (NW-SE trending), has been suggested as being the northern edge of the Ionian slab [*Marani and Trua*, 2002, and references therein]. The existence of shallow asthenosphere can be explained by a (shallow depth) slab window below the southern Apennines chain [*Patacca and Scandone*, 1989; *Amato et al.*, 1993; *Lucente et al.*, 1999], or slab detachment [*Spakman and Wortel*, 2004, and references therein]. Furthermore, the position of the low-Q_P anomaly corresponds to the area proposed by other authors as site for the window (see, e.g., cell B5 of *Pontevivo and Panza* [2006]).

[65] In summary, the pattern of *LQA*/*LVA* could be explained by the presence of shallow asthenospheric mate-

rial flowing around the Ionian slab's edges, in agreement with the *Gvirtzman and Nur* [1999] model, as proposed by *Marani and Trua* [2002] to explain the rapid vertical growth of the Marsili volcano.

[66] More insight on the material/fluid flow in the Calabrian Arc subduction zone can come from the observation that the mantle wedge is closest to the Wadati-Benioff zone at a depth where we have intense seismicity (100–200 km depth; see Figure 12). This close spatial correspondence between intermediate-depth seismicity and the *LQA/LVA* could be related to a slab dehydration process, where fluids are migrating from the slab into the mantle wedge. Through this process the melting temperature of rocks in the mantle wedge is lowered and at the same time the rock in the slab becomes more brittle. Slab embrittlement through dehydration reactions in oceanic lithosphere has been proposed as mechanism to explain the occurrence of intermediate-depth earthquakes [see, e.g., *Hacker et al.*, 2003, and references therein]. A link between a strong low-Q_P anomaly in the mantle wedge, seismicity at 100–200 km depth, slab dehydration, and mantle melting has been observed by *Schurr et al.* [2003] for the Andean subduction zone. The same authors, starting from the pattern of low-Q_P regions, reconstructed the fluid and melt pathways through the mantle wedge, which cover large lateral distances. In a similar way we can interpret the low-Q_P/low-V_P regions branching from the mantle wedge proper, as pathways for fluid and melt transport. The branch going from the Ionian slab mantle wedge toward Vesuvius could help explain why there are strong geochemical affinities between the subduction-related components of magmas from Vesuvius and Stromboli [*Peccerillo*, 2001]. In fact, this strong compositional similarity has been explained by the existence of a common upper mantle source, for Stromboli and Vesuvius, which is likely to be contaminated by the Ionian plate sediments and fluids [*Peccerillo*, 2001, and references therein]. On the other hand, the fact that there is coexistence of IAB and OIB magmas from volcanoes within this subduction zone, possibly points to a complex flow and multiple mantle magma sources. A further exploration of these topics can be the subject of a future work.

[67] We have previously mentioned a recent work by *Chiarabba et al.* [2008] (hereinafter referred to as C). In general, for the *Vp* models we find a good agreement between ours and C, although their resolved volume is more extended due to a higher number of traveltimes used (7828). There is some agreement but also consistent differences in the Q_P models both in the extension of the resolved part and in the anomaly distribution. In both models we find the high-Q_P anomaly associated with the slab and the low-Q_P anomaly in northern Sicily. On the other hand, other parts of the Q_P model in C disagree with their V_P model and with the heat flow distribution, leading to some inconsistencies in the interpretation. For example, in C the existence of a slab interruption (window) below the southern Apennines/northern Calabria, which we also propose as a possible interpretation, is inferred only from traveltime data and is not supported by the Q_P model, as there are high-Q_P values. On this ground it is difficult to substantiate that there are high temperatures, and thus the presence of asthenospheric material. Another main discrepancy is in the Q_P values found north of the Aeolian Arc, where there are very high heat flow values [*Della Vedova et al.*, 1991a, 1991b; *Zito et al.*, 2003] and where we find a strong low-Q_P anomaly which corresponds to the mantle wedge, while in C there is the continuation of a high-Q_P anomaly corresponding to the slab. This area of low-V_P, high-Q_P and high-V_P/V_S is explained in C by the presence of magmatic fluids at 150 km depth, as we also propose, but it is hard to reconcile the presence of fluids, and thus low viscosity, with high-Q_P values. Such significant differences in the two models can be explained by the number of t^* data used (2100 in our study versus 1151 waveforms in C), and the different methods applied (spectral ratio versus absolute spectrum method).

[68] In summary, the position of the anomalies in the V_P and Q_P models, their comparison with known important tectonic structures, and the location of seismicity, help us understand the position and state of the slab and its relation to the mantle wedge. The slab is delimited by two important tectonic structures which include the SAN onshore in the N-NE and the TL in the S-SW and could be the site for windows or detachment of the Ionian slab, and explain the presence of asthenosphere at superficial depths. Furthermore, efficiency of transmission of *P* and *S* waves from slab events points to discontinuity of rock physical properties across TL toward western Sicily and across SAN toward the north, and continuity for waves going toward Apulia, at least for the wavelengths considered in this study (about 1–10 km).

[69] We are aware of the resolution limits of our models, and of the possibility of some artifacts in the inversion procedure (especially for the Q_P inversion as shown in section 3.3). However, as we have been rather conservative in our choice of inversion regularization and model parameterization, we are confident that the interpreted anomalies, found on the same scale and position of anomalies successfully retrieved in the synthetic tests (section 3.3), come from very strong variations of Q_P and V_P, and thus are reliable. Finally, observation of *P*- and *S* wave transmission (this study and *Mele* [1998]) gives an independent evidence of strong variations in Q_P (Qs) and the existence of very low Q_P (Qs) areas.

5. Conclusions

[70] In this work, starting from local deep earthquake data, we derived crustal and upper mantle 3-D attenuation and velocity models below the Calabrian Arc subduction zone. The data used for the inversion, traveltimes and spectral ratios, come from short-period (natural period 1s) seismometers recordings (INGV permanent network). Synthetic tests, ray distribution and coverage show which part of the models are reliable and prone to interpretation. Furthermore, the good agreement of the Q_P and V_P anomalies and with other geophysical data, increases our level of confidence for the models. The studied area covers a volume part of a geodynamic system which includes the Tyrrhenian Basin and the Apennines. We find the following.

[71] 1. A main low-Q_P/low-V_P anomaly located, between 100 and 200 km depth, below the eastern part of the Marsili Basin where there are very high heat flow values, and branching out to reach Moho depths in the direction of

the Vesuvius and the southern Apennines, toward northern Sicily and toward the southwestern tip of Calabria and the Ionian Sea. It appears that the anomaly below Calabria/Ionian Sea could be separated by a body of high-Q_P/high-V_P from the main deep low-Q_P/low-V_P anomaly, but a study with higher resolution is necessary to confirm this. The part of the main low-Q_P/low-V_P anomaly found in proximity of the Wadati-Benioff zone where there is intense seismic activity (150–200 km depth), is interpreted as the mantle wedge. The position of the anomaly and its elongated form can be explained by dehydration of the slab (and its embrittlement) where fluids lower the melting temperature of the overlying asthenosphere. Then the low-Q_P anomaly is caused by presence of fluids and melt, and the branches could represent pathways for fluid and melt migration through the mantle wedge up to crustal depths. This pattern can help in imaging the flow of hot mobile material in this area and to better understand its relation to volcanism. In particular, it can help our understanding of the strong geochemical affinities between magmas found at Stromboli and Vesuvius.

[72] 2. A high-V_P (to a lesser extent Q_P) anomaly representing the subducting Ionian lithosphere and containing seismicity. This steeply descending *HVA* (partially *HQA*) volume is seen down toward the bottom of the model (about 200 km), is limited by volumes of *LVA/LQA* and by transition zones corresponding to important tectonic structures (see below).

[73] 3. A high-Q_P/high-V_P anomaly representing the thick Adriatic continental lithosphere. This volume of rock together with the subducting Ionian lithosphere appear in the models as a continuous body forming a waveguide in which the high-frequency part of the wavefield from deep events can propagate.

[74] 4. Transition zones across which we have strong variations of Q_P (between 50 and 100%) and V_P (up to 10%), corresponding to important tectonic lines which have been proposed as the southwestern and northeastern limits of the oceanic Ionian lithosphere. Interestingly, the position of the low-Q_P/low-V_P anomalies correspond to sites for slab windows or slab detachment hypothesized by other authors and by the *Gvirtzman and Nur* [1999] model to explain Mount Etna's relation to the subduction zone and the rapid vertical growth of the Marsili volcano [*Marani and Trua*, 2002].

[75] Considering the scale of the present work, and the limits of our models stemming both from a less than ideal station event geometry and from the approximations in the employed methodology, this 3-D Q_P model, together with the V_P model, can be a useful starting point to better define the slab-asthenosphere geometry and its relation to the Plio-Quaternary volcanism present in southern Italy.

Appendix A: Calculation of the Spectral Ratio of Equation (2)

[76] Starting from equation (1), $A_{ij} = A_{0j}(f; \theta_i, \varphi_i)\, S_i(f)\, A_{\mathrm{INS}}(f)\, B_{ij}(f)$, we make some simplifying hypotheses, as follows.

A1. Hypothesis I

[77] The attenuation function can be approximated by a frequency-independent Q in the frequency band of interest (1–5 Hz) $Q(f, r) = Q(r)$.

A2. Hypothesis II

[78] The source function can be decomposed into a spatial and a time (frequency) part $A_{0j}(f; \theta, \varphi) = A_{0j}(\theta, \varphi)\, A_{0j}(f)$. This is correct in our case, as the source directivity effects are negligible since selected earthquakes have rupture dimensions that are small in comparison to the length of the wave path (M < 4).

[79] Then equation (1) becomes

$$A_{ij} = A_{0j}(\theta, \varphi) A_{0j}(f) S_i(f) A_{\mathrm{INS}i}(f) G_{ij} \exp(-\pi f t^*_{ij}). \quad \text{(A1)}$$

A3. Hypothesis III

[80] The site effect transfer function is the same for all stations in the chosen frequency band (1–5 Hz). In other words, we are assuming that, in first approximation, the site transfer functions show the same frequency dependence for *Pn*.

[81] In order to decrease the number of unknowns in the problem, we use the reduced spectral ratio technique where, for each seismic event, we divide the amplitude spectra recorded at one station by the average (log) spectrum, $\overline{lnA_j}$, of all the recorded amplitudes from that event [*Evans and Zucca*, 1988]:

$$lnA_j = \sum_{i=1}^{N_j} lnA_{ij}/N_j, \quad \text{(A2)}$$

where N_j is the number of stations recording event j.

[82] Ideally, we would use, as denominator in the spectral ratio, spectra of signals recorded at a reference station located outside the study area. Though we do not have such a station, we do have the advantage of greater stability of the average spectrum.

[83] After applying *ln* to the terms of equation (A1), considering equation (A2), and eliminating common terms, we obtain a linear equation

$$lnA_{ij} - \overline{lnA_j} = C_{ij} + f\pi(\overline{t^*_j} - t^*_{ij}) = C_{ij} + \pi f \Delta t^*_{ij}, \quad \text{(A3)}$$

where $\overline{t^*_j} = (1/N_j) \sum_{i=1}^{N_j} t^*_{ij}$ is the average t^* for event j. Variable Δt^*_{ij} is often called relative t^*.

[84] **Acknowledgments.** The authors would like to thank Paolo Favali, Giuliana Mele, Aybige Akinci, Caterina Montuori, and, particularly, Francesco Frugoni for their helpful comments. Also, thanks go to Roberto Tardini for his help in assembling the data set, the Laboratorio Grafica e Immagine I.N.G.V. for their help with Figure 1, and Laura Beranzoli for her support. Figures 3–12 were generated using GMT mapping tools [*Wessel and Smith*, 1991]. We are grateful to Harley Benz for making his code FDTOMO available. Finally, we would like to thank the associate editor, Giancarlo Neri, and an anonymous reviewer for their helpful suggestions.

References

Amato, A., B. Alessandrini, and G. B. Cimini (1993), Teleseismic wave tomography of Italy, in *Seismic Tomography: Theory and Practice*, edited by H. M. Iyer and K. Hirahaha, pp. 361–397, CRC Press, Boca Raton, Fla.

Argnani, A. (2000), The southern Tyrrhenian subduction system: Recent evolution and neotectonic implications, *Ann. Geofis.*, *43*, 585–607.

Baccheschi, P., L. Margheriti, and M. S. Steckler (2007), Seismic anisotropy reveals focused mantle flow around the Calabrian slab (Southern Italy), *Geophys. Res. Lett.*, *34*, L05302, doi:10.1029/2006GL028899.

Barba, S., R. Di Giovambattista, and G. Smeriglio (1995), Italian seismic databank allows on-line access, *Eos Trans. AGU*, *76*(9), 89, doi:10.1029/95EO00042.

Benz, H. M., B. A. Chouet, P. B. Dawson, R. A. Kahr, and J. A. Hole (1996), Three-dimensional *P* and *S* wave velocity structure of Redoubt Volcano, Alaska, *J. Geophys. Res.*, *101*, 8111–8128, doi:10.1029/95JB03046.

Bianco, F., E. Del Pezzo, M. Castellano, J. Ibanez, and F. Di Luccio (2002), Separation of intrinsic and scattering attenuation in the Southern Apennine zone, Italy, *Geophys. J. Int.*, *150*, 10–22, doi:10.1046/j.1365-246X.2002.01696.x.

Calcagnile, G., and G. F. Panza (1981), The main characteristics of the lithosphere-asthenosphere System in Italy and surrounding regions, *Pure Appl. Geophys.*, *119*, 865–879, doi:10.1007/BF01131263.

Catalano, R., C. Doglioni, and S. Merlini (2001), On the Mesozoic Ionian Basin, *Geophys. J. Int.*, *144*, 49–64, doi:10.1046/j.0956-540X.2000.01287.x.

Cheng, H.-X., and B. L. N. Kennett (2002), Frequency dependence of seismic wave attenuation in the upper mantle beneath the Australian region, *Geophys. J. Int.*, *150*, 45–57, doi:10.1046/j.1365-246X.2002.01677.x.

Chiarabba, C., L. Jovane, and R. Di Stefano (2005), A new view to the Italian seismicity using 20 years of instrumental recordings, *Tectonophysics*, *395*, 251–268, doi:10.1016/j.tecto.2004.09.013.

Chiarabba, C., P. De Gori, and F. Speranza (2008), The southern Tyrrhanian subduction zone: Deep geometry, magmatism and Plio-Pleistocene evolution, *Earth Planet. Sci. Lett.*, *268*, 408–423, doi:10.1016/j.epsl.2008.01.036.

Cimini, G. B. (1999), P wave deep velocity structure of the southern Tyrrhenian subduction zone from nonlinear teleseismic traveltime tomography, *Geophys. Res. Lett.*, *26*, 3709–3712, doi:10.1029/1999GL010907.

Cimini, G. B. (2004), Tomographic studies of the deep structure of the Tyrrhenian-Apennine system, in *From Seafloor to Deep Mantle: Architecture of the Tyrrehanian Backarc Basin*, *Mem. Descr. Carta Geol. d'It*, vol. XLIV, edited by M. P. Marani, F. Gamberi, and E. Bonatti, pp. 15–28, Agenzia per la Prot. dell'Ambiente e per i Serv. Tec. (APAT), Rome.

Cimini, G. B., and P. De Gori (2001), Nonlinear P wave tomography of subducted lithosphere beneath the central-southern Apennines (Italy), *Geophys. Res. Lett.*, *28*, 4387–4390, doi:10.1029/2001GL013546.

Civello, S., and L. Margheriti (2004), Toroidal mantle flow around the Calabrian slab (Italy) from SKS splitting, *Geophys. Res. Lett.*, *31*, L10601, doi:10.1029/2004GL019607.

D'Agostino, N., A. Avallone, D. Cheloni, E. D'Agostino, S. Mantenuto, and G. Selvaggi (2008), Active tectonics of the Adriatic region from GPS and earthquake slip vectors, *J. Geophys. Res.*, *113*, B12413, doi:10.1029/2008JB005860.

Della Vedova, B., F. Mongelli, G. Pellis, and G. Zito (1991a), Campo regionale del flusso di calore nel Tirreno, in *Atti del 10° GNGTS*, pp. 817–825, Esagrafico, Rome.

Della Vedova, B., F. Mongelli, G. Pellis, P. Squarci, L. Taffi, and G. Zito (1991b), Heat flow map of Italy, Cons. Naz. delle Ric., Pisa, Italy.

Del Pezzo, E., M. Simini, and J. M. Ibanez (1996), Separation of intrinsic and scattering Q for volcanic areas: A comparison between Etna and Campi Flegrei, *J. Volcanol. Geotherm. Res.*, *70*, 213–219, doi:10.1016/0377-0273(95)00056-9.

Di Giovambattista, R., and S. Barba (1997), An estimate of hypocentre location accuracy in a large network: Possible implications for tectonic studies in Italy, *Geophys. J. Int.*, *129*, 124–132, doi:10.1111/j.1365-246X.1997.tb00941.x.

Di Stefano, R., C. Chiarabba, F. Lucente, and A. Amato (1999), Crustal and uppermost mantle structure in Italy from the inversion of *P*-wave arrival times: Geodynamic implications, *Geophys. J. Int.*, *139*, 483–498, doi:10.1046/j.1365-246x.1999.00952.x.

Evans, J. R., and J. J. Zucca (1988), Active high-resolution seismic tomography of compressional wave velocity and attenuation structure at Medicine Lake volcano, northern California Cascade Range, *J. Geophys. Res.*, *93*, 15,016–15,036.

Evans, J. R., and J. J. Zucca (1993), Active source, high-resolution (NeHT) tomography: Velocity and Q, in *Seismic Tomography: Theory and Practice*, pp. 695–732, Chapman and Hall, London.

Faccenna, C., P. Davy, J.-P. Brun, R. Funiciello, D. Giardini, M. Mattei, and T. Nalpas (1996), The dynamics of back-arc extension: An experimental approach to the opening of the Tyrrhenian Sea, *Geophys. J. Int.*, *126*, 781–795.

Faccenna, C., F. Funiciello, D. Giardini, and P. Lucente (2001), Episodic back-arc extension during restricted mantle convection in the central Mediterranean, *Earth Planet. Sci. Lett.*, *187*, 105–116, doi:10.1016/S0012-821X(01)00280-1.

Fehler, M., M. Hoshiba, H. Sato, and K. Obara (1992), Separation of scattering and intrinsic attenuation for the Kanto-Tokai region, Japan, using measurements of S-wave energy versus hypocentral distance, *Geophys. J. Int.*, *108*, 787–800, doi:10.1111/j.1365-246X.1992.tb03470.x.

Frepoli, A., G. Selvaggi, C. Chiarabba, and A. Amato (1996), State of stress in the Southern Tyrrhenian subduction zone from fault-plane solutions, *Geophys. J. Int.*, *125*, 879–891, doi:10.1111/j.1365-246X.1996.tb06031.x.

Giampiccolo, E., S. Gresta, and F. Rasconà (2004), Intrinsic and scattering attenuation from observed seismic codas in southeastern Sicily, *Phys. Earth Planet. Inter.*, *145*, 55–66, doi:10.1016/j.pepi.2004.02.004.

Goes, S., R. Govers, and P. Vacher (2000), Shallow mantle temperatures under Europe from *P* and *S* wave tomography, *J. Geophys. Res.*, *105*, 11,153–11,170, doi:10.1029/1999JB900300.

Gvirtzman, Z., and A. Nur (1999), The formation of Mount Etna as the consequence of slab rollback, *Nature*, *401*, 782–785, doi:10.1038/44555.

Hacker, B. R., S. M. Peacock, G. A. Abers, and S. D. Holloway (2003), Subduction factory: 2. Are intermediate-depth earthquakes in subducting slabs linked to metamorphic dehydration reactions?, *J. Geophys. Res.*, *108*(B1), 2030, doi:10.1029/2001JB001129.

Hoshiba, M., A. Rietbrock, F. Sherbaum, H. Nakahara, and C. Haberland (2001), Scattering attenuation and intrinsic absorption using uniform and depth dependent model—Application to full seismogram envelope recorded in northern Chile, *J. Seismol.*, *5*, 157–179, doi:10.1023/A:1011478202750.

Italiano, F., M. Martelli, G. Martinelli, and P. M. Nuccio (2000), Geochemical evidence of melt intrusions along lithospheric faults of the southern Apennines, Italy: Geodynamic and seismogenic implications, *J. Geophys. Res.*, *105*, 13,569–13,578, doi:10.1029/2000JB900047.

Karato, S. (1993), Importance of anelasticity in the interpretation of seismic tomography, *Geophys. Res. Lett.*, *20*, 1623–1626, doi:10.1029/93GL01767.

Karato, S., and B. Karki (2001), Origin of lateral variation of seismic wave velocities and density in the deep mantle, *J. Geophys. Res.*, *106*, 21,771–21,783, doi:10.1029/2001JB000214.

Karato, S., and H. A. Spetzler (1990), Defect microdynamics in minerals and solid state mechanisms of seismic wave attenuation and velocity dispersion in the mantle, *Rev. Geophys.*, *28*, 399–421, doi:10.1029/RG028i004p00399.

Kennett, B. L. N., E. R. Engdahl, and R. Buland (1995), Constraints on seismic velocities in the Earth from traveltimes, *Geophys. J. Int.*, *122*, 108–124, doi:10.1111/j.1365-246X.1995.tb03540.x.

Kissling, E., W. L. Ellsworth, D. Eberhart-Phillips, and U. Kradolfer (1994), Initial reference models in local earthquake tomography, *J. Geophys. Res.*, *99*, 19,635–19,646, doi:10.1029/93JB03138.

Kissling, E., U. Kradolfer, and H. Maurer (1995), *VELEST User's Guide—Short Introduction*, technical report, Inst. of Geophys. and Swiss Seismol., Serv. Eidg. Tech. Hochsch., Zurich.

Lucente, F. P., C. Chiarabba, G. B. Cimini, and D. Giardini (1999), Tomographic constraints on the geodynamic evolution of the Italian region, *J. Geophys. Res.*, *104*, 20,307–20,327, doi:10.1029/1999JB900147.

Malinverno, A., and W. B. F. Ryan (1986), Extension in the Tyrrhenian sea and shortening in the Apennines as a result of arc migration driven by the sinking of the lithosphere, *Tectonics*, *5*, 227–245, doi:10.1029/TC005i002p00227.

Mann, M. E., and J. M. Lees (1996), Robust estimation of background noise and signal detection in climatic time series, *Clim. Change*, *33*, 409–445, doi:10.1007/BF00142586.

Marani, M. P., and T. Trua (2002), Thermal constriction and slab tearing at the origin of a superinflated spreading ridge: Marsili volcano (Tyrrhenian Sea), *J. Geophys. Res.*, *107*(B9), 2188, doi:10.1029/2001JB000285.

Mele, G. (1998), High-frequency wave propagation from mantle earthquakes in the Tyrrhenian Sea: New constraints for the geometry of the south Tyrrhenian subduction zone, *Geophys. Res. Lett.*, *25*, 2877–2880, doi:10.1029/98GL02175.

Mele, G., A. Rovelli, D. Seber, and M. Barazangi (1997), Shear wave attenuation in the lithosphere beneath Italy and surrounding regions: Tectonic implications, *J. Geophys. Res.*, *102*, 11,863–11,875, doi:10.1029/97JB00262.

Mele, G., A. Rovelli, and D. Seber (1998), Compressional velocity structure and anisotropy in the uppermost mantle beneath Italy and surrounding regions, *J. Geophys. Res.*, *103*, 12,529–12,543, doi:10.1029/98JB00596.

Mongelli, F., P. Harabaglia, G. Martinelli, P. Squarci, and G. Zito (1996), Nuove misure di flusso geotermico in Italia meridionale: Possibili impli-

cazioni sismotettoniche, in *Atti 14° Convegno del Gruppo Naz. di Geofisica della Terra Solida*, pp. 929–939, Cons. Naz. delle Ric., Rome.
Montuori, C., G. B. Cimini, and P. Favali (2007), Teleseismic tomography of the southern Tyrrhenian subduction zone: New results from seafloor and land recordings, *J. Geophys. Res.*, *112*, B03311, doi:10.1029/2005JB004114.
Neri, G., B. Orecchio, C. Totaro, G. Falcone, and D. Presti (2009), Subduction beneath southern Italy close the ending: Results from seismic tomography, *Seismol. Res. Lett.*, *80*(1), 63–70.
Paige, C. C., and M. A. Saunders (1982), LSQR: An algorithm for sparse linear equations and sparse least squares, *Trans. Math. Software*, *8*, 43–71, doi:10.1145/355984.355989.
Panza, G. F., R. B. Raykova, E. Carminati, and C. Doglioni (2007), Upper mantle flow in the western Mediterranean, *Earth Planet. Sci. Lett.*, *257*, 200–214, doi:10.1016/j.epsl.2007.02.032.
Park, J., C. R. Lindberg, and F. L. Vernon III (1987), Multitaper spectral analysis of high-frequency seismograms, *J. Geophys. Res.*, *92*, 12,675–12,684, doi:10.1029/JB092iB12p12675.
Patacca, E., and P. Scandone (1989), Post-Tortonian mountain building in the Apennines: The role of the passive sinking of a relic lithosphere, in *The Lithosphere in Italy*, *Adv. Earth Sci. Res.*, vol. 80, edited by A. Boriani et al., pp. 157–176, Acc. Naz. Lincei, Rome.
Peccerillo, A. (2001), Geochemical similarities between the Vesuvius, Phlegraean Fields and Stromboli volcanoes: Petrogenic, geodynamic and volcanological implications, *Mineral. Petrol.*, *73*, 93–105, doi:10.1007/s007100170012.
Peccerillo, A. (2005), *Plio-Quaternary Volcanism in Italy: Petrology, Geochemistry, Geodynamics*, Springer, Berlin.
Piromallo, C., and A. Morelli (1997), Imaging the Mediterranean upper mantle by *P* wave travel time tomography: Preliminary results, *Annal. Geofis.*, *40*, 963–979.
Piromallo, C., and A. Morelli (2003), *P* wave tomography of the mantle under the Alpine-Mediterranean area, *J. Geophys. Res.*, *108*(B2), 2065, doi:10.1029/2002JB001757.
Podvin, P., and I. Lecompte (1991), Finite difference computation of travel times in very contrasted velocity models: A massively parallel approach and its associated tools, *Geophys. J. Int.*, *105*, 271–284, doi:10.1111/j.1365-246X.1991.tb03461.x.
Pontevivo, G., and G. F. Panza (2006), The lithosphere-asthenosphere system in the Calabrian Arc and surrounding seas—southern Italy, *Pure Appl. Geophys.*, *163*, 1,617–1,659, doi:10.1007/s00024-006-0093-3.
Richards, P. G., and W. Menke (1983), The apparent attenuation of a scattering medium, *Bull. Seismol. Soc. Am.*, *73*, 1005–1021.
Romanowicz, B. (1995), A global tomographic model of shear attenuation in the upper mantle, *J. Geophys. Res.*, *100*, 12,375–12,394, doi:10.1029/95JB00957.
Rosenbaum, G., and G. S. Lister (2004), Neogene and Quaternary rollback evolution of the Tyrrhenian Sea, the Apennines, and the Sicilian Maghrebides, *Tectonics*, *23*, TC1013, doi:10.1029/2003TC001518.
Roth, E. G., D. A. Wiens, and D. Zhao (2000), An empirical relationship between seismic attenuation and velocity anomalies in the upper mantle, *Geophys. Res. Lett.*, *27*, 601–604, doi:10.1029/1999GL005418.
Sanders, C. O. (1993), Local earthquake tomography: Attenuation—theory and results, in *Seismic Tomography: Theory and Practice*, pp. 676–694, Chapman and Hall, London.
Sato, H., M. Fehler, and R.-S. Wu (2000), Scattering and attenuation of seismic waves in the lithosphere, in *Handbook of Earthquake and Engineering Seismology*, edited by W. H. K. Lee, chap. 13, pp. 195–208, Elsevier, New York.
Selvaggi, G., and C. Chiarabba (1995), Seismicity and *P*-wave velocity image of the southern Tyrrhenian subduction zone, *Geophys. J. Int.*, *121*, 818–826, doi:10.1111/j.1365-246X.1995.tb06441.x.
Serri, G. (1990), Neogene-Quaternary magmatism of the Tyrrhenian region: Characterization of the magma sources and geodynamic implications, *Mem. Soc. Geol. Ital.*, *41*, 90–94.
Serri, G., F. Innocenti, and P. Manetti (2001), Magmatism from Mesozoic to present: Petrogenesis, time-space distribution and geodynamic implications, in *Anatomy of a Mountain: The Apennines and the Adjacent Mediterranean Basins*, edited by G. B. Vai and P. I. Martini, pp. 77–104, Springer, New York.
Schurr, B., G. Asch, A. Rietbrock, R. Trumbull, and C. Haberland (2003), Complex patterns of fluid and melt transport in the central Andean subduction zone revealed by attenuation tomography, *Earth Planet. Sci. Lett.*, *215*, 105–119, doi:10.1016/S0012-821X(03)00441-2.
Sgroi, T., T. Braun, T. Dahm, and F. Frugoni (2006), An improved seismicity picture of the southern Tyrrhenian area by the use of OBS and land-based networks: The TYDE experiment, *Ann. Geophys.*, *49*, 801–817.
Spakman, W. (1991), Delay time tomography of the upper mantle below Europe, the Mediterranean, and Asia Minor, *Geophys. J. Int.*, *107*, 309–332, doi:10.1111/j.1365-246X.1991.tb00828.x.
Spakman, W., and R. Wortel (2004), A tomographic view on western Mediterranean geodynamics, in *The Transmed Atlas: The Mediterranean Region from Crust to Mantle*, pp. 31–52, Springer, New York.
Speranza, F., and M. Chiappini (2002), Thick-skinned tectonics in the external Apennines, Italy: New evidence from magnetic anomaly analysis, *J. Geophys. Res.*, *107*(B11), 2290, doi:10.1029/2000JB000027.
Teng, T. L. (1968), Attenuation of body waves and the Q structure of the mantle, *J. Geophys. Res.*, *73*, 2195–2208, doi:10.1029/JB073i006p02195.
Trua, T., G. Serri, and P. L. Rossi (2004), Coexistence of IAB-type and OIB-type magmas in the southern Tyrrhenian back-arc basin: Evidence from recent seafloor sampling and the geodynamic implications, in *From Seafloor to Deep Mantle: Architecture of the Tyrrehanian Backarc Basin*, *Mem. Descr. Carta Geol. d'It*, vol. 44, edited by M. P. Marani, F. Gamberi, and E. Bonatti, pp. 83–96, Agenzia per la Prot. dell'Ambiente e per i Serv. Tec. (APAT), Rome.
Wessel, P., and W. H. F. Smith (1991), Free software helps map and display data, *Eos Trans. AGU*, *72*(41), 441.
Zito, G., F. Mongelli, S. De Lorenzo, and C. Doglioni (2003), Heat flow and geodynamics in the Tyrrhenian Sea, *Terra Nova*, *15*, 425–432, doi:10.1046/j.1365-3121.2003.00507.x.

T. Dahm, Institut für Geophysik, Universität Hamburg, Bundestrasse 55, D-20146 Hamburg, Germany.
S. Monna, Istituto Nazionale di Geofisica e Vulcanologia, Via di Vigna Murata 605, Rome 00143, Italy. (monna@ingv.it)

3 New insights from seismic tomography on the complex geodynamic evolution of two adjacent domains: Gulf of Cadiz and Alboran Sea

JOURNAL OF GEOPHYSICAL RESEARCH: SOLID EARTH, VOL. 118, 1–15, doi:10.1029/2012JB009607, 2012

New insights from seismic tomography on the complex geodynamic evolution of two adjacent domains: Gulf of Cadiz and Alboran Sea

S. Monna,[1] G. B. Cimini,[1] C. Montuori,[1] L. Matias,[2] W. H. Geissler,[3] and P. Favali[1]

Received 5 July 2012; revised 28 November 2012; accepted 29 November 2012.

[1] In this study, we present a three-dimensional *P* wave upper-mantle tomography model of the southwest Iberian margin and Alboran Sea based on teleseismic arrival times recorded by Iberian and Moroccan land stations and by a seafloor network deployed for 1 year in the Gulf of Cadiz area during the European Commission Integrated observations from NEAR shore sourcES of Tsunamis: towards an early warning system (EC NEAREST) project. The three-dimensional model was computed down to 600 km depth. The tomographic images exhibit significant velocity contrasts, as large as 3%, confirming the complex evolution of this plate boundary region. Prominent high-velocity anomalies are found beneath Betics-Alboran Sea, off-shore southwest Portugal, and north Portugal, at sublithospheric depths. The transition zones between high- and low-velocity anomalies in southwest and south Iberia are associated to the contact of oceanic and continental lithosphere. The fast structure below the Alboran Sea-Granada area depicts an L-shaped body steeply dipping from the uppermost mantle to the transition zone where it becomes less curved. This anomaly is consistent with the results of previous tomographic investigations and recent geophysical data such as stress distribution, GPS measurements of plate motion, and anisotropy patterns. In the Atlantic domain, under the Horseshoe Abyssal Plain, the main feature is a high-velocity zone found at uppermost mantle depths. This feature appears laterally separated from the positive anomaly recovered in the Alboran domain by the interposition of low-velocity zones which characterize the lithosphere beneath the southwest Iberian peninsula margin, suggesting that there is no continuity between the high-velocity anomalies of the two domains west and east of the Gibraltar Strait.

Citation: Monna, S., G. B. Cimini, C. Montuori, L. Matias, W. H. Geissler, and P. Favali (2013), New insights from seismic tomography on the complex geodynamic evolution of two adjacent domains: Gulf of Cadiz and Alboran Sea, *J. Geophys. Res. Solid Earth*, *118*, doi:10.1029/2012JB009607.

1. Introduction

[2] The geodynamic evolution of the southwestern Iberian margin and the Alboran Sea is the result of the complex interaction between the African and the Eurasian plates (Figure 1). At present, there is convergence between the two plates at a rate of ~5 mm/year [*Stich et al*., 2006]. The plate boundary is clearly defined from the Gloria fault to the Gorringe Bank [*Zitellini et al*., 2009]. From the Gorringe Bank proceeding to the east, across the Strait of Gibraltar, the boundary is diffuse [*Sartori et al*., 1994] with different locations having been proposed for it [e.g., *Rovere et al*., 2004]. A narrow band of deformation (SWIM Fault Zone, SFZ in Figure 1) is considered as a precursor to the formation of a new transcurrent plate boundary between Iberia and Africa [*Zitellini et al*., 2009].

[3] Two main geodynamic evolution models have been proposed so far in literature for the Alboran Basin System:

[4] 1. The collision of Europe and Africa led to lithospheric thickening during the Paleogene. The thickened continental lithosphere was later (~20 Ma) detached by convective removal [*Platt and Vissers*, 1989] or by delamination [*Seber et al*., 1996; *Calvert et al*., 2000]. The collapse of this lithosphere caused extension of the Alboran basin and uplift around the margin.

[5] 2. The subduction of oceanic lithosphere caused extension within the Alboran Basin in the Miocene by slab rollback [*Royden*, 1993; *Lonergan and White*, 1997; *Bijwaard and Spakman*, 2000; *Gutscher et al*., 2002] or by slab detachment [*Zeck*, 1996]. Starting from their geometrical and structural similarity, a common origin has been proposed for the Calabrian and Gibraltar Arcs. In this reconstruction, the Arcs formed from the fragmentation of a single subduction zone during the tectonic evolution of the Central-Western Mediterranean region [*Faccenna et al*., 2004 and references therein].

Additional supporting information may be found in the online version of this article.

[1]Istituto Nazionale di Geofisica e Vulcanologia, Rome, Italy.
[2]Centro de Geofísica, Universidade de Lisboa, Lisbon, Portugal.
[3]Alfred-Wegener-Institut für Polar- und Meeresforschung, Bremerhaven, Germany.

Corresponding author: S. Monna, Istituto Nazionale di Geofisica e Vulcanologia, Rome, Italy. (stephen.monna@ingv.it)

2169-9313/12/2012JB009607

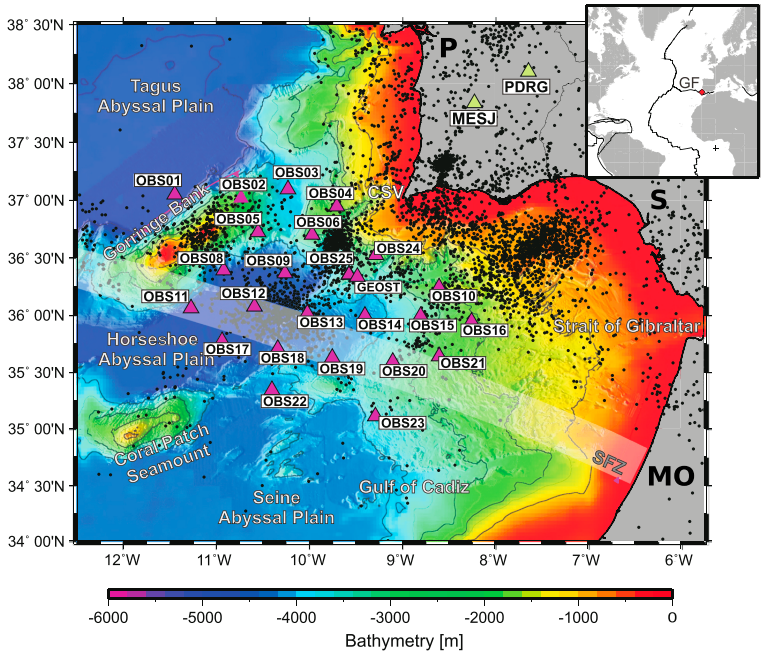

Figure 1. Map of the Gulf of Cadiz and surrounding regions showing seismicity related to the main tectonic features and the NEAREST land stations and marine network (green and purple triangles, respectively). The marine network includes 24 OBS plus GEOSTAR seafloor observatory. Epicentral locations are from the bulletin of the Institute of Meteorology Lisbon (http://www.meteo.pt/en/publicacoes/tecnico-cientif/noIM/boletins/). CSV = Cape St. Vincent; S = Spain; P = Portugal; MO = Morocco; SFZ = Swim Fault Zone. In inset, GF = Gloria Fault. Adapted from *Geissler et al.* [2010].

[6] Different geophysical observations have been interpreted within the proposed geodynamic models. Magma evolution in time and space shows a volcanism which could be explained by a subduction scenario [*Duggen et al.*, 2004], but it has also been invoked in support of delamination [*Zeck*, 1996] and of the convective removal models [*Platt and Vissers*, 1989; *Platt*, 1998; *Turner et al.*, 1999]. Tomographic studies show a high-velocity body under the Alboran Sea, which has been interpreted as a continuous subducting slab [*Gutscher et al.*, 2002; *Piromallo and Morelli*, 2003], as a broken-off slab [*Blanco and Spakman*, 1993], and as lithosphere which has undergone delamination [*Calvert et al.*, 2000]. The pattern obtained from seismic anisotropy studies supports models involving a westward retreating slab [*Buontempo et al.*, 2008; *Bokelmann et al.*, 2010; *Diaz et al.*, 2010]. Measures on dispersion of *P* waves are compatible with subducted oceanic lithosphere [*Bokelmann and Maufroy*, 2007].

[7] The two domains, Alboran Sea and Atlantic domain (Gulf of Cadiz), east and west of the Gibraltar Strait, show differences in their geophysical and seismological characters. In the Alboran domain, Bouguer anomaly modeling shows that the base of the lithosphere ranges from 140 km depth in the Gibraltar Strait to less than 45 km depth in the easternmost Alboran Sea [*Tornè et al.* 2000; *Zeyen et al.*, 2005]. The average heat flow in the western Alboran basin is 69 ± 6 mW/m^2 with a generally increasing trend toward the center of the basin and to the east. In contrast, the heat flow pattern in the eastern Alboran Basin shows an average value of 124 ± 8 mW/m^2, which remains rather constant over the whole area [*Polyak et al.*, 1996]. Moderate superficial seismicity and a seismic gap between 20 and 60 km depth has been observed in the Alboran Sea (Figure 2). There is intermediate-depth seismicity, located near the Strait of Gibraltar within 120 km depth and distributed in a very narrow north-south oriented vertical band [*Seber et al.*, 1996]. Deep earthquakes are rare and occur at the bottom of the transition zone (~630 km depth) under southern Spain in the Granada area [*Buforn et al.*, 2004], and no Benioff zone is visible. Under the Alboran Sea and southern Spain, mostly extensional and strike-slip focal mechanisms are reported and a combination of seismic and GPS data points to a transtensional regime [*Stich et al.*, 2003, 2006].

[8] In the Atlantic domain, heat flow is high above the Horseshoe Abyssal Plain (approximately 52–59 mW/m^2), and it decreases eastward across the Gulf of Cadiz prism, attaining minimum values (~40 mW/m^2) toward the Gibraltar Strait [*Grevemeyer et al.*, 2009]. The low values and trend of the heat flow are typical for active thrusting and could be explained by an east-dipping subduction model, which may or may not be active [*Grevemeyer et al.*, 2009 and references therein]. There is evidence in the Gulf of Cadiz for subcrustal earthquakes down to 60 km depth. A recent study based on the NEAREST marine array data [*Geissler et al.*, 2010] shows

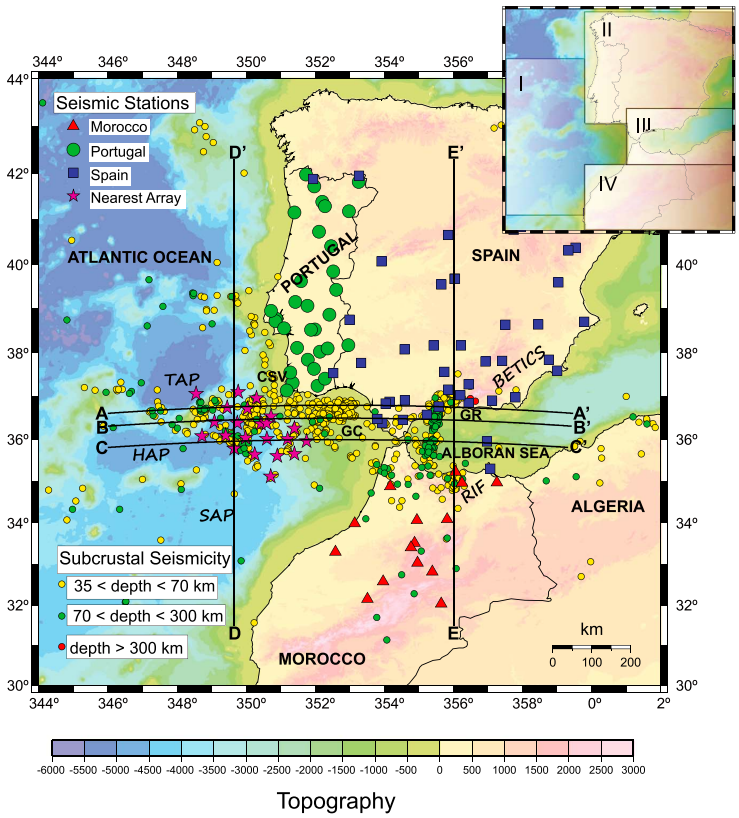

Figure 2. Map of seismic stations used for the tomographic inversion. Stars represent marine stations from the NEAREST array (24 OBS/H, GEOSTAR) and two broadband land stations (MESJ, PDRG) installed in southern Portugal during the 2007–2008 experiment. The integrated array consists of 111 receivers. Colored dots represent subcrustal seismicity at different depth intervals. Land stations are part of the permanent networks of Spain (blue squares), Portugal (green circles), and Morocco (red triangles). Hypocentral locations are from http://www.02.ign.es/ign/layoutIn/sismoFormularioCatalogo.do (Instituto Geográfico Nacional Spain). GR = Granada area; CSV = Cape St. Vincent; GC = Gulf of Cadiz; SAP = Seine Abyssal Plain; HAP = Horseshoe Abyssal Plain; TAP = Tagus Abyssal Plain. AA′, BB′, CC′, DD′, and EE′ show the traces of the profiles shown in Figure 9. The inset shows the four regions used for the crustal correction of the traveltime residuals.

that the observed seismicity is contained in a seismogenic layer of ~140 Ma old oceanic lithosphere and aligned along north-northeast–south-southwest and west-northwest–east-southeast striking structures. In the Gulf of Cadiz, repeated GPS measurements and focal mechanisms, which are mainly reverse and strike slip, point to a transpressive plate boundary [*Stich et al.*, 2005; *Geissler et al.*, 2010]. These studies show that there is a change of stress regime going across the Gibraltar Strait from transtensional in the Alboran domain to transpressive in the Atlantic domain.

[9] Tomographic models proposed so far do not give much information on the upper-mantle structure west of Gibraltar Strait due to the lack of long-term data series at the sea bottom. In particular, a clear image of the transition between the African and the Eurasian continental domain and the Atlantic oceanic domain is still lacking. Knowledge of the Atlantic domain and of the passage to the Alboran domain can also put some constraints on the models describing the geodynamic evolution of the Alboran domain. An open question is the present relation of the Atlantic and Alboran domains.

[10] We present a three-dimensional (3-D) tomography model imaging the upper-mantle structure below the Gulf of Cadiz-Alboran region. The inclusion, for the first time, of the Atlantic domain was possible, thanks to data recorded during a long-term (1 year) marine experiment in the Gulf of Cadiz in which 24 Ocean Bottom Seismometer (OBS) and GEOSTAR seafloor observatory were deployed, in the frame of the activities of the EC NEAREST project.

2. Data Set

[11] During the NEAREST experiment [*Carrara and NEAREST Team*, 2008], a seafloor seismic network was deployed for 1 year (August 2007–August 2008) in the Gulf

of Cadiz and off-shore Cape St. Vincent, with average spacing of ~50 km (Figure 1). This network comprised 24 stations (OBS/H) from the German DEPAS pool, each equipped with a three-component Guralp CMG-40 T broadband seismometer with 60 s-50 Hz response (OBS) and a High Tech HTI-04-PCA/ULF hydrophone (OBH). The same type of seismometer was installed on board the GEOSTAR deep-sea multiparameter observatory deployed in the same period. Furthermore, two broadband land stations were installed in southern Portugal at the beginning of the experiment (Table S1). The OBS/H internal clocks were synchronized with GPS signal before the deployment, and the same operation was repeated on ship after the instruments were recovered. A linear drift correction was applied a posteriori, which was, on the average ~0.53 s/year. For nine OBS/H, onboard synchronization was not possible, and we applied the drift corrections calculated during other experiments where the same instruments were deployed. Figure 2 shows the seismic stations used in the inversion for the velocity structure.

[12] Direct *P* phases from 67 teleseismic events were identified on waveforms recorded by 25 seafloor stations, the two temporary land stations, and by some other land stations when digital seismograms were available from the European Integrated Data Archive (EIDA; http://eida.rm.ingv.it). This data set was selected from more than 200 $M_w \geq 5.5$ events, which occurred during the experiment, with epicentral distance between 25° and 95°. To obtain better ray coverage, we also added 89 teleseisms recorded by the Moroccan, Portuguese, and Spanish seismic networks (Figure 2) in the period January 2007–June 2009. The corresponding arrival times were extracted from the ISC bulletin (http://www.isc.ac.uk), which also includes readings of later arrivals as pP, sP, PcP, and core phases as PKPdf. Our teleseismic data set consists of 152 events (130 P, 16 pP, 3 sP, and 3 PcP) with at least 10 *P* wave recordings, for a total of 6238 *P* wave arrival times for the tomography. Figure 3 shows the azimuthal distribution of the teleseismic sources with the epicentral locations provided by the National Earthquake Information Center (NEIC) earthquake catalogs (http://earthquake.usgs.gov/research).

[13] To estimate cross-correlation delays of the first *P*-arrival on the waveform data we employed the semi-automated multichannel cross-correlation (MCCC) technique (*VanDecar and Crosson*, 1990) on the vertical channel of the unfiltered data (Figure 4). MCCC calculates relative phase arrivals by maximizing a cross-correlation matrix. After a first visual inspection, there is a preliminary selection of waveforms, and then MCCC is applied. We estimated an average error for MCCC data of 0.17 s. This estimation is 1.5–2 times the error computed by the MCCC routine. We took this more conservative approach as MCCC is known to underestimate the error (down to a fraction of the sampling interval) [*Tilmann et al.*, 2001]. For bulletin data, mostly from impulsive *P* phases, we estimated an average arrival time error of 0.45 s. The entire data set of the 6238 *P* wave arrival times has an average error of 0.43 s, corresponding to a data variance (noise) of 0.18 s^2. OBS data with very low signal-to-noise ratio and time picks yielding absolute residuals of more than 10 s or relative residuals (see below) exceeding ±2.0 s were excluded from the data set. These thresholds were included to mitigate the effect of large data errors (outliers) often associated to incorrect phase identification or mispicking. Data inversion with a 2 s cutoff applied to the traveltime residuals can still take into account significant differences between the real Earth and the standard model.

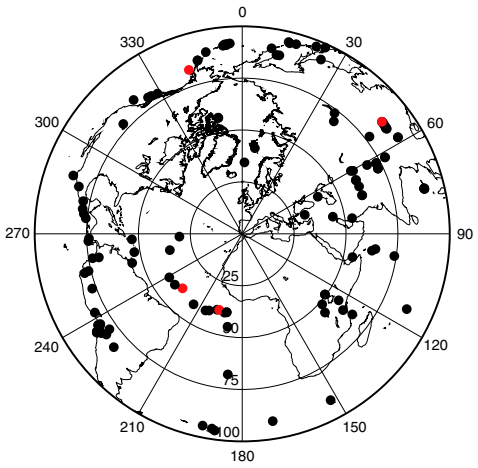

Figure 3. Azimuthal equidistant map of teleseismic sources (projection center at 37.0°N–7.0°W) selected for the analysis. The events are distributed over a wide range of back azimuths. Epicentral distance ranges from 30° to 100°. Red circles represent the events used for the residual maps in Figure 5.

3. Relative Arrival Time Residual Analysis

[14] Relative residuals are widely used in regional arrival time teleseismic tomography to constrain the 3-D seismic structure of a local model volume beneath a seismic array. The main reason for using this methodology is that relative residuals are not significantly affected by source mislocations (errors in origin time and hypocentral location), differences between the actual and the reference source-receiver raypath below the investigated Earth volume nor by large-scale variations in mantle structure [*Aki et al.*, 1977; *Evans and Achauer*, 1993]. Their inversion, however, does not produce absolute velocity, but only relative perturbations calculated starting from an initial velocity model. In other words, the resulting velocity structure only reflects deviations about some unknown average earth model, as the layer-average velocities are not constrained by the inversion and act as free parameters [*Koch*, 1985].

[15] In this study, we computed relative residuals on event per event basis by subtracting a weighted average residual from each absolute traveltime residual. The absolute residual, for a given seismic phase, is the difference between the observed and the predicted arrival time. The weighted average event residual was obtained using data weights $1/\sigma^2_{pick}$, where σ_{pick} is the error associated to each arrival time. For those events composed by both MCCC and ISC data, this computation was carried out separately for each subset of teleseismic arrivals. This separation takes into account the likely possibility that the data subsets may have different baselines. We found that this correction improves the data fit.

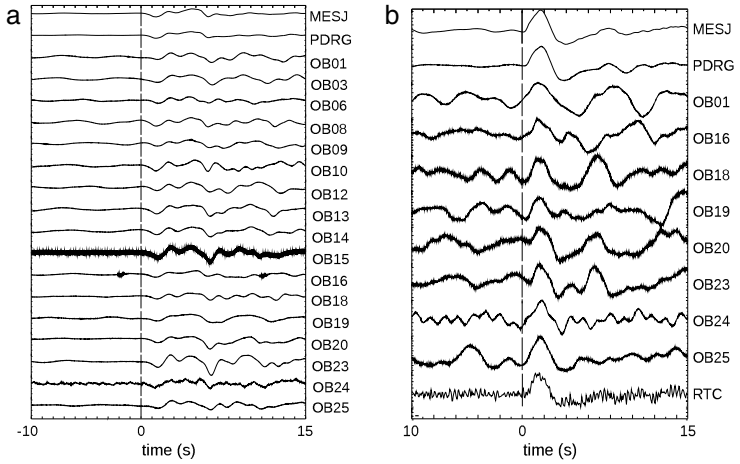

Figure 4. Example of waveforms used for MCCC analysis for (a) M6.4 event from China and (b) M6.3 from Chile. Vertical bars identify *P* wave first break. Other examples of MCCC are shown if Figure S1 in the supporting information.

[16] Before the residual computation, the observed arrival times were corrected for Earth's ellipticity [*Dziewonski and Gilbert*, 1976] and station topography/bathymetry (negative for the seafloor instruments), while the predicted traveltimes, based on the ak135 global velocity model [*Kennett et al.*, 1995], were corrected for sedimentary and crustal structure. Four velocity models were applied for the crustal correction (Table 1). These models were extracted from recent studies and from the European Moho depth map by *Grad et al.* [2009]. The oceanic model, in particular, takes into account the NEAREST wide-angle seismic survey [*Sallarès et al.*, 2011]. We consider these models as representative of the different average structure of the continental and oceanic domains within the study area (see inset in Figure 2). For a given teleseismic ray, the crustal correction was computed as the difference between the traveltime in the local structure and the one in the ak135 velocity model, backtracking the ray from the Earth's surface down to the reference depth of 50 km. Values of the crustal terms range from −0.3 s for the land stations to 0.20 s for the rays ending at the seafloor receivers.

Table 1. Crustal Velocity Models Used for the Different Sectors Shown in the Inset of Figure 2[a]

Depth (km)	*P* wave velocity (km/s)	Layer
I		
0	3.50	Sediment
6	5.80	Upper crust
12	6.50	Lower crust
16	8.00	Upper mantle
II		
0	6.00	Upper crust
10	6.25	Middle crust
24	6.75	Lower crust
31	8.00	Upper mantle
III		
0	6.00	Upper crust
12	6.40	Middle crust
25	6.80	Lower crust
33	8.00	Upper mantle
IV		
0	6.00	Upper crust
12	6.30	Middle crust
24	6.60	Lower crust
38	8.00	Upper mantle

[a]**I**, Gulf of Cadiz (Atlantic Ocean Domain) from *Gutsher et al.* [2009], *Fullea et al.* [2010], and *Sallares et al.* [2011]; **II**, Iberian Peninsula from *Diaz and Gallart* [2009] and references therein; **III**, Betics and Rif from *Serrano et al.* [2003], *Fullea et al.* [2007], *Diaz and Gallart* [2009], and *Fullea et al.* [2010]; **IV**, Atlas from *Zeyen et al.* [2005].

[17] The pattern of relative arrival time residuals provides a first indication of the heterogeneity in the Earth's velocity structure inside the study volume. Negative residuals imply the presence of high-velocity anomalies, whereas positive values indicate low-velocity structures. In Figure 5, we show some significant examples of traveltime residual maps calculated for four events approaching the network from different azimuthal sectors. The residual analysis shows features that we can associate to velocity contrasts within the target volume, giving us an idea of the average properties of the studied volume and their azimuthal dependence. These results give a first indication of the 3-D velocity anomalies that exist below the study volume. The main features observed from the residual maps are as follows:

[18] Earlier arrivals are measured for waves approaching the Alboran Sea and the Southern Iberian margin from northeast, south, and north (Figures 5a, 5b, and 5d). This pattern suggests the presence of a clear high-velocity body below the Alboran Sea and Southern Iberian margin.

[19] Later arrivals are observed along the western Iberian margin for waves approaching from northeast, south, and southwest (Figures 5a, 5b, and 5c). This observation can be explained by the presence of a low-velocity body underlying the western Iberian margin, from northern Portugal to the Gulf of Cadiz.

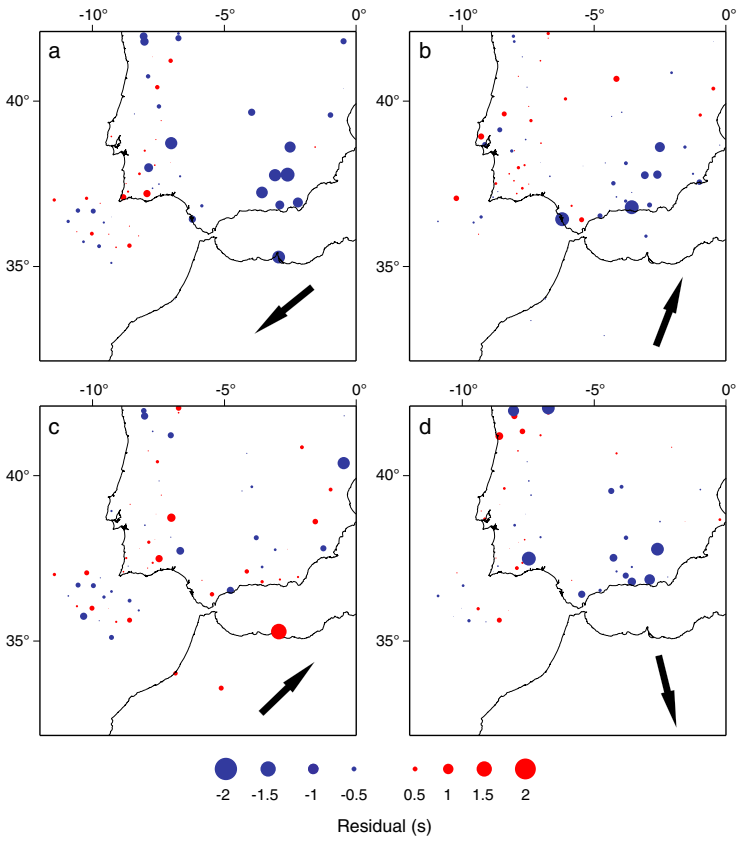

Figure 5. Pattern of relative arrival time residuals. (a) Eastern Sichuan (China) M7.9 back azimuth 53°, distance 86°. (b) Central mid-Atlantic ridge M5.9, back azimuth 196°, distance 37°. (c) Central mid-Atlantic ridge M6.5, back azimuth 226°, distance 37°. (d) Alaska Peninsula (USA) M6.3. back azimuth 345°, distance 87°. Arrows show back azimuth for each event. Epicenters of the events used for the residual maps are the red circles in Figure 3.

[20] We observe a passage, from the Atlantic domain below the OBS network to southwestern Iberia, from earlier to later arrival times (Figures 5a, 5b, and 5c). This passage suggests a separation of the velocity structure in the two domains, as clearly displayed in the cross sections of Figure 9a.

4. Inversion Method and Model Parameterization

4.1. Inversion Method

[21] The iterative nonlinear teleseismic tomography procedure developed by *Rawlinson et al.* [2006] has been applied to map relative arrival time residuals as 3-D *P* wave velocity anomalies. As mentioned earlier, inversion of relative traveltime residuals produces a 3-D velocity structure starting from an average (usually 1-D) earth model. Although this known background/reference model is needed for the forward calculation of theoretical traveltimes, the resulting velocity perturbations cannot be considered relative to it, as relative residuals poorly constrain vertical variations in wave speed. However, if the target volume is large enough, we may assume that the horizontally averaged velocities are close to the layer velocity of the initial model [*Leveque and Masson*, 1999], which should be representative of the correct regional structure. Under this assumption, which is normally made in this kind of upper-mantle studies [*Shomali et al.*, 2011, and reference therein], nonlinear iterative teleseismic tomography can improve the reconstruction of the velocity structure. This improvement is also demonstrated by numerical computations [*Koch*, 1985].

[22] The ak135 spherical earth model [*Kennett et al.*, 1995], modified for the crustal structure described in the previous section, was used as initial reference model for the inversion. The tomography scheme of *Rawlinson et al.* [2006] uses cubic B spline functions to define a continuous smooth velocity field from a 3-D grid of velocity nodes in spherical coordinates. The fast marching method (FMM), which is a robust, computational, and efficient grid-based eikonal solver [*Sethian and Popovici*, 1999], is used to compute the evolution of teleseismic wavefronts and the traveltimes from the base of the model volume to the array

of receivers on the surface. Outside this volume, the Earth is assumed to be spherically symmetric, which allows the use of a 1-D global reference model to rapidly compute the traveltimes from the distant sources to all grid nodes at the bottom.

[23] In the following, we give the basic formulation of the tomographic method applied, referring the reader to the *Rawlinson et al*. [2006] study and references therein for a detailed description. In particular, their Figure 8 provides a schematic diagram showing the FMM approach to calculate traveltimes.

[24] The inverse problem for the model parameters **m** (the velocity anomalies) is solved by minimizing an objective function $S(\mathbf{m})$ of the form:

$$S(\mathbf{m}) = (\mathrm{g}(\mathbf{m}) - \mathbf{d}_{\mathrm{obs}})^{\mathrm{T}}\mathbf{C}_{\mathrm{d}}{}^{-1}(\mathrm{g}(\mathbf{m}) - \mathbf{d}_{\mathrm{obs}}) + \varepsilon(\mathbf{m} - \mathbf{m}_0)^{\mathrm{T}}\mathbf{C}_{\mathrm{m}}{}^{-1}(\mathbf{m} - \mathbf{m}_0) + \eta\mathbf{m}^{\mathrm{T}}\mathbf{D}^{\mathrm{T}}\mathbf{D}\mathbf{m} \quad (1)$$

where $\mathrm{g}(\mathbf{m})$ are the predicted residuals, $\mathbf{d}_{\mathrm{obs}}$ are the observed residuals, $\mathbf{C}_{\mathrm{d}}$ is the a priori data covariance matrix, $\mathbf{m}_0$ is the reference model, $\mathbf{C}_{\mathrm{m}}$ is the a priori model covariance matrix, and **D** is a second derivative smoothing operator. The square root of the diagonal entries of matrix Cm indicates the uncertainty associated with the initial model parameter values. The constraints supplied by the data will result in changes to these uncertainties. ε and η are the damping and the smoothing parameter, respectively. They govern the trade-off between how well the solution satisfies the data, the proximity of the solution model to the starting model, and the smoothness of the solution model. Equation (1) is minimized through an iterative sequence of linearized inversions in which the FMM and a subspace inversion method are successively applied to solve the forward problem and to estimate the model perturbation $\delta\mathbf{m}_{\mathrm{i}}$, respectively. The subspace inversion method operates by projecting the quadratic approximation of $S(\mathbf{m})$ onto a much smaller n-dimensional model space. The set of vectors that span the n-dimensional subspace are computed based on the gradient vector and Hessian matrix in model space. Finally, singular value decomposition is used to produce an orthonormal basis of linearly independent vectors removing those vectors that are redundant.

[25] For an objective function of the form of equation (1), the perturbation δm_i is given by

$$\delta\mathbf{m}_{\mathrm{i}} = -\mathbf{A}\left(\mathbf{A}^{\mathrm{T}}\left(\mathbf{G}^{\mathrm{T}}\mathbf{C}\mathrm{d}^{-1}\,\mathbf{G} + \varepsilon\mathbf{C}\mathrm{m}^{-1} + \eta\mathbf{D}^{\mathrm{T}}\mathbf{D}\right)\mathbf{A}\right)^{-1}\mathbf{A}^{\mathrm{T}}\boldsymbol{\gamma} \quad (2)$$

where **A** is the $M \times n$ projection matrix (M unknowns, n-dimensional subspace), **G** is the matrix of Frechét derivatives and $\boldsymbol{\gamma}$ is the gradient vector ($\partial\boldsymbol{S}/\partial\mathbf{m}$). Once matrix **A** has been computed and orthonormalized, vector $\delta\mathbf{m}_{\mathrm{i}}$ is rapidly obtained by the inversion of the $n \times n$ matrix, then added to the current model velocity $\mathbf{m}_{\mathrm{i}}$ to produce the new model $\mathbf{m}_{\mathrm{i+1}} = \mathbf{m}_{\mathrm{i}} + \delta\mathbf{m}_{\mathrm{i}}$ [*Kennett et al.*, 1988; *Rawlinson et al.*, 2006].

4.2. Model Parameterization

[26] The starting model defined for the upper-mantle structure below the study region spans 600 km in depth, 14.0° in latitude (from 30.0°N to 44.0°N), and 18.0° in longitude (from 16.0°W to 2.0°E). It comprises 8316 velocity nodes at 60 km spacing in all three dimensions (depth, latitude, and longitude). The horizontal bounds of such 3-D grid ensure that all the waveforms of our teleseismic data set pass through the base of the model, which is needed to assign traveltimes at all bottom nodes and start FMM correctly. We used the ak135 global reference model [*Kennett et al*., 1995] to set the initial P wave velocity below the depth spanned by the crustal correction. The input grid model incorporates the velocity profiles used for the crustal correction for each sector (Figure 2 and Table 1).

[27] The damping and the smoothing parameters were set to 5 and 2.5, respectively, by examining the trade-off between minimizing the data misfit and reducing the model complexity. This analysis was performed following the three step procedure suggested by *Rawlinson et al*. [2006], which is based on trade-off curves between data variance and model roughness and data variance and model variance. Finally, arrival time error estimates from the picking analysis were used to form the diagonal elements of the data covariance matrix ($\mathbf{C}_{\mathrm{d}}$), while the square root of the diagonal elements of the model covariance matrix ($\mathbf{C}_{\mathrm{m}}$) were set to 0.30 km/s.

5. Tomography Results

5.1. Resolution Tests

[28] To investigate the extent to which the P wave model is constrained by the data, we performed synthetic resolution tests using the same raypath geometry of the observational teleseismic data set to compute synthetic traveltime residuals. We choose to apply the so-called "checkerboard test," in which the input velocity model consists of alternating regions of fast and slow anomalies with a length scale equal (or greater) to the smallest wavelength structure recovered in the solution model. The inversion of the synthetic data set will attempt to recover the checkerboard pattern, showing the regions of the model that can be considered well resolved. In spite of some limitations [*Leveque et al*., 1993; *Husen et al*., 2003], checkerboard tests have become a standard way of addressing model resolution as their results can be promptly visualized. In particular, they give a good estimate of the amount of smearing present in the tomographic images. The spatial resolution of our tomographic images was performed using different checkerboard patterns to explore a variety of wavelengths [*Nolet*, 2008]. In the test, we varied the cell size from 60 to 120 km by including nodes with zero perturbation, with a maximum velocity perturbation of ±0.50 km/s (~±6%). Gaussian noise was added to the synthetic data, with standard deviations of 0.5 and 0.2 s sets to simulate the noise content of the ISC and OBS data, respectively. These values are slightly greater than the error estimated for the two subsets of arrival times (see section 2). The error assigned to ISC data is in line with the results of *Gudmundsson et al.* [1990] for teleseismic P phases (0.39–0.9 s). Comparing all the results obtained by using the different grids, we found a resolution width (the minimum cell size that could be distinguished well) of about 100 km. Figures 6 and 7 show the results of the test for horizontal (see also Figure S2) and vertical slices, respectively. Note that the checkerboard pattern varies in latitude, longitude, and depth. Reconstruction is partial in the south due to poor raypath coverage in northern Morocco. Although smearing of anomalies is present in some regions of the model, especially along the northwest-southeast direction (Figure 6) and along raypaths at the border of the model (Figure 7),

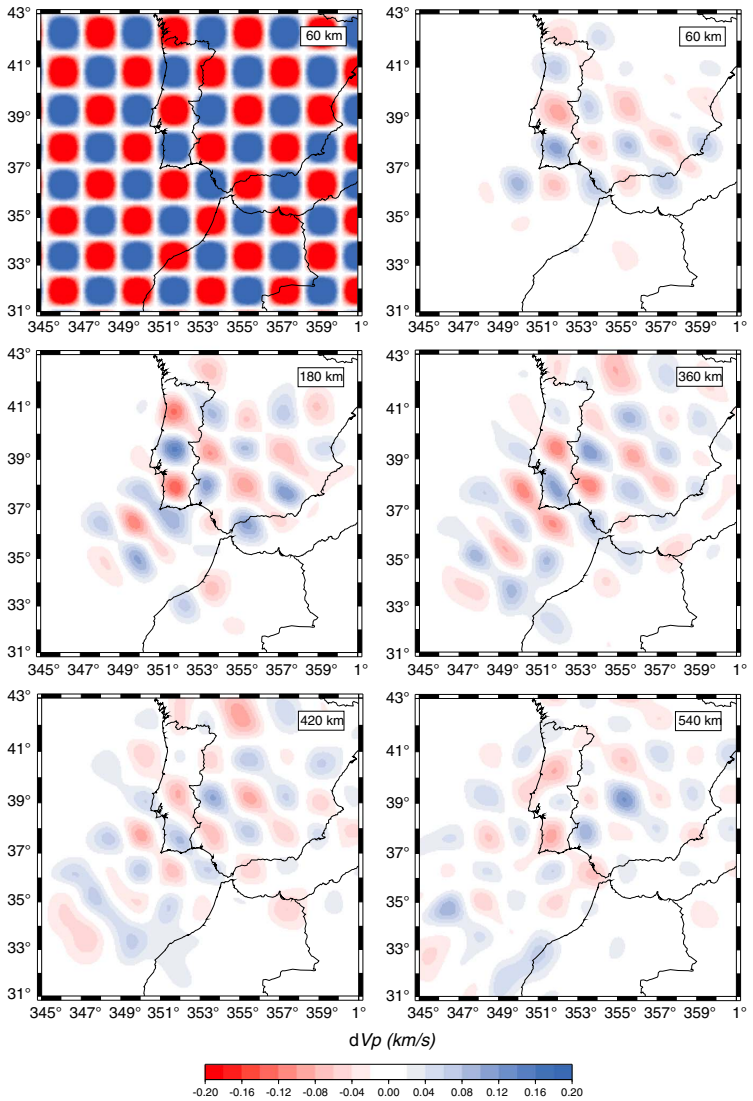

Figure 6. Input checkerboard velocity models and recovered patterns obtained by inverting a synthetic data set, for a sample of slices. The other slices are given in Figure S2. The test gives an indication of the regions of the model well constrained by the data.

the overall recovery of the checkerboard pattern is good. The velocity anomalies imaged with real data inversion that we interpret (see the following sections) fall in the well resolved part of the model and represent structures with wavelength comparable or larger than the scale length of our synthetic model.

5.2. Three-Dimensional Velocity model

[29] The tomographic inversion was carried out through five iterations, using a subspace dimension equal to 18 and the selected damping and smoothing values. In addition to velocity parameters, station terms were also included as unknowns in the inversion. These terms, one for each receiver, were computed mainly to absorb shallow velocity perturbations unconstrained by the teleseismic ray geometry and/or not completely accounted by the applied crustal correction (Figure S3 in supporting information).

[30] The final 3-D velocity model reduces the data variance by 26% from 0.53 to 0.39 s^2, which corresponds to an RMS data residual reduction from 727 to 628 m s. Although the variance improvement is not very high, we find that the computed velocity models show small differences (in size

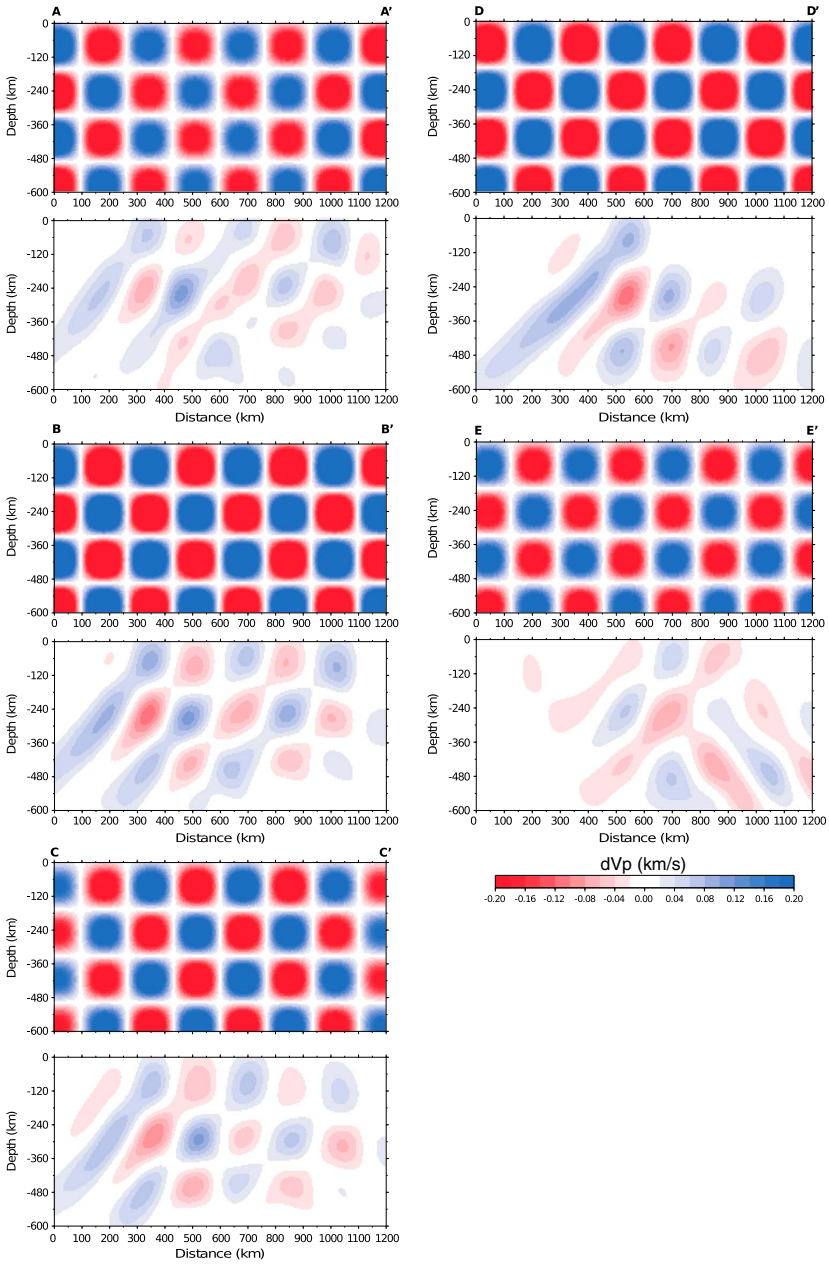

Figure 7. Input checkerboard velocity models and recovered patterns along the vertical slices crossing the grid model in (a) the east-west direction (AA′, BB′, and CC′) and (b) in the north-south direction (DD′ and EE′). The tracking latitude/longitude of the profiles (Figure 2) is the one used for the velocity cross sections.

and magnitude of the anomalies) with respect to realistic variations of the inversion parameters (damping, smoothing, and inversion grid size). We found that the data fit improved with the application of the crustal and baseline residual corrections. The level of RMS reduction depends particularly on the sparse array geometry and the data noise level, which is increased by the large number of bulletin data. Figure S4 shows the initial and solution traveltime residual histograms.

[31] In the following paragraphs, we describe the velocity field computed at the third iteration as only minor improvements (<1%) in the data fit were obtained through the successive inversion steps. A comparison with the residual analysis shows that the main anomalies in the 3-D model are consistent with the features shown in the residual maps (Figure 5). Figure 8 shows a series of horizontal slices extracted from the continuous *P* wave solution model at the labelled depths. At the shallowest depth (60 km), high-velocity anomalies are found in the

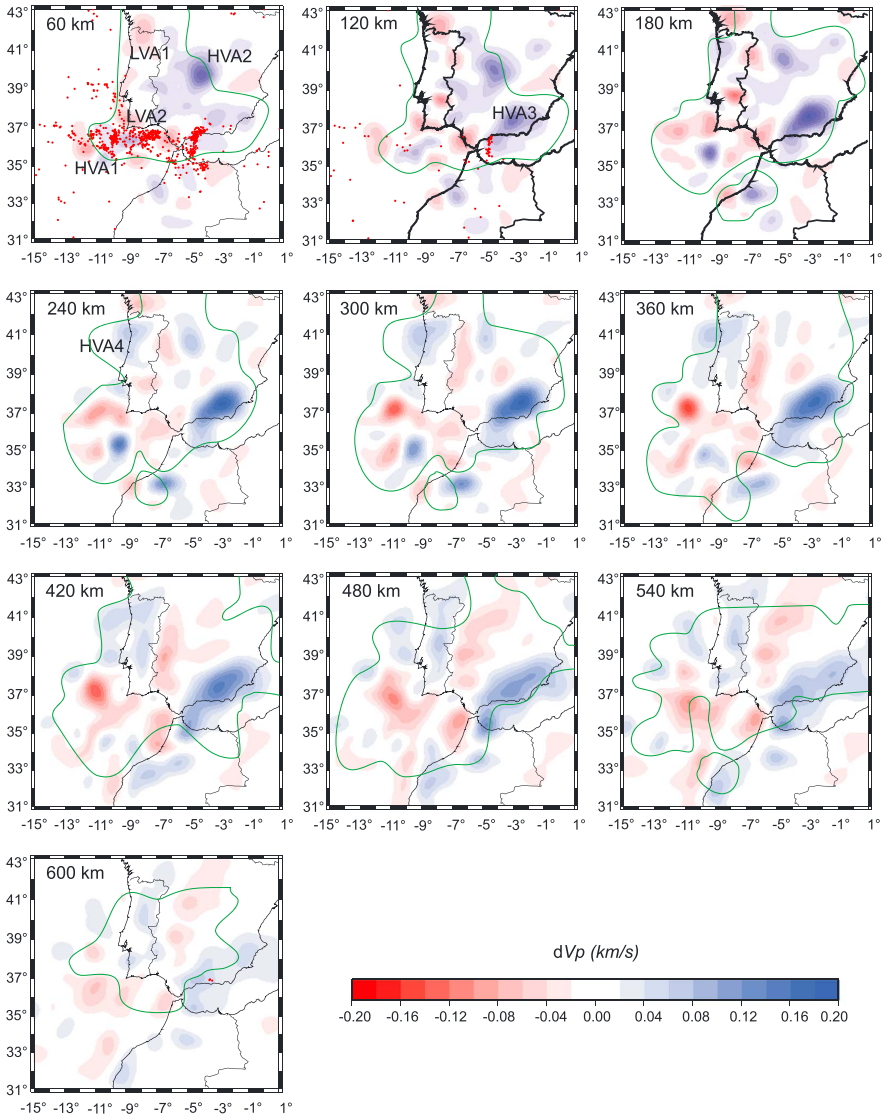

Figure 8. Horizontal slices through the 3-D solution model showing the lateral heterogeneities in the investigated upper-mantle structure. Labels show the depth at which the slices are taken. The *P* wave velocity model is represented as perturbations from the composite starting model described in subsection 3.2. Dots represent the local seismicity at the slice depth ±30 km. The green contour includes the resolved part of the model. This curve was drawn on the basis of the checkerboard test. Hypocenter locations of local seismicity comes from the Instituto Geográfico Nacional Spain catalog 1980–2010 (812 events with M > 3, and depth >35 km).

Atlantic ocean beneath the area covered by the NEAREST array (HVA1), in central Iberia (HVA2), and the Alboran Sea (HVA3). A low-velocity zone appears in northern Portugal (LVA1). A series of low-velocity anomalies (LVA2) are also visible going from the Gibraltar Strait to the Atlantic domain along the southwest Iberian Margin. At 120 km depth, HVA3 becomes larger extending from the Alboran Sea to the Granada region where it is stronger. At

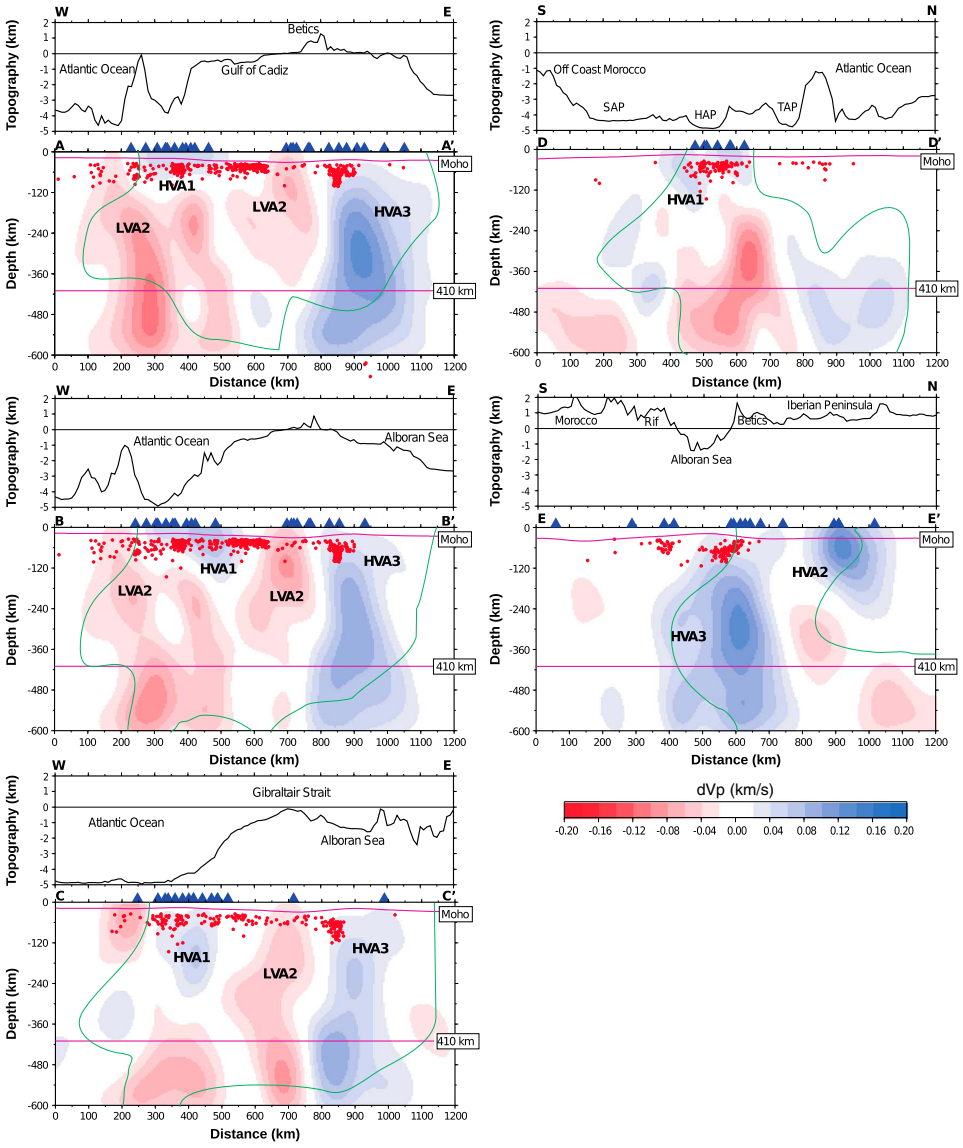

Figure 9. Cross sections through the 3-D solution model, computed along the great circle paths shown in Figure 2. (a) Cross sections AA′, BB′, and CC′ display the seismic structure from west to east. (b) Cross sections DD′ and EE′ cut the modeled volume from south to north. In DD′, SAP indicates the Seine Abyssal Plain; HAP, Horseshoe Abyssal Plain; TAP, Tagus Abyssal Plain. Blue triangles and red dots indicate the seismic stations and the subcrustal seismicity located within a 100 km wide zone centered on the profile. Topography/bathymetric profiles are from the Global-Integrated-Topo/Bathymetry Grid (GINA) [*Lindquist et al.*, 2004]. Moho topography is from the European Moho depth map [*Grad et al.*, 2009]. The green contour includes the resolved part of the model. Hypocenters deeper than 600 km show the deep events below the Granada region (AA′).

180–300 km depth, HVA3 becomes more pronounced and takes an L-shaped form. LVA1 now extends along the Portugal-Spain border toward the southwest Iberian Margin. Starting from 180 km depth down to 300 km, a clear high-velocity anomaly (HVA4) is imaged beneath northern Portugal. This feature becomes stronger at greater depths, extending to the Atlantic domain and to south Portugal. Below the NEAREST array, in the Gulf of Cadiz, LVA2 appears as a continuous east-west oriented band. HVA1 becomes stronger in this depth range.

[32] In the deeper part of the model, across the mantle transition zone at 360–600 km depth, HVA3 loses its curvature and is oriented northeast-southwest with its southern tip very close to the Gibraltar Strait. HVA4 extends north-south below Portugal and is bordered to the southwest (Atlantic domain) and to the east (central Iberia) by wide low-velocity anomalies. The bottom of the model at 600 km depth shows HVA3 below the Alboran Sea. Below HVA3, there is the deep seismicity corresponding to the Granada area.

[33] The west-east vertical profiles in Figure 9a, which cross the southern tip of the Iberian peninsula (AA′ and BB′) and the Gibraltar Strait (CC′), show the transition from the Atlantic to the Alboran domain. The three sections shows that HVA3 extends from ~60 km depth to the base of our model, and its maximum width is ~300 km in the EW direction below the Granada region (AA′). West of HVA3, beneath the Gulf of Cadiz, LVA2 extends from the top of the model down to ~250 km depth in AA′ and BB′, and it reaches the transition zone below the Gibraltar Strait in CC′. Going toward the Atlantic, we find (below the OBS array) HVA1 surrounded by LVA2. HVA1 is at least 200 km wide and is visible down to ~240 km depth. Section CC′ runs from the Atlantic ocean to the Alboran Sea across the Gibraltar Strait. It displays the part of HVA3 underlying the Alboran Sea and shows the width of the slab (100–200 km).

[34] The south-north cross sections in Figure 9b go through the Atlantic domain (DD′) and the Alboran Sea and Spain (EE′). Moving from south to north, section DD′ shows the north-south extension of HVA1, approximately 250 km, underlain by the deeper part of LVA2. Section EE′ crosses the Alboran Sea and shows the north-south extension of HVA3 (approximately 300 km). Subcrustal seismicity is distributed along an arc-shaped belt with the deeper events contained in the uppermost part of HVA3. To the north, below central Iberia, we find HVA2, which is visible down to ~200 km depth.

6. Discussion

[35] The investigated area, which includes the Alboran Sea and the Gulf of Cadiz, has proven to be quite complex, as reflected by its numerous and sometimes conflicting interpretations found in literature. Despite several geophysical measurements, a more comprehensive understanding of the area has been hindered by the lack of long-term instrumental coverage at sea. The NEAREST experiment, thanks to sea-floor seismological recordings, allows us to better resolve the upper-mantle structure of this area.

[36] In the following discussion, we will concentrate on the Atlantic (southwest Iberian margin and Cadiz Gulf) and Alboran Sea domains. We will discuss our results with reference to the two main geodynamic models mentioned in the introduction, i.e., subduction and delamination below the Alboran Sea.

6.1. Implications for Subduction With Rollback

[37] Consistently with previous tomography studies [*Calvert et al*., 2000; *Piromallo and Morelli*, 2003; *Spakman and Wortel*, 2004], our model shows a prominent high-velocity body below the Alboran Sea area (HVA3; Figures 8 and 9), suggesting the presence of cold, fast lithosphere visible down to the bottom of our model at 600 km. Thanks to our improved data set, with respect to previous studies, we are able to have a more reliable and defined image of this high-velocity body. HVA3 extends continuously from the southern Iberian Margin, below the Granada area where the scarce deep seismicity occurs, to under the Alboran Sea where there is intermediate-depth seismicity. Its geometry is L-shaped at shallower depths, and below 300 km it shows an elongated shape extending toward the Strait of Gibraltar and northern Morocco. Recent geophysical observations point to the effects of subduction (active or extinct) with westward rollback of oceanic lithosphere below the Alboran Sea. Anisotropy patterns are more consistent with a slab rollback model than with delamination or convective removal of lithosphere models [*Buontempo et al*., 2008; *Diaz et al*., 2010]. Seismic wave dispersion measurements point to the oceanic nature of the sinking lithosphere [*Bokelmann and Maufroy*, 2007]. All these observations suggest the existence of subduction with rollback, either active or extinct, below the Alboran Sea. Some authors have proposed the existence of a continuous lithospheric slab going from the Atlantic domain, across the Gibraltar Strait, to below the Alboran Sea [*Gutscher et al*., 2002, and references therein]. However, subduction, if it exists, must be either very slow or finished, as implied by GPS data, which show small to none differential motion across the Gibraltar Strait [*Stich et al*., 2006; *Serpelloni et al*., 2007]. An important element imaged in our model is a strong discontinuity between the seismic structure of the lithospheres in the Alboran and Atlantic domains (cross sections AA′, BB′, and CC′; Figure 9a), which is not resolved by previous tomographic studies. Although the part just south of the Gibraltar Strait is poorly resolved, especially in the shallower layers (Figure 8), the synthetic test shows that if there were a continuous slab coming from the Atlantic domain subducting below the Alboran Sea, we should be able to detect it.

6.2. Implications for Delamination

[38] Not all data can be explained by a subduction rollback mechanism. In fact, although deep seismicity is usually associated with a subduction process, the intermediate-depth seismicity below the Alboran Sea has a distribution which is not typical of subduction zones. In contrast to the nearby Calabrian Arc [Central Mediterranean, see for example *Montuori et al*., 2007], which also has a small curvature radius, there is no well defined Benioff plane. Intermediate-depth seismicity is found only within the top of the high-velocity body represented by HVA3 (Figures 9a and 9b). There seems to be a gap of seismicity between 30 and 50 km [*Buforn et al*., 2004], whereas a great majority of hypocenters are found above 150 km depth. Similarly, in the Vrancea area there is a gap between 40 and 70 km depth, while intermediate-depth seismicity is contained above 170 km depth. The seismic gap

for Vrancea has been explained as being possibly due to a decoupled seismogenic zone from the overriding plate [*Sperner et al*., 2001]. Furthermore, studies of igneous rocks also imply a complex geodynamic time-space evolution of the Western Mediterranean region. Thermal models for metamorphic units from the floor of the Alboran Basin are consistent with postcollisional rapid exhumation and associated heating. Geochemical and geochronological data show a transition from postcollisional subduction related to intraplate-type magmatism which occurred between 6.3 and 4.8 Ma [*Duggen et al*., 2005]. These processes imply a role for lithospheric delamination [*Platt*, 1998].

[39] Now we will try to determine a geodynamic evolution that is compatible with the above constraints and our tomography. The high-velocity body under the Alboran Sea area appears as isolated, adjacent to a pronounced low-velocity anomaly, and possibly separated from the overlying lithosphere. The recovered geometry suggests its evolution in time: the older section of the slab, corresponding to a planar deeper part (Figure 8), was subjected to rollback and not (or minimally) deformed by the Africa-Eurasia compression, whereas the younger, shallower part, found above ~300 km depth, was subjected both to rollback and compression and still is subjected to the African-Eurasia compression, which caused its arcuate shape. The separation of the high-velocity oceanic lithospheric structure in the Atlantic and Alboran domains in our model is consistent with a subduction with westward rollback process that has come to a stop east of the Gibraltar Strait, in agreement with the reconstruction proposed by *Lonergan and White* [1997]. This evolution of the slab geometry also agrees with the sequence of tectonic events reconstructed by *Iribarren et al*. [2007], who favor a westward slab retreat process active from Middle to Late Miocene time. Successively, oceanic subduction with rollback triggered continental-edge delamination under northwestern Africa and southern Iberia, as proposed by *Duggen et al.*, 2004 on the basis of petrological studies.

[40] Now we will comment other interesting parts of the model. A clear high-velocity anomaly, HVA1, is imaged for the first time under the NEAREST array, in an area roughly underlying the Horseshoe Abyssal Plain. This area is part of a diffuse convergent margin where old oceanic lithosphere is hypothesized [*Zitellini et al*., 2009; *Geissler et al*., 2010]. The thickness of HVA1 (~80–150 km in cross sections AA′–BB′; Figure 9a) agrees with values proposed in literature for old (~140 Ma) oceanic lithosphere [*McKenzie et al*., 2005; *Conrad and Lithgow-Bertelloni*, 2006]. Low-velocity anomalies are also visible, LVA1 and LVA2. LVA2 together with HVA1, define what we interpret as the passage from the Atlantic oceanic to the Iberian continental lithosphere (Figures 8 and 9a). The passage from HVA1 to LVA2, in the southwest-northeast direction, is in good agreement with the position of the south Portuguese stress regime anomaly observed by *Stich et al.* (2003) and marks the transition from oceanic to continental crust. HVA1 is visible from the crust down to sublithospheric depths. The east-west shape of HVA1 suggests incipient subduction (Figure 9a). In fact, the Gorringe bank (Figure 1) is considered an example of young incipient margin that could develop into a subduction zone [*Gurnis et al.*, 2004].

[41] At sublithospheric depths, below the Atlantic domain, we image wide areas of lower than standard *P* wave seismic velocities (LVA2), down to the bottom of our model. At these depths, it is commonly agreed that temperature plays a first order role in determining lateral seismic velocity heterogeneity [e.g., *Ranalli*, 1996], so we interpret such low values (down to approximately −0.16 km/s, about −2% of the reference value) as being due to the presence of a hot upper mantle. Isotopic and geochemical studies show that the magmatism of western Portugal and of the adjacent Atlantic domain that occurred during the Mesozoic can be explained by the presence of a common sublithospheric regional mantle melting anomaly [*Merle et al*., 2006; *Miranda et al*., 2009, and references therein]. Recent data show that this thermal anomaly is likely the source of tertiary and quaternary alkaline magmatism in the eastern North Atlantic region [*Merle et al*., 2006; *Grange et al*., 2010]. The space-time evolution of magmatism in this region has been explained by assuming that the Iberian plate has rotated (approximately 30° anticlockwise) above a fixed deep-rooted thermal anomaly (mantle plume) [*Sibuet et al.*, 2004; *Grange et al*., 2010].

[42] Although it is outside the main area of interest, we briefly comment on the persistent feature HVA4, imaged beneath Portugal from 180 km depth down to the bottom of the model. Generally, high-velocity bodies found at these depths are associated to colder and denser sinking lithosphere commonly considered of oceanic origin.

7. Conclusions

[43] Teleseismic tomography has been used to investigate the 3-D seismic structure of the upper mantle beneath the Alboran and Atlantic domains using seafloor recordings from the Gulf of Cadiz integrated with land-based seismic data. Thanks to the seafloor data we obtained a first image of the upper-mantle west of the Gibraltar Strait and an improved image of the Alboran Sea high-velocity anomaly. Information extracted from our model, crossed with independent geophysical and geological data, can be explained by a now extinct oceanic subduction below the Alboran domain, with westward rollback. Subduction stopped east of the Gibraltar Strait and was superseded by continental-edge delamination.

[44] The recovered geometry of the slab suggests its evolution in time. The older part, 360 km depth and below, is planar and could represent a time when rollback was the main force acting on the slab. The more superficial part, 300 km and above, has a curvature with a small radius which could be the result of the African-Eurasian compression acting on the slab in a clamp-like effect. This effect possibly contributed to the end of rollback and influenced the transition toward the new regime.

[45] The plate boundaries between oceanic lithosphere and continental domains are imaged in our 3-D model as lateral passages between high and low seismic velocity at lithospheric depths. The separation of two high-velocity bodies in the Atlantic and the Alboran domains suggests that the two lithospheres could have been subjected to independent geodynamic evolution, although in both the still active Eurasian-African compression played an important role.

[46] The results coming from this study are promising and show that long-term marine measurements are needed to define the upper-mantle structure west of the Gibraltar Strait and to clarify the passage between the uppermost mantle of the Atlantic and Alboran domains. In the future, by extending the area covered by the NEAREST array, especially off the Moroccan coast, we may get a more complete picture of crust and upper-mantle in the two domains and better understand their relation.

[47] **Acknowledgments.** The NEAREST project was funded by EC (GOCE, contract no. 037110). The authors thank Captain E. Gentile, the crew, G. Carrara, all participants of the R/V URANIA expeditions in 2007 and 2008, and N. Zitellini for coordinating the project. We are grateful to all people and institutions involved in the NEAREST project. We thank the "German Instrument Pool for Amphibian Seismology (DEPAS)," hosted by the Alfred Wegener Institute Bremerhaven, for providing the ocean-bottom seismometers. We thank John Platt and two anonymous reviewers for their useful comments which helped us improve the manuscript. We also thank T. Dahm and F. Frugoni for the useful discussions and D.-T. Ton-That for helping with the english revision. We thank N. Rawlinson for providing the original form of the inversion code, J. C. VanDecar and R. S. Crosson for making the MCCC code available, and F. Tilmann for useful suggestions. Most figures were produced using GMT software [*Wessel and Smith*, 1991].

References

Aki, K., A. Christofferson, and E. Husebye (1977), Determination of the three-dimensional seismic structure of the lithosphere, *J. Geophys. Res.*, *82*, 277–296.

Bijwaard, H., and W. Spakman (2000), Nonlinear global P-wave tomography by iterated linearised inversion, *Geophys. J. Int.*, *141*,71–82.

Blanco, M. J., and W. Spakman (1993), The P-wave velocity structure of the mantle below the Iberian Peninsula: Evidence for a subducted lithosphere below southern Spain, *Tectonophy.*, *221*, 13–34.

Bokelmann, G., and E. Maufroy (2007), Mantle structure under Gibraltar constrained by dispersion of body waves, *Geophys. Res. Lett.*, *34*, L22305, doi:10.1029/2007GL030964.

Bokelmann, G., E. Maufroy, L. Buontempo, J. Morales, and G. Barruol (2010), Testing oceanic subduction and convective removal models for the Gibraltar arc: Seismological constraints from dispersion and anisotropy, *Tectonophys.*, doi:10.1016/j.tecto.2010.08.004.

Buforn, E., M. Bezzeghoud, A. Udıas, and C. Pro (2004), Seismic sources on the Iberia-African plate boundary and their tectonic implications, *Pure Appl. Geophys.*, *161*, 623–646.

Buontempo, L., G. H. R. Bokelmann, G. Barruol, and J. Morales (2008), Seismic anisotropy beneath southern Iberia from SKS splitting, *Earth Planet. Sci. Lett.*, *273*, 237–250, doi:10.1016/j.epsl.2008.06.024.

Calvert, A., E. Sandvol, D. Seber, M. Barazangi, F. Vidal, G. Alguacil, and N. Jabour (2000), Propagation of regional seismic phases (Lg and Sn) and Pn velocity structure along the Africa–Iberia plate boundary zone: Tectonic implications, *Geophys. J. Int.*, *142*, 384–408, doi:10.1046/j.1365-246x.2000.00160.x.

Carrara G., and NEAREST Team (2008), NEAREST 2008 CRUISE PRELIMINARY REPORT R/V URANIA, 1st Aug 2008- 04th Sept 2008, Technical Report ISMAR-CNR,(http://nearest.bo.ismar.cnr.it/documentation/REPORT_NEAREST_2008_completo.pdf).

Conrad, C. P., and C. Lithgow-Bertelloni (2006), Influence of continental roots and asthenosphere on plate-mantle coupling, *Geophys. Res. Lett.*, *33*, L05312, doi:10.1029/2005GL025621.

Díaz, J., and J. Gallart (2009), Crustal structure beneath the Iberian Peninsula and surrounding waters: a new compilation of deep seismic sounding results, *Phys. Earth Planet. Int.*, *173*, 181–190, doi:10.1016/j.pepi.2008.11.008.

Díaz, J., J. Gallart, A. Villaseñor, F. Mancilla, A. Pazos, D. Córdoba, J. A. Pulgar, P. Ibarra, and M. Harnafi (2010), Mantle dynamics beneath the Gibraltar Arc (western Mediterranean) from shear–wave splitting measurements on a dense seismic array, *Geophys. Res. Lett.*, *37*, L18304, doi:10.1029/2010GL044201.

Duggen, S., K. Hoernle, P. Van Den Bogaard, and C. Harris (2004), Magmatic evolution of the Alboran Region: the role of subduction in forming the western Mediterranean and causing the Messinian Salinity Crisis, *Earth and Planet. Sci. Lett.*, *218*, 91–108.

Duggen, S., K. Hoernle, P. Van Den Bogaard, and D. Garbe-Schönberg (2005), Post-Collisional fransition from subductionto intraplate-type magmatism in the westernmost Mediterranean: Evidence for continental-edge delamination of subcontinental lithosphere, *J. Petr.*, *46*, 6, doi:10.1093/petrology/egi013.

Dziewonski, A. M., and F. Gilbert (1976), The effect of small, aspherical perturbations on travel times and a re-examination of the corrections for the ellipticity, *Geophys. J. R. Astron. Soc.*, *44*, 7–17.

Evans, J. R., and U. Achauer, (1993), Teleseismic velocity tomography using the ACH method: theory and application to continental-scale studies, in Seismic Tomography: Theory and practice, edited by H. M. Iyer and K. Hirahara, pp. 319–360, Chapman & Hall, London.

Faccenna C., C. Piromallo., A. Crespo-Blanc, L. Jolivet, and F. Rossetti (2004), Lateral slab deformation and the origin of the western Mediterranean arcs, *Tectonics,*. *23*, TC1012, doi:10.1029/2002TC001488.

Fullea, J., M. Fernàndez, H. Zeyen, and J. Vergés (2007), A rapid method to map the crustal and lithospheric thickness using elevation, geoid anomaly and thermal analysis. Application to the Gibraltar Arc System and adjacent zones, *Tectonophys.*, *430*, 97–117, doi:10.1016/j.tecto.2006.11.003.

Fullea, J., J. C. Afonso, M. Fernàndez, J. Vergés, and H. Zeyen (2010), The structure and evolution of the lithosphere—asthenosphere boundary beneath the Trans-Mediterranean region, *Lithos*, *120*(1–2), 74–95.

Geissler, W. H., et al. (2010), Focal mechanisms for sub–crustal earthquakes in the Gulf of Cadiz from a dense OBS deployment, *Geophys. Res. Lett.*, *37*, L18309, doi:10.1029/2010GL044289.

Grad, M., T. Tiira, and ESC Working Group (2009), The Moho depth map of the European Plate, *Geophys. J. Int.*, *176*, 279–292, doi:10.1111/j.1365-246X.2008.03919.x.

Grange M., U. Schärer, R. Merle, J. Girardeau, and G. Cornen (2010), Plume-Lithosphere Interaction during Migration of Cretaceous Alkaline Magmatism in SW Portugal: Evidence from U-Pb Ages and Pb-Sr-Hf Isotopes, *J. Petr.*, *51*(5), 1143–1170.

Grevemeyer I., N. Kaul, and A. Kop (2009), Heat flow anomalies in the Gulf of Cadiz and off Cape San Vincente, Portugal , *Mar. Petrol. Geol.*, *26*, 795–804.

Gudmundsson, O., J. H. Davies, and R. W. Clayton (1990), Stochastic analysis of global traveltime data: mantle heterogeneity and random errors in the ISC data, *Geophys. J. Int.*, *102*(1), pp. 25–43.

Gurnis, M., C. Hall, and L. Lavier (2004), Evolving force balance during incipient subduction, *Geochem. Geophys. Geosyst.*, *5*, Q07001, doi:10.1029/2003GC000681.

Gutscher, M. A., J. Malod, J. P. Rehault, I. Contrucci, F. Klingelhoefer, L. Mendes–Victor, and W. Spakman (2002), Evidence for active subduction beneath Gibraltar, *Geology*, *30*, 1071–1074, doi:10.1130/0091-7613.

Gutscher, M.-A., S. Dominguez, G. K. Westbrook, and P. Leroy (2009), Deep structure, recent deformation and analog modeling of the Gulf of Cadiz accretionary wedge: Implications for the 1755 Lisbon earthquake, *Tectonophys.*, *475*, 85–97, doi:10.1016/j.tecto.2008.11.031.

Husen, S., R. Quintero, E. Kissling, and B. Hacker (2003), Subduction-zone structure and magmatic processes beneath Costa Rica constrained by local earthquake tomography and petrological modelling, *Geophys. J. Int.*, *155*, 11–32.

Iribarren, L., J. Vergés, F. Camurri, J. Fullea, and M. Fernandez (2007), The structure of the Atlantic-Mediterranean transition zone from the Alboran Sea to the Horseshoe Abyssal Plain (Iberia-Africa plate boundary), *Mar. Geol.*, *243*, 97–119.

Kennett, B. L. N., M. S. Sambridge, and P. R. Williamson (1988), Subspace methods for large scale inverse problems involving multiple parameter classes, *Geophys. J. Int.*, *94*, 237–247.

Kennett, B. L. N., E. R. Engdhal, and R. Buland (1995), Constraints on seismic velocities in the Earth from traveltimes, *Geophys. J. Int.*, *126*, 555–578.

Koch, M. (1985), A numerical study on the determination of the 3-D structure of the lithosphere by linear and non-linear inversion of teleseismic travel times, *Geophys. J. R. Astron. Soc.*, *80*, 73–93.

Leveque, J.-J., and F. Masson (1999), From ACH tomographic models to absolute velocity models, *Geophys. J. Int.*, *137*, 621–629.

Leveque, J. J., L. Rivern, and G. Wittlinger (1993), On the use of the checker-board test to assess the resolution of tomographic inversions, *Geophys. J. Int.*, *115*, 313–318.

Lindquist, K. G., K. Engle, D. Stahlke, and E. Price (2004), Global Topography and Bathymetry Grid Improves Research Efforts, *Eos Trans. AGU*, *85*(19), 186.

Lonergan, L., and N. White (1997), Origin of the Betic-Rif mountain belt, *Tectonics*, *16*, 504–522.

McKenzie D., J. Jackson, and K. Priestley (2005), Thermal structure of oceanic and continental lithosphere, *Earth Plan. Sci. Lett.*, *233*, 337–349.

Merle, R., U. Schärer, J. Girardeau, and G. Cornen (2006), Cretaceous seamounts along the continent-ocean transition of the Ibeian margin: U-Pb ages and Pb-Sr-Hf isotopes, *Geochem. Cosmochim. Acta*, *70*, 4950–4976.

Miranda R., V. Valadares, P. Terrinha, J. Mata, M. do Rosario Azevedo, M. Gaspar, J. C. Kulberg, and C. Ribeiro (2009), Age constraints on

the Late Cretaceous alkaline magmatism on the West Iberian Margin, *Cretaceous Res.*, *30*, 575–586.

Montuori, C., G. B. Cimini, and P. Favali (2007), Teleseismic tomography of the southern Tyrrhenian subduction zone: New results from seafloor and land recordings. *J. Geophys. Res.*, *112*, B03311, doi:10.1029/2005JB004114.

Nolet, G. (2008), A Breviary of Seismic Tomography: Imaging the Interior of the Earth and the Sun. Cambridge University Press, Cambridge, 344 pp., ISBN 978-0-521-88244-6.

Piromallo, C., and A. Morelli (2003), P wave tomography of the mantle under the Alpine-Mediterranean area, *J. Geophys. Res.*, *108*(B2), 2065, doi:10.1029/2002JB001757.

Platt, J. P., and R. L. M. Vissers (1989), Extensional collapse of thickened continental lithosphere: A working hypothesis for the Alboran Sea and the Gibraltar arc, *Geology*, *17*, 540–543.

Platt, J. P. (1998), Thermal evolution, rate of exhumation, and tectonic significance of metamorphic rocks from the floor of the Alboran extensional basin, western Mediterranean, *Tectonics*, *17*, 5, 671–689.

Polyak, B. G., et al. (1996), Heat flow in the Alboran Sea, western Mediterranean. *Tectonophys*. *263*, 191–218.

Ranalli, G. (1996), Seismic tomography and mineral physics, in Seismic Modelling of the Earth Structure, edited by E. Boschi, G. Ekström, and A. Morelli., pp. 443–459, Ist. Naz. di Geofis., Rome.

Rawlinson, N., A. M. Reading, and B. L. N. Kennett (2006), Lithospheric structure of Tasmania from a novel form of teleseismic tomography, *J. Geophys. Res.*, *111*, B02301, doi:10.1029/2005JB003803.

Rovere M., C. R. Ranero, R. Sartori, L. Torelli, and N. Zitellini (2004), Seismic images and magnetic signature of the Late Jurassic to Early Cretaceous Africa-Eurasia plate boundary off SW Iberia, *Geophys. Int.*, *158*, doi:10.1111/j.1365-246X.2004.02339.x.

Royden, L. H. (1993), Evolution of retreating subduction boundaries formed during continental collision, *Tectonics*, *12*, 629–638.

Sallarès, V., A. Gailler, M.-A. Gutscher, D. Graindorge, R. Bartolomé, E. Gràcia, J. Díaz, J. J. Dañobeitia, and N. Zitellini (2011), Seismic evidence for the presence of Jurassic oceanic crust in the central Gulf of Cadiz (SW Iberian margin), *Earth Planet. Sci. Lett.*, doi:10.1016/j.epsl.2011.09.003.

Sartori, R., L. Torelli, N. Zitellini, D. Peis, and E. Lodolo (1994), Eastern segment of the Azores–Gibraltar line (central–eastern Atlantic): an oceanic plate boundary with diffuse compressional deformation, *Geology*, *22*, 555–558.

Seber, D., M. Barazangi, A. Ibenbrahim, and A. Demnati (1996), Geophysical evidence for lithospheric delamination beneath the Alboran Sea and Rif-Betic mountains, *Nature*, *379*, 785–790.

Serrano, I., D. Zhao, and J. Morales (2003), Seismic tomography from local crustal earthquakes beneath eastern Rif mountains of Morocco, *Tectonophys.*, *367*, 187–201.

Serpelloni, E., G. Vannucci, S. Pondrelli, A. Argnani, G. Casula, M. Anzidei, P. Baldi, and P. Gasperini (2007), Kinematics of the Western Africa-Eurasia plate boundary from fochal mechanisms and GPS data, *Geophys. J. Int.*, *169*, 1180–1200, doi:10.1111/j.1365-246X.2007.03367.x.

Sethian, J. A., and A. M. Popovici (1999), 3-D traveltime computation using the fast marching method, *Geophysics*, *64*, 516–523.

Shomali, Z. H., F. Keshvari, J. Hassanzadeh, and N. Mirzaei (2011), Lithospheric structure beneath the Zagros collision zone resolved by non-linear teleseismic tomography, *Geophys. J. Int.*, *187*, 394–406, doi:10.1111/j.1365-246X.2011.05150.x.

Sibuet, J.-C., S. P. Srivastava, and W. Spakman (2004), Pyrenean orogeny and plate kinematics, *J. Geophys. Res.*, *109*, B08104, doi:10.1029/2003JB002514.

Spakman W., and M. J. R. Wortel (2004), A tomographic view on Western Mediterranean Geodynamics, in The Transmed Atlas, the Mediterranean region from crust to mantle, edited by W. Cavazza, F. M. Roure, W. Spakman, G. M. Stampfli, P. A. Ziegler eds., Springer, 31–52.

Spemer, B., F. Lorenz, K. Bonjer, S. Hettel, B Müller, and F. Wenzel (2001), Slab break-off or abrupt cut or gradual detachment? New insights from Vrancea Region (SE Carpathians, Romania)., *Terra Nova*, *13/3*, 172–179.

Stich, D., C. J. Ammon, and J. Morales (2003), Moment tensor solutions for small and moderate earthquakes in the Ibero-Maghreb region, *J. Geophys. Res.*, *108*(B3), 2148, doi:10.1029/2002JB002057.

Stich, D., F. Mancilla, and J. Morales (2005), Crust-mantle coupling in the Gulf of Cadiz (SW-Iberia), *Geophys. Res. Lett.*, *32*, L13306, doi:10.1029/2005GL023098.

Stich, D., E. Serpelloni, F. Mancilla, and J. Morales (2006), Kinematics of the Iberia-Maghreb plate contact from seismic moment tensors and GPS observations, *Tectonophysics*, *426*, 295–317.

Tilmann, F. J., H. M. Benz, K. F. Priestley, and P. G. Okubo (2001), P-wave velocity structure of the uppermost mantle beneath Hawaii from travel time tomography, *Geophys. J. Int.*, *146*, 594–606.

Tornè, M., M. Fernàndez, M. C. Comas, and J. I. Soto (2000), Lithospheric structure beneath the Alboran Basin: results from 3D gravity modeling and tectonic relevance, *J. Geophys. Res.*, *105*(B2), 3209–3228.

Turner, S. P., J. P. Platt, R. M. M. George, S. P. Kelley, D. G. Pearson, and G. M. Nowell (1999), Magmatism associated with orogenic collapse of the Betic–Alboran Domain, SE Spain, *J. Petrol.*, *40*, 1011–1036.

VanDecar, J. C., and R. S. Crosson (1990), Determination of teleseismic relative phase arrival times using multi-channel cross correlation and least squares, *Bull. Seis Soc. Am.*, *80*, 150–169.

Wessel, P., and W. H. Smith (1991), Free software helps map and display data, *Eos Trans. AGU*, *72*(41), 441.

Zeck, H. P. (1996), Betic-Rif orogeny: Subduction of Mesozoic Tethys lithosphere under eastward drifting Iberia, slab detachment shortly before 22 Ma, and subsequent uplift and extensional tectonics, *Tectonophys.*, *254*, 1–16.

Zeyen, H., P. Ayarza, M. Fernàndez, and A. Rimi (2005), Lithospheric structure under the western African-European plate boundary: A transect across the Atlas Mountains and the Gulf of Cadiz, *Tectonics*, *24*, TC2001, doi:10.1029/2004TC001639.

Zitellini, N., et al. (2009), The quest for the Africa–Eurasia plate boundary west of the Strait of Gibraltar, *Earth Planet. Sci. Lett.*, *280*, 13–50, doi:10.1016/j.epsl.2008.12.005.

README file describing the auxiliary material for Paper 2012JB009607

New insights from seismic tomography on the complex geodynamic evolution of two adjacent domains: Gulf of Cadiz and Alboran Sea

S. Monna[1], G.B. Cimini[1], C. Montuori[1], L. Matias[2] , W.H. Geissler[3], and P. Favali[1]

1 Istituto Nazionale di Geofisica e Vulcanologia, Rome, Italy.
2 Centro de Geofísica, Universidade de Lisboa, Lisbon, Portugal.
3 Alfred-Wegener-Institut für Polar- und Meeresforschung, Bremerhaven, Germany.

Monna, S., G.B. Cimini, C. Montuori, L. Matias, W.H. Geissler, and P. Favali (201x), New insights from seismic tomography on the complex geodynamic evolution of two adjacent domains: Gulf of Cadiz and Alboran Sea, J. Geophys. Res, xxx, XXXXXX,doi:10.1029/2012JB009607, 2012.

Introduction
This auxiliary material is composed by 4 Figures and 1 Table. The captions below explain the meaning of the material.

Figure S1 Examples of MCCC analysis for three events of moderate magnitude: a) 2 October 2007, Alaska Peninsula, Mw6.3. b) 14 April 2008, South Sandwich Islands, Mw6.0. c) 27 July 2008, Central Mid-Atlantic Ridge, Mw5.9.

Figure S2 Input checkerboard velocity models and recovered patterns obtained by inverting a synthetic data set for the slices not shown in Figure 6.

Figure S3 Station terms computed by the 3D inversion. Positive station terms imply the presence of shallow low-velocity anomalies; negative station terms imply the presence of shallow high-velocity anomalies. Station terms represent shallow structure beneath each receiver that cannot be adequately constrained by teleseismic ray geometry and crustal correction.

Figure S4. a) Initial and b) solution relative traveltime residual histograms.

Table S1. Information on the seismic stations installed during the NEAREST project.

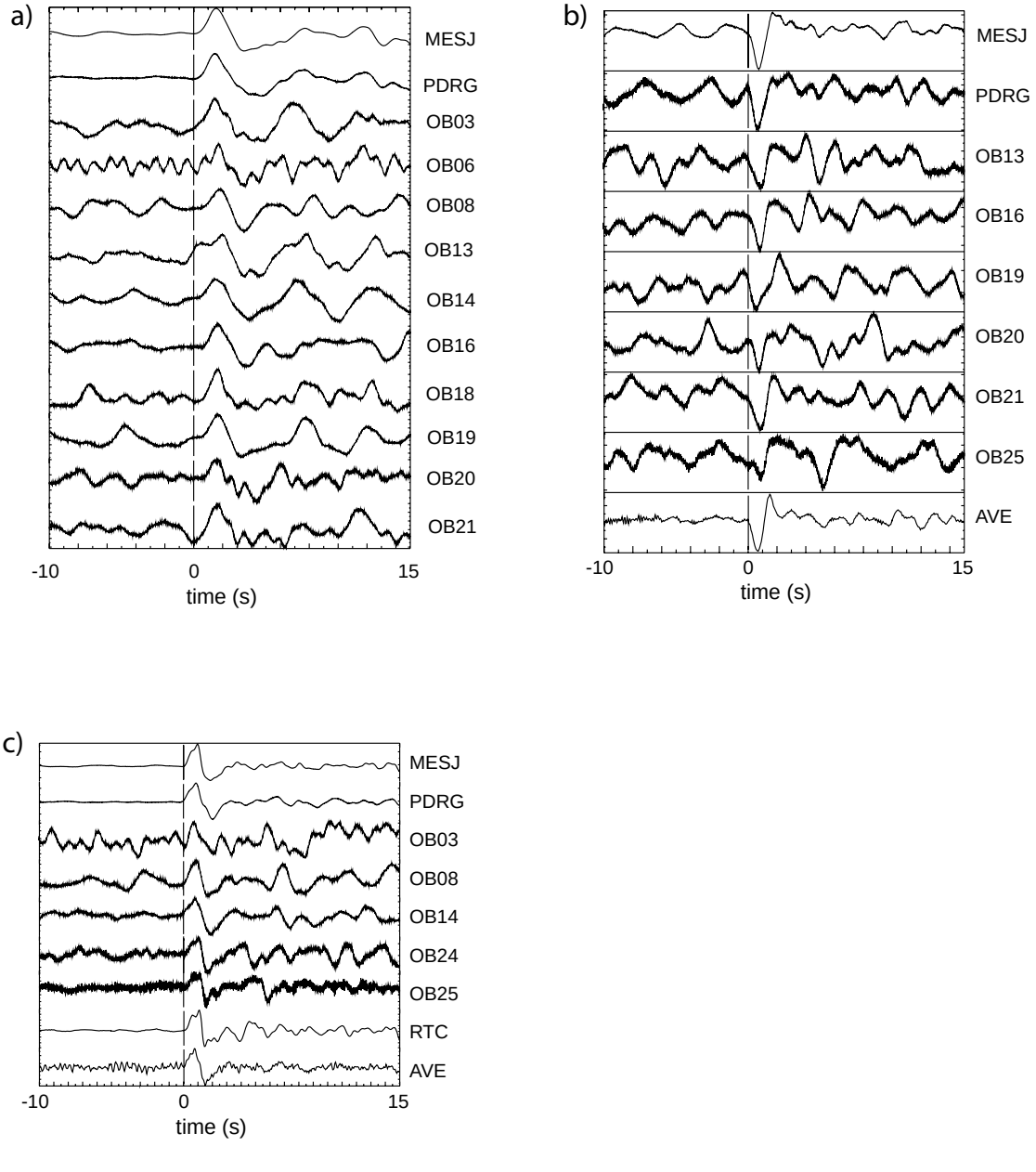
a)
MESJ
PDRG
OB03
OB06
OB08
OB13
OB14
OB16
OB18
OB19
OB20
OB21
-10
0
15
time (s)
b)
MESJ
PDRG
OB13
OB16
OB19
OB20
OB21
OB25
AVE
-10
0
15
time (s)
c)
MESJ
PDRG
OB03
OB08
OB14
OB24
OB25
RTC
AVE
-10
0
15
time (s)

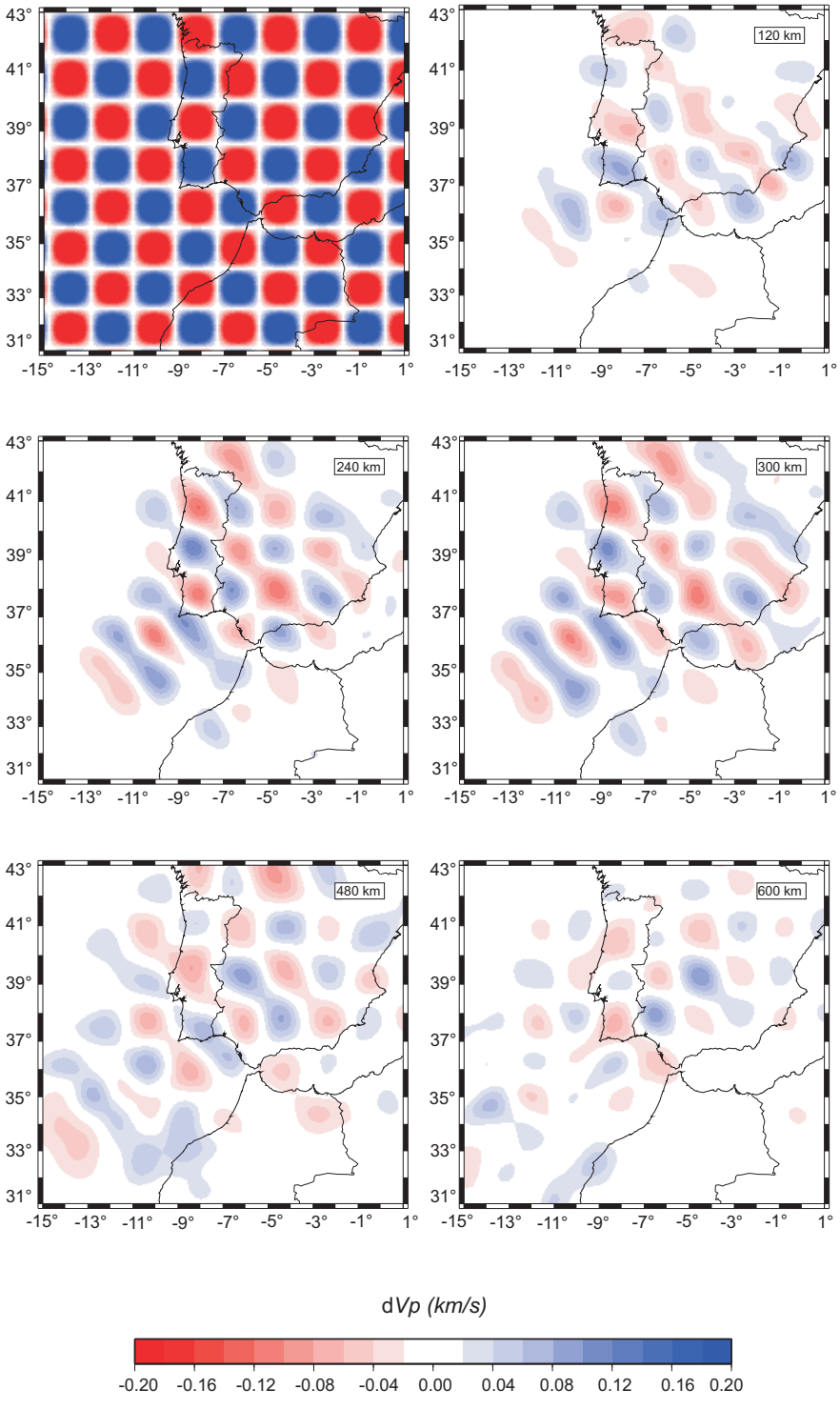
120 km
240 km
300 km
480 km
600 km
43°
41°
39°
37°
35°
33°
31°
-15° -13° -11° -9° -7° -5° -3° -1° 1°
dVp (km/s)
-0.20 -0.16 -0.12 -0.08 -0.04 0.00 0.04 0.08 0.12 0.16 0.20

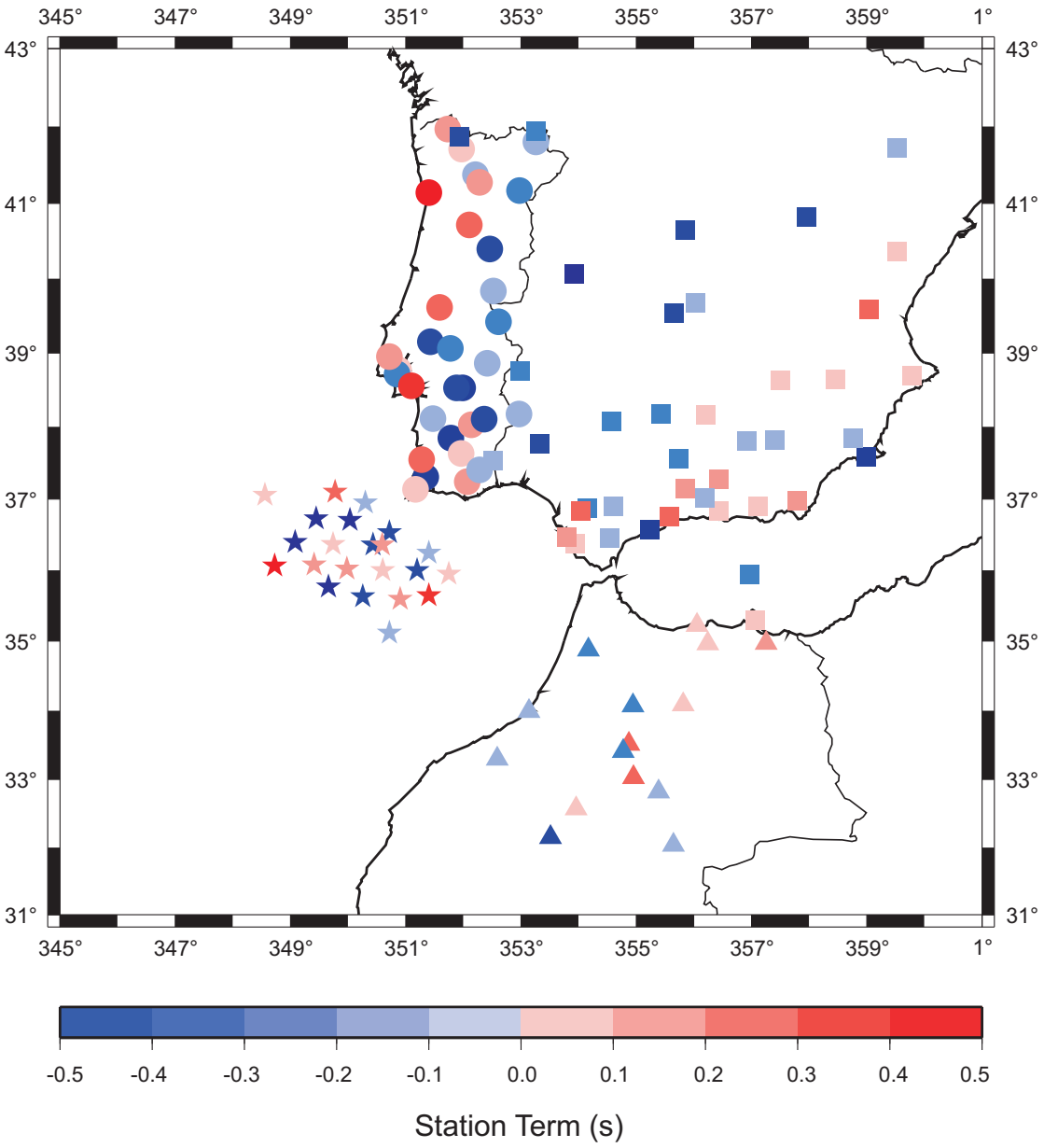
345°
347°
349°
351°
353°
355°
357°
359°
1°
43°
41°
39°
37°
35°
33°
31°
-0.5
-0.4
-0.3
-0.2
-0.1
0.0
0.1
0.2
0.3
0.4
0.5
Station Term (s)

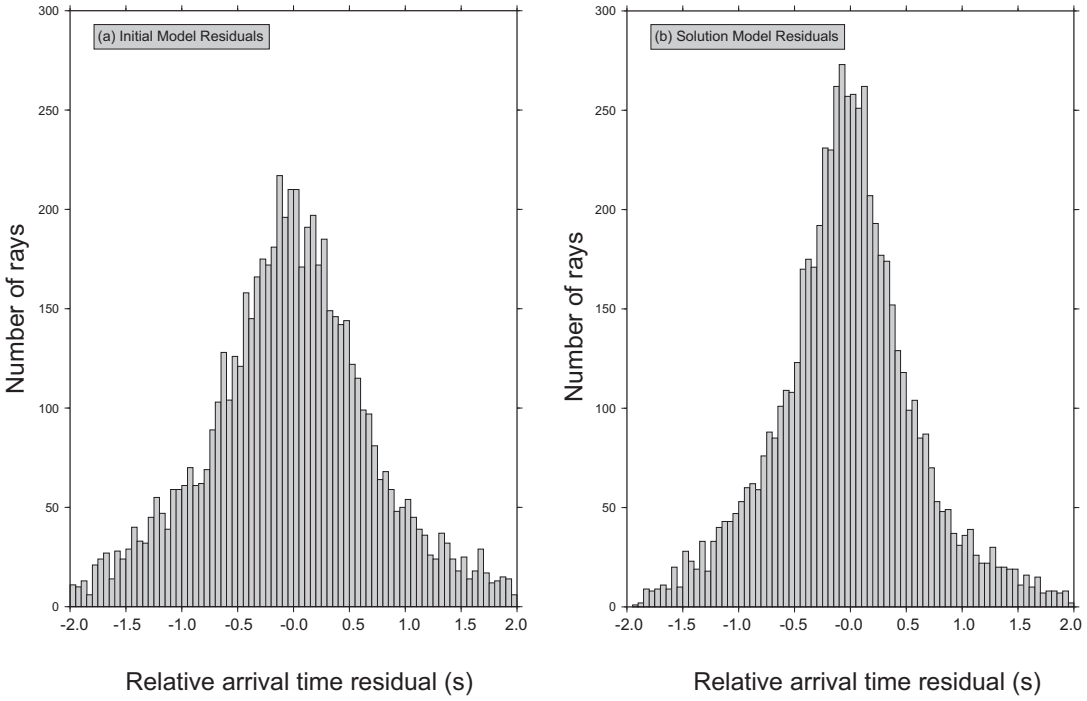
(a) Initial Model Residuals
(b) Solution Model Residuals
Number of rays
Relative arrival time residual (s)
0
50
100
150
200
250
300
-2.0
-1.5
-1.0
-0.5
-0.0
0.5
1.0
1.5
2.0

Offshore					
Code	Lat	Lon	Alt(m)	Sensors	F0
OBS01	37.05	-11.45	-5100	CMG-40T-OBS	60sec
OBS02	37.026	-10.734	-2270	CMG-40T-OBS	60sec
OBS03	37.100	-10.230	-3932	CMG-40T-OBS	60sec
OBS04	36.9518	-9.7018	-1993	CMG-40T-OBS	60sec
OBS05	36.73	-10.55	3095	CMG-40T-OBS	60sec
OBS06	36.7085	-9.969	-2956	CMG-40T-OBS	60sec
OBS07	36.365	-9.495	-3205	CMG-40T-OBS	60sec
OBS08	36.3976	-10.9212	-4671	CMG-40T-OBS	60sec
OBS09	36.37	-10.260	-4811	CMG-40T-OBS	60sec
OBS10	36.2499	-8.6014	-2067	CMG-40T-OBS	60sec
OBS11	36.0655	-11.2728	-4855	CMG-40T-OBS	60sec
OBS12	36.0805	-10.5899	-4860	CMG-40T-OBS	60sec
OBS 13	36.02	-10.02	-4494	CMG-40T-OBS	60sec
OBS14	36.0007	-9.4003	-4212	CMG-40T-OBS	60sec
OBS15	35.9985	-8.7997	-3357	CMG-40T-OBS	60sec
OBS16	35.9496	-8.2505	-2069	CMG-40T-OBS	60sec
OBS 17	37.778	-10.939	4765	CMG-40T-OBS	60sec
OBS18	35.7113	-10.339	-4605	CMG-40T-OBS	60sec
OBS19	35.6325	-9.7505	-4287	CMG-40T-OBS	60sec
OBS20	35.5981	-9.0995	-3449	CMG-40T-OBS	60sec
OBS21	35.6456	-8.6005	-2566	CMG-40T-OBS	60sec
OBS22	35.350	-10.400	-4095	CMG-40T-OBS	60sec
OBS23	35.117	-9.285	-3747	CMG-40T-OBS	60sec
OBS24	36.5315	-9.2819	-2439	CMG-40T-OBS	60sec
OBS25	36.3597	-9.5714	-3234	CMG-40T-OBS	60sec
GEOST	36.3646	-9.4814	-3207	CMG-40T-OBS	60sec
Onshore					
Code	Lat	Lon	Alt	Sensors	F0
PDRG	38.108	-7.638	102	STS2	120sec
MESJ	37.84	-8.22	230	STS2	120sec

4 Spectral ratio synthetic tests

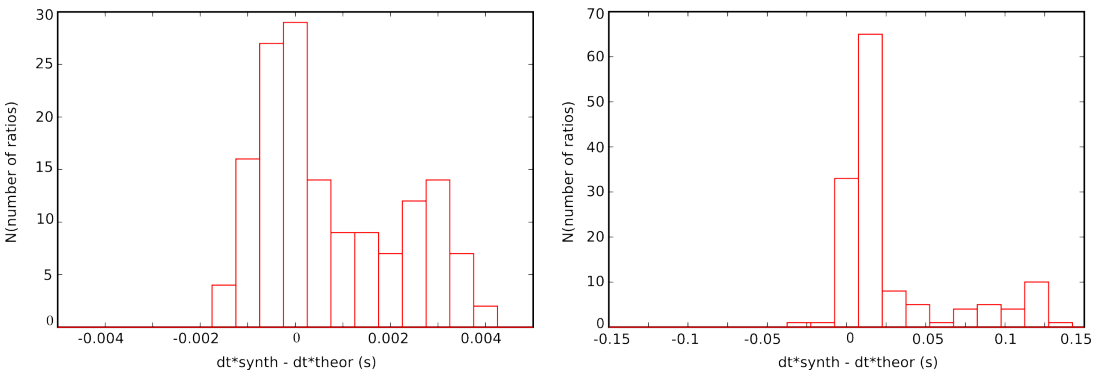

(a) P-wave (b) S-wave

Figure .1: Error distribution no noise added.

In this chapter we show more results of synthetic tests applied to the spectral ratio algorithm. With reference to the ratios calculated for the model shown in figure 2.6 we consider the error distribution for six trials when no noise is added to data, is shown in figure .1 for P (150 spectral ratios) and S (132 spectral ratios). In this case for the P-wave $\frac{\overline{E(\delta t^*{}_p)}}{\Delta\delta t^*{}_p} = 0.001s/0.2s \simeq 0.5\%$, while for the S-wave $\frac{\overline{E(\delta t^*{}_s)}}{\Delta\delta t^*{}_s} = 0.02s/0.7s \simeq 3\%$. There are bigger absolute errors but also bigger δt^* variations between the two sectors thus lowering the relative error. As expected the greatest errors come from the waves traveling through the low-Q sector (epicentral distances $\geq$ 250 km), which have lower amplitudes and smaller frequency band with good signal to noise ratio. If pseudo-random gaussian noise is added, there is still a good fit both for P (figure .2(a)) and S (figure .2(b)). Increasing noise levels does increase scattering about the theoretical curves but not dramatically. Added noise amplitude is up to about 5 % of the signal amplitude for waves traveling in the low-Q sector. The effect of noise, as expected, is to increase relative error amplitude but it is still within an acceptable range (figures .2, .3): $\frac{\overline{E(\delta t^*{}_p}}{\Delta\delta t^*{}_p} = 0.003s/0.2s \simeq 2\%$, $\frac{\overline{E(\delta t^*{}_s}}{\Delta\delta t^*{}_s} = 0.03s/0.7s \simeq 4\%$. It is interesting to notice that the addition of random noise tends to "correct" the shape of the histograms with respect to the noiseless case (compare figures .1 and .3). Also, this systematic trend is visible when a different reference station is used, as shown for example in figure .4.
Another important effect of noise on spectral ratios calculated for the S-wave is in controlling the acceptable frequency interval where the signal to noise ratio is greater than a chosen threshold. In order to have a sufficient number (or any at all) of accepted S-wave spectral ratios for the stations receiving low-Q waves the condition on the width of the accepted frequency interval needs to be relaxed by choosing a smaller value (for example

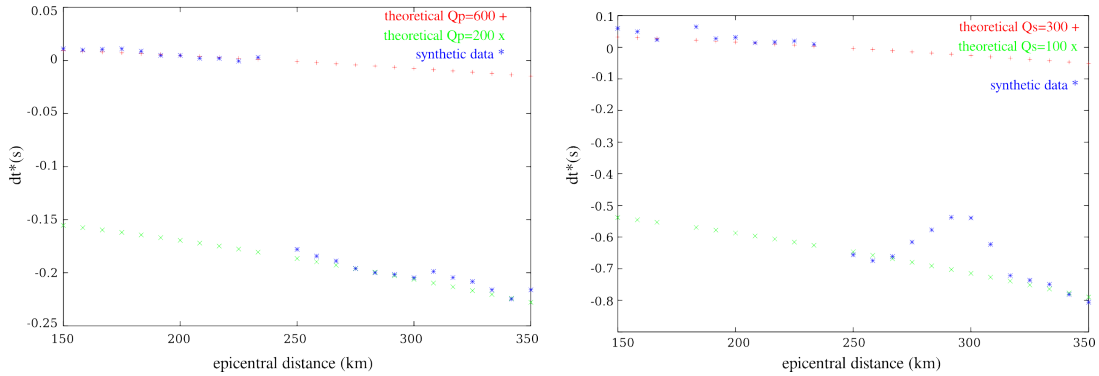

(a) P-wave. $Q_1 = 600$, $Q_2 = 200$, $V_p = 7.8km/s$ (b) S-wave. $Q_1 = 300$, $Q_2 = 100$, $V_s = 4.5km/s$

Figure .2: Effect of data noise on the difference between synthetic and theoretical δt^*. Model as shown in Figure 2.6, with noise added.

2 Hz instead of 3 Hz) than the one valid for P and S waves traveling in a high-Q region. In this way the spectral ratios are calculated on a smaller portion of the spectrum.

Tests were also performed using different lengths of the data record on which the ratio is performed (from 3 s up to 7 s), showing that results of the algorithm are stable as long as the interval includes the seismic phase. Also, the algorithm is stable with respect to the choice of the reference station (figure .4 shows one example) and the moving average used to smooth the spectra has little influence on the results.

The effect of source parameters, i.e. source depth and magnitude was also verified. In the previous case the source was at 355 km depth and had Mw=3.5. If the source magnitude is increased to Mw=4.5 (30 times the seismic moment of the previous case) the results are comparable to the lower magnitude case, which is not surprising since this factor is frequency independent (the corner frequency was kept constant) and so it doesn't influence the calulation of δt^*. On the other hand it is expected that the source depth, which determines the path of the wave to the station, will be a relevant factor for δt^*.

In conclusion, in the case of simple Earth models, for which we can find an analytical relation for δt^*, the calculation of δt^* using spectral ratios fits well with the theoretical curves when there is a strong variation in Q_p and Q_s. Also, the algorithm is sensitive to variations in δt^* in the case of a homogeneous model when it depends on epicentral distance only, although relative errors are quite large for the S-wave. Finally, the tests show that the algorithm is stable with respect to the addition of gaussian noise and variation of significant controlling parameters, supporting the method's reliability.

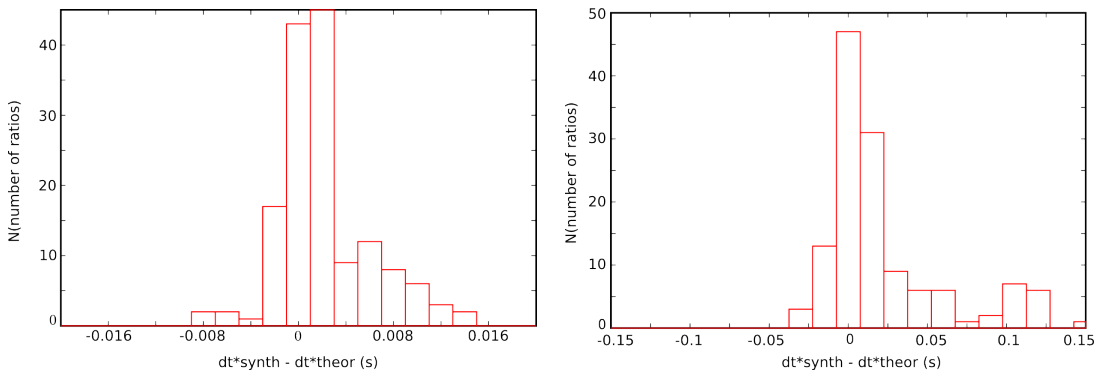

(a) P-wave (b) S-wave

Figure .3: Effect of noise on error distribution.

A final observation regards the bump observed for the S-waves at epicentral distances between about 250-300 km (for example figure .4). This effect comes from the S-wave distorsion due to the generation of an inhomogeneous P-wave at the free surface at the critical angle. In fact, the critical distance X_c when inhomogeneous P-wave appear can be easily calculated. For an incident S_v wave converted to a reflected P wave, we have $(1/V_s)\sin(i) = (1/V_p)\sin(r)$, and for the critical angle $(1/V_s)\sin(i_c) = (1/V_p)$ so $i_c = 35.2°$. Given hypocentral depth $h = 355$ km, $V_p = 7.8$ km/s, and $V_s = 4.5$ km/s, we have $X_c = h\arctan(35.2°) = 250.7$ km, in agreement with the synthetic tests.

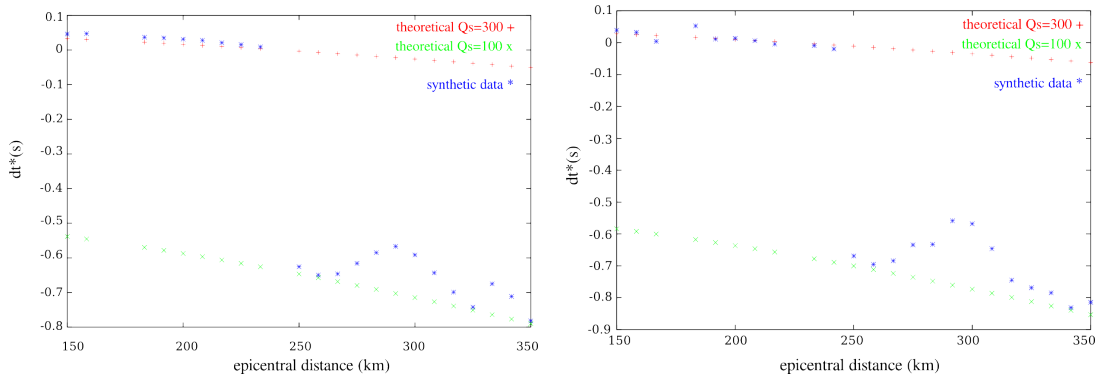

(a) Reference station # 12

(b) Reference station # 10

Figure .4: Effect of reference station on δt^* (S-wave example)

5 Algorithm for t^* calculation

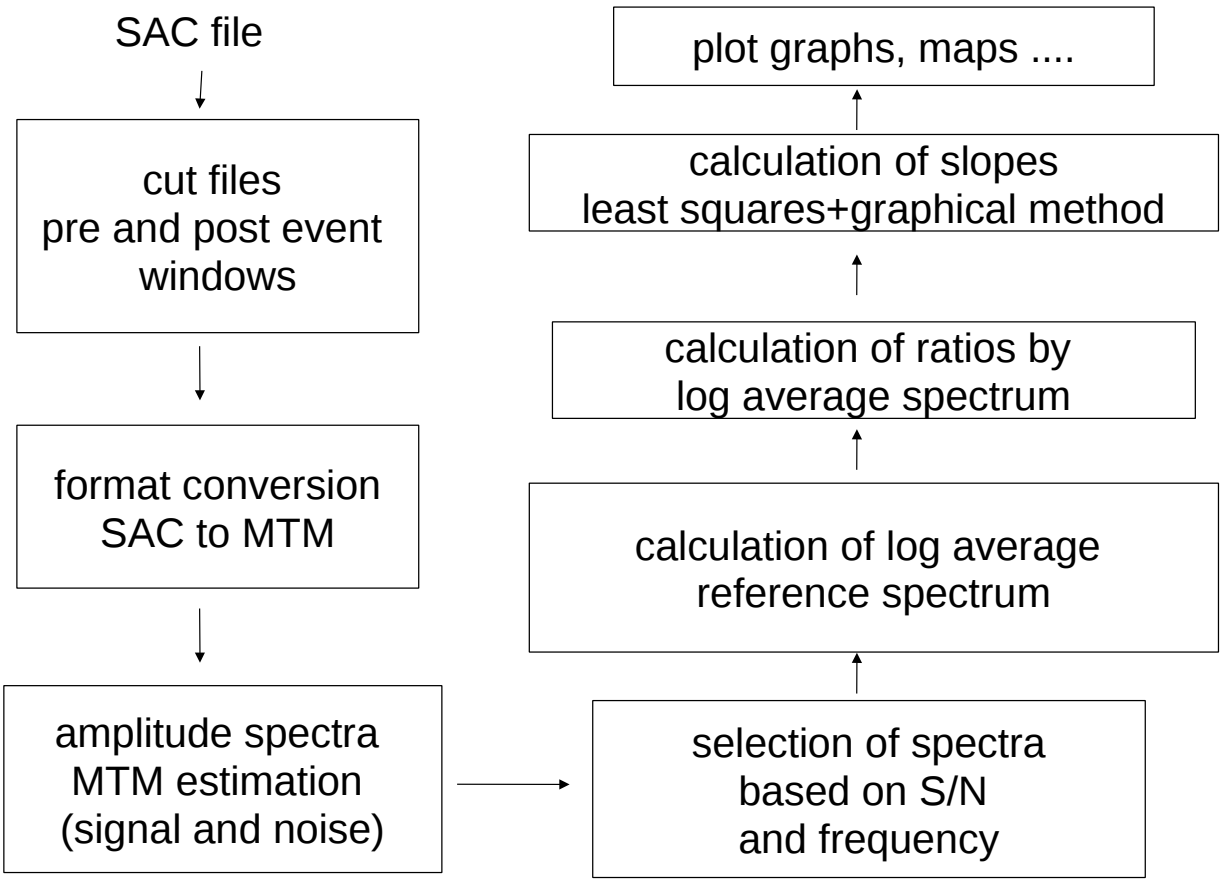

The entire procedure is automated by using linux bash shell scripts and can be used by anyone given some training. The seismic data is handled through SAC macros. The spectral estimation is by the MultiTaper Method (Park et al. 1987; Mann and Lees 1996. Graphical part for linear approximation is by GNUPLOT (Williams et al. 2010) and linear approximation is by a GNU OCTAVE (Eaton 2002) algorithm. Some graphs are generated by GMT scripts (Wessel and Smith 1991).

6 Multi-channel cross-correlation

To pick first P-arrivals we employed the multi-channel cross-correlation technique (MCCC; VanDecar and Crosson 1990) on unfiltered data. This technique is semi-automated in the sense that it needs to be applied event by event, and the algorithm parameters need to be calibrated. MCCC calculates relative traveltime residuals by maximizing a cross-corelation matrix. MCCC outputs the temporal shifts, for each channel (Z component of the station recording a given event), that give the optimal alignment of the waveforms. To apply MCCC bash-Shell scripts were applied and theoretical traveltimes calculated via tau-p (Crotwell et al. 1999). Then, after a visual inspection there is a first selection of waveforms and then MCCC is applied. MCCC output shows the (optimal) cross-correlation coefficient for each trace and warns the user if cycles are skipped (which could mean that the wrong phase was picked for one or more traces). Also, an error is associated with the residual for each trace. Finally, a set of traces is chosen and an output file is obtained with the picks and their associated errors. Tilmann et al. (2001) have argued that the errors calculated by MCCC are underestimated, in fact, it can happen that the error is a fraction of the sampling interval. For this reason, taking a more conservative approach, we have decided to multiply this error by a factor of 1.5-2.

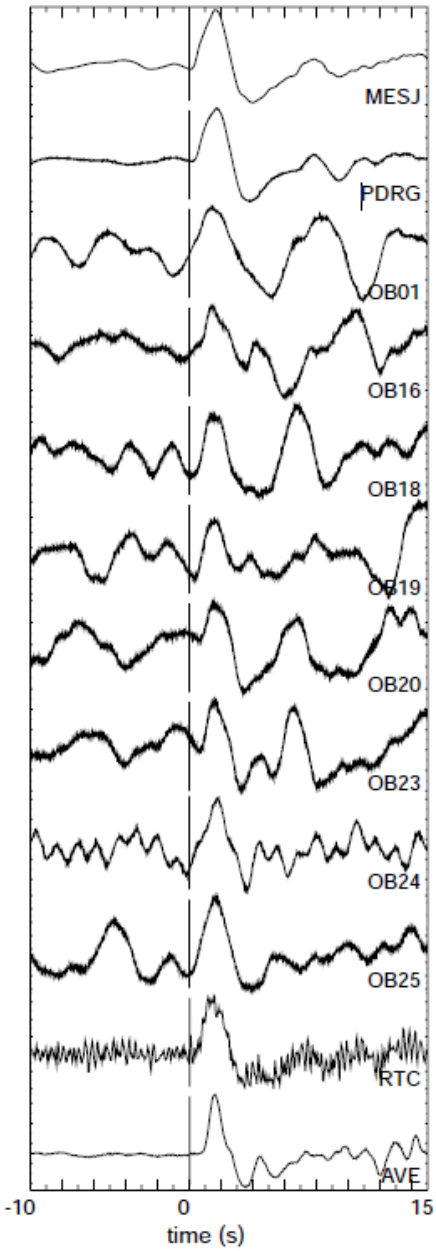

Figure .5: Waveform stack obtained on a M6.3 event from Tarapaca Chile, after applying MCCC. Epicentral distance from the OBS array $\simeq 80°$.

7 Aknowledgements

Through the years I have received help from many people. First I would like to acknowledge Prof. Dahm's guidance through the evolution of my work. I greatly benefited from his rigorous approach to scientific problems and from his positive attitude. During my visits to the Geophysics department in Univerisy of Hamburg, I found an atmosphere of support, welcome, and friendliness. I would particularly like to thank two colleagues there: Simone Cesca for kindly sharing his office, Lars Krieger for his help, and Christel Meinardt for her support with administrative matters. I would also like to thank Ms. Kutlu, Ms. Dal Corso, Araksik Martirosian, and Alberto Frepoli for their kind support.

I was able to continue my Ph.D. research thanks to the financial support of INGV (Istituto Nazionale di Geofisica e Vulcanologia, Italy) and in particular thanks to the RIDGE group coordinators Paolo Favali and Laura Beranzoli. The Geophysics Department at University of Hamburg also helped fund my visits to its campus.

I would like to thank Bruno Alessandrini for helping me better understand the extent to which a tomography model can be interpreted and not to take an inversion result for granted even when the residuals are very small. Harley Benz has kindly provided me the FDTOMO code has personally given me precious suggestions on several occasions. Thanks to Tiziana Sgroi for discussions on seismo-tectonics of the Southern Tyrrhenian area and Pasquale De Gori for discussions on seismic tomography. Finally, I thank Thomas Brown for his encouragement and help in this long project.

I would like to give specific thanks and acknowledge the contributions of the people who have been involved in each of the three papers the comprise this dissertation.

Regarding the papers presented in this thesis, many people were involved with different aspects of the work.

1) Umbria-Marche: Luisa Filippi has helped me greatly thanks to her experience on local earthquake data and with the FDTOMO code. Luisa and Bruno Alessandrini helped me with my first steps in the world of LET. Paolo Favali and Laura Beranzoli have greatly improved the paper by applying a critical but constructive approach. Carlo Doglioni was particularly kind for his friendly review and very useful suggestions. Francesco Frugoni patiently answered my questions on the Umbria-Marche stratigraphic sequence. Of course thanks are due to the people behind the seismic data collection from the different networks: the Italian National Seismic Network (INGV), and the temporary networks (French and Italian Institutions). Finally, during most of this work I was a guest of the Italian National Seismic Survey.

2) Southern Tyrrhenian Sea-Southern Apennines: My Ph.D. tutor and co-author Prof. Torsten Dahm has followed all the steps of this work, and his suggestions were especially important during the development of the spectral ratio calculation procedure and during the model interpretation part. Of course this work would not be possible without the

data coming from the Italian National Seismic Network managed by INGV. Andrea Argnani and Francesco Frugoni have greatly helped me to understand geological aspects related to Italy and the Tyrrhenian Sea.

3) Cadiz Gulf-Alboran Sea: Giovanni Battista Cimini performed the teleseismic tomography inversion and has improved the procedure by including crustal corrections. Caterina Montuori was very involved in the data processing and the interpretation of the model, which required getting acquainted with a massive amount of literature on the area. Wolfram Geissler and Luis Matias were fundamental in the NEAREST passive OBS experiment, in the data pre-processing and in their constructive and critical contribution to the paper. I would like to thank Frederik Tilmann for kindly providing the cross-correlation code with some very useful explanations, and J. C. VanDecar and R. S. Crosson for making it available. Thanks to all the people who contributed to the NEAREST project, in particular to the passive OBS part (WP3), and Nevio Zitellini, the project coordinator. Of course thanks are due to the crews and personnel involved with the OBS deployment and retrieval (R/V Sarmiento de Gamboa, UTM/CSIC, Spain; R/V Urania CNR, Italy). Prof. Dahm has followed the work-course and provided useful suggestions and critique.

Finally, I thank my parents and Dan-Thanh for their convincing and positive support during my very long course of studies, even in my moments of doubt.